Weldability of a Dual-Phase Sheet Steel by the Gas Metal Arc Welding Process

by

Trevor J. Burns

A thesis
presented to the University of Waterloo
in fulfillment of the
thesis requirement for the degree of
Master of Applied Science
in
Mechanical Engineering

Waterloo, Ontario, Canada, 2009

I hereby declare that I am the sole author of this thesis. This is a true copy of the thesis, including any required final revisions, as accepted by my examiners.

I understand that my thesis may be made electronically available to the public.

Trevor J. Burns

Abstract

Dual-phase (DP) sheet steels have recently been used for automotive manufacturing to reduce vehicle weight and improve fuel economy. Dual-phase steels offer higher strength without reduced formability when compared to conventional high strength low alloy (HSLA) steels and so thinner gauge DP sheet steel can be used to meet the same design requirements. The DP steel microstructure is comprised of dual-phase mixture hard martensite particles, which provide strength, in a soft ferrite matrix, which provides ductility. Fusion welding processes, such as gas metal arc welding (GMAW), are used to join DP sheet steels; however, the heat input from fusion welding can cause the martensite islands to decompose into softer islands of tempered martensite. This can reduce the joint efficiency and cause premature localized necking in the region where tempered martensite forms.

The weldability of coated 1.65 mm Cr-Mo DP600 (dual-phase 600 MPa) sheet steel welded using the pulsed gas metal arc welding (GMAW-P) process was assessed. Processes with a range of GMAW-P weld heat inputs were developed to make full penetration bead-on-plate welds that had similar bead geometry. The range of weld heat input was between 193 J/mm and 347 J/mm. Uniaxial transverse weld tensile tests of welds that were made at high heat input fractured in the heat affected zone (HAZ), welds that were made at low heat input fractured in the base metal (BM), which is most desirable, and at intermediate welding heat inputs, fracture locations were mixed. Heat input was compared to corresponding weld HAZ half-width measurements and it was shown that as heat input increased, HAZ half-width increased as well; this followed an expected linear trend. The ultimate tensile strength (UTS) was not diminished in specimens that exhibited BM fracture and 100% joint efficiency was achieved. Welded DP600 specimens that failed in the HAZ had minimal (< 5%) reduction of UTS.

During the welding process development phase, the same range of heat input was used to make bead-on-plate full penetration welds onto coated 1.80 mm HSLA (high strength low alloy) sheet steel to

assess its weldability. It was found that all of the welds fractured in the BM during uniaxial transverse weld tensile testing and, therefore, had achieved 100% joint efficiency.

It was shown that by increasing the strength grade of DP sheet steel to DP780 and DP980, 100% joint efficiency was not retained. To better understand why high heat input welding caused HAZ fracture, low heat and high heat input welds that had consistently fractured in the BM and HAZ, respectively, were used to assess the differences between BM and HAZ fracture mechanisms.

Fractographic analysis of BM and HAZ fracture surfaces of the dual-phase steels showed that fracture had occurred due to micro-void coalescence for both types of failure; however, the HAZ fracture had greater reduction of cross-sectional area and the surface had more numerous and smaller shear tearing ledges. Examination of the microstructure showed that there were decomposed martensite islands in the region the HAZ fracture; these likely increased ductility and led to a more significant tri-axial stress state. However, decomposed martensite was also found in the HAZ of welds that had BM fracture. The low and high heat input welds had similar reduction of martensite percentage (~3 – 4%) in the subcritical (SC) region of the HAZ; immediately below the Ac_1 temperature where transformation from a BCC ferrite to FCC austenite occurs. Each weld HAZ was assessed with an average through-thickness microhardness (ATTH) profile. Four distinct regions of hardness were identified: hard intercritical (IC), which was formed by heating between Ac_1 and Ac_3 temperatures, soft subcritical (S-SC), hard subcritical (H-SC), and base-metal (BM). The width of the S-SC was slightly larger (~10%) for the HAZ fracture weld; however, the degree of softening (~8 – 11 $VHN_{ATTH/200g}$) compared to BM hardness was similar for both. It appeared that HAZ fracture could be shifted to the BM by reducing the width of the S-SC so that the surrounding hard IC (+40 – 50 $VHN_{ATTH/200g}$) and H-SC (+5 – 10 $VHN_{ATTH/200g}$) could support the S-SC and prevent a tri-axial stress state from developing; this is similar to increased strength of brazed joints caused by optimal gap width.

Using this knowledge base, new welds were made onto different sheet thickness (1.20 mm and 1.80 mm) Cr-Mo DP600 sheet steels and onto higher strength grades of 1.20 mm Cr-Mo DP780 and 1.20 mm Mn –Si DP980 sheet steels. These were compared with the heavily studied 1.65 mm Cr-Mo DP600 sheet steel described above. The 1.80 mm DP600 sheet steel (welded with the same range of heat input) fractured in the BM during all uniaxial transverse weld tensile tests; this was caused by a 4% increase in sheet thickness. The majority of thinner 1.20 mm welds fractured in the HAZ; there was one BM fracture for the DP600 sheet steel. Only the DP980 had a significant drop in UTS (~28%), and the DP600 and DP780 approached 100% joint efficiency (based on the UTS). The same distinct regions of hardness were observed for Cr-Mo DP600 and Cr-Mo DP780. The Mn-Si DP980 did not exhibit an H-SC and had a significantly wider S-SC (~80% wider) when compared to welds of similar heat input and sheet thickness. This suggested that the presence of an H-SC region could improve joint efficiency. It also suggested that material chemistry played an important role in reducing the extent of softening during welding; however, the martensite percentage for the DP600, DP780, and DP980 were different (approximately 7.5%, 20%, and 46%, respectively) and this could also have affected the observed S-SC widths.

It was concluded that GMAW-P welded DP600 sheet steel shifted from a HAZ fracture to a more desirable BM fracture location during uniaxial transverse weld tensile testing as the S-SC region of hardness was narrowed. A narrow S-SC was supported by the adjacent hard IC and H-SC regions, which limited diffuse necking in the vicinity of the S-SC region. Diffuse necking continued to thin out material in the BM region, where there was a greater reduction in cross-sectional area prior to the onset of localized necking, and, therefore, the BM entered a state of higher stress than the S-SC and failed once it reached UTS. This was not observed for a higher strength grade of DP780 sheet steel, which had higher degree of softening, because, diffuse necking was not sufficient to reduce the BM cross-sectional area and hence the level of stress in the S-SC reached the UTS before the UTS was reached in the BM.

Acknowledgements

I would like to extend this thank you towards my supervisors, Dr. D.C. Weckman and Dr. N. Zhou for their invaluable guidance and support that helped me during my studies.

I thank Elliot Biro for the many hours of project discussion, including help with the Lepera's Tint etch, the arrangement of lab time at the ArcelorMittal Dofasco R&D facilities, and supplying my labs at the University of Waterloo with Dofasco steel. I would also like to thank Jon Vandeventer of ArcelorMittal Dofasco for conducting uniaxial tensile tests and arranging the machining of tensile specimens.

I would like to thank Victor H. Baltazar H. and Dr. Sushanta Kumar Panda of the Centre for Advanced Materials Joining (CAMJ) for discussion of issues pertaining to the welding of dual-phase steel. I would also like to thank Siu Kei Tang and Elliot Powidajko of CAMJ for helping with laboratory equiptment setup and usage. Thanks to Lee Upshall for the setup of a data acquition system for my welding station.

Thank you to Rick Forgett, Charlie Boyle, Jorge Cruz, Kwai Chan, and John Potzold of the Engineering Machine Shop for help with machining components used during my studies and answering questions about proper maching practice.

And finally, thank you to my Mother and Father for supporting me, guiding me, and helping out with an occansional meal.

You cannot direct the wind,

But you CAN adjust your sails...

Spoken like an engineer.

You CAN direct the wind,

Just give me some time...

Spoken like a true engineer.

(at time of writing, www.google.com returned only 9 entries for "you can direct the wind")...

(of course, there were 1,010,000 entries for "you can control the wind", but who's counting anyways?)

Table of Contents

List of Tables

List of Figures

Nomenclature

Microstructural Regions:

- Ac_1 Microstructure: Temperature at which austenization begins
- Ac_3 Microstructure: Temperature at which austenization is completed
- AGB Prior Austenite Grain Boundary
- BM Base Metal
- FB Fusion Boundary
- FZ Fusion Zone
- GG Grain Growth Region
- GR Grain Refined Region
- HAZ Heat Affected Zone
- IC Intercritical region of microstructure
- H-SC Hardened Subcritical region of microstructure
- SC Subcritical region of microstructure
- SP Supercritical Region
- S-SC Softened Subcritical region of microstructure
- TM Tempered Martensite
- UB Upper Bainite

All Other Nomenclature:

- α Ferrite Phase
- γ Austenite Phase
- $\% \gamma_A$ Volume Fraction of Austenite for Process A
- $\% \gamma_B$ Volume Fraction of Austenite for Process B
- Fe_3C Cementite

- σ_{YS} Yield Stress
- σ_{UTS} Ultimate Tensile Stress
- A_{BM} Tensile Specimen: Cross-sectional Area of Base Metal Microstructural Region
- A_{SC} Tensile Specimen: Cross-sectional Area of Subcritical Microstructural Region
- AC Alternating Current
- AHSS Advanced High Strength Steel
- ANSI American National Standards Institution
- ARDP As-Rolled Dual-Phase
- ASM International Society for Materials (formerly American Society for Metals)
- ASTM American Society for Testing and Materials
- ATTH Average Through-Thickness Hardness
- AWS American Welding Society
- BCC Body Centered Cubic
- BCT Body Centered Tetragonal
- $C_{Martensite}$ Carbon Percentage in Martensite Phase
- $C_{Ferrite}$ Carbon Percentage in Ferrite Phase
- $C_{Nominal}$ Carbon Percentage in Parent Steel Chemistry
- CAFE Corporate Average Fuel Economy
- CCT Continuous Cooling Time-Temperature Transformation
- CE Carbon Equivalent
- CO Carbon Monoxide
- CO_2 Carbon Dioxide
- CTWD Contact-Tip-to-Workpiece Distance
- d Diameter
- DC Direct Current
- DCEN Direct Current Electrode Negative

- DCEP Direct Current Electrode Positive
- DOE Design of Experiments
- DOS Degree of Softening
- EDS Energy Dispersive Spectrometry
- FCC Face Centered Cubic
- GA Galvanealed coating
- GI hot-dipped Galvanizied coating
- GMAW Gas Metal Arc Welding
- GMAW-SC Gas Metal Arc Welding in Short Circuit Metal Transfer Mode
- GMAW-CV Gas Metal Arc Welding with a Constant Voltage
- GMAW-P Gas Metal Arc Welding with a Pulsed Voltage
- DP Dual-phase
- f Data Sampling Frequency
- h Sheet Thickness
- H_{rel} Relative Linear Heat Input
- $Hardness_{BM}$ Average Vickers Hardness in the Parent Steel
- $Hardness_{HAZ,min}$ Minimum Vickers Hardness Occuring in the Weld HAZ
- HSLA High Strength Low Alloy
- HTDP Heat-Treated Dual-Phase
- i LEM-LT 505-S output voltage
- I Current
- ipm Inches Per Minute
- LBW Laser Beam Welding
- L_{weld} Measured Length of the Weld
- $\%M_A$ Volume Fraction of Martensite for Process A
- $\%M_B$ Volume Fraction of Martensite for Process B

- $M_{C\%,A}$ Weight Percent Carbon in a Martensite Island for Process A
- $M_{C\%,B}$ Weight Percent Carbon in a Martensite Island for Process B
- M_S Martensite Start Temperature
- MIG Metal Inert Gas
- N Number of Voltage/Current Data Points Collected
- P Applied Load during Uniaxial Tensile Testing
- P_{avg} Average Welding Power
- RSW Resistant Spot Welding
- S Local True Stress in a Uniaxial Tensile Specimen for a given Weld Region
- SEM Scanning Electron Microscope
- t_{p-3} Cooling Time Duration from p = 600±20°C to 300°C
- t_{8-5} Cooling Time Duration from 800°C to 500°C
- t_{weld} Weld Time Duration
- T_A Intercritical Annealing Temperature for Process A
- T_B Intercritical Annealing Temperature for Process B
- TB## Weld Parameter Set Code Name
- TRIP Transformation Induced Plasticity
- TS Travel Speed
- UTS Ultimate Tensile Strength
- UTS_{BM} Ultimate Tensile Strength of a Parent Steel Tensile Specimen
- $UTS_{weld\ joint}$ Ultimate Tensile Strength of a Welded Tensile Specimen
- UTS_{S-SC} Local Ultimate Tensile Strength for the Softened Subcritical Weld Region
- $v_{measured}$ Measured Weld Travel Speed
- v LEM-LV100 output voltage
- V Voltage
- VFM Volume Fraction of Martensite

- VHN — Vickers Hardness Number
- VHN_{ATTH} — Average Through-Thickness Vickers Hardness Number
- WFS — Wire Feed Speed
- y — Measured Depth of Weld Root Penetration
- YP — Yield Point Designation
- YPE — Yield Point Elongation
- YS — Yield Strength
- YS_{IC} — Local Yield Strength of the Intercritical Weld Region
- $YS_{H\text{-}SC}$ — Local Yield Strength of the Hardened Subcritical Weld Region
- YS_{BM} — Local Yield Strength of the Base Metal Weld Region
- $YS_{S\text{-}SC}$ — Local Yield Strength of the Softened Subcritical Weld Region

Chapter 1: Introduction to Joining of Dual-Phase Steels

In the past decade, automotive manufacturers have been pursuing different methods for improving fuel economy to meet standards that have become part of legislation set out by governments. As an example of this, most recently, the Obama administration in the United States proposed legislation to "mandate a 5 percent annual increase in fuel economy for model years 2012 through 2016" and "would push the corporate average fuel economy, or CAFE, standard to a fleet-wide average of 35.5 miles per gallon by 2016" [1]. Although the proposal was not in effect at the time of this study, it does illustrate the efforts by governments to push automotive manufactures to attain higher levels of fuel efficiency. At the time of writing, the CAFE standard passed for the 2011 model year was "27.3 mpg for the light duty fleet, which includes passenger cars and light trucks" [2].

This legislation is meant to reduce the dependency on non-renewable resources like fossil fuels and to reduce CO_2 emissions that are harmful to the environment. For automotive manufactures to meet required legislative standards different methods to improve fuel economy have been considered, some of which include: improved auto body aerodynamics, improved engine efficiency, direct changes to the fuel that is consumed, and reducing the vehicle weight. The methods that are being used to improve fuel economy are also required to meet vehicle design requirements to maintain passenger safety and it is desirable to maintain a relative ease of manufacturing to limit expenses [3].

Methods to reduce vehicle weight include redesign of vehicle architecture and the development and use of higher strength-to-weight ratio alloys. The focus of this study is on the method for reducing vehicle weight by utilizing a higher strength-to-weight ratio alloy. Regardless of how society will power the future generations of vehicles in automotive and other transportation sectors, there will always be benefits from utilizing lighter weight materials. It has been possible to reduce vehicle weight by selecting materials that have higher strength-to-weight ratios than conventional materials that have been used to manufacture automotive structural components in the past. Materials such as aluminum and magnesium

alloys, carbon fibre reinforced composites, and the group of advanced high strength steels (AHSS) have all been in development. In the current automotive industry infrastructure, knowledge, and skill base, ferrous alloys such as steels and cast irons have been dominating the automotive sector and still remain the most economical material in use. As a material commodity, over 800 million tons of steel are produced each year compared to 24 million tons for the second ranking metal, which is aluminum [4]; and hence when steel is used for manufacture, material expenses are decreased. Advanced high strength steels offer increased strength over conventional steels, such as high strength low alloy (HSLA) steel, without significant reductions in formability. This allows thinner gauge sheets to be used during manufacturing while still meeting design requirements. The reduced sheet gauge provides the aforementioned reduction in weight because the mass density of AHSS is very similar to traditional steel [3].

One important grade of AHSS is dual-phase (DP) steels, which have a microstructure that is comprised of two phases: martensite and ferrite. The ferrite acts as a softer matrix material that provides the steel with good formability. The ferrite matrix is interspersed with coherent islands of harder martensite, which increase the strength of the steel. The strength of DP steel increases as the volume fraction of martensite within the ferrite matrix is increased, but there is also a reduction in ductility. Dual-phase steels are designated based on the ultimate tensile strength (UTS) of the material, e.g., DP steel that has a UTS of 600 MPa is designated as 'DP600'. Depending on the grade, chemistry, and manufacturing process used to make the DP steel, there may also be small formations of bainite/carbide precipitates and retained austenite present in the microstructure.

1.1: **Dual-phase Sheet Steel Processing**

An example of a typical DP steel microstructure is shown in Figure 1.1. In the image, the ferrite matrix appears grey and martensite appears white. The hardened martensite islands disrupt elastic/plastic flow during loading. The volume fraction of martensite islands within the ferrite matrix and the ferrite grain size are the main factors that affect the DP steel strength [5]; as the volume of martensite fraction

increases or as the ferrite grain size decreases, the DP steel hardness will also increase. The shape and orientation of the martensite islands can also affect the DP strength and cause the steel to exhibit anisotropic mechanical properties; elongated bands of martensite can be formed during processing, which is known as banding [6].

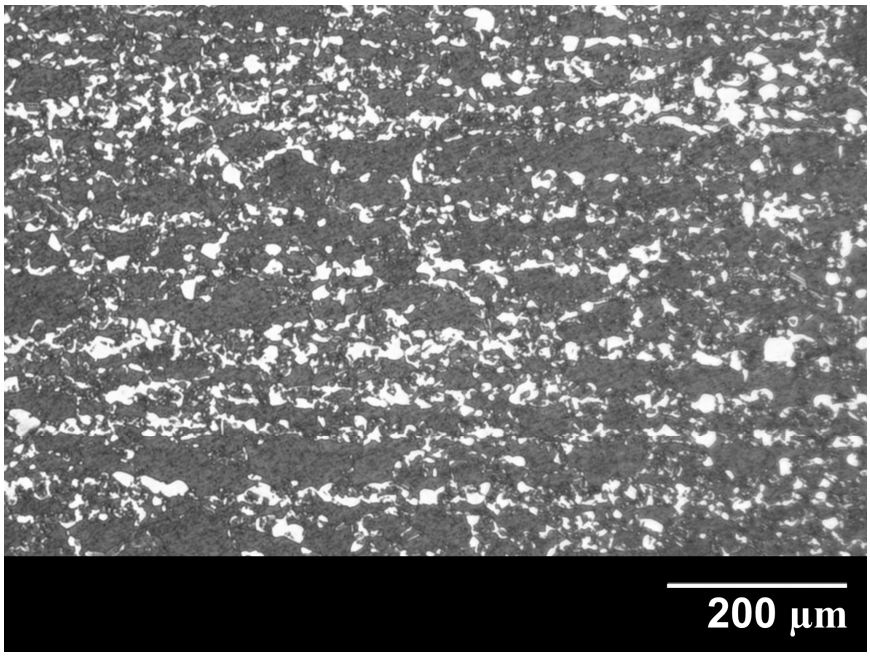

Figure 1.1: An image of a typical DP780 dual-phase steel microstructure. Martensite appears white and ferrite appears grey. (etched with the Lepera's Tint [7]).

To produce the dual-phase microstructure, the steel is elevated to a temperature that transforms the base microstructure from a B.C.C. ferrite (α) phase to an F.C.C. austenite (γ) phase. This occurs in the intercritical region, and hence, is known as an intercritical annealing. The intercritical region of an Fe-Fe_3C binary phase diagram is shown in Figure 1.2. In the diagram, the ferrite region is labelled 'α', the austenite region is labelled 'γ', and the intercritical region is labelled 'α + γ', which denotes that both phases exist simultaneously. Depending on the annealing temperature and the intercritical region characteristic limits (Ac_1 and Ac_3 lines), a different volume fraction of austenite can be formed during intercritical annealing; a higher volume fraction is obtained as the temperature is elevated closer to the Ac_3 line, above which, complete transformation to austenite occurs. Intercritical annealing is illustrated

on the diagram with two different annealing temperatures, T_A and T_B; this represents two different processes, A and B, which can be used for the same nominal steel composition. Based on the diagram, intercritical annealing at T_A (~750°C) produces a volume fraction of austenite of approximately 20%. When the higher annealing temperature T_B (~810°C) is used, a larger volume fraction of austenite, measuring approximately 50%, is formed. The volume fraction of austenite from intercritical annealing is a direct reflection of the DP steel martensite volume fraction that is obtained after quenching, because upon quenching, the steel from the intercritical annealing temperature, all austenite present after intercritical annealing will transform to martensite.

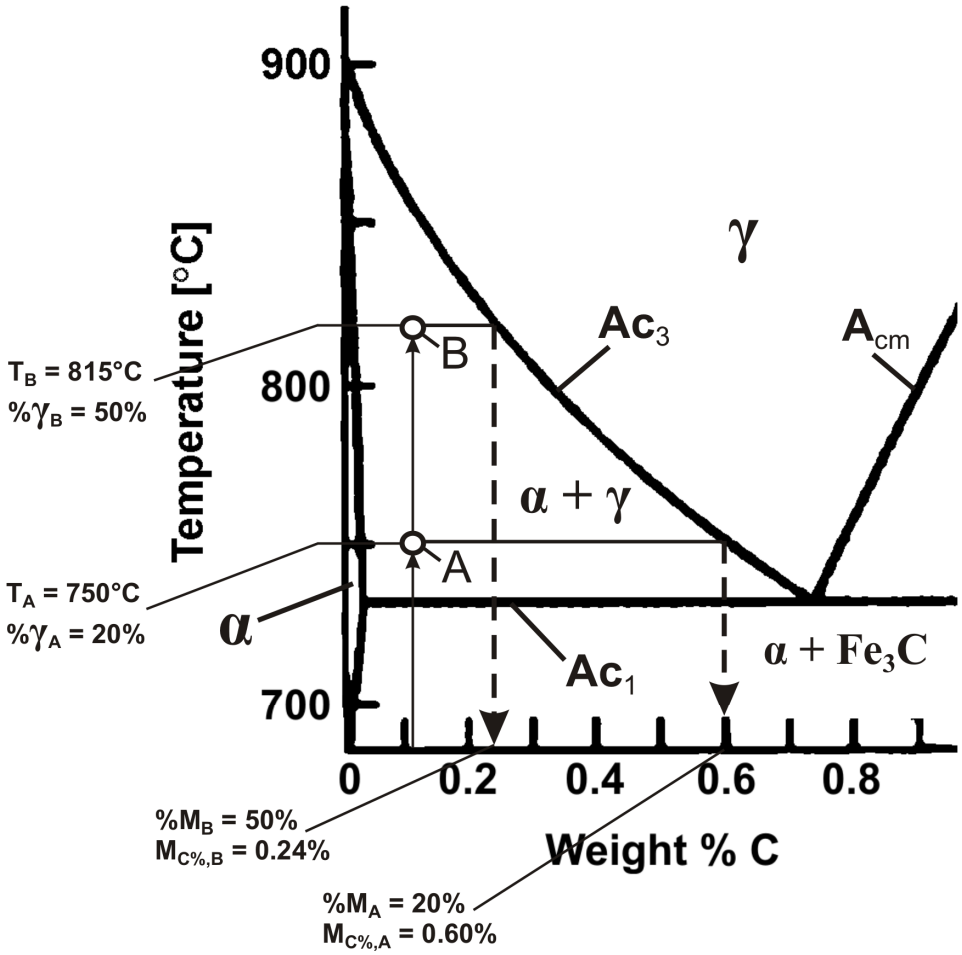

Figure 1.2: The intercritical region of a plain carbon steel Fe-Fe_3C binary phase diagram. Example intercritical annealing processes, A and B, used to make the dual-phase microstructure are shown. (taken from [8]).

Austenite has significantly higher carbon solubility than ferrite, and during quenching to martensite, the carbon is trapped in the interstitial spaces of the BCT martensite crystal structure because there is not sufficient time for carbon diffusion. To improve the likeliness of forming martensite during rapid cooling (known as hardenability), substitutional alloying elements are added to the nominal composition of the steel. These alloying elements help to impede carbon diffusion and decrease the critical cooling rate to form martensite, i.e., the steel continuous cooling time-temperature transformation (CCT) curve limits are moved down and to the right or longer times so that martensite can be formed with slower cooling rates [9]. For the examples from the diagram, the resulting martensite carbon content for process A is 0.60% and the result for process B is 0.24%. So, for DP steel, as the volume fraction of martensite is increased, the martensite carbon content decreases.

Intercritical annealing is usually performed on a cold-rolled or hot-rolled sheet steel and is known as heat-treated dual-phase (HTDP) steel [6]. The manganese content is typically high (to increase the steel hardenability) and during hot-rolling, the manganese segregates as MnS inclusions that can become elongated in the direction of rolling. During subsequent intercritical annealing, areas that are manganese-rich tend to form into martensite bands [6]. Another DP steel processing method involves controlled cooling of a fully austenitized sheet steel during hot-rolling through the intercritical region [3]. This method is known as as-rolled dual-phase (ARDP) steel. Hot rolling is used for refining the ferrite grain size where a smaller ferrite grain size will lead to higher strength. This method tends to require less manganese and is, therefore, less likely to form martensite bands [6].

A comparison of the typical engineering stress-strain characteristics for DP600 steel is shown in Figure 1.3. Dual-phase sheet steel that has similar yield strength to a conventional HSLA sheet steel will exhibit a higher UTS while maintaining similar engineering strain to failure, i.e., % elongation [3]. The DP600 engineering stress-strain curve is shown in the figure with a curve for a HSLA steel that has similar yield strength of approximately 350 MPa and similar total elongation for comparison. The two steels differed in UTS, where the HSLA had lower UTS of 450 MPa when compared to the 600 MPa

UTS of the DP sheet steel. The DP steels do not have an upper or lower yield point like the conventional HSLA steels, which improves formability by eliminating a detrimental discontinuous yielding stage and eliminates unsightly Lüders bands. Instead, DP steels follow a continuous yielding curve during deformation.

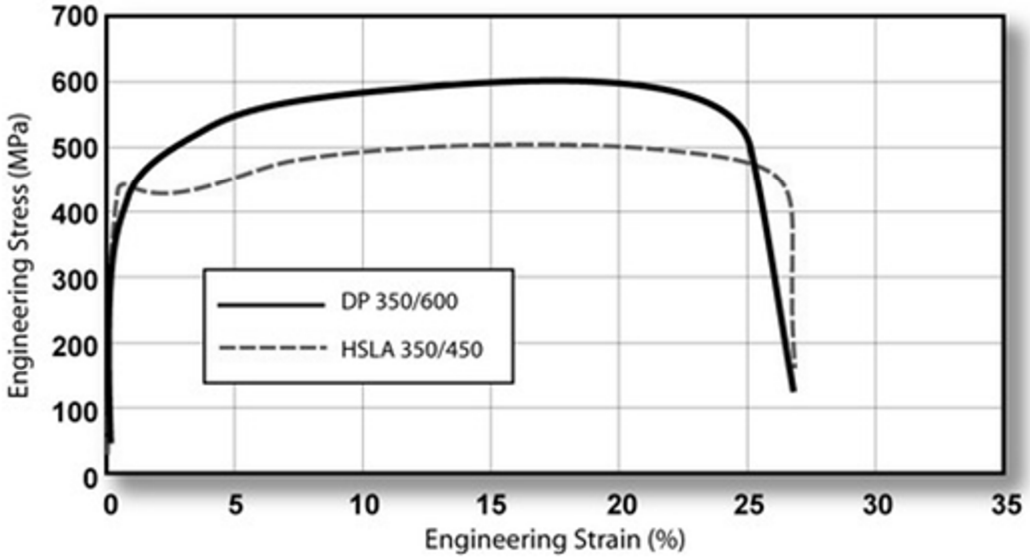

Figure 1.3: Comparison between HSLA and DP600 steel that had similar yield strength (350 MPa). (taken from [3]).

A drawback of the DP steel microstructure is that when the steel is elevated to temperatures approaching the carbon steel A_1 line, i.e., the eutectoid temperature 727°C (see Figure 1.2), there is potential for decomposition of the martensite phase. Completely decomposed martensite is known as tempered martensite. A fully tempered martensite island has reduced hardness compared to the prior martensite hardness. Therefore, tempering of the interspersed martensite islands leads to softening of DP steel and potentially a reduction in strength. The rate of martensite decomposition is affected by the base steel chemistry and the heating and cooling rates that it experiences during processing or manufacturing stages.

1.2: **Martensite Tempering**

Dual-phase steel can soften when it is elevated in temperature due to the decomposition of the hardened martensite islands (known as martensite tempering). An example of tempered martensite is shown in Figure 1.4. Martensite tempering occurs when environmental conditions initiate carbon diffusion within a martensite body; this occurs when a martensite body is elevated in temperature. The temperature at which decomposition of the martensite phase is most rapid is just below the A_1 temperature, which is approximately 727°C for plain carbon steels (see Figure 1.2). As the temperature is decreased from this point, the rate of decomposition also decreases. The microstructure of a fully tempered martensite island in plain carbon steel is a mixture of Fe_3C carbide particles (cementite) in a ferrite matrix; there is no martensite left upon the completion of tempering [9].

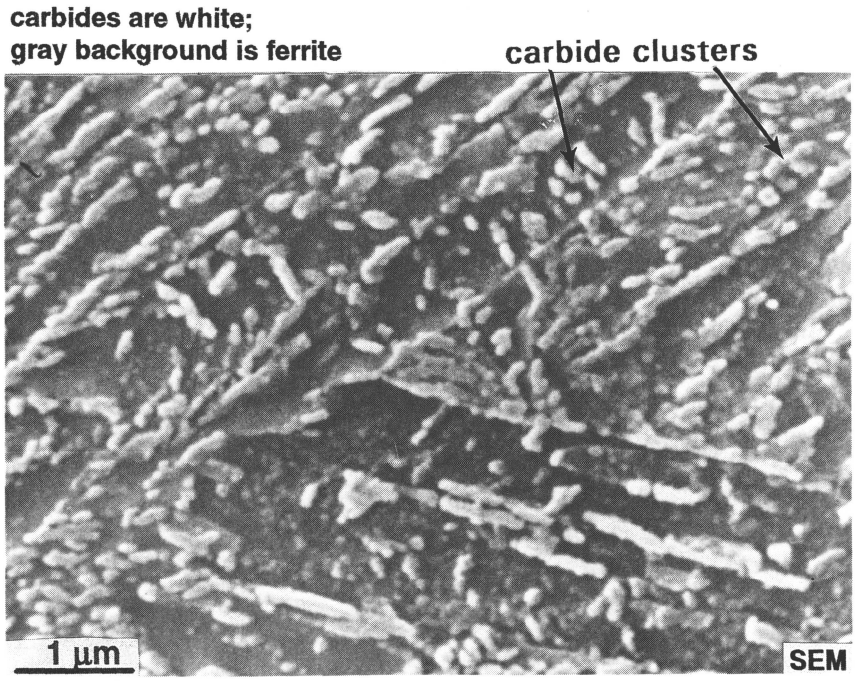

Figure 1.4: An example of the microstructure of a tempered martensite obtained from tempering a fully martensitic microstructure in a 0.5% C steel for 45 minutes at 470°C. (taken from [9]).

The hardness of tempered martensite in plain carbon steel decreases as the tempering temperature increases. An example of this is shown in Figure 1.5 [9]. Martensite tempering of plain carbon steel is

typically categorized into three stages, which are: a first stage temperature range of 50 – 200°C during which the transitional ε-carbide precipitates, second stage range of 200 – 300°C where retained austenite transforms into bainite giving an increase in specific volume, and a third stage range above 300°C during which the transitional carbides transform into cementite, Fe_3C [10]. The transformed cementite coarsens as the time duration and temperature are increased closer to the steel A_1 temperature, and as the cementite coarsens the hardness decreases.

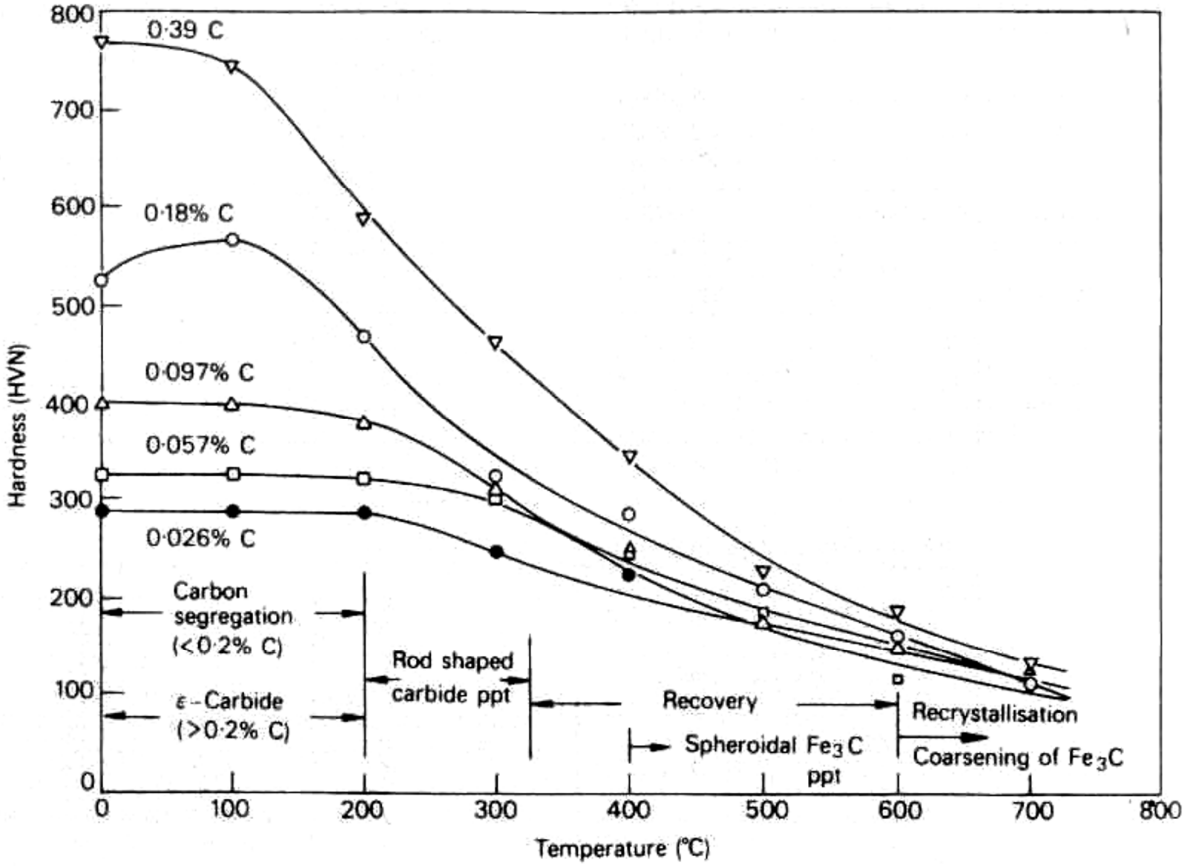

Figure 1.5: A typical tempering curve showing the decrease in hardness for different isothermal heat treatment temperatures (held for 1 hr). (taken from [9]).

Automotive components and sheet metal structures are typically joined by using a welding process to create a permanent joint. In the automotive industry, the most widely used processes are

resistance spot welding (RSW), laser beam welding (LBW), and gas metal arc welding (GMAW). These are all fusion welding processes and are listed in order from the highest to lowest heating and cooling rates generated within the steel during the welding process.

During welding of DP steels, a softened region of the microstructure is formed, which is located adjacent to the line of the weld heat affected zone (HAZ) where the steel was heated to the Ac_1 temperature during welding. This is frequently referred to as the Ac_1 line in the HAZ. An example image tempered martensite in a welded DP sheet steel is shown in Figure 1.6. In the image, carbide formations appear white and the ferrite matrix appears grey; islands of tempered martensite are labelled 'TM'. The degree of softening in this region is dependent on the welding process heat input and is dependent on the prior martensite volume fraction in the DP steel BM. Higher welding heat input is expected to create a wider softened region that has coarser cementite within the tempered martensite islands. Lower

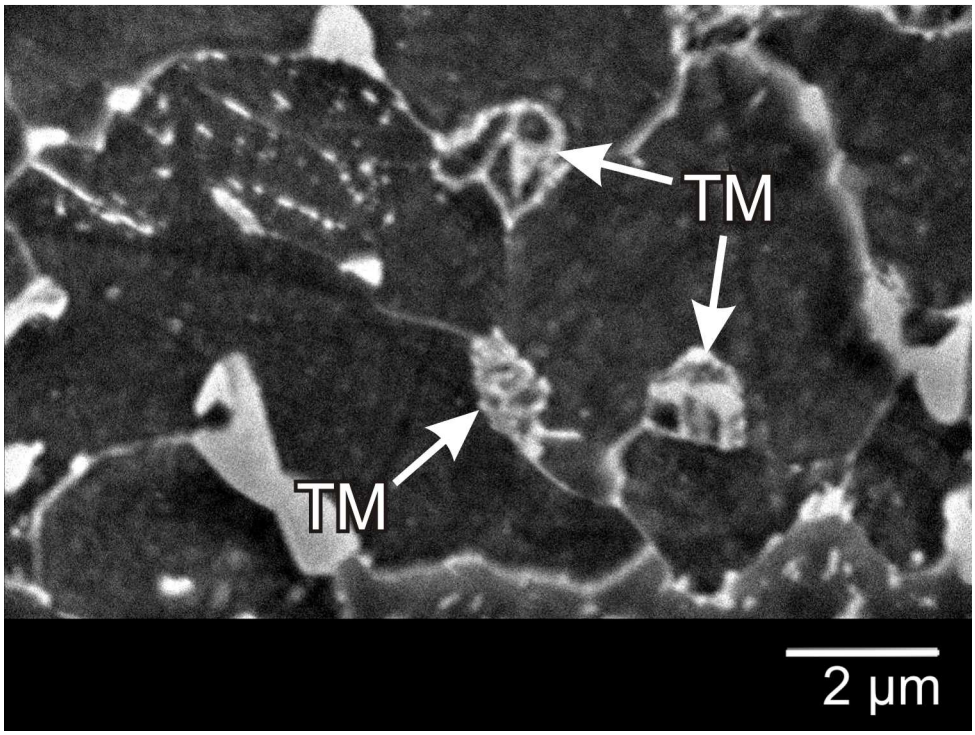

Figure 1.6: SEM image of tempered martensite (TM) in a DP600 sheet steel GMAW-P weld HAZ. (2% Nital etch).

strength grades of DP steel (DP600) are expected to have less softening because there are fewer martensite islands in the base-metal microstructure compared to higher strength grades (DP780, DP980); this means a greater proportion the microstructure is ferrite, which remains relatively unaffected in terms of hardness. Also, due to the high hardenability of DP steels, the weld fusion zone (location of the highest cooling rates) can potentially become very hard and consequently be very brittle. The weld HAZ microstructure transforms significantly when compared to the prior DP microstructure and extends from the prior base-metal (BM) to the weld fusion boundary (FB). As weld process heating and cooling rates increase, the size of the HAZ will decrease and softening will be less; however, all of the processes cause martensite decomposition to varying degrees.

1.3: **Fusion Welding: Pulsed Gas Metal Arc Welding**

The focus of this study was the weldability of DP sheet steels by the GMAW welding process. Welding joints made using the GMAW process typically experience the highest heat input, and the lowest heating and cooling rates of all of the welding processes used in the automotive industry to join DP sheet steels. As an example of the differences between the different fusion welding processes that are used in the automotive industry, the range of cooling rates of the resistance spot welding (RSW) weld process is approximately 2,000°C/s-100,000°C/s, for a laser beam welding (LBW) weld the range is approximately 500°C/s-5,000°C/s, and for a GMAW weld, the range is approximately 10°C/s-100°C/s [11]. Welding heating/cooling rates are non-isothermal and vary depending on the relative position to the heat source. Thus, the fusion welding HAZ exhibits a continuous transition of microstructure that extends from the base-metal to the fusion zone; at each infinitesimal step through the HAZ it can be assumed that a different microstructure exists. A larger affected region will exist with fusion welds that use a higher heat input to form a weld.

The GMAW process is typically used to weld thicker gauge sheets (1 – 3 mm), is used for joints that can only be accessed from one side of the component, and is used at joints where the expected loading will be highest, because increased joint strength requirements can be realized by applying longer

weld lengths [3]. Through use of the consumable filler metal inherently used in the GMAW process, fusion zone microstructure that is potentially causing loss of joint efficiency in other fusion processes can be manipulated. A GMAW welding system also has a lower capital cost compared to LBW and therefore can help reduce production expenses. The GMAW process is typically used to join lower strength grades of DP steel (e.g., DP600); however, it can be used to weld higher strength grades (DP780, DP980), but these weld joints will potentially exhibit a greater loss of strength when compared to lower heat input fusion welding processes [3].

In the present study, a pulsed gas metal arc welding (GMAW-P) process was used to examine the effects of weld heat input on the softening of DP sheet steel and the mechanical performance of simple bead-on-plate welded joints. The GMAW-P process has a pulsed voltage waveform and has an advantage of lower heat input at similar deposition rates when compared to the conventional constant voltage gas metal arc welding (GMAW-CV) process. In automotive welding, this is advantageous because weld penetration can be maintained for similar travel speeds at reduced heat input. Based on previous experience with welding these alloys, reducing the weld heat input was expected to result in reduced softening of the DP sheet steels in the HAZ.

Figure 1.7 shows a general schematic of a GMA welding system. The GMAW process uses a consumable electrode (2) to establish an electric arc (1) between the electrode tip and the workpiece. The electrode is continuously fed via wire feed rollers (4) into the molten pool at a constant rate, known as the wire feed speed (WFS). The arc that forms between electrode tip and the workpiece acts as the heat source for melting the base-metal and the tip of the electrode wire. A molten pool (12) is created due to the heat input from the electric arc and due to the heat input from the metal droplets transferred from the tip of the electrode into the molten pool. The molten pool solidifies to form a permanent joint as the welding torch (7) is moved along the weld joint. Constant voltage DC power supplies are normally used for GMA welding as this helps to maintain a constant welding arc gap during welding where the arc gap is generally proportional to the welding voltage used [12].

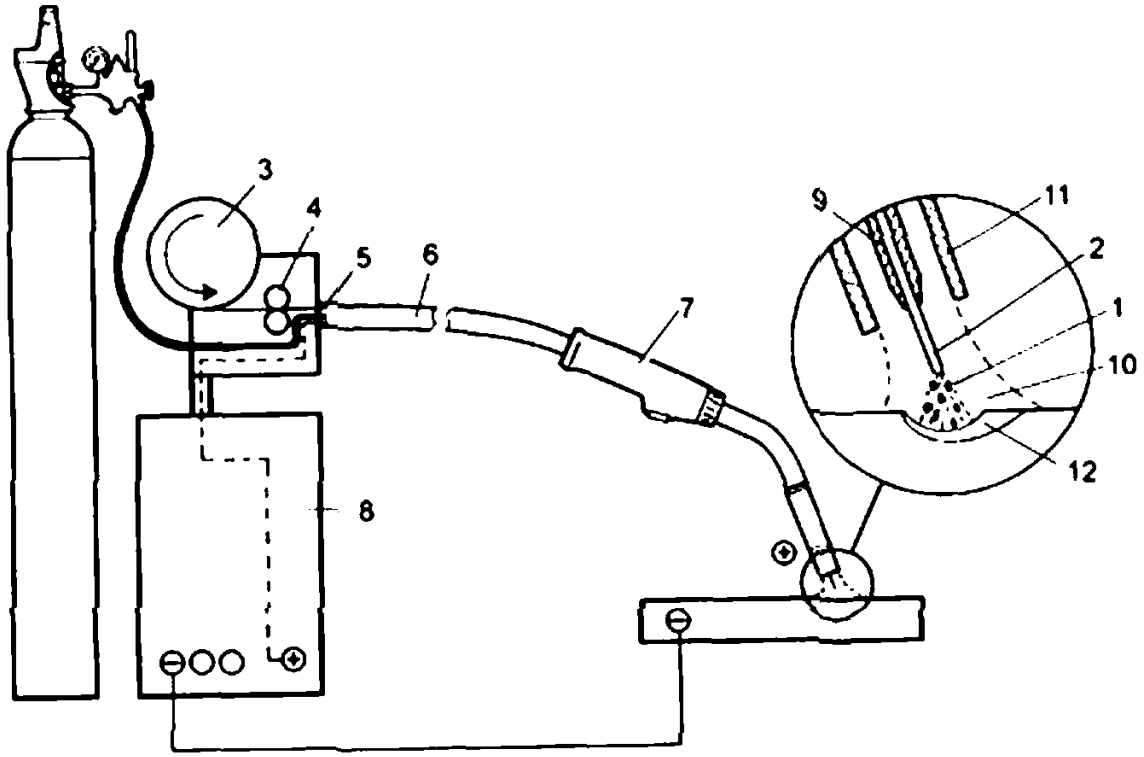

Figure 1.7: A general schematic for the setup of a GMAW system. The diagram shows 1) welding arc 2) consumable electrode 3) electrode reel 4) wire feed rollers 5) gas shielding and power supply connection 6) wire feed/shielding gas guiding tube 7) GMAW torch and trigger 8) power supply 9) contact tip 10) shielding gas flow 11) nozzle 12) molten welding pool. (taken from [13]).

Electron flow across the arc can be setup as direct current electrode positive (DCEP), direct current electrode negative (DCEN), pulsed DC or can be alternating current (AC). In GMAW, alternating current is generally not used, because it causes instability of the arc and of the electrode melting rate. In DCEP, also known as reverse polarity, the negative terminal of the power supply is connected at the workpiece and electrons within the arc are emitted from the workpiece towards the electrode. This creates higher heat input at the electrode tip and increases the melting rate of the electrode [12]. In DCEN, also known as straight polarity, the negative terminal of the power supply is connected to the welding torch and electrons are emitted from the tip of the electrode towards the workpiece. This creates an increase in heat input at the workpiece; however, the electrode melting rate is lower than DCEP and so

tends to have less total heat input to the workpiece [12]. In most GMAW applications, DCEP is used, as it gives better penetration and has better arc stability and higher electrode melting rates; however, certain electrodes specify the polarity that should be used. The GMAW setup shown in Figure 1.7 is DCEP. The path of electric flow is from the power source (8) to the contact tip of the welding torch (9); the electrode makes contact with the contact tip as it is fed towards the workpiece. The arc is established when the electrode tip makes contact with the workpiece and closes the circuit path. The return path of the circuit is from the workpiece to the power supply; the workpiece is grounded for safety. A shielding gas (10) is supplied to the torch nozzle (11), which protects the molten pool from the atmosphere; and prevents gas-metal reactions such as CO boil that can cause pores to form within the molten pool, which act as crack initiation sites.

For the GMAW welding process, the electrode tip is simultaneously fed into the weld pool as it melts off. The rate at which the electrode melts is dependent on the following independent parameters: electrode wire diameter, electrode composition, electrode polarity, voltage, contact-tip-to-workpiece distance (CTWD), and WFS. As the electrode extends from the contact tip, it rises in temperature due to resistive electrical heating and the surrounding heat from the arc. When sufficient temperature is reached, a molten bead will form at the tip. This molten bead can be stripped off the end of the electrode and enter the weld pool by a number of different mechanisms. The major contributing forces that act on the molten bead are the electromagnetic force, known as the Lorentz force, the viscous drag from the plasma stream generated by the arc, and the force of gravity [14]. There are different modes of metal transfer depending on the relative magnitude of these forces: short circuit transfer, globular transfer, and spray transfer. Spray transfer has an expanded definition, which includes: projected spray, streaming spray transfer, and rotational spray transfer [15].

The modes of metal transfer that are important to distinguish for this study are short circuit transfer and the projected and streaming forms of spray transfer. The other modes of transfer will not be discussed further. The most important traits to distinguish for each transfer mode are the heat input, weld

penetration, and weld quality. The basic principles and the tradeoffs between short circuit and spray transfer are described below.

A short circuiting (SC) mode of metal transfer occurs at low voltages when the electrode tip makes contact with the molten weld pool. An example of a single cycle of the SC metal transfer process is shown in Figure 1.8. The SC mode of metal transfer occurs because the electrode melting rate is not sufficient to create and expel a molten bead from the electrode tip prior to contact with molten weld pool. The electromagnetic pinch force is insufficient at low voltage to detach a molten droplet as it forms. The necessary pinch force only occurs after contact with the weld pool when there is a short circuit and spike in the welding current. At these high currents, high Lorentz forces cause pinching and necking of the molten metal and the resultant reduction in surface tension forces result in detachment of the molten bead [14]. As the electrode makes contact, it causes the electrical path to short and the arc to extinguish (step H, I, and A in the image). The electrical resistance at the electrode/workpiece interface decreases significantly and the welding current rapidly increases (step B, C, and D in the image). This spike in

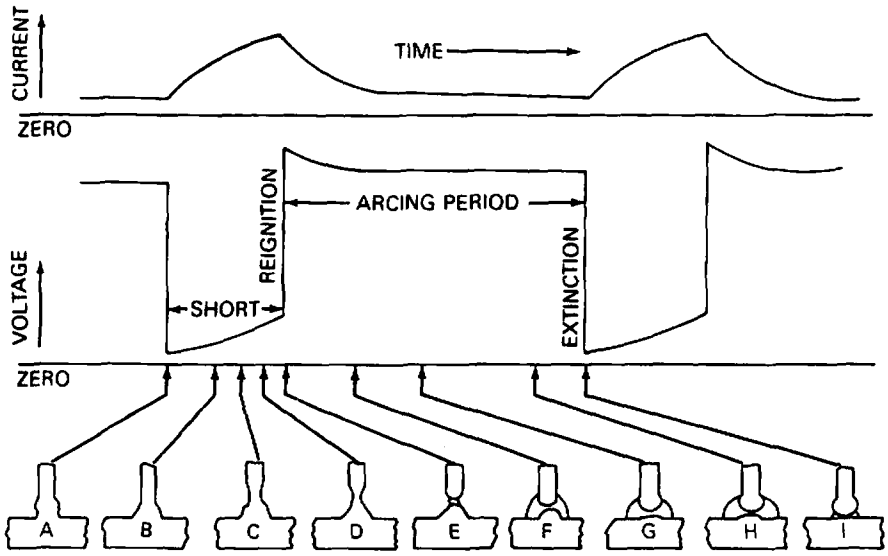

Figure 1.8: The general mechanisms that occur during GMAW short circuit (SC) metal transfer. (taken from [13]).

current causes the electrode to rapidly melt off, which can occur violently, causing the ejection of molten metal; this is known as spatter. Typically spatter solidifies on and adjacent to the weld location and requires post processing to remove it. Spatter is detrimental to joint fatigue because it creates an abundance of sites for crack initiation on the workpiece surface; spatter is also detrimental to component aesthetics. After the molten bead detaches and the electrode is no longer in contact with the weld pool the arc re-ignites and the process is repeated. Short circuit welds typically have low heat input and give low penetration through the joint [16]. CO_2 shielding gas is normally used because it is less expensive than Ar; however, use of this reactive gas means that electrode wires with elevated levels of oxide scavenging elements such as Al and Si must be used to prevent CO boil.

Spray metal transfer occurs when higher welding voltages and Ar-rich shielding gases are used. This creates a larger arc gap, thereby allowing the electrode tip to melt off before making contact with the molten weld pool. A molten bead that is formed at the electrode tip is stripped off the end of the electrode and projected towards the weld pool as shown in Figure 1.9. In this mode, the arc is continuous and does not extinguish. The molten bead droplet in projected spray transfer has a diameter that is similar to the electrode diameter. In streaming spray transfer, the bead becomes smaller in diameter than that of the electrode. Molten droplets melt off at a frequency of approximately 100 Hz in projected spray transfer and up to approximately 1000 Hz in streaming spray transfer [14]. Spray metal transfer occurs at a higher heat input than short circuiting transfer mode, but is also occurring at a higher deposition rate. This increases penetration into the workpiece and allows faster torch travel speeds. Penetration is also increased because in spray transfer the molten beads are being propelled towards the weld pool at high velocities causing ‘finger’ weld penetration geometry, as shown in Figure 1.9. The image shows typical finger weld geometry and a streaming jet of molten beads being projected from the electrode; the diameters of the beads are smaller than the electrode diameter, hence this schematic is for streaming spray transfer. A typical spray transfer process will have an Argon shielding gas with an addition of CO_2. The CO_2 addition promotes more favourable weld pool wetting, which allows higher travel speeds to be

obtained while maintaining good weld bead geometry. A requirement for this mode of metal transfer is that the Ar shielding gas must have less than 20% CO_2 in the mixture [17].

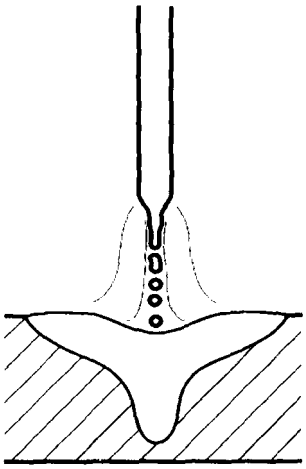

Figure 1.9: Example of streaming spray transfer and a 'finger' weld penetration geometry. (taken from [13]).

The transition from short circuit transfer mode to spray transfer mode for GMAW occurs at a transition current. Figure 1.10 is a diagram that shows an example of the approximate current that can be expected for different diameter electrodes over a range of WFS. The diagram is for steel electrodes in DCEP using Ar–2% O_2 shielding gas [13]. With the increased penetration possible with spray transfer mode, travel speed can be increased in order to reduce the total heat input to the weld (the time of heat input exposure can be decreased). Other benefits of spray transfer are that spatter is significantly reduced and potentially eliminated and higher melting rates and metal deposition rates are possible relative to SC transfer [16].

When joining DP sheet steels in automotive applications, the higher heat input rates associated with spray transfer can be detrimental because it causes greater softening in the HAZ and weld joint quality issues such as burn-through become problematic. Typical sheet steel welding is performed using a short circuiting metal transfer mode, because it has a lower heat input and lower weld root penetration;

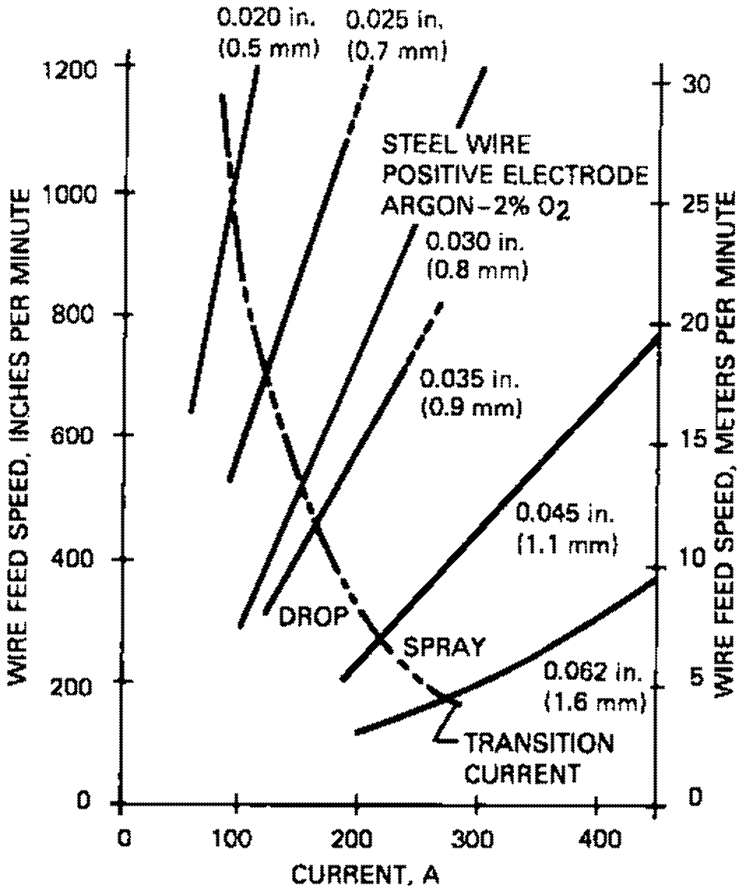

Figure 1.10: The approximate transition current for a GMAW process using a steel electrode in DCEP (straight polarity) and an Argon – 2% O_2 shielding gas. (taken from [13]).

this helps to avoid burning through the sheet steel. The low heat input of an SC transfer mode also helps to limit DP HAZ softening. In automotive welding, processing time effects cost and therefore faster travel speeds are desirable; however, the high heat input and high depth of penetration of a spray transfer mode, which helps to provide a high travel speed, can cause sheet steel burn-through and limit the weld process operating window. To alleviate these problems a GMAW-P process has been selected for welding during this study. A GMAW-P process was chosen because a clean (minimal spatter) and high penetration weld can be produced while reducing the total heat input to the weld [16].

A typical GMAW-P waveform is shown in Figure 1.11. It consists of the following four parameters: peak current, peak time duration, background current, and background time duration [13]. The GMAW-P waveform can attain a lower heat input than with a conventional GMAW-CV process because a CV process must be maintained above the spray transition current whereas a pulsed waveform only rises above the transition current for long enough to form a molten bead and strip it off the end of the electrode. The lower background current must be sufficient only to maintain an arc. The average current over the pulsing cycle can be adjusted so that it is lower than the transition current for spray transfer and, therefore, spray conditions are obtained with GMAW-P at a lower average power input [16]. This can be advantageous when welding DP sheet steels, because high metal deposition rates can be realized while minimizing softening in the HAZ and avoiding burn-through.

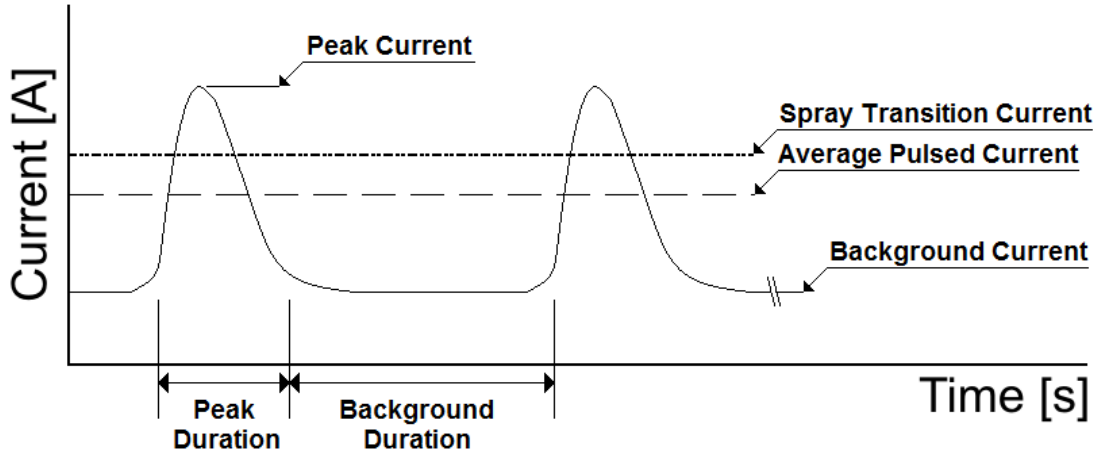

Figure 1.11: A schematic of a typical GMAW-Pulsed waveform. The peak current is used to produce spray metal transfer mode, but the lower background current gives an average current that is lower than a GMAW-CV spray current for the same electrode and shielding gas.

1.4: **Objectives of the Present Work**

The objective of this study was to examine the weldability of coated dual-phase sheet steels, specifically DP600, when using the GMAW-P welding process and to develop an understanding of how tempering of martensite in the HAZ of GMAW-P welds affected DP sheet steel fracture. By developing this knowledge base, methods to improve GMA welded DP sheet steel joint efficiency could be proposed. In

the following Chapter 2, a literature review of the past knowledge of welded DP sheet steel softening and fracture mechanisms is provided. Chapter 3 contains an overview of the equipment and setup that was used to conduct welding trials and also outlines how the experimental work was conducted. The results and discussion are provided in Chapter 4. Finally, the conclusions of the study are listed in Chapter 5 as well as recommendations for the direction that future research of GMAW welding of DP sheet steel should take.

Chapter 2: Literature Review

The following literature review focuses on the effects of GMAW welding heat input on DP sheet steel mechanical properties; however, other fusion welding processes are also reviewed to cover a larger range of heating and cooling rates. The literature review is separated into three sections: dual-phase steel mechanical properties for uniform base-metal, isothermal tempering kinetics in relation to DP sheet steel and the mechanical properties of uniformly tempered DP sheet steel, and the effects of non-isothermal tempering from fusion welding heat input on DP sheet steel mechanical properties where the focus will be on GMAW welding of DP sheet steels.

2.1: Dual-phase Steel Mechanical Properties

Over the course of development, the mechanical properties for dual-phase sheet steel have been widely studied and control over those properties has been well established. To better understand the effects of softening due to martensite tempering, the following section details the known mechanical properties for unaffected (as received) DP sheet steel base-metal.

The superior ductility of DP steels compared to conventional HSLA steels has been observed by Davies [5] who confirmed that at a given level of strength, DP steels exhibit higher levels of ductility than conventional HSLA steels. Lawson *et al.* [18] suggested that a combination of good strength and ductility in DP steels was associated with significant amounts of epitaxial ferrite (formed after intercritical annealing) in conjunction with a retained ferrite matrix and martensite islands. As mentioned in Chapter 1, DP steels exhibit a continuous yielding phenomenon, which is beneficial to formability. Okamoto *et al.* [19] observed that a DP steel with as little as 1 to 2% martensite-plus-austenite volume fraction was sufficient for continuous yielding to occur during deformation and that internal stress existing before or during tensile testing was the main cause of the continuous yielding phenomenon. Lawson *et al.* [18] also noted that a continuous yielding behaviour was caused by increasing the martensite volume fraction.

Davies [5], Okamoto *et al.* [19], and Lawson *et al.* [18] all found that the strength of DP sheet steel was directly proportional to the martensite volume fraction. Davies [5] went further to suggest that DP sheet steel strength was dependent only on the martensite volume fraction and the ferrite grain size; he found that Nb and Mn additions in the DP alloy produced grain refinement, which increased strength and that Mo additions did not appear to affect grain size. He also suggested that Mn additions from 0.72 to 1.48 % lead to an increase in the volume fraction of martensite. He further noted that the strength of individual martensite islands was not a factor for the strength of DP sheet steels. This was contrary to expected belief that individual martensite hardness would have a larger affect on DP steel strength. Okamoto *et al.* [19] found that differences in DP steel strength between steels that had similar martensite volume fractions were caused by the ferrite hardness. Lawson et al. [18] noted that the ferrite grain size was not affected by intercritical annealing; however, they found differences in the strengths of DP steels that had similar martensite percentages, but had been produced by different intercritical annealing temperatures. Lawson *et al.* [18] suggested that epitaxial ferrite growth that formed around martensite islands during cooling (after intercritical annealing) was more prevalent in DP steels that had higher intercritical annealing temperatures and that epitaxial ferrite growth could cause a difference in DP steel strength. Avtar *et al.* [20] studied the effects of transformed (epitaxial) ferrite on the impact fracture properties of DP steel and suggested that the transformed ferrite may differ in orientation and composition when compared to the DP steel retained ferrite.

Davies [5] found that DP sheet steel strength was independent of the carbon content of the individual martensite island. While it is well known that the strength of martensite increases as carbon content increases, it was unclear to Davies [5] why the strength of DP sheet steel did not depend on the strength of the martensite islands. The individual strength of a martensite island is affected by: hardening by substitutional alloying, hardening by interstitial alloying, precipitation hardening, prior austenite grain size, strengthening by substructure, and microplastic deformation and rapid work hardening [10]. In steel,

the most influential of these strengthening mechanisms is hardening by interstitial alloying; either through carbon or nitrogen additions.

As the carbon content in martensite increases, the hardness also increases. An example of this is shown in Figure 2.1. The hardness of martensite reaches a limit at approximately 0.6%C. The addition of alloy elements appears to have minimal effect on martensite hardness [5,9]. The martensite BCT crystal lattice c/a ratio also increases as the interstitial carbon content increases [10]; as the c/a ratio approaches 1.0, the martensite acts more like ferrite. In DP steel, the interstitial carbon atoms tend to diffuse into the austenite phase during intercritical annealing and hence the nominal carbon content of the sheet steel does not reflect the carbon content of the martensite phase. The carbon content of martensite islands varies with the intercritical annealing temperature and lower martensite carbon contents can be expected at higher temperatures (via the Lever rule for the prior austenite). Therefore the hardenability of austenite close to the Ac_3 line will be lower than the hardenability of the austenite at the Ac_1 line. Individual martensite hardness may have an effect in microhardness testing of DP steel because microhardness indentations will cause the martensite islands to become plastically deformed; however, this was not found in the literature that was investigated.

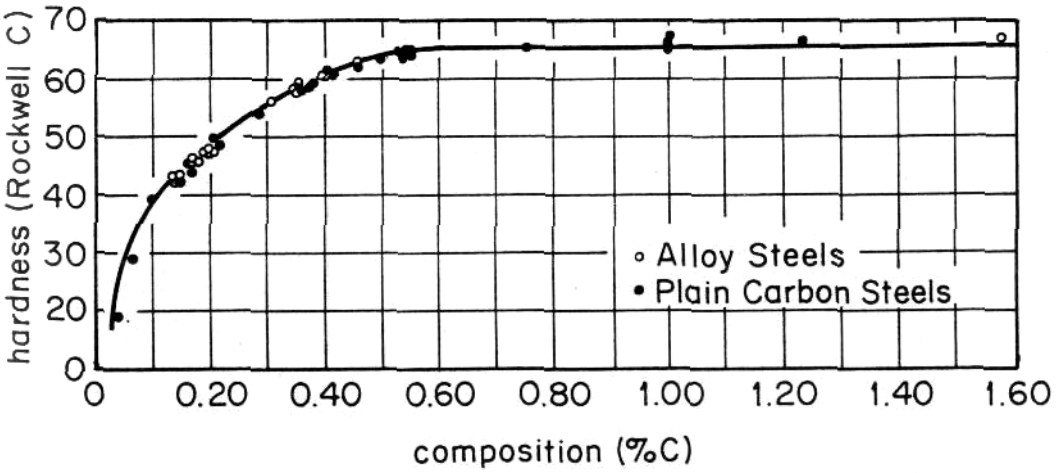

Figure 2.1: The hardness of martensite as a function of the carbon composition. The hardness does not appear to be affected by other substitutional alloy elements. (taken from [9]).

Davies [5] suggested that the reasoning for this was not necessarily independent of martensite carbon content. The collective reasoning that he suggested for DP steel strength being independent of martensite carbon content was that high carbon martensite may fracture prior to rupture and hence not improve strength, that martensite strength may be lower in a ferrite matrix than within an austenite matrix (retained austenite increases with an increase in carbon content), and that autotempering of high carbon martensite may occur so that only 0.4% carbon remains in solution in martensite bodies, regardless of the martensite volume fraction. Contrary to what Davies [5] had suggested, Ahmad *et al.* [21] argued that the strength of DP steel was proportional to the martensite volume fraction and the carbon content of the martensite. In that study, it was suggested that higher carbon content in DP steel (and hence higher carbon martensite) improved the UTS and reduced the ductility; however, DP steels that had less than 30% martensite volume fraction were not studied.

Chen *et al.* [22] attempted to clarify the effect that martensite carbon content has on DP steel mechanical properties. The tensile strength of DP steel was observed to increase as the nominal carbon content increased for a constant martensite volume fraction. This observation was contrary to Davies [5]. It was suspected that an increase in martensite volume fraction, regardless of the carbon content, could increase tensile strength due to a higher dislocation density in the retained ferrite matrix. It was also suggested that in DP steels, the martensite phase does not reach its UTS, even once necking has occurred.

Okamoto *et al.* [19] observed that in a carbon (0.02 wt. %) and manganese (2.1 wt. %) DP steel, the microstructure contained a small amount of pearlite, twinned martensite, and retained austenite. These second phases were observed to be enriched in C and Mn (examined by an electron probe micro analyser). The Mn enrichment was found to be approximately double the value of the nominal steel composition. This suggested that austenite and subsequent formations of martensite islands should not be considered to exhibit the nominal alloy composition. The same analysis on a continuously annealed dual-phase steel was found to have minimal Mn segregation due to a shortened soaking time; this suggested that tempering of these two different processed DP steels could also be very different.

The presence of non-martensitic phases in a DP steel microstructure was recorded by Davies [5] and Okamoto *et al.* [19]. The non-martensitic phases were attributed to low hardenability and insufficient cooling rates. In both studies, as the intercritical annealing temperature was increased, cementite particles were absorbed into austenite regions and upon quenching, the martensite volume fraction increased. Davies [5] suggested that the strength of air cooled DP alloys should have high hardenability to ensure that the strength is independent of annealing temperature. In a later study, Davies [23] stated that rich chemistry DP steel containing approximately 1.5%-Mn and 0.1 – 0.3% V, Cr, and/or Mo could be air cooled (~20°C/sec) to achieve a martensite-ferrite microstructure, whereas lean chemistry DP steel that contained only 0.6% Mn had to be water quenched (~2000°C/sec) to attain a dual-phase microstructure. Similarly, in a study by Okamoto *et al.* [19], an increase in YS and UTS were attributed to faster cooling rates that resulted in higher martensite volume fractions within a DP steel microstructure; this was shown to be dependent on annealing temperature for cooling rates slower than 320°C/h. Lawson *et al.* [18] and Avtar *et al.* [20] presented microstructural evidence that at lower cooling rates there was more epitaxial ferrite transforming from intercritical annealed austenite than there was to martensite. Furthermore, as the intercritical annealing temperature was decreased, the amount of austenite transformation into epitaxial ferrite decreased. Lawson *et al.* [18] attributed this to increased hardenability due to higher austenite carbon content. Ahmad *et al.* [21], using a nominal composition with high Cr (0.91%), observed that after quenching there was a significant amount of martensite and attributed this to good hardenability.

Steinbrunner *et al.* [24] defined the stages of yielding during uniaxial tensile testing to follow either diffuse necking or a diffuse plus localized necking prior to complete fracture. From this definition, a diffuse neck develops in thin sheet after plastic instability, which incurs significant contraction strains in the tensile specimen width and thickness directions; a tri-axial strain state is developed. A subsequent localized neck forms when there are additional through-thickness strains after flow constraints limit further strain in the width direction; there is significant through-thickness sheet thinning that significantly limits the usable post-uniform strain. Steinbrunner *et al.* [24] observed that the likeliness of localized

necking of a DP sheet steel uniaxial tensile specimen increased as the martensite volume fraction increased and as the tensile specimen width increased. In both cases, the expected fracture was by ductile rupture, a process that occurs in three stages, which was described as: void nucleation, growth, and coalescence. Due to higher local strain, the void density was higher during localized necking.

The nucleation of micro-voids in DP sheet steels has been associated with non-metallic incoherent inclusions or with martensite islands [21, 24]. Void nucleation due to martensite islands was observed to be from decohesion between the ferrite-martensite interfaces, by the separation of fractured martensite islands, and by the separation of adjacent and deformed martensite islands. Of these, Steinbrunner *et al.* [24] found that the dominant mechanism for nucleation was at fractured martensite islands; however, growth of voids after nucleation was dominated by the ferrite-martensite interface. Growth of voids was observed to extend in the direction of the tensile axis [21, 24]. Furthermore, they suggested that erroneous conclusions could be derived from analyses that focus on void nucleation adjacent to the fracture surface (analysis by longitudinal sectioning), because this area was typically dominated by interface decohesion. Steinbrunner *et al.* [24] determined that the critical local strain for nucleation by an island of fractured martensite was approximately 5%.

By interpreting different models, Lawson *et al.* [18], suggested that during early stages of DP steel plastic deformation, strain only accumulates in the soft ferrite matrix. After martensite deformation starts, the strain accumulation becomes comparable within both phases. This suggests that the start of martensite deformation should be dependent on carbon content and the morphology of the martensite structure. Davies [5] found that martensite fracture was not present at strains of 5% in DP sheet steels that had less than 40% volume fraction of martensite. Crack formation in martensite was more prevalent when the carbon content was high and the DP steel martensite volume fraction was high enough so that banding occurred [5]. Avtar *et al.* [20] suggested that transformed ferrite may increase the susceptibility of DP steel to cleavage fracture during impact testing; furthermore, there was evidence that an increase in the amount of transformed ferrite leads to an increase in crack initiation energy and decreased

propagation energy. They reported that transformed ferrite may have a higher Mn content and a higher resulting hardness than retained ferrite; the softer retained ferrite was believed to have better resiliency to crack nucleation as it could incur larger plastic strains. This echoed the suggestion by Davies [5] that martensite in an austenite matrix (hardness data presented in Figure 2.1) may exhibit different strength than martensite in a ferrite matrix.

Davies [23] and Speich *et al.* [25] both observed brittleness in as-quenched rich alloyed DP sheet steels. Davies [23] found that high alloyed DP steels should be tempered in excess of 120°C to avoid embrittlement, whereas for lean alloyed DP steels, ductility was shown to increase from 15 to 22% total elongation after sitting at room temperature for 2 hours. The issue of embrittlement in rich alloy DP steels was suggested to be caused by a large volume expansion of higher carbon martensite during quenching, by likeliness for autotempering in lean alloy DP steel due to a higher martensite start (M_s) temperature, and/or by the presence of V in rich alloy DP steels that could reduce the strain-aging response of the ferrite matrix [23].

From the literature presented in this section, dual-phase steels with similar martensite volume fractions that have martensite islands with differing carbon content do not appear to have differences in strength; however, it may be that extremely low (< 0.10-wt %C) martensite carbon content has not been tested. Low martensite carbon content may have existed in DP steels that had low nominal carbon content and a high martensite volume fraction. Davies [5] reported that in DP sheet steels with a martensite volume fraction above 50%, the strength appeared to be independent of ferrite grain size and that this was suspected to be caused by an increased amount of martensite precracking. These studies have not documented the actual carbon weight percentage in the martensite; estimates were based on simple Level rule calculations. In early stages of deformation, DP steel with low carbon martensite islands may incur martensite fracture or elongation prior to the expectations laid out by these studies. Steinbrunner *et al.* [24] considered this notion that low carbon martensite islands with reduced cross-section could locally deform and fracture, which would lead to premature void nucleation.

Speich *et al.* [25] described the plastic incompatability of hard and soft phases in a discussion on the effects of carbon content on the hardness of the martensite phase. If martensite carbon content was sufficiently high so that martensite strength was above the strength of the deforming ferrite matrix, then it would be expected to not have an effect on the DP steel strength; however, if the martensite strength were to drop below the strength of the deforming ferrite matrix, then it could affect both strength and ductility. The literature does show that the martensite volume fraction is the most important factor for DP sheet steel strength and ductility, and that changes affecting martensite volume fraction will change the DP steel mechanical properties. This leads to the detrimental effects of heat input and the decomposition of martensite, which is covered in the next section on dual-phase steel tempering.

2.2: **Dual-phase Steel Tempering and the Effect on Mechanical Properties**

In this section, the literature on the mechanical properties of uniformly tempered DP sheet steels will be discussed. In the majority of studies described in this section, isothermal tempering over long tempering periods (approximately 1 hour) was used to examine the effects of tempering on DP sheet steel mechanical properties. A welding heating and cooling cycle occurs within seconds and, therefore, the isothermal tempering conditions that were studied do not directly reflect the conditions that occur within a weld HAZ; however, similar trends may occur and will be investigated further in the subsequent section that covers literature related to the effects of welding of DP steel.

Before examining the effects of tempering on the dual-phase microstructure and mechanical properties, a brief study by Grange *et al.* [26] is presented to show the effect that the presence of different alloying elements are expected to have on the hardness of tempered martensite. In the study by Grange *et al.* [26] the effects of Mn, P, Si, Ni, Cr, Mo, and V on martensite hardness in the quenched state and over a range of tempering temperatures were studied. Tempering was for 1 hour at isothermal conditions. These alloying additions were compared with hardness data for plain carbon steel in similar quenched and tempered states. Jha *et al.* [27] stated that the presence of alloying additions can affect tempering by modifying the segregation of tramp atoms (S, P, Sb, etc.) to prior austenite grain

boundaries, by potentially changing the transformation characteristics of retained austenite, and by potentially changing the nature and composition of precipitated carbides. It was also suggested that the diffusion rate of these substitutional alloying elements was too low to have a noticeable effect [23].

Alloy additions create a fourth stage of tempering and change the temperature ranges for the other three stages [10]. Grange *et al.* [26] found that the hardness of a quenched martensite particle was not quantitatively affected by the addition of the alloys. In general, tempered martensite hardness was observed to decrease as the tempering temperature increased; however, when tempering above 204°C, all of the alloying additions were observed to retard martensite softening when compared to the hardness of tempered martensite from plain carbon steel. As the percentage of an alloy addition was increased in a martensite particle, the resulting tempered martensite hardness also increased when compared to the baseline plain carbon tempered martensite hardness for any given tempering temperature above 204°C. Alloy additions were observed to have ranges of tempering temperatures where the resulting difference in hardness compared to the plain carbon tempered martensite was greatest; these represented tempering temperatures where a given alloy addition was most effective at limiting softening. The alloying additions P and Ni had the same effectiveness for limiting softening at all tempering temperatures. The alloying addition of Si was most effective for limiting softening at a tempering temperature of 316°C. Manganese was most effective for reducing softening over a tempering temperature range between 427°C to 649°C. For Cr, the most effective tempering temperature was 427°C. For Mo, the most effective tempering temperatures were over the range 538°C to 592°C. For V, the most effective tempering temperature was 649°C.

Martensite in alloyed steels can have secondary hardening due to a fourth stage of tempering and the precipitation of alloy carbides with high solute content [9,10]. An example of secondary hardening is shown in Figure 2.2. The chart shows an isothermal (1 hour) tempering curve of martensite that was formed for a 2% Mo – 0.1% C steel. At approximately 600°C there is a peak in hardness that is above the

quenched fully martensitic hardness value; this corresponded to the effective temperature range described by Grange *et al.* [26].

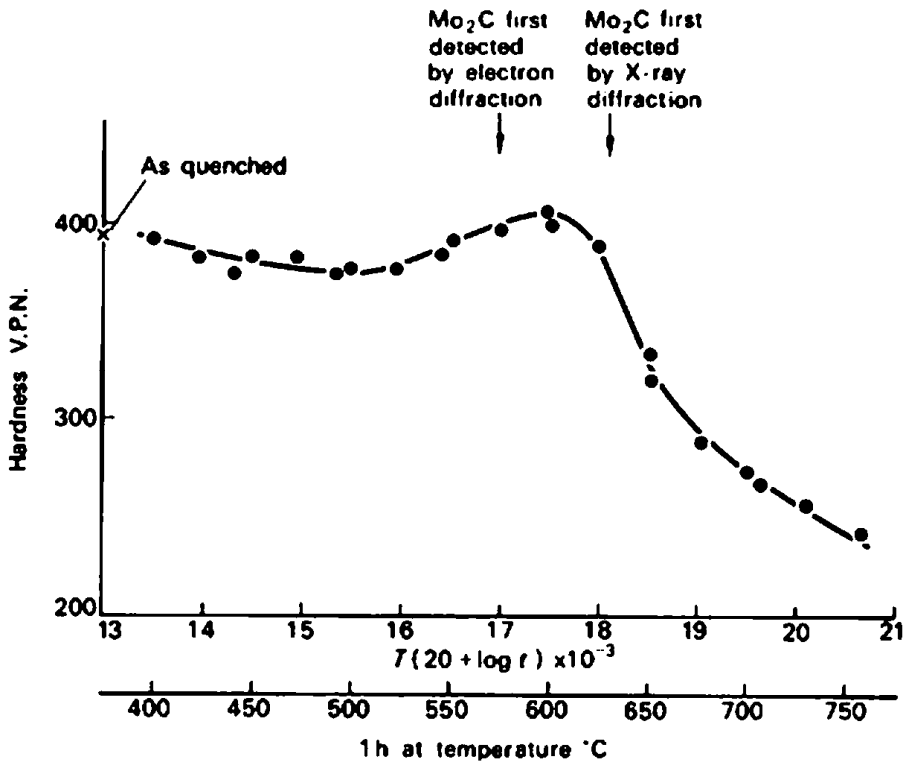

Figure 2.2: Hardness data obtained from the isothermal (1 hour) tempering of a 2% Mo – 0.1% C steel. The data shows data for tempered martensite that was observed to have secondary hardening. (taken from [10]).

These effective tempering temperatures and ranges of temperatures represent possible methods for reducing the softening in the weld HAZ and, based on the isothermal martensite tempering of alloy steels, there is potential for a hardened region to form in a weld HAZ due to secondary hardening; this would occur below the Ac_1 temperature in the subcritical (SC) region of microstructure. A weld HAZ is not directly represented by the isothermal conditions that were used during the study by Grange *et al.* [26]; however, microstructural regions of a weld HAZ microstructure may reflect the mechanical properties of alloyed tempered martensite. Certain locations of the HAZ microstructure may be more effectively prevented from softening due to the presence of a given alloy addition.

Studies on the tempering of DP steels have shown that as tempering temperature was increased, the yield strength (YS) and ultimate tensile strength (UTS) decreased for plain carbon DP steels [28]. In contrast, for alloyed DP steels, studies have shown that the UTS decreased but the YS increased as the tempering temperature was increased [23,25,27, 29 , 30]. However, it was also suggested that the composition of the DP martensite islands was important. Alloyed DP steels that had high martensite percentage may not show an increase in YS after tempering [31]. The percent elongation increased after tempering during all of the studies that were investigated. After tempering, most DP steels were observed to have discontinuous yielding.

In the following studies, the focus of the work was on the mechanical properties of specific compositions of DP steel. These examples show how different combinations of alloying additions affect the DP steel mechanical properties after isothermal tempering. Although experiments that were conducted for this thesis were done using Cr-Mo DP sheet steel, the following explores how tempering affected a number of different alloyed DP steels.

Joarder *et al.* [28] found that after isothermally tempering a plain carbon DP steel (0.1%C, 0.8%-Mn, and 0.31%-Si) the YS and UTS decreased. Percent elongation increased and discontinuous yielding returned after tempering at temperatures above 200°C. The observed reduction in strength was most severe after tempering at 200°C; at tempering temperatures above 200°C the YS and UTS drecreased gradually. Compared to DP steels that had richer alloy content, plain carbon DP steel did not show an increase in YS after any degree of isothermal tempering. This was contrary to other studies that had been conducted, and so Joarder *et al.* [28] stated that the mechanical properties of tempered DP steels depended on the steel composition, the intercritical annealing temperature, and the quench cooling rate. Panda *et al.* [31] confirmed this belief by observing that Cr-Mo DP steel with high martensite volume fraction did not show an increase in YS after tempering; whereas, lower martensite volume fractions produced from the same nominal composition showed an increase in YS after tempering. This had likely occurred because

martensite alloy content was lower for the DP steel that had a higher martensite volume fraction; due to a higher intercritical annealing temperature during processing.

Speich *et al.* [25,29] observed that the UTS of as-quenched 1.5%-Mn DP steels increased smoothly with increasing martensite percentage. The UTS of the tempered DP sheet steel was observed to decrease for low (200°C) and the high (650°C) tempering temperatures; the reduction in UTS was more severe (~35% reduction compared to < 5% reduction) for the high tempering temperature. DP steel that had a higher as-quenched martensite percentage also had higher UTS after tempering. For both tempering temperatures, the total elongation and the percent area of reduction were observed to increase; this increase was higher for the 650°C tempering temperature. In a later study, Speich *et al.* [29] examined the differences of mechanical properties between Mn DP steel (0.12%C and 1.5%-Mn) and Mn-Si-V DP steel (0.12%C, 1.7%-Mn, 0.58%-Si, and 0.04%-V). The Mn-Si-V DP steel was found to have a higher retained austenite percentage (~9%) compared to the Mn DP steel (~3%); Rashid *et al.* [30] also observed a high percentage of retained austenite (~10%) in Vanadium containing DP steel. The Mn-Si-V DP steel was more resistant to tempering at low temperature (200°C for 1 hour) than the Mn DP steel and there was very little evidence of carbide precipitation at interlath martensite boundaries; however, at a higher tempering temperature (400°C for 1 hour), both steels had significant precipitation and individual carbide particles could be resolved with an SEM. The UTS of the Mn DP steel decreased more rapidly (for a given tempering temperature) when compared to the UTS of the Mn-Si-V DP steel. After tempering above 400°C, the two steels were observed to have very similar ductility; this was attributed to retained austenite decomposition in the Mn-Si-V DP steel, which is described later in this section.

For vanadium DP sheet steel (0.1%C, 1.5%-Mn, 0.5%-Si, and 0.1%-V) Rashid *et al.* [30] observed that the YS increased as the tempering temperature increased (isothermal for 1 hour) and the UTS decreased as the tempering temperature increased; this observation was consistent with the study by Speich *et al.* [29]. The mechanical properties were unaffected up to a tempering temperature of 200°C for 1 hour. Above this temperature, the mechanical properties were affected and at a tempering temperature

of 500°C for 1 hour, the YS had increased approximately 29.5% and the UTS had decreased approximately 12.0%; a discontinuous yielding condition returned to the steel.

Similar observations were made by Jha *et al.* [27] for Cr-Mo DP sheet steel (0.06%C, 1.0%-Mn, 0.9%-Si, 0.4%Cr, and 0.35%-Mo) after isothermal tempering. The UTS was observed to decrease (15% after 500°C isothermal temper) and the YS was observed to increase as the tempering temperature increased. The YS reached a maximum (40% increase) at a tempering temperature of 300°C, and then slightly decreased in strength when tempered above this temperature; this was similar to a study by Panda *et al.* [31]. Discontinuous yielding returned to the steel after tempering above 100°C; the yield point elongation (YPE) increased as the tempering temperature was increased, but reached a maximum at 300°C and did not show further signs of change when tempered above this temperature. For Cr-Mo DP steel, Jha *et al.* [27] divided tempering into two ranges, which were below 300°C and above 300°C. In the range below 300°C, no significant microstructural changes were observed; however, carbon diffusion occurred and changes in ferrite and martensite strength were observed. In the tempering range above 300°C, carbon diffused out of the martensite to form well defined carbide particles. Martensite hardness decreased as the tempering temperature increased due to carbon diffusion out of the martensite body; however, at approximately 300°C the hardness was held relatively constant. Jha *et al.* [27] suggested that this was due to ε-carbide precipitation that had been identified. At higher tempering temperatures, above 300°C, ε-carbide was replaced by cementite formations and the hardness continued to decrease. This was also stated as a possible reason for the peak YS that had been observed after isothermal tempering at approximately 300°C.

Davies [23] observed that lean alloy (0.6%-Mn) DP steels softened more rapidly than rich alloy (1.5%-Mn, 0.1 - 0.3%-V/Cr/Mo) DP steels as the tempering temperature was increased; at lower tempering temperatures, the difference in both hardness and tensile strength were not substantially different. He also observed that the degree of tensile strength reduction for a rich alloyed air-cooled DP steel was lower than a rich alloyed water-quenched DP steel after being tempered at 450°C for 5 minutes;

however, the initial UTS and post-tempered UTS for the rich alloyed water-quenched DP steels were both higher than the respective air-cooled DP steels. Davies [23] found that the YS increased upon tempering for air cooled and water-quenched DP steels (aged for 20 – 30 mins. at 170°C). He suggested that this strengthening was a result of carbon diffusion that pinned free dislocations in the ferrite and/or formed fine iron-carbides. This increase in YS was observed at low temperature isothermal conditions, and subsequent tempering at higher temperature (above 300°C) led to a reduction of YS. A similar increase in YS was observed for an air cooled DP steel containing vanadium that had been tempered at temperatures above 300°C for 5 minutes. In both tempering experiments, he found that the UTS steadily decreased as the tempering temperature was increased. The increase in YS suggested that a discontinuous yielding behaviour was returning to the steel. In a similar study, Speich *et al.* [25] observed that discontinuous yielding behaviour returned to 1.5%-Mn DP sheet steel after high temperature (650°C) tempering for 1 hour; at low tempering temperature (200°C), discontinuous yielding only returned for DP steels that had a low martensite volume fraction (and hence had high martensite carbon content). They suggested that the increase in YS after tempering was due to a reduction of residual stress caused by a volume contraction that accompanies carbide precipitation within the martensite phase; this was based on a residual-stress model. In the context of welding DP steel, an increase in the YS of a weld HAZ tempered region could cause differences in the cross-sectional area of a welded uniaxial transverse weld tensile specimen during loading. This could cause more significant diffuse necking in the BM compared to the HAZ; more substantial diffuse necking in the BM could reduce the cross-sectional area and surpass critical strain required for void nucleation.

Effects from tempering non-martensitic phases in DP steels were also investigated. The main effects that were observed came from austenite decomposition, retained ferrite recovery, and cementite/carbide coarsening. In the following studies, individual microstructural changes that were suggested to cause the changes to DP steel mechanical properties after tempering have been investigated.

Okamoto *et al.* [19] measured approximately 1.0% retained austenite in a 0.02%C and 2.06%Mn DP sheet steel. When the retained austenite was quenched in liquid nitrogen (-196°C) from room temperature, the retained austenite transformed to martensite and subsequent tempering of the steel led to discontinuous yielding; the same effect was observed after 5% deformation at room temperature. In DP steel where retained austenite was present, tempering did not lead to discontinuous yielding. Furthermore, they suggested that retained austenite may suppress martensite tempering. Retained austenite has minimal decomposition at slow cooling due to manganese enrichment in DP steel [19]. Rashid *et al.* [30] observed that a vanadium DP sheet steel that had approximately 10% retained austenite in the as-quenched microstructure decomposed to an upper bainitic structure. Retained austenite decomposition occurred over the a tempering temperature range of 300°C (~10% decomposition) to approximately 400°C (~90% decomposition). Speich *et al.* [29] observed similar retained austenite decomposition in a Mn-Si-V DP steel after isothermal tempering at 400°C. The decomposition of retained austenite decreased the UTS and ductility of their DP sheet steel [30]. This was because retained austenite had transformed to martensite during deformation of as-quenched DP steel, but once the DP steel was tempered, the austenite had decomposed to bainite, which had a lower strength than martensite. Speich *et al.* [29] observed a reduction in percentage of retained austenite after DP steel was plastically deformed. Observations of Cr-Mo DP steel showed that there were minimal amounts of retained austenite [27].

Davies [23] suggested that higher carbon content martensite islands retain more strength after tempering and that this leads to more elongation for a given tensile strength. This reflected the general stages of tempering for higher carbon martensite that were described by Petty [10]. From that text, after the first stage of tempering (50 - 200°C) a high carbon martensite (> 0.25%C) was shown to decompose into ε-carbide + martensite (0.25%C). This suggests that decomposition from a high carbon martensite will retain the strength of a 0.25%C martensite after this early stage of tempering. The ε-carbide should not appear in tempered martensite that initially has less than 0.25%C; it is a transitional-carbide for the

nucleation and growth of cementite. The presence of ε-carbide has also been suggested to cause an increase in the hardness of martensite in the early stages of tempering [10,28]. The precipitation of ε-carbide in martensite is more likely with higher Si content because Si stabilizes its formation [10,27,28]. During tempering of a vanadium DP steel, Rashid *et al.* [30] and Speich *et al.* [29] observed dislocation pinning due to the precipitation of fine vanadium carbonitride precipitates (found in retained ferrite phase) and suggested that these might result in secondary hardening. These precipitates coarsened as the tempering temperature was increased. Rashid *et al.* [30] suggested that this could have caused the higher YS and reduced ductility that had been observed.

Zhu *et al.* [32] studied how alloy element segregation occurred in cementite during tempering of martensitic steel. In the study, the hardness of plain carbon (0.4%C) martensite was compared with a martensite that contained Mn/Si/Ni/Cr/Mo after different tempering conditions were applied. Both steels softened after tempering to just below 300°C; the degree of softening for both steels was similar. Above a 300°C tempering temperature, the alloyed martensite softening was significantly slowed when compared to the plain carbon martensite; there was a 50% difference in hardness between the alloyed and non-alloyed tempered martensite after tempering at 500°C for 1 hour. During tempering of martensite from a Fe-C-Si steel, there was no enrichment of Si in precipitated ε-carbide or in cementite; Si enriched zones existed adjacent to cementite that had precipitated in the martensite [32]. Zhu *et al.* [32] observed that reduced softening was caused by Si rejection from cementite, which reduced the rate of cementite coarsening; this occurred around 300°C. Cementite coarsening was also reduced by other alloy additions due to their slow diffusion rates.

Speich *et al.* [25,29] observed that at a low tempering temperature (200°C for 1 hour) there was carbide precipitation at martensite interlath/interplate boundaries and some carbide precipitation in the ferrite matrix; whereas, at a high tempering temperature (650°C for 1 hour) carbide precipitation in martensite coarsened and there was a significant decrease of the dislocation density in the ferrite matrix. Joarder *et al.* [28] found that martensite islands had a twinned plate morphology in a plain carbon DP

steel that had a 24% martensite volume fraction and a lath morphology when the martensite volume fraction was increased to 35%. After tempering at 200°C, they observed ε-carbide precipitation in the steel with 24% martensite and plate-shaped cementite precipitated within the laths of the steel that had 35% martensite. This suggested that the martensite carbon content was lower in the DP steel that had a 35% martensite volume fraction; in the range 0.67 – 1.00%C, martensite morphology begins to change from laths to plates [33] and ε-carbide precipitation only occurs in martensite with a carbon content of 0.25% or greater [10]. Tempering at higher temperature (600°C for 1 hour) led to spheroidization of cementite and recovery of the martensite lath substructure. Based on this, Joarder *et al.* [28] and Panda *et al.* [31] concluded that the tempering kinetics of martensite islands in DP steel was very similar to that of a fully as-quenched martensitic body in plain carbon steel.

Jha *et al.* [27] stated that the strength of as-quenched martensite was dependent on the martensite substructure (lath and plate twin size), the dislocation density that is generated from the phase transformation specific volume change (more notable in laths), the degree of tetragonality of the B.C.T. martensite lattice, and coherency strains at ferrite-martensite interfaces due to lattice mismatch. During martensite tempering, strength shifts into the ferrite matrix due to carbon diffusion; this is reflected by the increase in YS (governed by ferrite strength) and the decrease in UTS (governed by martensite strength). Tempering causes the martensite substructure to transform (carbide precipitation and growth), the dislocation density to decrease, and for carbon diffusion out of the martensite particle to occur, which decreases the BCT a/c ratio and coherency strains (decrease in lattice mismatch).

Davies [23] stated that DP steel strength was very dependent upon the strength of the martensite phase and that martensite decomposition (tempering) reduces the strength of DP steel; this was contrary to his previous work [5]. He may have meant that tempering reduced the martensite volume fraction; however, in his previous study he did state that the role of martensite carbon content was unclear, so this may have been spurred by new information. He stated that higher carbon martensite was stronger but less ductile and therefore was more susceptible to local facture (for a hole punching operation). On the topic

of DP sheet steel fracture mechanism, Speich *et al.* [25] stated that the critical strain for void nucleation (martensite fracture and ferrite-martensite decohesion) and the strain to tear the ferrite ligaments that join these voids equate to the total strain for fracture. An increase in the martensite percentage decreases the ferrite ligament distance between martensite particles and this reduces the total strain at failure. Tempering DP steel causes the martensite phase to lower in hardness and increase the critical strain required for void nucleation, which results in a greater reduction of area after fracture. Joarder *et al.* [28] and Panda *et al.* [31] observed that pockets of cleavage facets within a dimpled surface existed in as-quenched fractographs for plain carbon DP steels that had 24% and 35% martensite volume fractions; there were more cleavage facets with higher martensite volume fraction. They found that after tempering these two DP steels at 600°C, the fractographs changed to include only ductile dimple surfaces.

From the literature, it appears that tempering is affected by alloying additions so that over a range of tempering temperatures, a given steel composition would be observed to have varied rates of softening. It is generally difficult to specify these temperature ranges for DP steels of different alloy content because of complex interactions that occur. In terms of welding, a DP steel weld HAZ will be affected due to martensite tempering and the ranges of tempered HAZ microstructure could reflect the isothermal tempered ranges; softening may be limited or prevented over portions of a tempered HAZ of alloyed (or possibly unalloyed, if ε-carbide precipitates) DP steel. Although the detrimental effects that heat inputs have on DP steel can be expected to occur in a welded sample, a weld HAZ is not a uniformly tempered zone as studied by the literature found in this section. At all locations throughout a DP weld HAZ, mechanical properties will vary and it is the interaction of these mechanical properties across the HAZ that will govern fracture mechanisms for welded DP sheet steel. In the following section, studies that focused on the mechanical properties of DP steels that were affected by a welding thermal cycle are reviewed.

2.3: **Welded Dual-phase Steel and the Effect on Mechanical Properties**

The final portion of this literature review presents past work in which the effects of weld thermal cycles on the mechanical properties of DP steel has been studied. These studies focused on how the weld HAZ softens due to the heat of welding and on how DP welded joints react to applied loads.

In an early study on DP steel weldability, Ghosh *et al.* [34,35] studied the effects of weld heat input on Cr-Mo DP steel when using a flash butt-welding process. He stated that martensite tempering of the Cr-Mo DP steel during welding was expected at a temperature of approximately 600-650°C. The weld HAZ microstructure was distinctly divided into regions of different morphology that were parallel to the weld centerline; these different regions of morphology had different plastic flow characteristics and governed mechanical properties. Ghosh [34] found that the weakest (softest) region in the HAZ occurred approximately $6-7$ mm from the weld centerline; this was around a peak HAZ temperature of 600-650°C and was attributed to the presence of tempered martensite that was identified by SEM examination. In his study, he used forced water spray cooling to prevent martensite tempering. He found that the DP parent steel microhardness was 252 VHN, after welding with forced water cooling the softened zone hardness was 245 VHN, and after welding without forced cooling the softened zone hardness was 220 VHN. This suggested that by changing the cooling rate, the degree of DP HAZ softening could be reduced.

In a later study, Biro and Lee [36] investigated how material chemistry, weld heat input, and GMAW weld transfer mode affected DP steel softening in the HAZ of GMA welds. They made bead-on-plate welds using GMAW short circuit transfer and pulsed spray transfer and compared the HAZ softening behaviour for rich (Mn-Si-Cr-Mo / $CE_{[37]} = 0.36$) and lean (Mn-Si / $CE_{[37]} = 0.23$) alloy DP600 sheet steels. Microhardness profiles were used to identify the DP weld HAZ. They used 5 parameters to characterize the effects of the weld thermal cycle on the DP steel in the HAZ, which were: peak FZ hardness, peak HAZ hardness, degree of softening (difference between maximum softening and the BM

hardness), distance to maximum softening, and distance to BM hardness. Biro and Lee [36] attributed HAZ softening to the formation of tempered martensite, and identified tempered martensite islands at the location of maximum softening; this agreed with the observations by Ghosh [34]. They stated that minimum hardness occurred at the location of the HAZ where there was a division between tempered martensite and renucleated martensite. Figure 2.3 shows an example of microhardness profiles in which the effect of material chemistry is compared; the profiles that are shown were for a 5% prestrained coupon that was GMA welded with pulsed spray transfer. Rich DP steel chemistry increased peak HAZ hardness, decreased the degree of softening, and increased the distance to maximum softening. This study had shown that material chemistry can create different martensite tempering kinetics at different locations in the weld HAZ softened zone; it also affected austenitization and hardenability in the hardened HAZ. The weld fusion zone had similar hardness for both steels, which suggested that the composition of the GMAW filler metal was the dominant factor for determining FZ hardenability.

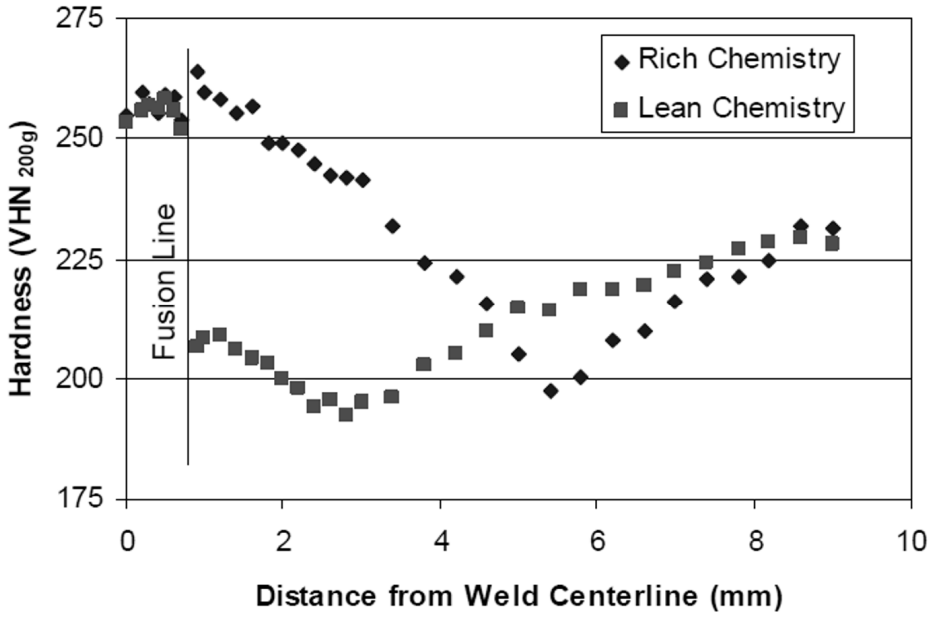

Figure 2.3: The effect of material chemistry on weld HAZ softening. (taken from [36]).

Biro and Lee [36] found that as weld heat input was increased, the peak HAZ hardness decreased, the degree of softening increased, and distance to maximum softening increased; this was an expected result and agreed with the work by Ghosh [34]. They found that the type of GMAW metal transfer mode did not appear to have an effect on welded DP steel HAZ hardness. They noted that higher heat input increased the time for carbon diffusion and the width of the softened zone increased as a larger portion of the steel was elevated to a temperature that was sufficient for carbon diffusion to occur. Furthermore, they suggested that a threshold heat input may exist where the degree of softening would reach a maximum. Above this suspected threshold, the degree of softening would not increase further. Hsu *et al.* [38] also studied the effects that the heat input from a GMA weld had on the mechanical properties of a DP600 steel. By analysing microhardness profiles, they observed softening (~20% hardness reduction) in the weld HAZ. They did not specify its exact location with respect to the Ac_1 line, but it appeared to be on the outskirts of the HAZ and adjacent to the BM. They stated that FZ hardness did not correlate well with heat input and suggested that the weld process had little effect on the weld FZ microstructure. This suggestion was contrary to the belief that critical cooling rates should affect weld metal hardening.

The effects of GMA weld process heat input on higher strength grades of DP sheet steel was examined by Conrardy *et al.* [39] using GMA welds made onto 1.54 mm Cr-Mo DP780 and 1.60 mm Cr-Mo DP980 sheet steel. Compared to the study by Biro and Lee [36], these can be classified as rich alloy DP steels. General observations of the weld HAZ were made using microhardness profiles. They found that both steels had higher hardness than the BM in the HAZ close to the FZ and that softened material existed adjacent to the Ac_1 line in the subcritical HAZ. In their analysis, they did not observe a noticeable difference between the microstructure in the softened zone and in the BM; however, they suggested that softening was due to the formation of tempered martensite. They observed an increase in degree of softening of approximately 30 – 40 VHN for the DP980 steel when compared to the DP780 and attributed this to the higher percentage of martensite in the DP980 BM.

The effect of prestrain on GMAW HAZ properties was investigated by Biro and Lee [36] and by Conrardy *et al.* [39]. Biro and Lee [36] prestrained (0%, 5%, and 10%) DP600 sheet steel coupons prior to GMA welding in order to simulate preformed automotive components; this increased the BM strength and hardness. Prestrain was found to affect the degree of softening and a higher prestrain produced a higher degree of softening. This was expected because prestrain had increased the BM hardness. Increasing prestrain was found to decrease the distance to maximum softening; however, welds that were made onto unstrained sheet had no evidence of softening. Biro and Lee [40] found that a lean chemistry DP600 steel that had 10% prestrain had a softened region that was between the Ac_1 line and the weld FZ of the HAZ; this was a region of newly formed microstructure that had nucleated after being fully austenitized by the GMAW weld thermal cycle. The weakest location of this weld was not in the tempered region of the HAZ. Similar to Biro and Lee [36], Conrardy *et al.* [39] analysed how prestrain (0% and 8%) affected softening in a GMAW HAZ for higher strength grades of DP steel. They found that 8% prestrain increased the DP780 BM hardness by approximately 10% and hence increased the degree of softening after welding. They observed that the same 8% prestrain produced a higher increase in hardness for the DP980 steel (~30%); this was attributed to greater dislocation density after prestrain. Prestrain did not affect the peak HAZ hardness for either steel.

The effect of GMAW filler metal was studied by Hsu *et al.* [38] and by Conrardy *et al.* [39]. Hsu *et al.* [38] found that an ER70S-6 filler metal achieved similar hardness in the weld FZ when compared to the Cr-Mo DP600 BM hardness. They found that a higher grade ER100S-G filler metal did not increase the transverse weld tensile strength of GMA welds made in DP600 sheet. The weld joint efficiency was base on the weakest point in the HAZ, which was the softened zone. They made butt welds with 4 mm thick DP600 steel using ER70S-6 or ER100S-G filler metal and Ar-CO_2 blends of shielding gas with a backing bar. The reinforcement height and backing bar were machined off prior to tensile testing. Conrardy *et al.* [39] found that an ER70S-6 filler metal was sufficient for a Cr-Mo DP780 weld, but that higher grade (ER100S-G) filler was suggested for tests on a Cr-Mo DP980 weld. The

ER100-G filler did not have any discernable effect on the strength of the DP780 welds. Using an ER70S-6 electrode, they observed similar hardness (~260 VHN) and microstructure (acicular ferrite and trace amounts of bainite) in the weld FZ for DP780 and DP980. They expected that this might have been too soft for the DP980 sheet steel. By switching to the higher grade ER100S-G electrode, the weld metal hardness increased (~300 VHN) and the microstructure was observed to have greater amounts of harder constituents (bainite and martensite). They stated that the weld metal microstructure and hardness were predominantly affected by the cooling rate. For the extremely rapid thermal cycles during RSW, Khan *et al.* [41] and Hernandez *et al.* [42] described interfacial fracture in the weld FZ, which was predominantly martensitic, for DP600 and DP780 sheet steel. RSW is an autogenous welding process and it is difficult to prevent the formation of a hardened FZ because DP steel chemistry has high hardenability. This shows the importance of the GMAW filler metal because, for DP steel welding, filler metal can be used in rich-chemistry steel to dilute the weld FZ and prevent excessive hardening and potential embrittlement.

The effect on the DP HAZ properties due to weld process cooling rate was studied by Ghosh *et al.* [34] and Conrardy *et al.* [39]. Ghosh [34] found that flash welding jaw distance, which affected the heating/cooling cycle, did not have a significant effect on peak temperature beyond a certain distance from the weld centerline, which depended on the net heat input; however, the cooling rates were observed to decrease as the jaw distance increased and this affected the HAZ microstructure for the same peak temperature. Fast cooling rates (short jaw distance or forced water cooling) reduced ferrite formation, enhanced martensite and bainite formation, and produced finer acicular ferrite in regions of microstructure that were fully austenitized by the welding heat input (immediately adjacent to the weld FZ). This was expected, because faster cooling rates were more likely to surpass the critical cooling rate to form martensite. Ghosh [34] used hardness profiles across the weld HAZ (from weld FZ to the BM) to reveal the location and approximate width of the softened zone. The width appeared to be larger for the weld without forced cooling. Regions that were closer to the weld centerline had significantly increased

in hardness compared to the BM hardness. These regions (above the Ac_3 line) had been fully austenitized during welding and had transformed to martensite, bainite, and acicular ferrite during cooling. The increase in hardness was substantially higher for the weld with forced cooling; this further suggested that the critical cooling rate to attain complete transformation to martensite was important for this region. Similar to the study by Ghosh *et al.* [34,35], Conrardy *et al.* [39] analysed GMA weld process cooling rate to observe different effects on DP HAZ softening. They established a high cooling rate by making butt welds with GMAW short circuit transfer and a copper backing bar and obtained a low cooling rate by using a GMAW-P spray transfer without a copper backing bar. For both DP780 and DP980, they found that a lower cooling rate produced a wider HAZ softened region, lower peak HAZ hardness, and slightly increased the degree of softening. This agreed with the results by Ghosh [34]. They attributed high peak hardness to a higher volume fraction of martensite for welds made with higher cooling rate; for low cooling rate the peak HAZ hardness was 260 VHN and for high cooling rate the peak HAZ hardness was 370 VHN. They suggested that the combination of the hardened HAZ and the softened HAZ act together to affect mechanical properties; although they did not provide further detail, this was important for understanding a DP steel softened HAZ fracture mechanism.

Xia *et al.* [43,44,45] studied the effect that HAZ softening had on welded Cr-Mo DP sheet steel mechanical properties by using two laser beam welding (LBW) processes. They used a Nd:YAG laser (high power density/low heat input) and a diode laser (low power density/high heat input), which provided two distinct ranges of weld heat input; both laser processes have relatively high power densities compared to GMAW. During their investigation, they used full penetration bead-on-plate welds made onto DP600 and DP980 steel. Xia *et al.* [43,44,45] found that the Nd:YAG laser produced a harder weld FZ in the DP600 sheet steel when compared to the FZ from a diode laser; this was attributed to the higher linear heat input of the diode laser. In contrast, the FZ in the DP980 sheet steel was observed to have similar hardness after welding with both lasers; this was due to the relatively high hardenability of the DP980 steel. The fusion zone microstructure was observed to be fully martensitic [43,44].

Xia *et al.* [43,44,45] examined the HAZ for evidence of a softened zone using microhardness profiles and found that the DP600 sheet steel only softened after welding with the diode laser; the Nd:YAG laser had created a weld without a softened zone due to sufficiently low heat input. For the DP980 sheet steel, there was evidence of a softened zone for both laser welding processes; however, the degree of softening was higher for the diode laser weld. The maximum degree of softening was located where the peak temperature during welding had reached the Ac_1 temperature for the steel. The amount of HAZ softening was directly proportional to the martensite volume fraction and ferrite within the softened region appeared to have minimal impact on the reduction of hardness [45]. The degree of softening increased as the weld travel speed was reduced (net heat input increased) and there was a threshold travel speed above which minimal softening was observed. They stated that a sufficiently shortened weld thermal cycle could prevent martensite (in the subcritical zone adjacent to the Ac_1) from fully tempering and confirmed this by observing the microstructural differences between a weld made at high travel speed (low degree of softening) with a weld made at low travel speed (high degree of softening). The amount of carbide precipitation within the martensite islands was significantly reduced in the welds made at high travel speeds [45] and in welds made with lower heat input welding processes [44]. Xia *et al.* [43] measured the distance from the weld centerline to the Ac_1 line. They found that as weld heat input was decreased, the distance to the softened zone and the width of the softened zone also decreased.

Xia *et al.* [45] found that HAZ softening could be correlated directly to the time required to heat the base-metal to its Ac_1 temperature. An example diagram that they proposed is shown in Figure 2.4. By using this correlation, they found that there was a threshold for the time spent at the tempering temperature whereby full martensite tempering would occur; additional time spent above the threshold would not produce any further softening. Likewise, there was also a threshold for the duration of time spent at the tempering temperature below which martensite tempering would be prevented from initiating. In the diagram, it can be seen that an upper and lower plateau had formed and that transition occurred at a given time, which represented the threshold to initiate tempering. These results confirmed the suggestion

by Biro and Lee [36]. In a similar statement, Ghosh *et al.* [34,35] suggested that the extent of tempering depended on $t_{p\text{-}3}$, which was the time duration that a region of microstructure was held within the temperature range $p = 600 \pm 20$ °C *to* 300°C. For flash butt-welded DP steel, forced water spray cooling was found to reduce the amount of tempered martensite within this region; however, it did not eliminate tempering completely. These studies suggested that with sufficiently low heat input and short heating and cooling times, it may be possible to prevent martensite tempering in DP steels during welding.

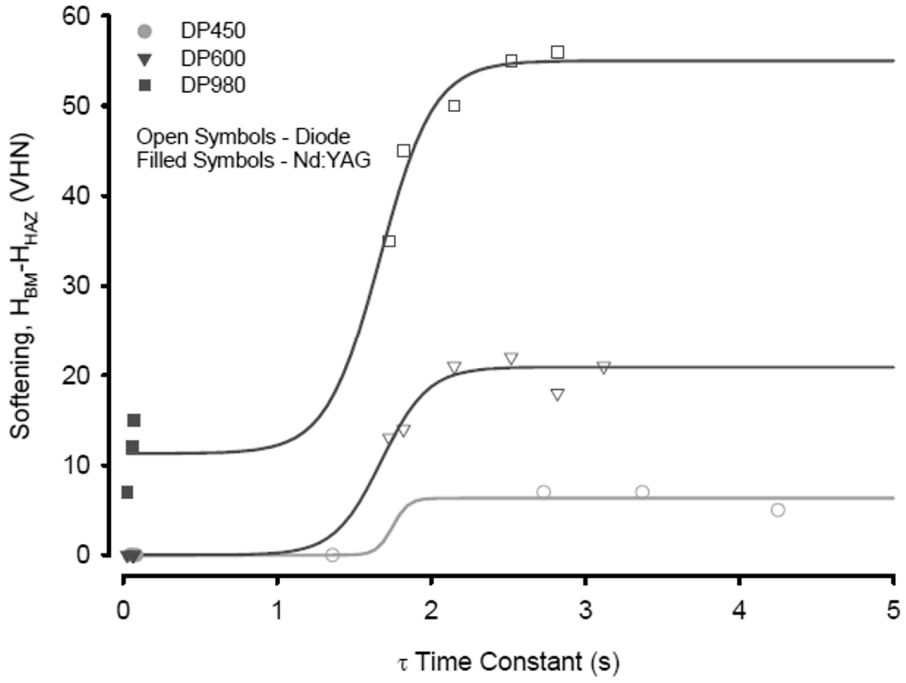

Figure 2.4: Degree of softening in DP steel was reduced by decreasing the amount of time spent at temperatures that initiate martensite tempering. (taken from [45]).

Uniaxial transverse weld tensile tests have been used in various studies to test joint efficiency and to examine how a DP steel weld HAZ affects strength and ductility of the welded joint. During uniaxial transverse weld tensile testing of flash butt-welded DP steel, Ghosh *et al.* [35] found that fracture occurred in either the softened HAZ (~6 – 7 mm away from weld centerline) or in the BM region (~20 mm away from weld centerline). Welds that were made without forced cooling fractured in the

softened HAZ and welds that had forced cooling fractured in the BM; this suggested that a higher degree of softening would be more likely to cause fracture in the softened HAZ region. Inclusions (incoherent particles) were identified in the BM microstructure; Ghosh *et al.* [35] stated that inclusions potentially had a more dominant role in BM fracture, because the softer HAZ had comparatively better flow characteristics. They suggested that percent elongation was higher for a BM fracture due to the restriction of necking caused by harder (non-tempered) martensite that was present adjacent to the BM fracture location. A transition of failure location from the HAZ to the BM was observed in this study. Ghosh *et al.* [35] suggested that the reason for the observed transition from a HAZ fracture to a BM fracture was due to the reduced softened region for the weld that fractured in the BM; however, this did not explain why the BM fracture specimen had not failed in the HAZ softened region.

Conrardy *et al.* [39] used uniaxial transverse weld tensile tests to characterize the mechanical properties of GMAW butt welded DP780 sheet steel. They observed that fracture occurred in the softened HAZ in 100% of their uniaxial transverse weld tensile tests. Joint efficiency ($UTS_{weld\ joint} \div UTS_{BM}$) was slightly higher for GMA welds made with a high cooling rate (~90% efficiency) when compared to welds made with a low cooling rate (~85-90% efficiency); this agreed with the observations made by Hsu *et al.* [38] who used uniaxial transverse weld tensile tests to determine the UTS of the welded DP600 steel. They used different GMAW variants, CV spray transfer (high heat input), pulsed spray transfer (moderate heat input), and a Tandem MIG ™ metal transfer system (low heat input) in order to create a wide range of weld heat inputs for their study. From tensile testing, the UTS was found to increase as the weld heat input decreased; however, the highest heat input only reduced the UTS by 5%. Although percent elongation is not normally measured from transverse welded uniaxial tensile tests [46], they reported that weld specimen percent elongation increased as the weld heat input was decreased. From the specimens that were tested, 78% fractured in the softened HAZ and 22% fractured in the BM. They suggested that the HAZ fracture was likely due to martensite tempering. While a transition of failure location from HAZ to BM was observed in this study, they did not correlate

it with heat input. These results suggested that DP600 steel had good weldability when welded with the GMAW weld process.

Xia *et al.* [44] observed decreases in the UTS of LBW welded Cr-Mo DP980 sheet steel after testing with uniaxial transverse weld tensile tests. There was an approximate 5% reduction of UTS from a low heat input Nd:YAG laser weld and an approximate 22% reduction of UTS from a higher heat input diode laser weld. These fractured in the softened subcritical region of the HAZ adjacent to the Ac_1 line. This suggested that higher heat input decreased UTS and caused the softened HAZ to become a more dominant factor for decreasing joint efficiency. The parent steel tensile results had shown anisotropic behaviour. Uniaxial loading that was parallel to the rolling direction achieved a higher UTS; this was attributed to the presence of banded martensite that only existed in higher strength grades of DP steel. Welds had been made transverse to the sheet rolling direction and, therefore, during loading, the sheet rolling direction was aligned with the uniaxial loading direction. Xia *et al.* [44] examined the fracture of the welded DP980 steel and found that void nucleation had occurred at tempered martensite islands due to decohesion with the ferrite matrix; however, the islands did not appear to be fully tempered and had only initiated carbide precipitation to inter-lath boundaries. In this state, the tempered martensite islands were still plastically inhomogeneous with the softer ferrite matrix. The final fracture was by void coalescence and ductile rupture.

Some work using Gleeble simulations was conducted in past studies. A Gleeble thermal simulation heat treats a metal specimen with high electrical current to create a rapid heating and cooling cycle and obtain a uniform microstructure throughout the specimen. For DP steels, this provides an opportunity to observe the effects of non-isothermal tempering typically experienced by the material during a welding process and provides the ability to characterize its effects on strength and ductility. This compliments the isothermal studies reported on in Section 2.2:. Gleeble thermal simulations have been used to reproduce welding thermal cycles in attempts to mimic a uniform weld softened zone in DP steel and to classify the strength of the softened zone.

Conrardy *et al.* [39] used a Gleeble thermal simulation to mimic the heating and cooling cycle that had occurred during GMA welding for a peak temperature isotherm of 1000°C. They used this thermal cycle to uniformly heat treat DP780 and DP980 sheet steel. The heating rate was 25°C/s. By analysing dilatometer width at different temperatures they found that the steel was fully austenitized upon heating through the temperature range of 720 – 860°C; this occurred over approximately 5.6 seconds. This showed that austenitization during GMA welding was not instantaneous, but did occur over a relatively short period and, therefore, other regions of the HAZ likely transformed over similar short ranges of temperature and time duration. This suggested that other peak temperatures could be evaluated with a similar approach. By measuring dilatometer width, the minimum peak temperature required to initiate austenitization could be evaluated; this would represent the peak temperature at the Ac_1, i.e., the location of maximum softening.

Xia *et al.* [44] used a Gleeble thermal simulation to reproduce a LBW softened zone microstructure uniformly across a DP980 uniaxial tensile specimen. The simulation used a heating rate of 300°C/s, a peak temperature of 650°C, a peak holding time of 1 s, and a cooling rate of 50°C/s; these parameters were selected to match observations from a typical LBW thermal cycle at the location of the softened zone. They found that the UTS of the uniformly softened specimen had decreased from the BM UTS of approximately 997 MPa to approximately 642 MPa (an approximate 35% reduction). They also found that the total elongation increased from 9.8% (DP980 BM) to 21% (uniformly softened). This confirmed that the softened zone had reduced strength and improved ductility; these properties had most likely contributed to localized necking in the softened zone during transverse weld tensile tests.

In a study by Biro and Lee [40], Gleeble thermal simulations were used to uniformly heat treat varying strength grades and compositions of DP sheet steel to mimic the microstructure that they had observed in a GMAW HAZ softened zone. They used uniaxial tensile specimens to characterize how the simulated weld thermal cycle had affected YS, UTS, and ductility. In their study, a lean chemistry ($CE_{[37]} = 0.23$) DP600, a rich chemistry ($CE_{[37]} = 0.36$) DP600, a lean chemistry ($CE_{[37]} = 0.31$) DP780, a

rich chemistry ($CE_{[37]}$ = 0.51) DP780, and a lean chemistry ($CE_{[37]}$ = 0.38) DP980 were tested. They also prestrained half of the steel test coupons to simulate the effect of forming on HAZ softened zone mechanical properties. During the simulated weld thermal cycle, the steel specimens were heated at a rate of 10°C/s, held at a peak temperature for 1.5 – 20 s, and then rapidly cooled with forced liquid nitrogen. The peak temperature was selected to be 15°C below a calculated Ac_1 temperature and all temperatures were within the range of 653 – 685°C. The heating cycle that they used appeared to be too slow, because it simulated a HAZ thermal cycle where it would take approximately 1 minute to reach peak temperature. During fusion welding of steel, the heating cycle typically takes place within seconds. They observed reduced hardness for the steels that were tested and that the reduction was the same after any hold time. Minimum hardness was achieved after the minimum hold time of 1.5 seconds. This was attributed to the slow heating and cooling cycle of the Gleeble simulation. The simulation had caused uniform tempering that represented a high heat input weld where full martensite tempering had occurred in the softened HAZ; this suggested that these samples would not differ significantly compared to isothermally tempered samples. Despite the slow Gleeble heating cycle, hardness results approximated actual GMAW HAZ softened zone hardness data for strained and unstrained samples. The prestrained coupons were observed to have a higher degree of softening, but also had a higher minimum hardness. This suggested that martensite becomes fully tempered in a typical GMAW subcritical HAZ (adjacent to the Ac_1 line); however, this study did not determine if a low heat input GMA weld could form a softened zone that had not been fully tempered. By using uniaxial tensile tests, they found that all of the uniformly tempered samples had reduced UTS when compared to the BM UTS; the reduction of UTS reflected the reduction of hardness that had been measured for those samples. They also observed the return of discontinuous yielding behaviour; an increase in YS was observed for samples that had been prestrained. For DP600, the reduction in UTS ranged from 10% (rich chemistry) to approximately 15% (lean chemistry), for DP780 the reduction ranged from 10% (rich chemistry) to 30% (lean chemistry), and a lean chemistry DP980 reduced by approximately 40%. They found that the reduction of UTS linearly correlated to the martensite volume fraction. They also suggested that prestraining was beneficial for retaining material

strength after tempering. This showed that the softened zone of a GMAW HAZ does become a weakened point for fracture to occur at; however, during uniaxial transverse welded tensile tests, the reduction of UTS was not observed to be as high as the reduction that was seen from uniformly tempered samples.

Biro and Lee [40] stated that an increase in YS (the return of an upper yield point) could prevent fracture in the softened HAZ and that fracture had been known to shift into the stronger BM in welded tubes made from lower strength DP600. They suggested that an increase in YS in the HAZ would cause the BM to yield and thin before the softened region, and that if thinning was significant, it would increase the stress being carried by the BM and fracture would occur there. They also argued that by prestraining prior to welding to increase the upper yield point and by using low welding heat input, a HAZ fracture could be prevented. Although this was for DP600, it could be possible to limit strength reduction that has been observed in higher strength grades DP780 and DP980 by following this suggestion.

Biro *et al.* [47] extended their work on why there is a shift in failure location of welded DP steels to GMAW lap fillet joints. They identified four distinct locations where fracture occurred during uniaxial transverse weld tensile tests and provided suggested fracture mechanisms for each. The four locations for fracture were: the FZ, the FZ/HAZ boundary, the softened HAZ, and the BM. They found that UTS for a FZ fracture decreased with increasing prestrain and increased with increasing filler metal strength. This fracture mode was attributed to the presence of porosity generated by vapourization of the zinc coating on the steel during welding. Heat input appeared to have an effect on the percentage of porosity; this was similar to the observations made by Conrardy *et al.* [39] for GMAW lap fillet welds on DP780 steel. They attributed porosity to gas being trapped between the upper and lower lapped coated DP sheets during weld solidification. For FZ/HAZ boundary fracture, Biro *et al.* [47] found that the UTS of welded DP780 steel was observed to decrease with increasing weld heat input. This was attributed to slower cooling rate in the HAZ, which would lead to softer microstructure. For a HAZ fracture location, UTS increased with increasing prestrain and for richer nominal chemistry, and the UTS decreased as the heat

input increased. Similar to butt welded and bead-on-plate welds, the HAZ fracture location for fillet lap welds was attributed to tempered martensite in the subcritical zone adjacent to the Ac_1 line. A BM fracture mode was not explained in detail, because it was not directly affected by weld process parameters and retained the mechanical properties of the parent steel; however, shifting to a BM fracture was discussed. They found that BM fracture occurred for welds with low BM hardness and low peak HAZ hardness; however, other than this, there was no further explanation of the reason for shifting to a BM fracture location. At high BM and peak HAZ hardness, the fracture was predominantly in the softened HAZ. As the peak HAZ hardness decreased and the BM hardness was still high, the fracture shifted to the FZ/HAZ boundary. They found that HAZ softening was not the predominant reason for a shift between the FZ/HAZ boundary and softened HAZ fracture locations. An increase in weld rotation of lap fillet joints during loading was found to cause fracture to occur at the FZ/HAZ boundary; rotation was believed to cause a stress concentration at the FZ/HAZ boundary. This increase of rotation was attributed to softer peak HAZ microstructure. This study focused examination on the reasons for a shift of fracture mode for lap fillet welds. It was found that the reasons for a shift between a softened HAZ fracture to a more preferable BM fracture were similar to their previous studies [36,40] of bead-on-plate welds.

In summary, from the literature, there is a potential for high weld metal hardness and fusion zone brittleness in autogenous DP sheet welds. Martensite tempering kinetics is affected by the steel composition. Sufficiently low weld heat input (or high cooling rate) can prevent full martensite tempering while prestrain on welded DP steel has been found to increase the degree of softening but also increased YS. Various methods for shifting the welded joint fracture location from the HAZ into the stronger BM have been suggested. Generally, sheet thickness was excluded from the studies found in the literature by using normalized equations; this was the case for the study by Xia *et al.* [45]. It was not clear how sheet thickness would affect fracture for GMA welds in DP steel. Typically, GMAW is not used for thin sheet steel welding in automotive manufacturing because of excessive heat input from spray metal transfer and because low heat input GMAW short circuit metal transfer does not have acceptable

bead quality and lacks root penetration. Pulsed spray transfer has been shown to effectively weld sheet below 2 mm in thickness and has similar net heat input compared to GMAW SC metal transfer. This was considered important for study because DP steel achieves good strength to weight ratio (and hence good fuel economy in automotive) based on decreasing the sheet thickness.

The literature showed that DP steel gets its high strength from its volume fraction of martensite and that, as the volume fraction increases, the strength of DP steel increases. Other factors that can increase DP steel strength are a finer ferrite grain size and higher carbon content of individual martensite particles. Martensite tempering causes the volume fraction of martensite to decrease, which is the main factor for loss of strength; tempering was also shown to increase DP steel ductility. There was also potential for increased YS of tempered DP steel, which was attributed to alloy carbide precipitation and secondary hardening.

From the literature, it is known that GMAW can be used to weld DP600 steel and retain high joint efficiency, and that HAZ fracture can be avoided. This suggested that it would be possible to create a transition of the failure location from the undesirable HAZ location to the more desirable base-metal location when GMA welding DP600 sheet steels. If a combination of GMA welding parameters could be found that consistently created a transition of the failure location, then the mechanisms responsible for this shifting from HAZ fracture into the stronger BM could be determined. It is also known that HAZ fracture and reduced joint efficiency are expected for higher strength grades of DP steel when welded with a GMAW process. The majority of HAZ fractures are associated with softening due to martensite tempering, but it is unknown if a GMA welding process can be optimized to achieve sufficiently low heat input in order to prevent full tempering from occurring. In simulated non-isothermal tests of uniformly tempered DP steel, it was shown that the softened zone does have reduced UTS and can have increased YS; but reasons for increased YS have only been studied in detail for isothermal tempering. Rich nominal chemistry can be used to limit DP steel softening, which appears to be fairly important to a high heat input welding process like GMAW; rich chemistry steels were shown to retard softening during

isothermal tempering of martensite. The strength grade of the filler metal did not appear to be a significant factor for determining joint strength, because the welds fracture in either the softened HAZ or the BM; however, if DP hardenability produces a brittle FZ, then filler metal can be used to dilute the weld metal and reduce the hardenability. Prestrain appeared to be a possible method for increasing HAZ YS and it was suggested that this could be a method for shifting the failure location. Fillet lap welds of DP sheet steel fractured in the HAZ for similar reasons as bead-on-plate welds. This suggested that the experiments for this thesis could use the simpler bead-on-plate weld geometry to avoid complications due to joint rotation in order to study the transition of fracture from the softened HAZ to the BM and the results would be expected to be applicable to more complicated joints.

Chapter 3: Experimental Apparatus and Methods

The first goal of this study was to make bead-on-plate GMAW-P welds on DP600 sheet steel using a range of welding heat inputs in order to determine a set of welding conditions that would give consistent base-metal failure and a second set of conditions that would give consistent HAZ failure during uniaxial transverse weld tensile testing. With the two conditions identified, the second goal was to compare the two different failure modes and determine why a transition of the failure location was occurring. By discovering the mechanism for the transition of failure in DP600, there could be avenues opened to apply the same reasoning to GMAW-P welding of higher grade dual-phase steels, such as DP780 and DP980.

To reach these goals, welding trials were conducted using a range of GMAW-P welding conditions to identify conditions that would create full penetration bead-on-plate welds that had minimal defects. The trials were conducted by varying the GMAW-pulsed waveforms, wire feed rates, travel speeds, and contact-tip-to-workpiece distances. The intention was to have similar weld bead geometries that were formed under different heat input and different heating and cooling rates.

A robotic welding station was used to form consistent linear welds using pre-existing GMAW-P waveforms. A data acquisition system was used to collect in-situ welding voltage and current data. A LaserStrobe video camera was used to observe the mode of weld metal transfer because it was desirable to perform all GMAW-P welds in streaming spray transfer mode.

In this chapter, an outline of all of the materials and GMAW consumables that were used for the study are presented. All of the procedures that were followed to create consistent full penetration welds are described. All equipment that was used for weld preparation is listed and respective setup procedures are given. All procedures for weld testing are listed with a brief description along with their intended purpose. Finally, post-processing analysis procedures are given.

3.1: **Experimental Materials**

This study was concerned with the metallurgical effects of GMAW-P heat input on dual-phase steel sheet and the subsequent effects on the DP sheet steel mechanical properties and failure locations. The materials that were used in the study are shown in Table 3.1. There were five dual-phase (DP) steels and one high strength low alloy (HSLA) steel used during the project. The table shows the base-metal thickness, coating type and weight, and mechanical properties as provided by the supplier, ArcelorMittal Dofasco, Inc. [48]. With each steel designation, there is a shorthand code ('##s') that was included for the purposes of this study in order to differentiate the various steel chemistries, grades, and sheet thicknesses. All of the steels have a protective zinc coating, where a GI coating type signifies a *hot-dipped galvanized* sheet and a GA signifies a *galvannealed* sheet.

Table 3.1: The base-metal physical properties for all materials used in the study. [48**]**

Steel Designation	Sheet Thickness h [mm]	Yield Strength σ_{YS} [MPa]	Ultimate Strength σ_{UTS} [MPa]	Total Elongation [%]	Coating Type	Coating Weight [g/m^2]
HSLA-'17s'	1.80	417.8	448.2	30.2	GI	150
DP600-'16s'	1.65	348.9	638.4	23.7	GI	137
DP600-'24s'	1.80	383.7	605.7	25.6	GI	128
DP600-'22s'	1.20	383.2	655.9	26.8	GA	94
DP780-'21s'	1.20	418.0	782.4	18.2	GI	144
DP980-'23s'	1.20	674	1061	12.0	GA	125

The typical microstructures of each steel grade are shown in Figure 3.1. The DP steels were produced at ArcelorMittal Dofasco, Inc. [48] by continuous casting, hot-rolling the billets down to the desired sheet thickness, and then intercritcally annealing with a rapid quench to form pockets of hardened

martensite in a ferrite grain matrix. The volume fraction of martensite islands was increased for the higher strength grades by holding the sheet steel at a higher temperature during the intercritical annealing step. The HSLA was precipitation-strengthened steel that was produced with continuous casting, then a controlled rolling process to obtain fine austenite grains (with some deformation) that transformed to fine ferrite grains upon cooling [49]. The rolling also provided the desired sheet thickness.

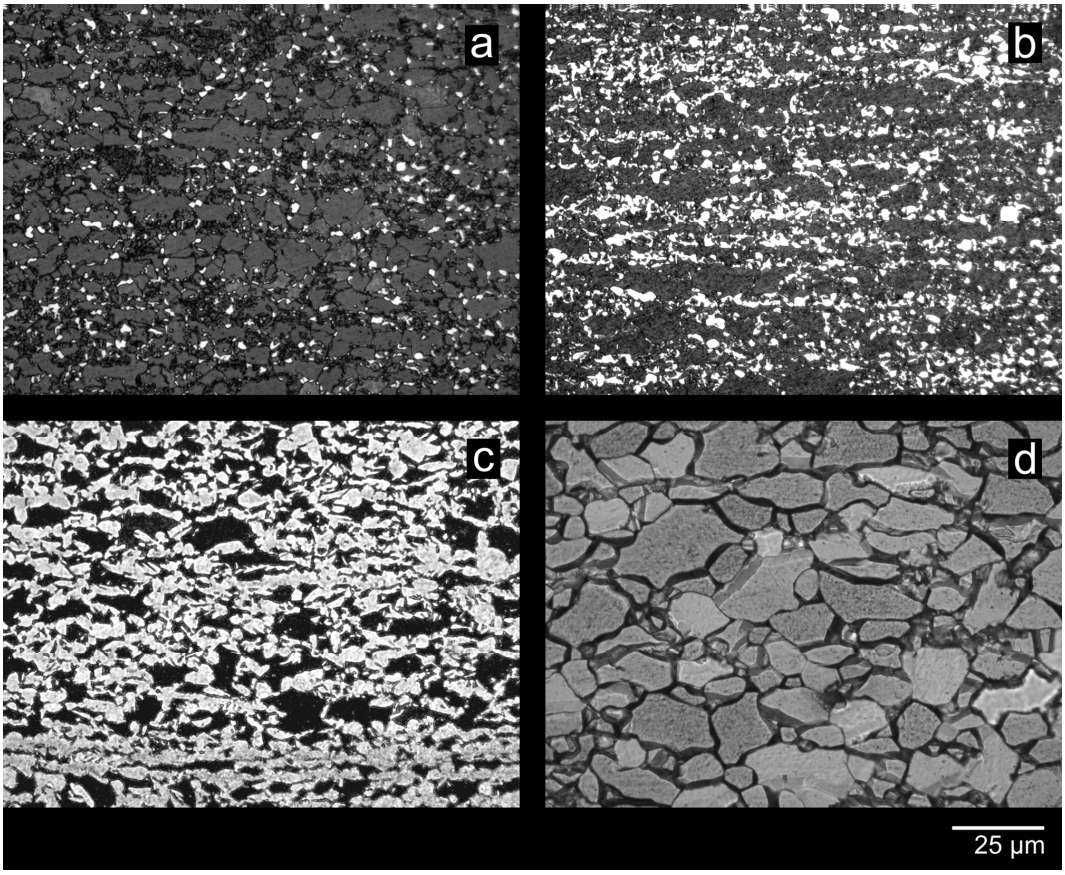

Figure 3.1: The base-metal micrographs for a) DP600-'16s' b) DP780-'21s' c) DP980-'23s' and d) HSLA-'15s'. The DP specimens were etched with the Lepera's tint [7]. Martensite islands appear white in those images. The HSLA specimen was etch with 2% Nital.

The compositions of the different steels were measured by ArcelorMittal Dofasco, Inc. [48] and are given in Table 3.2. All of the DP steels except for the DP980 grade were enriched with chromium and molybdenum and are therefore considered to be 'Cr-Mo type DP steels'. The HSLA steel was enriched

with copper to help with corrosion properties of the steel and is therefore considered a 'Weathering HSLA steel' [49].

Table 3.2: The base-metal compositions (wt%) as supplied by ArcelorMittal Dofasco, Inc. [48].

Steel Designation	C	Mn	Si	Cu	Ni	Cr	Mo	Al_{tot}	Ti	V	CE [37]
HSLA-'17s'	0.06	0.64	0.22	0.12	0.04	0.07	0.01	0.04	0.01	0.00	0.21
DP600-'16s'	0.11	1.57	0.17	0.03	0.01	0.19	0.21	0.04	0.02	0.00	0.47
DP600-'24s'	0.11	1.50	0.17	0.04	0.01	0.19	0.21	0.04	0.02	0.00	0.46
DP600-'22s'	0.11	1.53	0.18	0.04	0.02	0.19	0.21	0.04	0.02	0.01	0.46
DP780-'21s'	0.15	0.88	0.23	0.06	0.02	0.32	0.11	0.03	0.02	0.01	0.40
DP980-'23s'	0.15	1.50	0.31	0.02	0.01	0.02	0.01	0.05	0.00	0.00	0.43

In Table 3.2, a carbon equivalent (CE) value was calculated for each steel using Equation (3.1):

$$CE = \%C + A(C)\cdot\left\{5\cdot\%B + \frac{\%Si}{24} + \frac{\%Mn}{6} + \frac{\%Cu}{15} + \frac{\%Ni}{20} + \frac{\%Cr + \%Mo + \%Nb + \%V}{5}\right\} \quad \textbf{(3.1)}$$

where

$$A(C) = 0.75 - 0.25\cdot\tanh\left\{20\cdot\left(\%C - 0.12\right)\right\}$$

Equation (3.1) was based on the empirical equation proposed by Yurioka *et al.* [37]. This was the same CE value that was used by Biro and Lee [36] in their study on GMA welding of rich and lean DP600 sheet steels. In the production of the higher grade DP steels, holding at a higher intercritical annealing temperature produces more austenite for the quenching step, but also reduces the amount of carbon expected in the austenite and the subsequent martensite phase. This is compensated for by increasing the

average weight percent of carbon in the DP780 and DP980 steels mixtures. The CE value was included in Table 3.2 to provide an estimate of the likelihood of forming bainite and martensite in the heat affected zone (HAZ) during welding; a higher CE suggested higher hardenability.

Welding coupons were made by shearing the base-metal sheets. Two different coupon sizes were used in the study: a 254 mm × 76.2 mm coupon for initial weld parameter trials and a 254 mm × 203 mm coupon for mechanical testing of selected welds. The smaller 254 mm × 76.2 mm coupon was meant to conserve material during the weld procedure development experiments. The larger coupon size was based on the ASTM E 8-04M standard [50] for standard size uniaxial tensile specimens. The coupons were cleaned prior to welding by swabbing with n-Heptane to remove lubricants and dirt pickup from the surface.

The GMAW consumable electrode used for the study was a 0.9 mm ER70S-6 wire. The electrode mechanical properties appear in Table 3.3 and nominal composition for the electrode is given in Table 3.4. These nominal values were taken from the ASM Handbook [51]. This electrode wire was chosen because the as-welded filler metal closely matched the DP600 and HSLA grade steel mechanical properties, specifically the ultimate tensile strength. However, it did not match the higher grades of DP steel (DP780, DP980). This was allowed because the weld bead that forms during GMAW welding has a much larger cross-section during uniaxial tensile testing than the parent steel (the weld bead was not removed for any uniaxial tensile tests). The expected softened zone in the heat affected zone (HAZ) also decreased the need for a matching electrode. The ER70S-6 electrode has more Mn and Si, compared to a lower grade ER70S-3 electrode, to help reduce the amount of CO boil defects when using a reactive shielding gas containing oxygen and/or carbon dioxide.

Table 3.3: GMAW electrode mechanical properties as given by the ASM handbook [51].

Steel Electrode Designation	Diameter d [mm]	Yield Strength σ_{YS} [MPa]	Ultimate Strength σ_{UTS} [MPa]	Electrode Coating
ER70S-6	0.89	415.0	495.0	Copper

Table 3.4: GMAW electrode nominal composition as indicated by the ASM handbook [51]. The carbon equivalent value is included for comparison to the parent steel chemistry.

Steel Electrode Designation	C	Mn	Si	CE [37]
ER70S-6	0.05 - 0.17	1.40 - 1.85	0.80 - 1.15	0.31 - 0.41

Welds were shielded from the atmosphere with a Mig Mix Gold™ shielding gas, provided by Praxair [52]. The composition of the gas mixture was > 90% Argon and < 10% CO_2 [52]. This shielding gas was chosen based on the ANSI/AWS C5.6-89 standard, *Recommended Practices for Gas Metal Arc Welding* [13]. This standard indicated that Argon with 2-8% CO_2 should be used for GMAW streaming spray transfer on low-alloy steels. The shielding gas was supplied to the weld zone at a constant flow rate of 14 L/s.

3.2: **Experimental Apparatus**

All GMAW welds were made with a Fanuc 6-axis robot and Lincoln Powerwave 455/R GMAW power supply. The equipment setup is shown in Figure 3.2. The figure shows the general setup for the robot, the power supply and GMAW welding circuit, the data acquisition sensors (voltage and current), the LaserStrobe high-intensity video camera, and the welding table and workpiece clamping fixture.

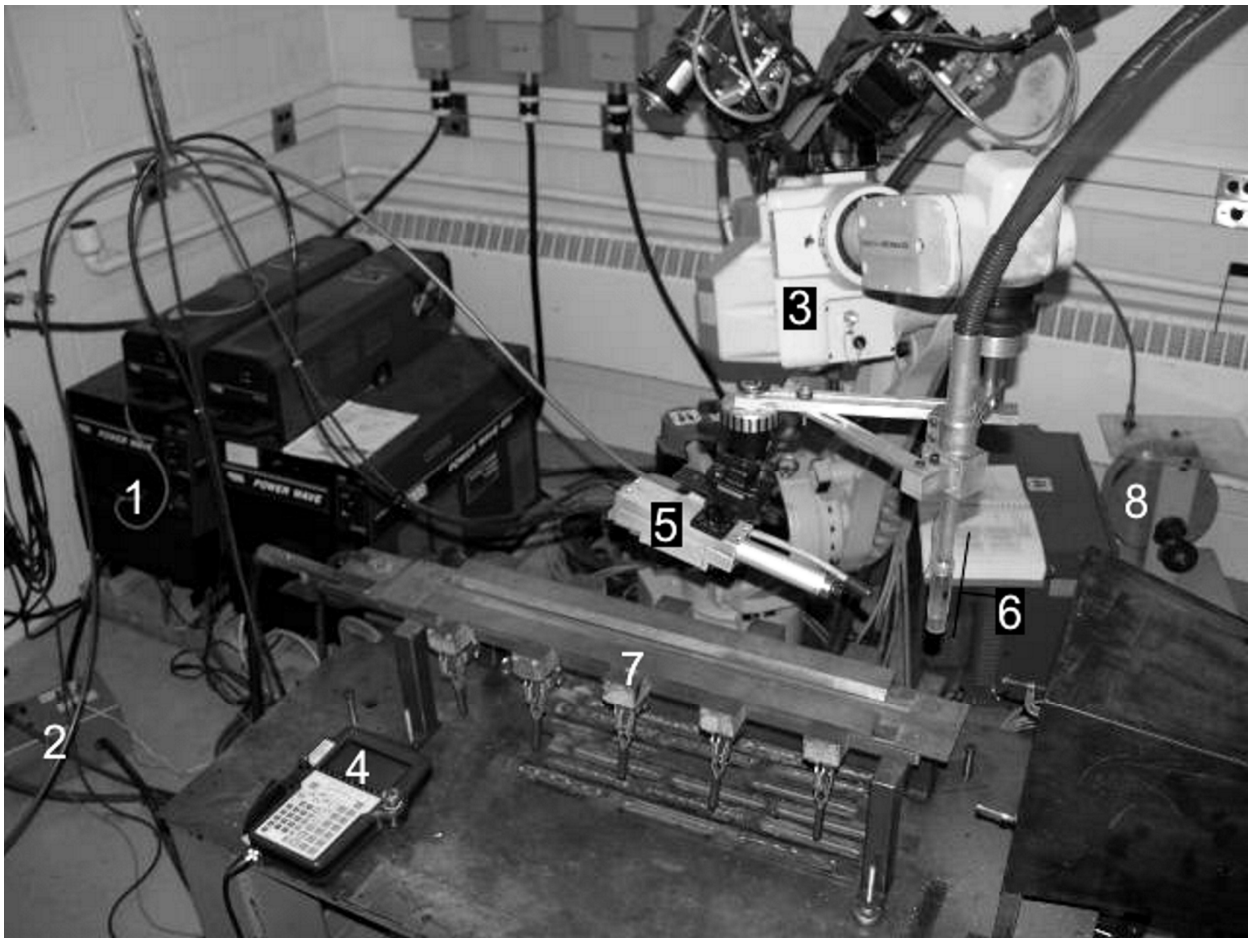

Figure 3.2: Welding setup used for the study. 1) Lincoln Powerwave 455/R Welding Power Supply 2) Data Acquisition Main Terminal 3) Fanuc Arcmate 120i 6-axis Robot 4) Fanuc Remote Controller 5) Laserstrobe High-intensity video camera and Nitrogen Strobe Laser 6) GMAW Torch 7) Workpiece Welding Table and Clamping Fixture and 8) Filler Wire Spool.

3.2.1: Fanuc Robot and GMAW-P Setup

The Lincoln Electric Powerwave 455/R power supply included pre-programmed pulsed gas metal arc welding (GMAW-P) process parameter schemes. The majority of welds conducted during the study were GMAW-pulsed spray transfer mode. A Lincoln Electric *crisp pulse 12* welding scheme was used. The Fanuc Arcmate 120i 6-axis robot was used for controlling the weld paths, the GMAW torch orientation and contact-tip-to-workpiece distance (CTWD), and stored all GMAW-P parameters. The Fanuc robot had direct control of the shielding gas outlet solenoid (not the gas flow rate), the wire feed activation and

wire feed speed (WFS), and the weld travel speed (TS). The robot was directly linked to the Powerwave 455/R and was used to input GMAW-P Trim values to the power supply. Trim was the Lincoln Electric term used to describe a pulsed voltage waveform. The Powerwave 455/R supplied the voltage to the welding circuit. The power supply used a voltage sensing connection to help stabilize the arc during welding [53]. This connection was clamped on the end of the work table near the weld end position.

The GMAW-P waveform that consisted of the four parameters: peak current, peak time duration, background current, and background time duration. The Powerwave 455/R had these four parameters collected under one parameter known as trim. Each trim value represented a waveform created by Lincoln Electric that was scaled to work with the specified WFS. During the study, there was no attempt made to modify the waveforms. Observations were made to select trim and WFS combinations that created streaming spray transfer welding conditions. The CTWD was also adjusted to vary the pulse output.

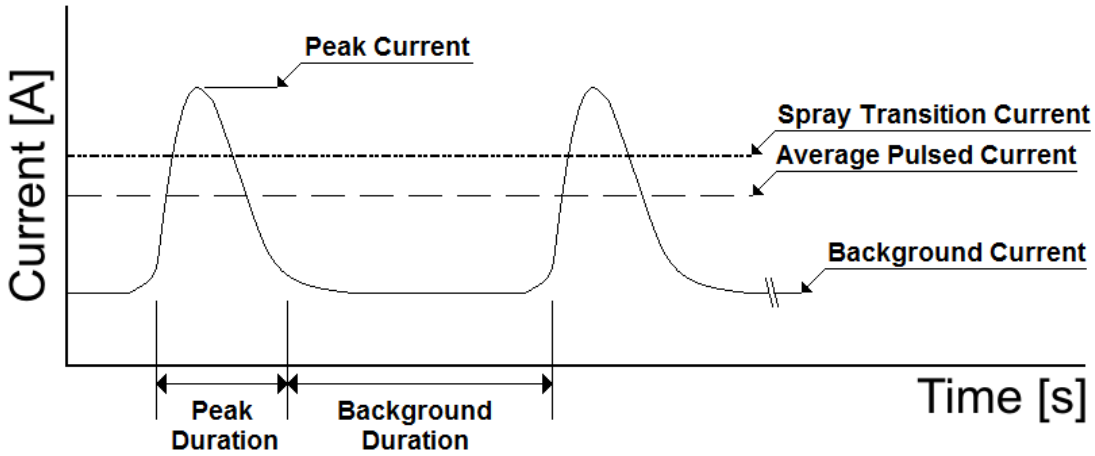

Figure 3.3: A schematic of a typical GMAW-Pulsed waveform. The intention of using a pulsed current is to mimic a spray metal transfer mode with an average current that is lower than a GMAW-CV transition spray current for the same electrode and shielding gas.

Weld start and finish locations were programmed using 'position registers' that were taught to the robot using the Fanuc remote controller. For the bead-on-plate welds, which were all single linear welds, two position registers (start and end), plus safety positions away from the weld were required. Position registers were taught to the robot by jogging the robot to the desired location relative to the workstation

and then recording that location into memory. The CTWD was measured prior to recording a new start or end position register by using a pre-measured block. The blocks were measured with a digital calliper. The GMAW torch orientation was also set at the start and end positions by using a level and a protractor. A 0° push angle and 90° work angle were used for all bead-on-plate welds.

The electrode was fed off of a spool to the torch using a wire feed roller. The feed roller system was directly linked to the Fanuc robot and the remote control was used to set the WFS. The controller was also used to jog the electrode to the torch. The wire feed roller speed was measured at the beginning of the study using a tachometer to verify that the Fanuc WFS was accurate.

The weld TS was also controlled by the Fanuc remote controller. Values for TS were inputted to the controller before each weld. The TS was not measured directly but was verified by using the voltage and current data acquisition system, which is described in the following section.

3.2.2: Data Acquisition System

To monitor the welding power, both welding voltage and welding current were measured using a data acquisition system. This allowed average power and instantaneous power to be calculated for each weld. The data was reviewed to check weld process stability and pulsed-waveform parameters.

The voltage was collected using an LEM-LV 100 closed-loop voltage transducer [54]. This transducer was connected to a point near the beginning of the torch head-cable and to a point on the workbench prior to the ground-cable. This gave a total voltage drop across the torch weld cable length, the contact tip, the electrode, the arc, and then the distance from the weld to the workbench connection point. The amperage data was collected during welding with an LEM-LT 505-S closed-loop current transducer [54]. The LEM current transducer was located on the Lincoln Powerwave 455/R ground-cable. It uses a Hall effect current measuring device [54]. Data readings were transferred onto a PC microcomputer with a PCI-9114 DAQ circuit board [55]. A program was modified [56] from a previous data collection file using Visual Basic [57] to output the DAQ data into a PCI file (specific to the PCI-

9114 circuit board). The PCI files were converted to readable text files using conversion software. The text files were then exported and used in Microsoft Excel [58].

The LEM current and voltage measuring devices output signals that were in the range of +/- 10 V. Current and voltage calibration equations were required to convert these voltages to the actual welding current and voltages. These calibration equations were established by outputting data to the PCI DAQ board from measurements made on a calibrated DC power supply. The LEM-LV 100 voltage transducer was used to measure voltages from the power supply over a range of 5-50 V in 5 V increments. The LEM-LT 505-S current transducer was used to measure amperages from the calibrated power source at 5, 15, 30, 150, and 500 A. A linear regression analysis of the data provided the following conversion equations:

$$V = 10.91v \quad \textbf{(3.2)}$$

$$I = 100.5i \quad \textbf{(3.3)}$$

where v is the output voltage from the LEM-LV 100 voltage transducer and i is the output voltage from the LEM-LT 505-S current transducer.

All welding voltage and current waveforms were reviewed in Microsoft Excel [58] using 'Conditional Formatting'. Cells in the Excel spreadsheet were formatted to be filled in with GREEN at high values and RED at low values. This allowed the general stability of the pulse waveforms to be observed at a glance. This was also used to remove run-in and crater weld data from the average power calculations and hence give an estimated 'steady' weld power.

A data acquisition sample frequency of 5000 Hz was used for the majority of welding (this could be adjusted if required). This frequency gave smooth pulsed waveform results when plotted. The frequency of the output data allowed the time duration of each weld to be measured. This was

accomplished for each weld by searching the data file and locating where current started and ended. The number of data points between the start and end locations could then be counted and converted to a time duration using Equation (3.4):

$$t_{weld} = \frac{N}{f} \tag{3.4}$$

where t_{weld} is the weld time in seconds (s) from when a current was first detected to when the current ended, N is the number of data points, and f is the data sampling frequency in Hertz (Hz). The weld length was then measured from the Fanuc position register used for the weld run-in location to the Fanuc position register used for the weld end crater. This distance was then inputted into Equation (3.5):

$$v_{measured} = \frac{L_{weld}}{t_{weld}} \tag{3.5}$$

where $v_{measured}$ is the measured weld TS used during welding in millimetres per second (mm/s), and L_{weld} was the measured length of the weld in millimetres (mm). The measured TS and inputted TS were compared for all of the welds as a means of verifying the Fanuc robot speed.

The welding power was also monitored. The voltage and current data from the DAQ system allowed an average power for the entire weld to be calculated. The average power was calculated with Equation (3.6):

$$P_{AVG} = \frac{\sum_{i=1}^{N} I_i}{N} \cdot \frac{\sum_{i=1}^{N} E_i}{N} \tag{3.6}$$

where P_{avg} is the average welding power in Watts (W), I is the current in amps (A), E is the electric potential in volts (V), and N is the number of data points collected. The voltage and current waveforms were reviewed in Microsoft Excel [58] using 'Conditional Formatting'. The general stability of each

GMAW-P waveform was observed and the run-in and crater weld power data was removed from the average power calculations. This gave an estimated 'steady' weld power that was then used to determine a relative heat input for each welding process.

The relative heat input per unit distance of each weld was calculated using Equation (3.7):

$$H_{rel} = \frac{P_{avg}}{v} \tag{3.7}$$

where H_{rel} is the relative heat input in Joules per millimetre (J/mm) and v is the travel speed in millimetres per second (mm/s). The heat input was designated in relative terms because there was no accounting made for weld process efficiency during the study. The relative size of the HAZ for a relative heat input was the focus of comparison for all welds.

3.2.3: The LaserStrobe Video Imaging System

It was important that consistent welds were produced for the study and it was desirable to have streaming spray transfer as the metal transfer mode. Although it was desirable to have streaming spray transfer mode, slight deviations were accepted and then noted for reference.

A LaserStrobe video imaging system was used to verify the mode of metal transfer during welding. A schematic of the video system is shown in Figure 3.4. The LaserStrobe system used a Model 4Z Nitrogen Laser (N50 rated by ANSI Z-136 as a Class IIIb laser) to act as a high intensity strobe light source. The CCD camera was fitted with a narrow band pass filter to only accept the reflected Nitrogen laser 337 µm wavelength and an image intensifier that amplified the reflected light and also provided temporal gating. This LaserStrobe system allowed video imaging of the GMAW weld pool and the electrode tip during welding at a frame rate of 30 Hz while significantly attenuating the bright light given off by the welding arc. As shown in Figure 3.2, the camera was attached to the end effector of the Fanuc robot so that it moved with the welding torch and could be focused on the arc at all times.

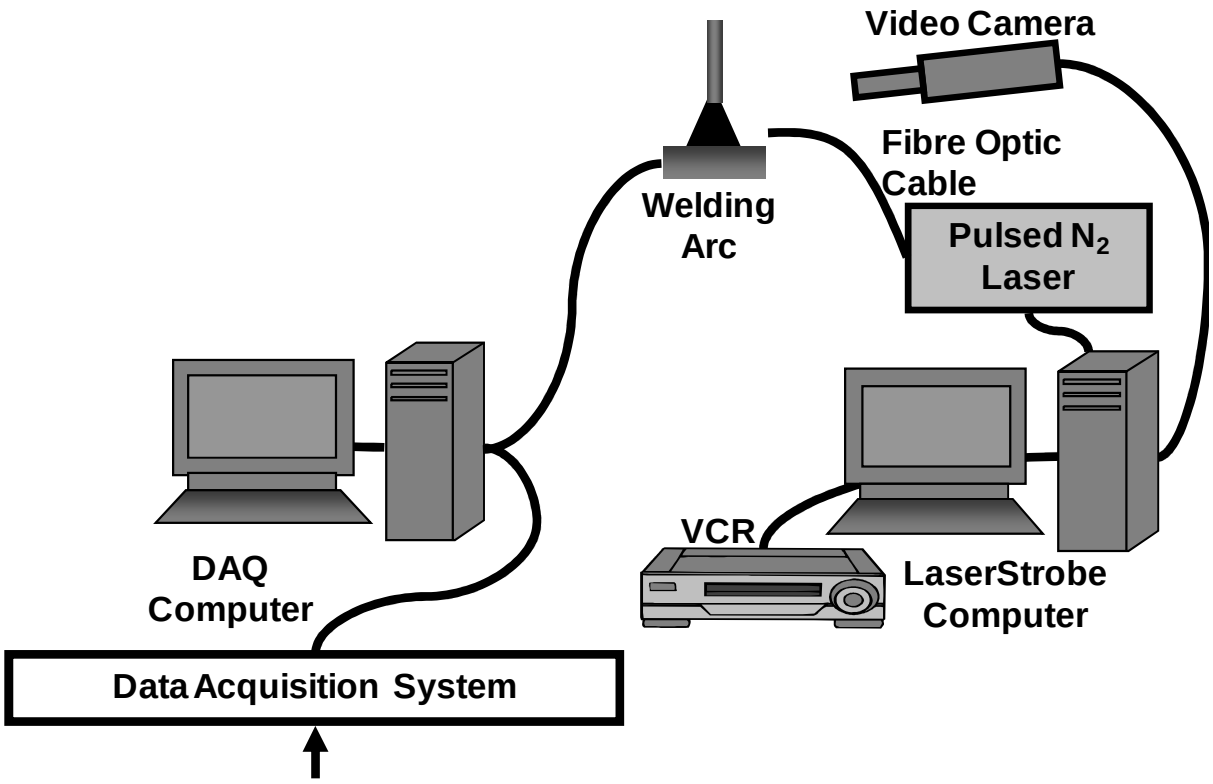

Figure 3.4: Schematic of the LaserStrobe video imaging system. Note that the DAQ system is not directly attached to the video feed. (taken from [59]).

Prior to welding, the Nitrogen laser and camera were activated and adjusted so that they were directed onto the workpiece where the electrode tip would feed. The laser was set so that it had a short high intensity burst (50 nano-second) at a pulse rate of 30 Hz. The video camera was connected to a VCR and a VHS tape was used to record the CCD image for post analysis.

3.2.4: Workpiece Clamping Fixture and Welding Table Setup

All welds were made using the same worktable with minor adjustments depending on the coupon size. A general schematic of the specimen clamping fixture is shown in Figure 3.5 and photographs of the worktable and clamping fixture are shown in Figure 3.6. The fixture was comprised of two large brass clamping bars and two 9.53 mm thick brass shims that were used for holding the weld coupons during welding. The shims held the welding coupons away from the copper backing plate. This setup created a

weld that had no backing. The back surface of the coupons received no back shielding gas during welding. The two larger brass clamping bars were used to hold the coupons in place.

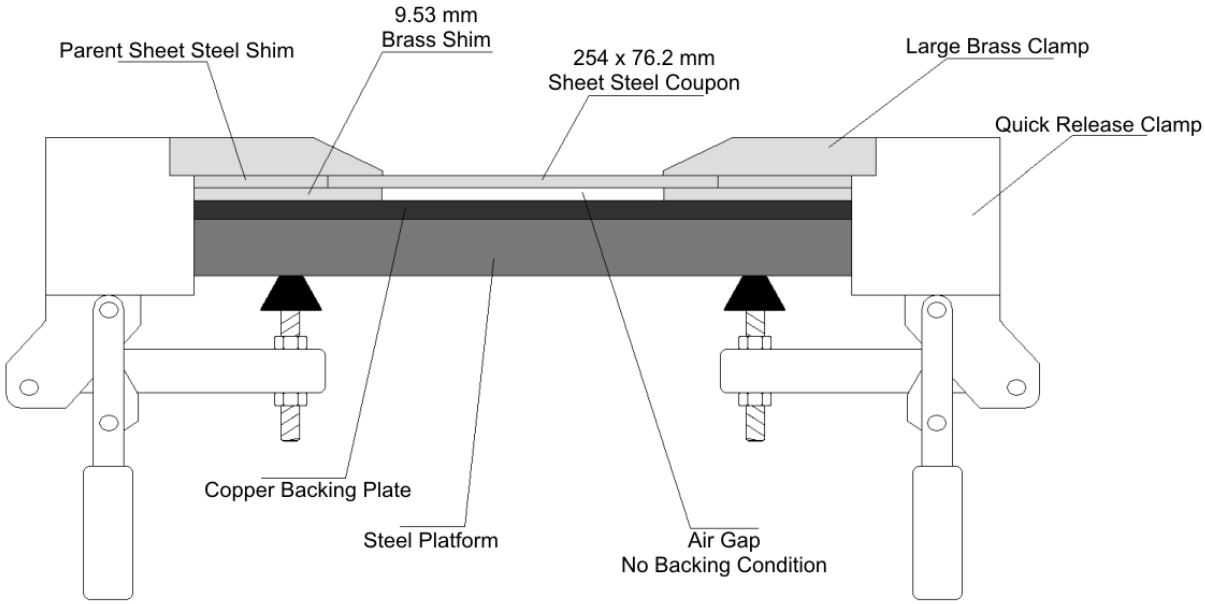

Figure 3.5: A cross-sectioned schematic showing the setup for a 254 × 76.2 mm sheet steel coupon and clamping fixture. Image not to scale.

To keep the large clamping bars level, shims made from the parent steel were placed adjacent to the weld coupon, as shown in Figure 3.6a. Each large brass clamping bar had 5 adjustable quick-release clamps that could be set for a specific steel sheet thickness. When performing welds on the small coupons (254 mm × 76.2 mm) all 5 quick-release clamps were used, as shown in Figure 3.6b. When welding the larger tensile coupons (254 mm × 203 mm) the central clamp was removed due to its interference with the wider workpiece and a pair of C-clamps was used instead (see Figure 3.6c). The image in Figure 3.6d shows an example setup to achieve the desired CTWD distance with a pre-measured block.

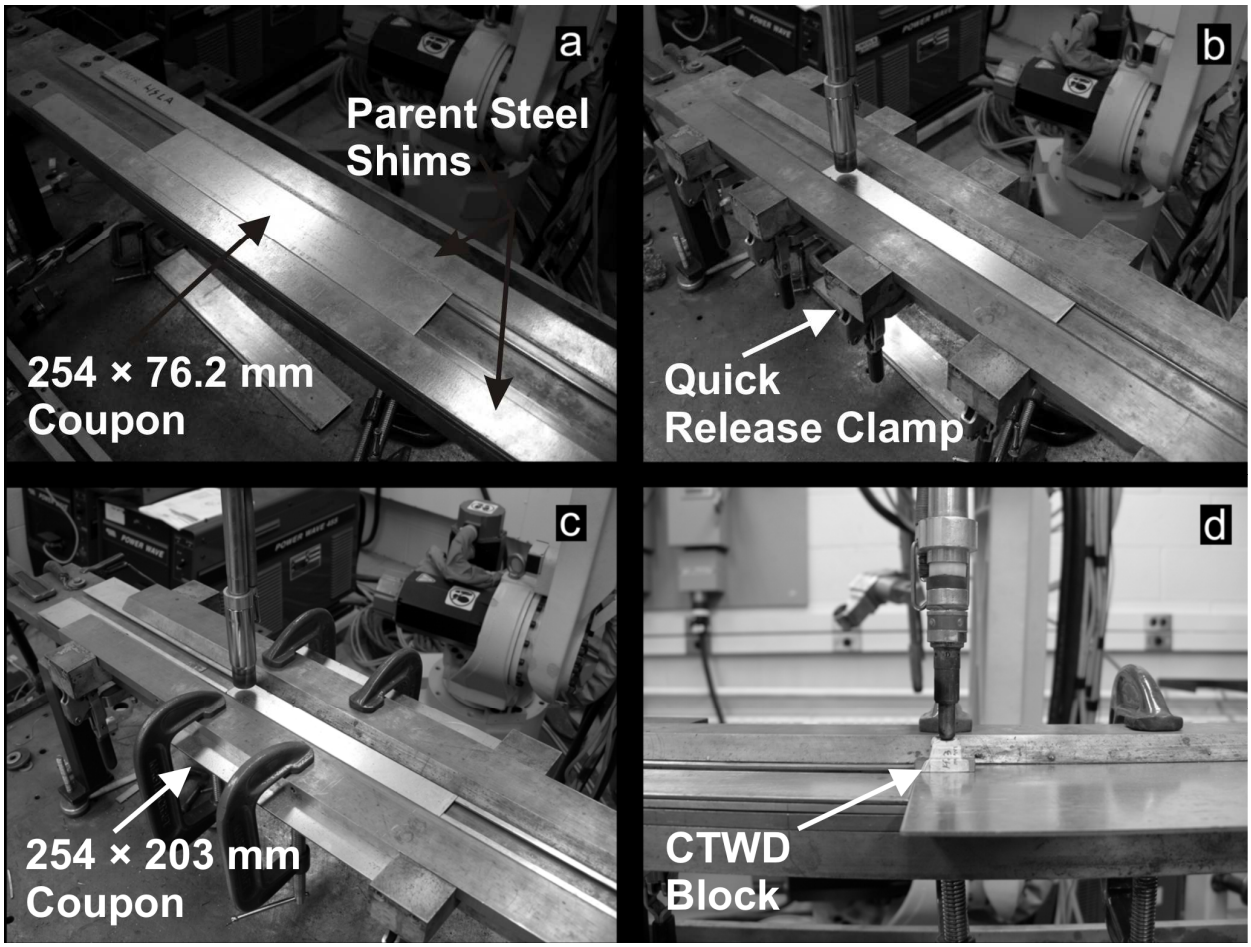

Figure 3.6: The welding worktable setup used during the study. a) The small weld coupon is shown prior to clamping, extra strips of parent sheet steel were required for the clamps in b) to rest upon, c) C-clamps have replaced two sets of quick-release clamps to allow clearance for the large tensile weld coupons, and d) the contact tip of the GMAW torch is being oriented against a pre-measured welding block.

A number of initial welding experiments were conducted to determine an appropriate spacing for the brass clamping bars. The arrangement used for these trials is shown in Figure 3.7. The large brass clamps and the brass shims could affect the weld FZ and weld HAZ by acting as heat sinks. They could change the nature of heat transfer away from the weld pool during welding and could affect the width of the HAZ; however, Ghosh [34] found that in flash butt welding setups, clamp spacing only had significant affects for high peak temperatures in the weld HAZ. To determine the heat sink effect, the brass clamps and brass shims were held down with C-clamps in a tapered alignment. The spacing was wide (59.95 mm) at the weld start and narrow (14.41 mm) at the weld end, which is shown in Figure 3.7a.

A coupon was cut from the 1.77 mm HSLA sheet steel. A set of weld parameters that gave a high heat input weld with no burn-through or other defects was selected. A bead-on-plate weld at the selected parameters was performed and is shown in Figure 3.7b. The clamp edge locations were scribed into the workpiece surface, and then the welded coupon was taken for measurement of the weld and HAZ widths using a stereo-microscope.

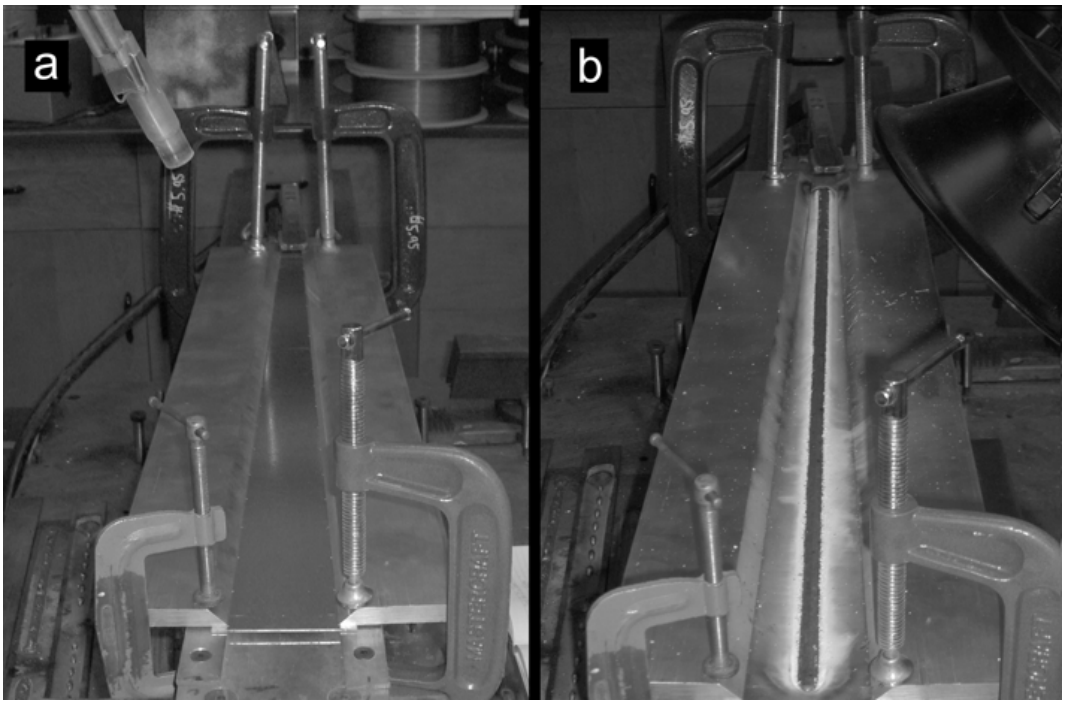

Figure 3.7: The clamping assembly setup for the clamp spacing trials. Image a) shows the unwelded coupon with the tapered clamping arrangement and image b) shows the welded coupon. Note: The weld start location was at the widest point of clamp spacing.

The weld bead width, the zinc coating vaporization isotherm width (estimated as 906°C peak temperature during welding [60]), and the zinc coating boiling isotherm width (estimated as 420°C peak temperature during welding [60]) were measured on the top surface of the welded coupon at different locations of clamp spacing (see Figure 3.8a). The measurements are shown in Figure 3.8b. From the plot it was determined that the zinc boiling isotherm (906°**)** was affected with at a clamp spacing of 26.0 mm or less. With clamp spacing larger than this, the boiling isotherm appeared to be relatively constant and the vaporization isotherm showed no change.

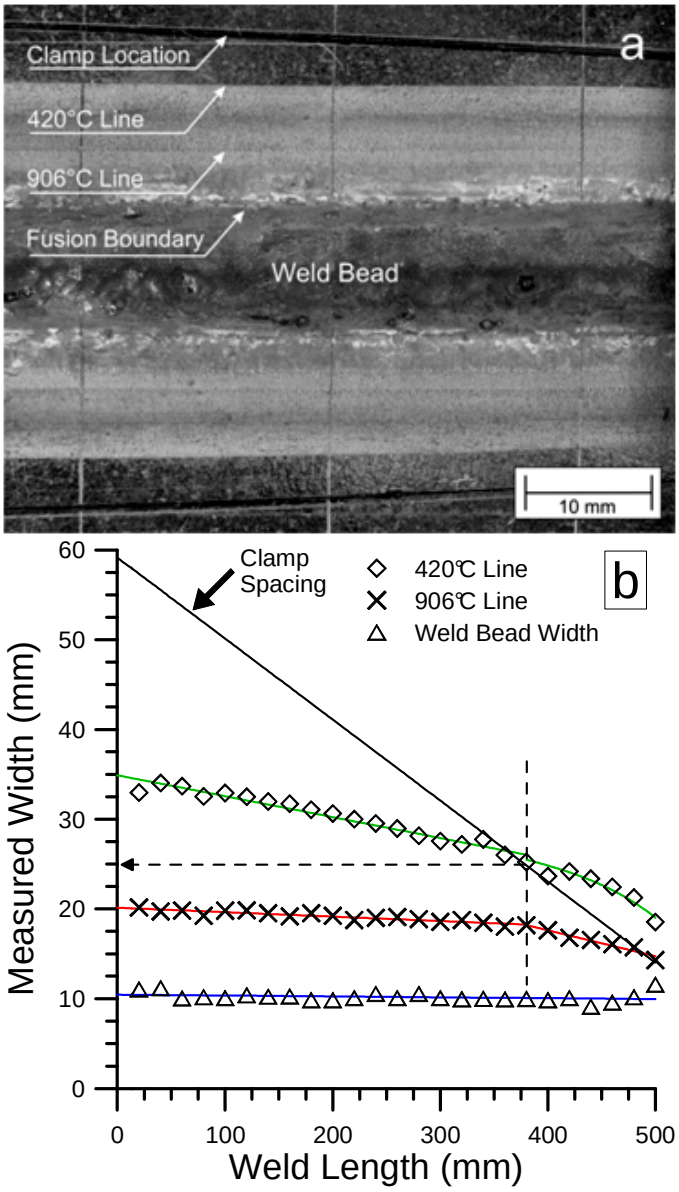

Figure 3.8: Measurements for the heat transfer interference trials. a) Shows a section of the weld used for measuring and has the 420°C and 906°C isotherms marked and b) gives the resulting measurements. The point of inflection for the 906°C isotherm was marked at approximately 26 mm.

This spacing was increased by a factor of 1.25 to give a spacing of 32.5 mm. Once this spacing was determined the large clamps and the brass shims were machined to an appropriate size and assembled and all subsequent welds were performed with a clamp spacing of 32.5 mm.

3.3: **Experimental Methods**

In this section, the testing methods used to make the GMAW-P DP sheet steel welds are outlined. The first goal was to create DP steel welds that failed in both the heat affected zone (HAZ) and the base-metal (BM).

The first experimental series was used to make GMAW-P welds on the DP600 '16s' sheet steel for a range of welding heat inputs that would result in tensile specimens that failed in the HAZ and tensile specimens that failed in the BM during uniaxial tensile testing. In the second experimental series, new welds were made in an attempt to create new conditions for a HAZ failure and a BM failure that could be compared with the first experimental series. Different DP sheet steel thicknesses were used to examine the effect on HAZ width and different DP sheet steel grades of strength were used to explore the effect of the degree of softening in the HAZ. Note that the experimental procedure and results for Experimental Series 2 are given in Appendix A.

3.3.1: Experimental Series 1 – Transition of Failure in GMAW-P Welded DP600 Sheet Steel

The goal for these welding trials was be to create a group of welds that covered a range of linear heat inputs while all attaining full root penetration through the sheet thickness. Once the range of heat input was established, the failure mode of each weld would be determined using uniaxial transverse weld tensile tests. A weld that gave 100% base-metal failure and a weld that gave 100% heat affected zone failure were identified. These two welds were then analysed through different methods of metallographic testing in order to determine why a transition of failure between a HAZ fracture and the BM fracture location had occurred.

The following independent weld parameters were varied in order to create a range of GMAW-P heat inputs: pulsing trim, wire feed speed (WFS), travel speed (TS), and contact-tip-to-workpiece distance (CTWD). These parameters were set prior to each weld. The dependent parameters that were monitored

were: welding current, welding voltage, weld root penetration, and HAZ dimensions. Geometrical dimensions were found by measuring weld cross-sections. Ideally, the welds would all have around 100% root penetration, although root penetrations greater than 100% were acceptable because the main comparison was between weld HAZ widths. Welds below 100% penetration were not acceptable. All welds that were conducted for this part of the study were bead-on-plate welds made in 254 mm × 76.2 mm HSLA '17s' sheet steel coupons.

The condition for full penetration would help to ensure that the different microstructural regions in the HAZ, which are caused by a gradient of heat transfer away from fusion zone (FZ), were relatively uniform through the thickness of the sheet. This would help when making HAZ half-width measurements, which would be used to compare the different welds. By having the lines in the HAZ microstructure along which the material had been heated to a maximum temperature equal to the Ac_1 and Ac_3 temperature (labelled here as the Ac_1 and Ac_3 lines) aligned normal to the sheet edges, it could also be assumed that the weld had 2D heat flow, and hence simplify the nature of the weld.

Three phases of weld trials were performed in order to select a set of welding parameters that would be used during the study. Phase 1 was carried out as a design of experiments (DOE) and is shown in Table 3.5. At the end of Phase 1 all of the welds from the DOE were measured for root penetration and the average welding power inputs were calculated. Welds with visible defects (porosity, burn-through, and internal pores) were catalogued and not used in any further testing. The welding arc was observed with the LaserStrobe video camera and the metal transfer mode was catalogued for reference.

The method for measuring root penetration is shown in Figure 3.9. Each weld was cross-sectioned in 3 locations and then measured using an optical microscope. The root penetration measurements were used to calculate percent penetration with Equation (3.8):

$$\%Penetration = \frac{y}{h} \cdot 100\% \qquad \textbf{(3.8)}$$

where *y* is the distance measured from the top surface of the sheet to the deepest point of penetration in millimetres (mm) and *h* is the sheet thickness in millimetres (mm).

Table 3.5: Design of experiments for Phase 1 welding trials. This gave 24 welds that were used for the Phase 2 welding trials.

Trim	WFS [mm/s]	TS [mm/s]	CTWD [mm]
0.75, 1.00	169	14.8	15
		27.5	
	212	14.8	
		27.5	
	254	14.8	
		27.5	
1.00, 1.25	169	14.8	20
		27.5	
	212	14.8	
		27.5	
	254	14.8	
		27.5	

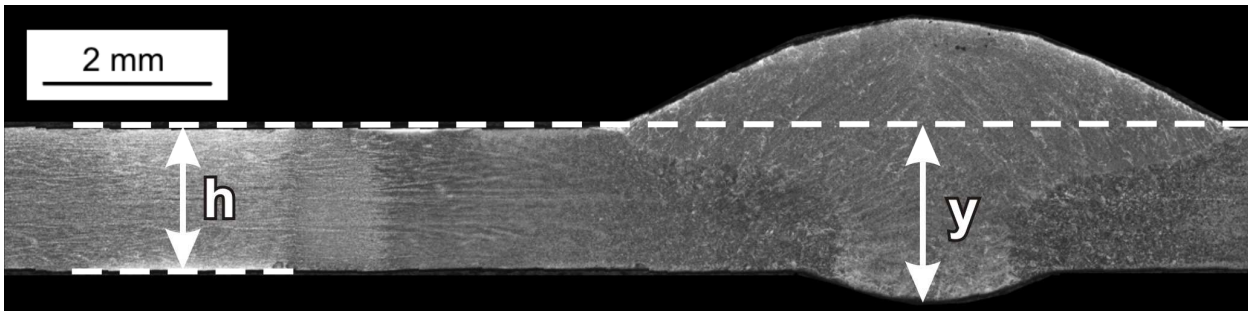

Figure 3.9: Root penetration measurement method. The dimension *h* represents the sheet thickness and the dimension *y* represents the distance from the top edge of the sheet to the maximum point of weld root penetration.

The data collected from the initial Phase 1 DOE was used during the Phase 2 welding trials for further refine the weld process conditions that would give 100% penetration welds at each different linear heat input. For this, the 24 welds from the DOE were grouped into weld 'families'. The families consisted of welds that had constant trim, WFS, and CTWD. Each family represented a single average

input power. The families only differed in weld TS and percent penetration. A linear interpolation between TS and percent penetration was used to determine a weld TS that would give approximately 100% root penetration. At the end of Phase 2, welds that had at least 80% root penetration were selected. These sets of weld parameters were used to make welds onto 1.65 mm DP600 ‘16s’ sheet steel. These welds were also cross-sectioned and measured for root penetration. The 1.80 mm HSLA ‘17s’ sheet steel was 0.15 mm thicker than the DP600 ‘16s’ sheet steel. This meant that using the same parameters would result in slightly higher root penetration in the DP600 sheet. This helped to ensure that all DP600 welds had at least 100% root penetration.

All of the selected DP600 ‘16s’ welds were measured for HAZ width to obtain an average distance from the weld centerline to the Ac_3 line and to the Ac_1 line. At this point during the study, the microstructure was analysed at the following locations throughout the DP600 ‘16s’ weld HAZ using the SEM: the fusion zone (FZ), the grain growth (GG) region and the grain refined region (GR), the intercritical (IC) region, the suspected softened zone in the subcritical (SC) region, and the base-metal. Microstructural analysis was focused on the suspect softened zone to observe decomposed martensite. Decomposed martensite was expected in this zone based on prior knowledge of martensite tempering.

To observe the relative hardness of each weld HAZ, Vickers microhardness profiles were conducted on one cross-section for each weld that was selected from Phase 2. A degree of softening measurement was made to classify the suspect softened zone in each weld HAZ. The cross-sections were analysed using the SEM to observe the microstructure in the area surrounding the suspect softened zone. It was hoped that this analysis would provide reasons for the different levels of hardness observed in the microhardness profiles.

Each selected weld parameter set was then used to make bead-on-plate welds in 254 mm × 203 mm DP600 ‘16s’ sheet steel coupons, which were machined into transverse weld tensile specimens. There were at least 5 tensile specimens made from each weld based on these dimensions.

The purpose of conducting uniaxial transverse weld tensile tests of welded specimens during the study was to determine the location of failure that occurred for a given set of welding parameters. The tensile specimens were tested to full fracture and the failure location was recorded. Each weld was compared relative to one and other and points of failure mode transition were marked on a HAZ Ac_1 half-width verses relative heat input plot.

Other data that was derived from the uniaxial tensile testing included the ultimate tensile strength (UTS) of the parent steel, the percent elongation of the parent steel, the relative UTS of welded specimens, and the relative displacements for welded specimens. Subsequent analysis of the tensile tests were performed to identify the fracture type (ductile or brittle fracture) for both parent steel and welded specimens, and the dominant mechanism for micro-void nucleation.

A set of Phase 3 welds were necessary if the tensile testing of Phase 2 DP600 '16s' welds did not provide a transition of the failure location. A transition of the failure location meant that there was at least one weld that gave 100% BM failure and at least one weld that gave 100% HAZ failure over the range of heat input. Two scenarios existed for the Phase 3 welding trials. In Scenario 1, all Phase 2 welds fractured in the BM. To achieve at least one weld with a HAZ failure location, a weld with a higher heat input and hence a wider HAZ compared to Phase 2 welds was required. In Scenario 2, all Phase 2 welds failed in the HAZ. To achieve at least one weld with a BM failure mode, a lower heat input with a narrower HAZ compared to Phase 2 welds was required. Phase 3 weld parameters were based on the Phase 2 weld that had a very wide or very short HAZ, which would depend on the fracture scenario from Phase 2.

After achieving the required failure mode criteria, the following tests were performed exclusively on a selected 100% BM fracture mode weld and a 100% HAZ fracture mode weld. Tests on the base-metal were also included as described in post-processing. Fracture surfaces were observed using the SEM to observe how the material failed and where fracture initiated. Partial fracture testing was conducted to

observe the differences in void nucleation between a BM failure and a HAZ failure and to compliment the findings from fracture surface analysis. Depletion of martensite in the weld HAZ was assessed by measuring volume fraction of martensite profiles for both welds. Microhardness maps were conducted to create a more complete image of the weld HAZ hardness and allow a measurement of the softened zone width.

3.4: **Post–Processing of Welds**

3.4.1: Weld Sectioning

Cross-sections of the welded and parent steel coupons were required for metallographic analysis during the study. The coupons were cut using a Struers Labotom-3 Abrasive Metallurgical Saw with a JK-Abrasives: A100-N6-JK saw blade. All cross-sections were cut from the middle of the welds where steady welding conditions were exhibited, well away from the transient run-in and end crater areas of the weld. Voltage and current data was used to check each individual weld to locate when a steady power input began (based on a stable pulsed waveform). The DAQ output frequency was 5000 Hz and steady and repeating waveforms in all welds occurred before at least 4500 data inputs. This translated to approximately 0.9 s of weld duration before attaining steady power input. At the DOE travel speeds, from 14.82 mm/s to 27.52 mm/s (35 ipm to 65 ipm), 0.9 s of weld duration gave weld lengths from 13 to 25 mm, respectively. Based on this analysis, all cross-sections were cut at least 30 mm away from the weld start and end points.

Two different types of cross-sections were used during the study: symmetrical cross-sections that included both sides of the weld (Figure 3.10a), and asymmetrical extended cross-sections for examining further into the base-metal (Figure 3.10b). The cross-section size depended on the mounting cup dimensions, which over the course of the study included 25 mm, 30 mm, and 35 mm cup diameters.

Cross-sections were de-burred with course 180 grit grinding paper and then set in a hydrochloric acid bath to remove the zinc coating. Any specimens that required the zinc coating were not placed in an acid bath. The samples were then flushed of excess acid under water, cleaned with methanol, air dried, and then cleaned in acetone to remove any remaining grease or oils.

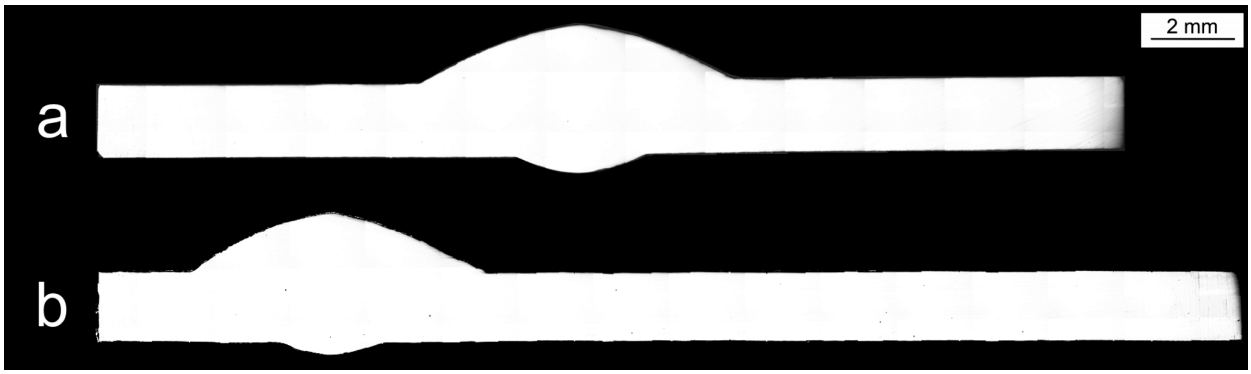

Figure 3.10: Cross-sections used for the study of welded samples: a) symmetrical and b) asymmetrical. The inflated regions on these specimens represent the weld fusion zone with reinforcement material and root penetration still intact.

3.4.2: Metallographic Analysis of the Weld Specimens

The sectioned weld specimens were mounted into a hardened 'puck' in preparation for grinding and polishing. Individual specimens for microhardness testing were mounted in black Bakelit, while multiple specimens for weld dimension measurements were mounted in cold-mount epoxy.

Manual grinding of small numbers of specimens were performed as follows: hand grinding on 180, 240, 320, 600, 800, and 1200 grit SiC paper. At each transition to a different grit paper the sample was cleaned in methanol and air blown to dry. Each stage also used a grinding direction that was at 90° to the previous step. A grinding step was only completed when all scratches were parallel to each other and scratches from the previous step were removed. All stages used water as a lubricant for grinding.

Automatic grinding at the university was performed using a Struers Planopol-3 automatic rotary grinder with a Struers Pedemax-2 rotary mounting fixture for grinding. The automatic grinder held 6 samples at a time, for sample mount sizes up to 35 mm in diameter. The process steps for automatic

grinding were: grinding until completely planar using 180 grit at force 3, and then with 320, 600, 800, 1200 coarse, and finally 1200 fine grit at force 5 for 1 minute. Cleaning was performed between the 800 to 1200 coarse grit paper step and between the 1200 coarse to 1200 fine grit step. The samples were cleaned by flushing with methanol and then drying with an air blower. All steps were performed at 300 rpm.

Ground samples were manually polished by going directly from the 1200 fine grit step to a finishing 1 µm diamond polishing step. The polishing was performed on a Microstar 2000: Forcipol 2V variable speed rotary grinder/polisher and diamond extender was sprayed onto the polishing cloth as a lubricant. A soft cloth polishing pad was kept exclusively for 1 µm diamond. Prior to polishing, samples were cleaned using a Branson 5210 Ultrasonic Cleaner (samples were placed in a beaker of methanol and then placed into the ultrasonic cleaner) so that grinding sheet granules would be less likely to contaminate the polishing pad. Polished samples were free of significant scratches and had a mirror finished surface. The polishing lubricant was removed as follows: washed in acetone, then washed in methanol, then washed in soapy water, then wiped with a soft tissue, then washed with methanol and blown dry with air. Samples were placed in a beaker of methanol and ultrasonically cleaned to remove diamond particles from the surface. Automatic grinding and polishing was also performed at ArcelorMittal Dofasco, Inc. [48].

The 2% Nital etchant was used on some samples by submersing a 1 µm diamond polished sample into the mixture for 6 to 8 seconds, then flushing with water, cleaning with methanol in an ultrasonic cleaner, and then air blown to dry. This dwell time allowed macroscopic features to be easily viewed at low magnification with the optical metallurgical microscope (×50 to ×1000 magnification). The 2% Nital etchant preferentially attacked areas of higher carbon content to reveal grain boundaries and phase boundaries, and provided the general macrostructure that was used to measure weld dimensions using the optical metallurgical microscope. Alternatively, a ‘light 2% Nital etch’ was applied, where the dwell time for submersion was 2 seconds. The purpose of the ‘light’ etch was for use at high magnification with the

SEM (×1000 to ×10000 magnification) to observe decomposed martensite in the weld HAZ. The shorter dwell time prevented significant/aggressive attack on the surface.

The Lepera's tint [7] was used to provide a distinction between different steel phases using an optical metallurgical microscope and quantitative image analysis. The Lepera's tint was comprised of a 4% picral methanol solution and a 1% aqueous sodium metabisulfate solution [7]. The two solutions were kept separate until the tint etch was to be used on a sample surface. A 50:50 mixture between the two solutions was made at the time of etching. This mixture was stirred for 15 seconds in a 50 ml beaker for sample submersion. The mixture was only usable for a few minutes and could usually be applied to 4 surfaces before it weakened. Samples were submerged in the mixture and gently agitated for approximately 30 seconds. A sample was only removed when its surface began to show a brownish formation on it. Samples were cleaned by lightly submerging in distilled water, then submerging in methanol, then into a second methanol bath, and finally blown dry with a very low pressure dry air stream. After etching it was important that nothing made contact with the sample surface because this would cause the tint to smudge or flake off.

An example of a DP600 '16s' steel sample that was etched with the Lepera's tint is shown in Figure 3.11. Martensite appears white, ferrite appears tan or brown, and bainite/carbides appear black or blue. The Lepera's tint [7] was used to estimate the volume fraction of martensite in the DP steel and was used to check for the depletion of martensite in the suspected softened zone of the weld HAZ subcritical region.

3.4.2.1: Heat Affected Zone Measurement

Once prepared, the weld cross-sections were examined using an optical microscope at ×50 magnification (×5 magnification lens and ×10 magnification eyepiece) and tiled images of the entire fusion zone (FZ) and both HAZ's out to the BM were created. The microstructure in the weld HAZ of material that was heated to a maximum temperature below the Ac_1 temperature was distinctly different

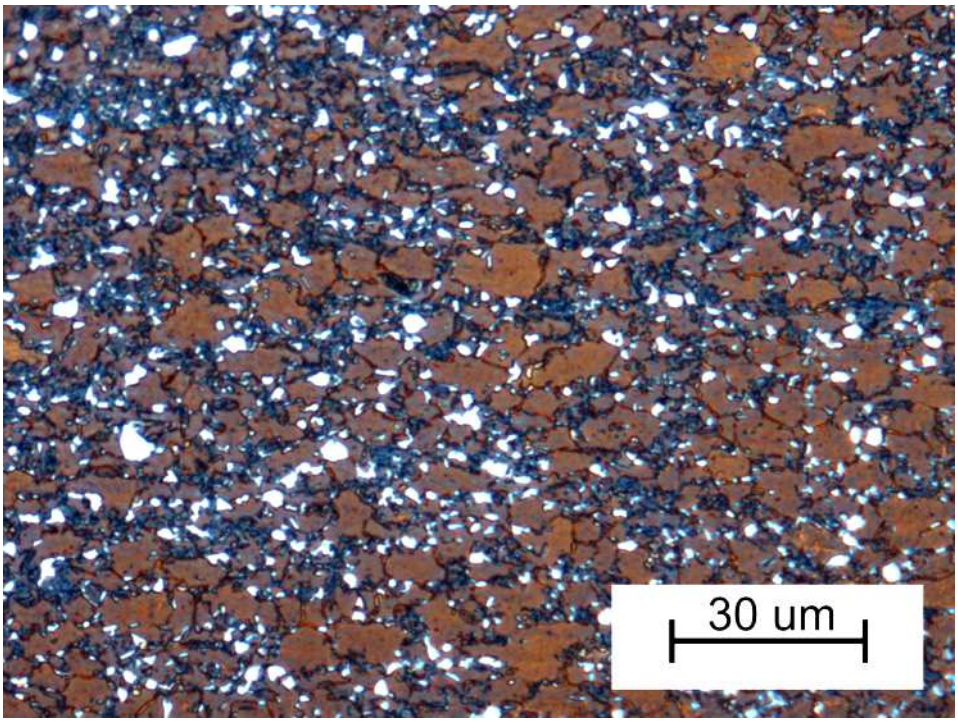

Figure 3.11: DP600 '16s' steel etched with the Lepera's tint [7], viewed with a metallurgical optical microscope at x500 magnification. Hardened martensite islands appear white, the ferrite matrix appears brown, and the remaining blackish-blue conglomerate was attributed to carbides/bainite.

than that of the material heated above the Ac_1 during welding. This allowed identification of distinct microstructural regions within the HAZ, e.g., the intercritical (IC) microstructural region contains base-metal that has been heated into the intercritical temperature range during welding [15].

A metallurgical microscope, in conjunction with Image-Pro image analysis software [61], was used to measure the following dimensions: weld toe-to-toe width (mm), weld root depth (mm), weld unit volume (mm^3), and the distances from the weld fusion zone (FZ) centerline to the fusion boundary (FB) (mm), the supercritical grain growth/grain refined (GG/GR) boundary (mm), the Ac_3 line (mm), and the Ac_1 line (mm). These distances from the FZ centerline were known as HAZ half-widths. During the study, only the root depth and the Ac_3 and Ac_1 HAZ half-width measurements were used for analysis. The remainder were measured for reference only. Several cross-sections of each weld were measured (specified in the experimental series) and an average for each weld was calculated. Both sides of the

welds were measured. The measurement was performed this way so that each HAZ width was being associated with the central point of heat input. This helped to give information on how well balanced the heat flow was from one side of a weld to the other, i.e., if two HAZ half-width measurements from the same cross-section were significantly different than the welding heat flow had likely been unbalanced.

Once the HAZ measurements were conducted, the data was organized on an X-Y scatter plot for Ac_1 HAZ half-width vs. relative heat input for all of the selected welds. This charted data represented the range of heat input that was used during uniaxial tensile testing to approximate the heat input for a transition of failure mode to occur.

3.4.2.2: SEM Imaging and EDS Analysis of Microstructure

High magnification images were taken with a Jeol JSM-6460 scanning electron microscope (SEM). It was used to make observations of specimen cross-sections and of fracture surfaces. It was also used to identify the composition of observed particles and inclusions through EDS analysis with an Oxford Instruments IncaX-sight that was equipped with the SEM.

3.4.2.3: Volume Fraction of Martensite and Martensite Depletion

An important property that was used during the study was volume fraction of martensite (VFM); also referred to as percent area of martensite. This value was a representation of how many hardened martensite islands existed in a given volume of microstructure. Expectation was that the higher strength grades of DP steel would have higher percent area of martensite. This property was also used to observe changes in the HAZ. By measuring VFM at different locations in the HAZ, it was expected that a lower percent area value would be found in the suspected softened zone.

Percent area of martensite was measured by using the Lepera's tint [7] to etch a polished specimen. Martensite islands appeared white and had excellent contrast against the tan-brown ferrite matrix when examined with an optical metallurgical microscope. Images were captured at ×500 magnification. The

Image-Pro software [61] associated with the microscope was used to measure the percent area of the three main phases. The three phases that were measured were ferrite, martensite, and bainite/carbides.

An example of how the ImagePro software [61] used contrast to measure percent area is shown in Figure 3.12. Each phase was given a mask by the software that covered a range of image contrast. On the example in the figure, the ferrite phase is represented with a green mask, the martensite phase is represented with a yellow mask, and bainite/carbides are represented with a red mask; only the green mask is shown in the image. The software allowed for each mask to be set based on a numerical contrast value so that dark areas could be marked as carbides, light areas could be marked as martensite, and the remaining areas were marked as ferrite. The software then calculated the percent area taken up by each mask over the entire image.

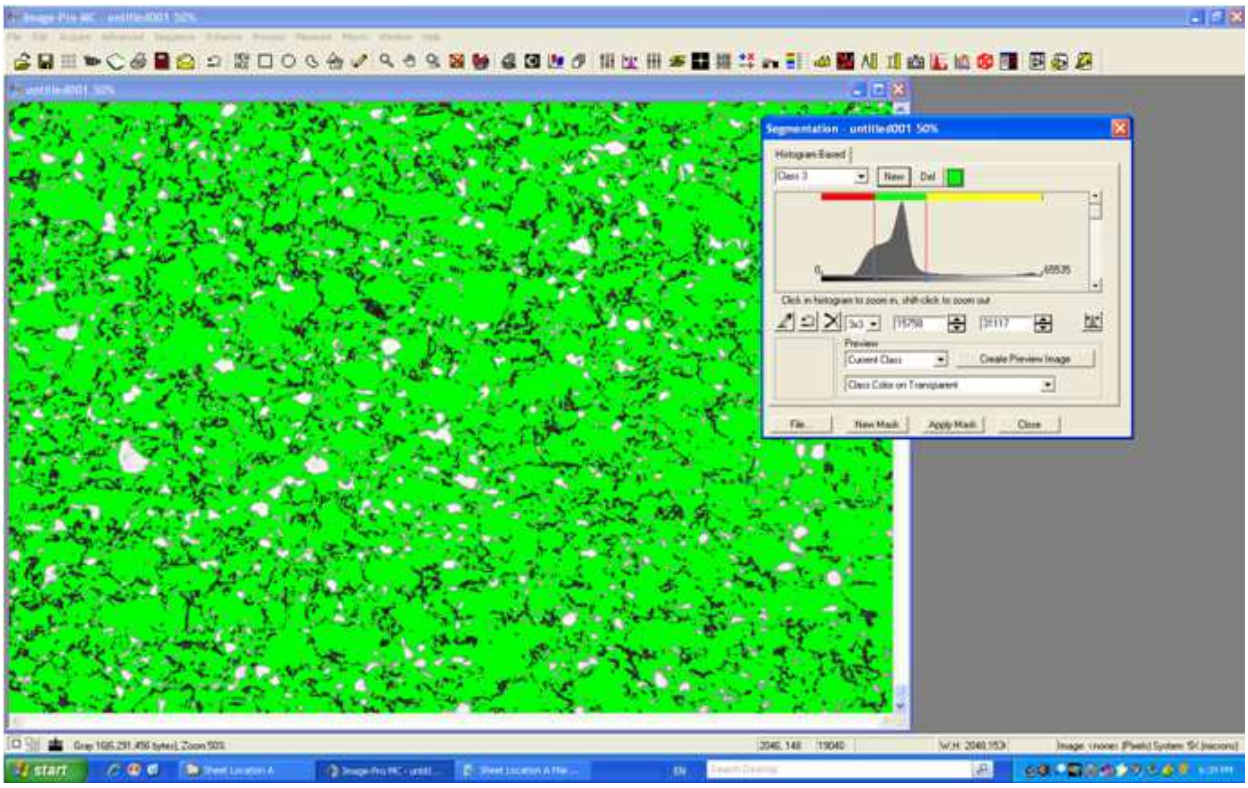

Figure 3.12: Image-Pro [61] percent area analysis that was used to measure volume fraction of martensite (VFM).

3.4.2.4: Base-metal Volume Fraction of Martensite Measurements

Base-metal samples were measured for VFM by creating a profile of percent area measurements across the thickness of the sheet steel specimen. A profile consisted of percent area of martensite measurements spaced 100 µm apart from one sheet edge to the other; measurements were at least 150 µm away from the sheet edges. An average value of the profile measurements was used as the base-metal VFM, which was used to compare with welded samples.

3.4.2.5: Weld HAZ Volume Fraction of Martensite Measurements

Volume fraction of martensite was measured in the weld HAZ using the metallurgical optical microscope and Image-Pro analysis [61], in conjunction with an asymmetrical weld cross-section that had been etched with the LePera's tint [7]. The Lepera's tint revealed tempered martensite in the welded DP steel subcritical HAZ. A high degree of tempering appeared as a dark blackish-blue bainite/carbide conglomerate and a low degree of tempering appeared as martensite islands that were stained with an off-white discolouration. The VFM for a given location in the HAZ was based on the unaffected white colouration that existed on the tempered martensite islands.

A VFM profile was made, starting with a measurement within the IC region of microstructure and moving outward to the base-metal. Measurements were made along a single axis that was set at a distance of 1/3 the sheet thickness from the bottom edge of the sheet. The distance between adjacent area fraction measurement locations was recorded in micrometers (µm). The Ac_1 line at the edge of the intercritical zone was set as the origin of the profile. The VFM profile was used to compare with microhardness profiles and maps.

The average percent area values of each phase were used to estimate the carbon weight percent in a martensite island; this was for reference purposes, to compare the different base materials that were used in the study. To make this estimate, the average area fraction of martensite was combined with the average area fraction of bainite/carbides to give an estimate of the amount of austenite that existed during

the DP base-metal intercritical annealing step of its processing. It was assumed that carbon levels in the austenite phase during intercritical annealing reached an equilibrium state. Using this assumption, a simple lever rule calculation was made using Equation (3.9):

$$C_{Martensite} = C_{Ferrite} + \frac{C_{Nominal} - C_{Ferrite}}{\%Austenite} \quad \textbf{(3.9)}$$

where $C_{Martensite}$ is the estimated carbon weight percent found in the martensite phase, $C_{Ferrite}$ is the carbon weight percent in ferrite of 0.02% given by a general steel phase diagram [33], $C_{Nominal}$ is the carbon weight percent of the base-metal nominal chemistry, and *%Austenite* is the measured area of martensite and bainite found with the Image-Pro software [61].

3.4.3: Uniaxial Tensile Tests

The purpose of conducting uniaxial transverse weld tensile tests of welded specimens during the study was to determine the failure mode that occurred for a given set of welding parameters. Other data that was derived from this test included: the ultimate tensile strength (UTS) of the parent steel, the percent elongation of the parent steel, the UTS of welded specimens, the relative displacement of welded specimens to fracture, the fracture type for both parent steel and welded specimens, and the dominant mechanism for micro-void nucleation.

The uniaxial tensile specimens were made in conformance with the ASTM E 8-04M standard [50]. This was in accordance with the AWS Standard for transverse welds [46]. The dimensions for the machined gauge length of the 'tensile dog-bones' are shown in Figure 3.13. Welds that were selected for tensile testing were made in 254 mm × 203 mm sheet steel coupons and welded transverse to the rolling direction. Welds were made down the center of the sheet and ran parallel to the 254 mm edge. The weld bead was not machined off of the coupon for any ASTM E 8-04M tests.

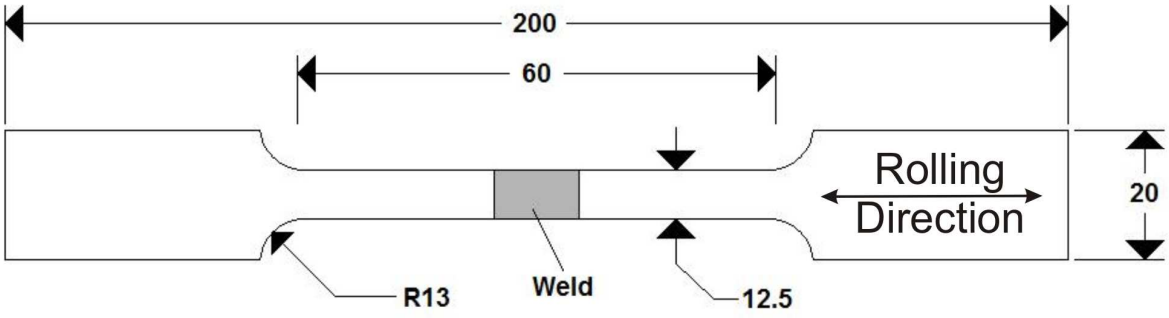

Figure 3.13: The dimensions for the transverse welded tensile specimens as specified by ASTM E 8-04M [50]. All dimensions are in millimetres (mm).

Welded coupons were sheered in the Engineering Machine Shop [62] using a sheering press starting from the 203 mm edge at the weld end location and making a new cut every 20 mm until the starting location of the weld was reached. This provided 20 mm × 203 mm strips that were used to machine transverse welded 'tensile dog-bones'. The machined edges were de-burred with a file to remove potential crack initiation sites. Tensile specimens were marked with their respective weld code designation and given a number based on their relative location along the weld. Sheared strips that that were within 30 mm of the weld run-in or crater locations were not used for 'tensile dog-bones'.

3.4.3.1: Uniaxial Tensile Complete Fracture Testing

There were two machines used for uniaxial tensile testing. A Model 4206 Instron Machine was located at the University of Waterloo. It had a 15000 kgf load cell and tests were conducted at a cross-head speed of 15 mm/min. A Model 3384 Instron Machine was located at ArcelorMittal Dofasco, Inc. [48]. It had a 15000 kgf load cell and tests were conducted at a cross-head speed of 25.4 mm/min. An extensometer was used during tests with unwelded base-metal specimens. An extensometer was not used for welded tensile specimens because each specimen had varying amounts of heat affected microstructure and hence varying mechanical properties across the gauge length.

After loading a tensile specimen to failure, the fractured specimen was photographed and kept for potential observations. Generally, observations using the SEM were only made on fracture surfaces immediately after fracture. The SEM had greater depth of focus than the optical metallurgical microscope and could therefore be used to observe the non-planar fractured surface. Some fracture specimens from welded samples were also cross-sectioned, mounted, polished, and etched for microstructural examination. A 'light' 2% Nital etch was used for this SEM analysis. Cross-sectioned specimens were used to verify the location of failure compared to the microstructure and to analyse the damaged area adjacent to the fracture surface to help determine where ultimate failure was initiating.

3.4.3.2: Uniaxial Tensile Partial Fracture Testing

To determine the dominant mechanism for void nucleation and final fracture, some tensile specimens from selected welds were loaded to the UTS using the University of Waterloo Model 4206 Instron Machine and removed just before fracture occurred. This provided a necked region that could be used to observe micro-void nucleation sites and determine where dominant cracks were initiating. The purpose of this experiment was to observe differences between a HAZ fracture and BM fracture location. Selected welds for this test had to have shown a consistent mode of failure during full fracture tests. During these tests, the cross-head speed was reduced from the full fracture test speed of 15 mm/min to a speed of 0.5 mm/min once the UTS had been reached. This speed reduction allowed a specimen to be brought slowly into a necked state and hence helped to prevent an accidental fracture from occurring.

Partially fractured zones were cross-sectioned parallel to the axial loading direction as shown in Figure 3.14. The cross-sections were then mounted, polished, and etched with a 'light' 2% Nital etch for examination with the SEM. The SEM was required for observation because micro-void nucleation was not visible at the low magnification of the optical microscope. The SEM could also be used to identify inclusions within the sheet steel using EDS analysis.

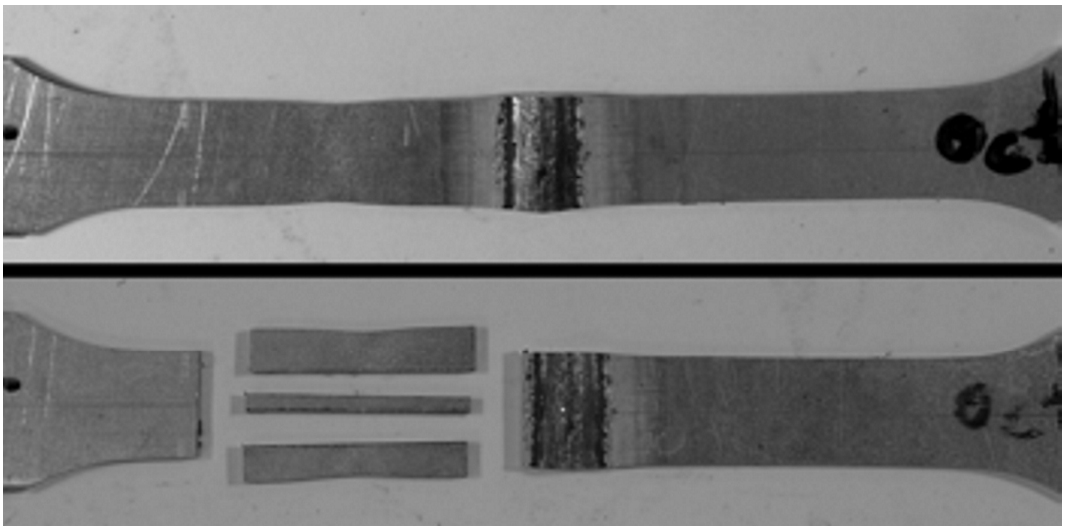

Figure 3.14: An example partially fractured weld tensile specimen that had been loaded just past localized necking in the BM. The necked region was cross-sectioned for examination.

Observations focused on locations where dominant cracks and micro-voids had formed. The following areas were of most interest: micro-voids surrounding hardened martensite islands, micro-voids surrounding decomposed martensite clusters, and micro-voids surrounding inclusions within the sheet steel. Martensite islands would also be examined for brittle fracture; micro-void nucleation from these sites had been described in the literature [24,63]. Differences in these nucleation mechanisms were compared between the different modes of uniaxial transverse weld tensile failure.

3.4.4: Vickers Microhardness Testing

Vickers hardness was a mechanical property used to quantify the relative affects of weld heat input on the DP sheet steel microstructure. It was expected that there would be softening of the DP steel just below the Ac_1 line in the HAZ microstructure. This softening would be represented as lower hardness when compared to the base-metal hardness. Two methods of using Vickers microhardness were used during the study, which were: microhardness profiling and microhardness mapping. Once hardness values were established, they were compared with the microstructure and used to help determine why different weld failure modes were occurring during uniaxial tensile testing.

Microhardness linear profiles were conducted to verify that suspected softening was occurring in the welded DP steel. Selected specimens for microhardness profiling were cross-sectioned, mounted, polished, and etched. A symmetrical cross-section was used for all welds. Only one line of indentations was used for each weld. The number of indentations varied on the weld being profiled because some welds required more indentations to cover larger HAZ's. Generally, there were 80 to 100 indentations made for each profile.

Microhardness profiles were conducted at ArcelorMittal Dofasco, Inc. [48] using a Clemex JS-2000 Automatic Vickers Microhardness tester. The Clemex machine was used to automatically perform indentations along a predefined line. The indentations were made using a diamond pyramid indenter at a load of 200 g force with a dwell time of 15 seconds. To prevent indentations from affecting the strain-field of adjacent indents, a minimum distance of three indent-widths was required. This was based on the ASTM E 92-82 standard for Vickers hardness testing [64]. Based on the maximum indent-width that was seen during the study (approximately 50 µm), the minimum spacing was 150 µm. Indentations were spaced 200 µm apart to give some excess area of unaffected microstructure. To create the weld HAZ microhardness profiles, a pre-programmed indentation pattern was inputted for the machine to follow. This pattern is shown in Figure 3.15. The pattern varied around the weld fusion boundary, where indents were located above and below the x-axis. By staggering the indents like this it was possible to keep the minimum spacing while increasing resolution over this portion of the indentation line.

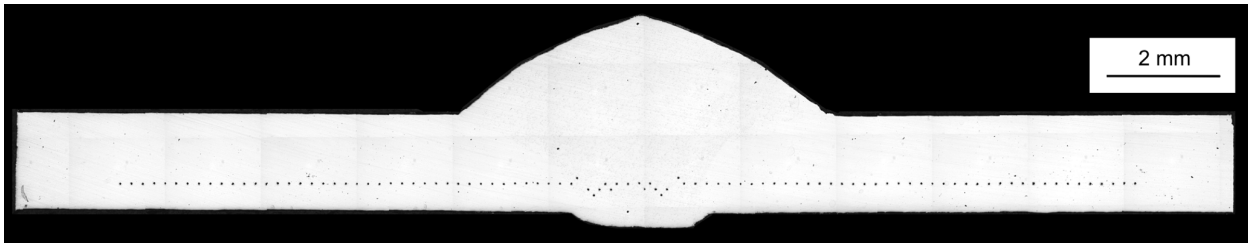

Figure 3.15: A polished specimen with an indented surface showing the pattern used for microhardness profiles. The image was taken at ×50 magnification.

For the microhardness profiles, it was important that the single line of indentations was made in a similar location on each weld cross-section. For all welds, the profile line was made at a distance of 1/3 the sheet thickness from the bottom edge of the specimen. This distance kept indentations away from the central band of hard martensite that would misrepresent the DP steel hardness; this was based on a suggestion by Biro [48]. The indentation line was made so that it was symmetrical around the weld centerline and so that it extended beyond the Ac_1 line of the HAZ. The indents were measured manually using the Clemex CMT software. The Vickers hardness values were calculated in the program and then exported to Microsoft Excel [58].

The base-metal was measured for Vickers microhardness by using a 3×3 square grid of indentations on a cross-section of unwelded parent sheet steel. The grid indentation spacing was 200 µm. An average base-metal hardness was calculated, which was compared with the weld HAZ microhardness profiles. The base-metal hardness was also used to calculate the degree of softening in the weld HAZ. Degree of softening was calculated by taking the minimum hardness value located in the weld subcritical region of microstructure. This was the location of suspected softening and this calculation followed the proposal by Biro and Lee [36] and Xia *et al.* [45]. Degree of softening was calculated with Equation (3.10):

$$DOS = Hardness_{BM} - Hardness_{HAZ,MIN} \quad \textbf{(3.10)}$$

where *DOS* is the degree of softening, $Hardness_{BM}$ is the base-metal average hardness, and $Hardness_{HAZ,MIN}$ is the minimum hardness in the weld subcritical region adjacent to the Ac_1 line. Both are measured in terms of a Vickers hardness number (VHN). A *DOS* value was calculated for both sides of the weld. These values were plotted against the relative heat input in order to observe a trend in softening.

Microhardness maps were conducted to develop a more complete representation of a weld HAZ when compared to the microhardness profiles. The mapping method gave greater resolution than the

linear profiles and it was possible to estimate the relative size of different regions in the HAZ, including the relative size of the suspected softened zone. The hardness maps only covered the range of microstructure from the base-metal to the IC zone. Microhardness mapping was performed in a similar fashion as the linear profiles. Mounted and polished specimens were brought to ArcelorMittal Dofasco, Inc. [48] and the Clemex JS-2000 Automatic Vickers Microhardness tester was used to indent the sample surface and measure hardness. Indentations were made with a 200 g force and a dwell time of 15 seconds. The mapping method differed from the profiles in the following ways. Instead of creating a single line of indents, the mapping method used a grid of indents as shown in Figure 3.16. The grid was staggered to meet the minimum indentation spacing of 150 µm. Mapping required approximately 1000 to 1500 indents and so testing time duration was excessive. To reduce testing duration, the Clemex machine could automatically measure indentations and hence reduce testing time. For automatic measurement, a polished specimen surface that gave good contrast between indents and surrounding material was required and hence specimens were left un-etched prior to mapping. The Clemex tester used visual recognition software to measure this contrast and calculate the microhardness.

Figure 3.16: A polished specimen with an indented surface showing the grid pattern used for microhardness mapping. The image was taken at ×50 magnification.

The maps were made on asymmetrical weld cross-sections. The mapping grid was aligned on the specimen so that it measured hardness out in the base-metal and then moved inwards toward the weld HAZ. Hardness values were monitored and, once the values represented the intercritical region hardness, the indentations were stopped. Maps were also made on unaffected base-metal samples over approximately 1 – 2 mm. Hardness data was exported to Microsoft Excel [58]. The Excel data file was

used in conjunction with the software, Surfer [65], to organize hardness data into a surface plot. Surfer was software that specialized in creating various surface plots of 3D data.

To further quantify the mapped microhardness data, average through-thickness hardness (ATTH) was calculated using columns of staggered indents through the thickness of the sheet. An example of a single column of indents that was used to calculate a single ATTH value is labelled 'A' in Figure 3.17. For weld samples, individual ATTH points were plotted verses their relative position to the Ac_1 line; this distance was measured to the midway point between the two adjacent columns of indents within a staggered column. This created a profile that could be used to identify different regions of average hardness. This profile was expected to have improved resolution over conventional microhardness profiles that used a single line of indents.

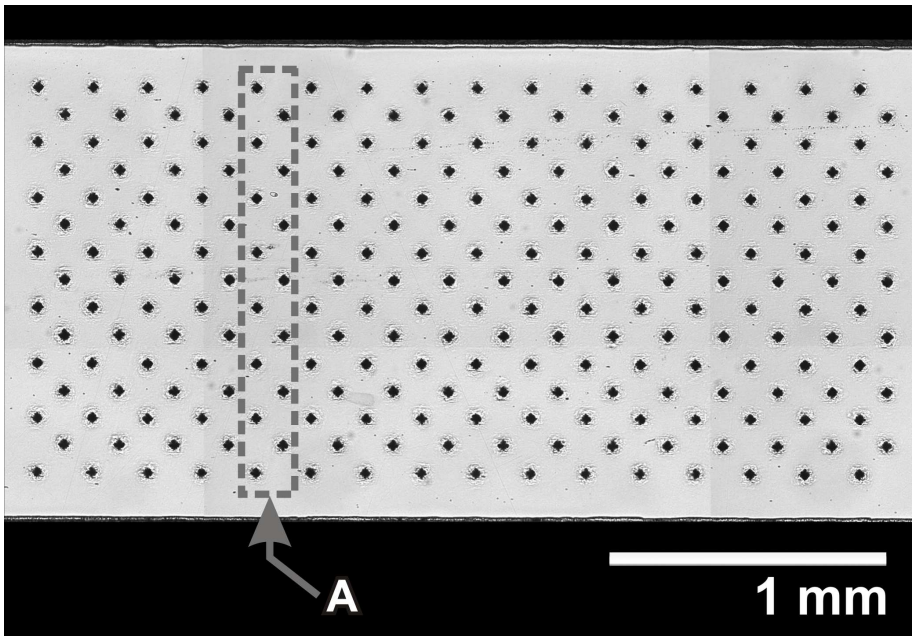

Figure 3.17: A column of staggered indents was used to calculate a single average through-thickness (ATTH) microhardness value.

In the following Chapter 4, the results from the study are presented. Interpretations of the results are discussed throughout the chapter, and theories on the welded DP sheet steel fracture mechanisms are developed and presented.

Chapter 4: Results and Discussion

The results for Experimental Series 1 are presented in this chapter. During Experimental Series 1, the weldability of the 1.80 mm HSLA '17s' sheet steel and of the 1.65 mm DP600 '16s' sheet steel with a GMAW-P welding process was evaluated. Welds were evaluated with microhardness profiles and maps to characterize distinct regions of hardness and then interpret the hardness by comparing to the local microstructure. Regions of softened microstructure were evaluated by measuring the depletion of martensite that had been caused by tempering from the weld heat input. The experiments in Series 1 were used to identify differences between a BM fracture and HAZ fracture in welded DP600 sheet steel during uniaxial transverse weld tensile tests. Fracture surfaces were used to determine the dominant mechanism for micro-void nucleation and crack formation that led to ultimate fracture. The results and discussion related to Experimental Series 2 may be found in Appendix A.

4.1: Experimental Series 1 – Transition of the Failure Location in GMAW-P Welded DP600 Sheet Steel

The goal of this experimental series was to determine the mechanisms that caused a welded DP sheet steel to fracture in the base-metal (BM) failure location during uniaxial transverse weld tensile testing and compare those mechanisms with a welded DP sheet steel that fractured in the heat affected zone (HAZ) failure location during uniaxial tensile testing. By determining what the failure mechanisms were and how they acted to cause these two types of weld failure it could be possible to provide methods for avoiding an undesirable HAZ failure in DP steel and provide a method for shifting the failure location to the BM.

4.1.1: Weld Procedure Development

The Phase 1 welding DOE was used to determine the GMAW-P weld process parameters that would produce full penetration bead-on-plate GMAW-P weld in 254 mm × 76.2 mm 1.80 mm thick galvanized

sheet HSLA ‘17s’ coupons. All of the welds that had no visible defects were cross-sectioned and measured for root penetration. The measurements for root penetration are shown in Table 4.1. The table includes the relative heat input for each weld and gives notes on weld defects. The weld defects that were found include: CO boil due to insufficient atmospheric shielding, intermittent weld bead geometry, and burn-through. These were defects that represented process instability and could be observed without destructive testing. Defective welds were not selected for Phase 2 weld development. The welds that were selected are highlighted with grey in the table.

The original DOE included three different trim values, which were: 0.75, 1.00, and 1.25. These were meant to achieve low, medium, and high heat input welding conditions so that analysis could be made on welds over a range of heat input. A trim of 1.00 (mid-point of the Lincoln Electric waveform range) was set up to be the medium range of heat input; however, early in the Phase 1 welding trials, it was found that a trim value of 0.75 was too low in power input. The welds made with a trim value of 0.75 welds did not achieve a spray-transfer mode and had significant short circuiting between the electrode and the weld pool. The 0.75 trim welds were discontinued. A trim of 1.15 was selected to act as the medium range of heat input. This helped to maintain a wide range of heat input and hence increase the chances of achieving a transition of failure during uniaxial tensile testing.

Video images recorded using the LaserStrobe video system to identify metal transfer mode are shown in Figure 4.1. These illustrate the new DOE, which used trim values of 1.00, 1.15, and 1.25; it was found that arc length increased as trim was increased, which explained why 0.75 trim (shorter arc) had short circuit transfer. The arcs for 1.00 and 1.15 trim had streaming spray-transfer (labelled ‘A’), and 1.25 trim appeared to have projected spray-transfer (labelled ‘B’). The edge of the weld pool is labelled ‘C’ and the electrode is labelled ‘D’,

Table 4.1: Phase 1 welding trial results.

Weld Code	Trim	TS [mm/s]	WFS [mm/s]	CTWD [mm]	H_{rel} [J/mm]	Root Penetration [%]	Defect(s)
TB43	1.00	14.8	169	14.3	268	128.5%	-----
TB45	1.00	27.5	169	14.3	143	49.3%	-----
TB47	1.00	14.8	212	14.3	316	147.6%	-----
TB48	1.00	27.5	212	14.3	170	58.5%	-----
TB49	1.00	14.8	254	14.3	365	-----	Burn-through
TB50	1.00	21.2	254	14.3	257	130.8%	-----
TB51	1.00	27.5	254	14.3	202	82.9%	-----
TB52	1.00	14.8	169	20	208	-----	Weld Porosity
TB55	1.25	14.8	169	14.3	449	130.5%	-----
TB56	1.25	14.8	169	20	380	124.9%	-----
TB57	1.25	27.5	169	20	184	-----	Thin Weld Bead
TB58	1.25	14.8	212	20	457	-----	Excessive Heat
TB59	1.25	27.5	212	20	224	-----	Inconsistent Weld Bead
TB60	1.25	14.8	254	20	524	-----	Burn-through
TB61	1.25	27.5	254	20	273	-----	Inconsistent Weld Bead
TB80	1.15	23.3	169	14.3	230	62.8%	-----
TB81	1.15	23.3	212	14.3	263	85.2%	-----
TB82	1.15	27.5	254	14.3	250	76.0%	-----

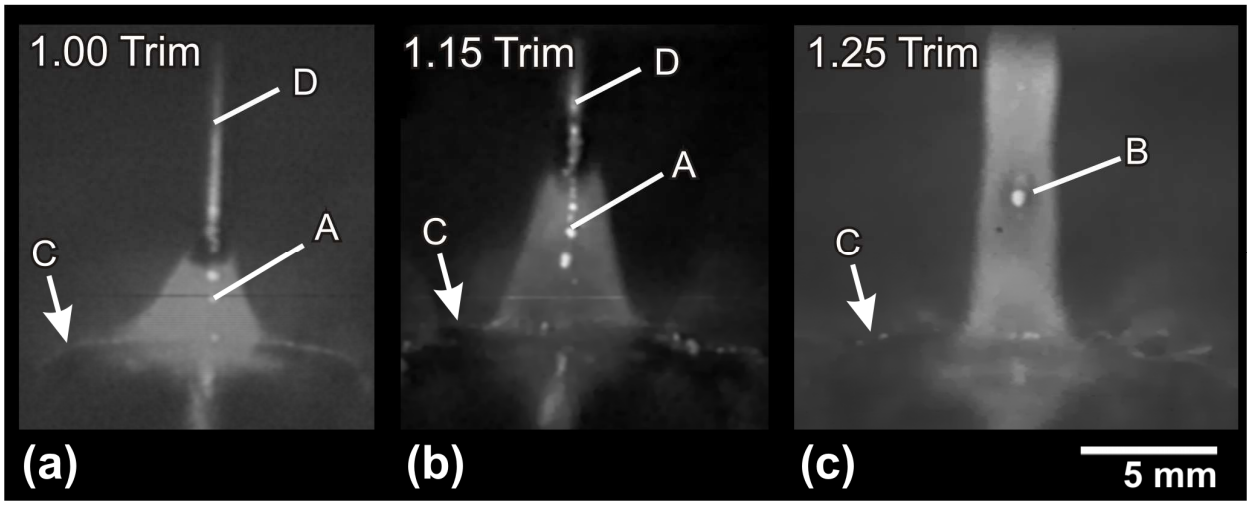

Figure 4.1: Example images of the three different GMAW-P spray transfer arcs used during weld procedure development. The arc length increased as the trim was increased from a) 1.00 to b) 1.15 to c) 1.25.

Phase 1 welds that were conducted with a 1.00 trim and 20 mm CTWD were discontinued early in the welding trials due to arc instability. This original DOE weld group was discontinued in favour of the 1.00 trim and 14.3 mm CTWD weld parameters. The only weld from this parameter set that is shown in the table is TB52. This weld had CO boil, which had occurred due to insufficient weld pool shielding from the atmosphere. The atmospheric shielding had been insufficient because the CTWD had been too large for the selected shielding gas flow rate. The shielding gas flow rate was adjusted for all subsequent welds made with a 20 mm CTWD by increasing flow from 14 L/sec to 18 L/sec. This new flow rate was also adopted for welds made with a 14.3 mm CTWD.

The welds that were made with a 1.00 trim and 14.3 mm CTWD were found to give stable and consistent weld bead geometry. The majority of these welds gave streaming spray-transfer conditions with minimal short circuiting. There was intermittent short circuiting that could be detected when the voltage and current measurements were reviewed. This was also observed with the LaserStrobe video recordings; however, it is difficult to show with images because there was no arc. These welds gave the desired range of root penetration and each non-defective weld was cross-sectioned and measured. An additional weld (TB50) was included in this set to replace the weld that had been made with the TB49 weld parameters, which had caused burn-through during welding.

The welds that were conducted with a trim of 1.25 were found to give satisfactory projected spray-transfer conditions. Observations suggested that the 20 mm CTWD (initially meant to allow for the larger 1.25 trim arc length) was too great and appeared to cause arc instability. The arc was observed to fluctuate and wander during processing at the higher travel speeds; the image of the arc shown in Figure 4.1c showed that the arc was very long and narrow, which likely caused instability when the travel speed was increased. This led to problems with the consistency of the weld bead geometry. At slower travel speeds, the arc had better stability, but it was found that the power input from these welds was high. When the travel speed was lowered, there was excessive heat input and the zinc melting point isotherm was visibly unstable. In one case, (TB60) there was burn-through. The only weld that was free from

defects was the weld made with the TB56 parameters and was the only weld from this set measured for root penetration. An additional 1.25 trim weld was included to observe how the arc stability changed with a change in the CTWD. This is represented in the table as weld TB55, which had a 14.3 mm CTWD. Weld TB55 appeared to give a more stable arc (minimal arc fluctuation) and was included for the root penetration measurements.

After completing the welds that had been included in the original DOE an additional three welds were conducted using the new trim of 1.15. These welds achieved stable streaming spray-transfer and were free from defects. All three of these welds were cross-sectioned and measured for root penetration.

Sample images from the Phase 1 welds are shown in Figure 4.2. The images show a 200 mm portion along the lengths' of some representative welds. In the images, the weld bead geometry can be observed on the top surface and the relative amount of penetration can be observed on the bottom surface. Welds that had consistent width, consistent reinforcement height, and were free from pores or undercut were considered the higher quality welds. On the images, the zinc melting (~420°C) isotherms are indicated with white dashed lines. The distance between the isotherms indicated the relative size of each weld HAZ. A weld with a relatively large span between the isotherms meant that the weld had a higher heat input than a weld with a smaller span between isotherms.

The image in Figure 4.2a represents a weld that had acceptable bead topography but lacked root penetration. The weld was made using the TB45 weld parameters, as shown in the table. It was cross-sectioned and measured to have a root penetration of 49.3%. The image in Figure 4.2b shows a weld with consistent weld bead geometry and close to full root penetration; this weld was made using the TB82 weld parameters. It was measured and found to have a root penetration of 76.0%. The weld in Figure 4.2c had consistent weld bead geometry and had fully penetrated through the sheet thickness. The weld was made using the TB47 weld parameters. It was measured and found to have a root penetration of 147.6%. These welds were selected for Phase 2 weld development, because the process travel speed

could be adjusted in order to change root penetration while maintaining consistent weld bead geometry [13].

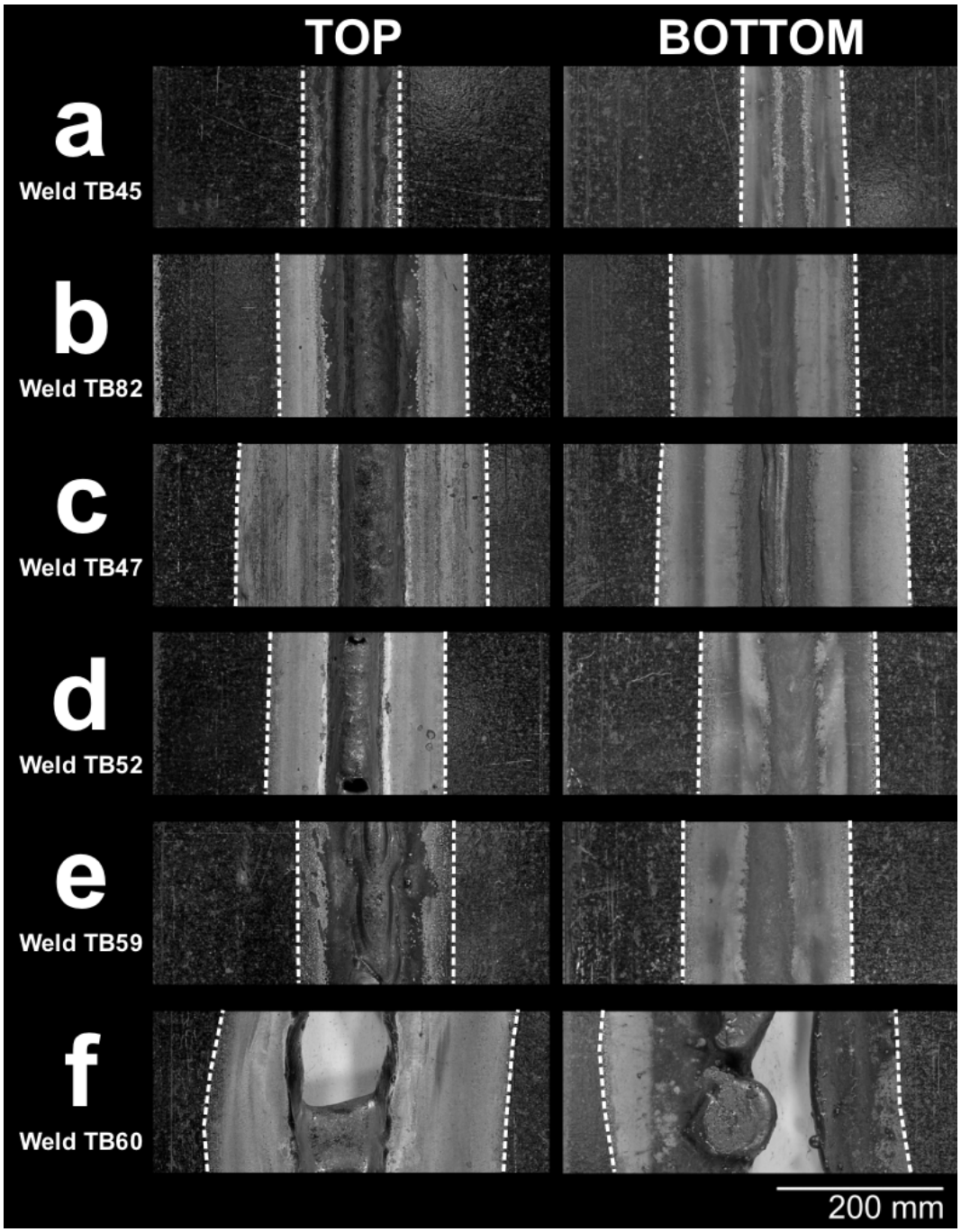

Figure 4.2: Example welds from the Phase 1 welding trials. Shown are a) a weld that had lack of penetration, b) a weld that had good bead geometry and sufficient root penetration, c) a weld that had excessive penetration, d) a weld that had porosity, e) weld with intermittent bead geometry, and f) a weld that had burn-through.

The image in Figure 4.2d shows a weld that had formed pores throughout the weld bead. This weld had been made using the TB52 weld parameters. The pores had formed due to CO boil because too much oxygen had reached the molten weld pool.

The image in Figure 4.2e represents a weld that had intermittent weld bead geometry. This weld was made using the TB59 weld parameters. Weld parameters that produced an intermittent weld bead were not selected for Phase 2 weld development. Typically, the zinc melting isotherms showed visible fluctuation. This fluctuation would also occur in the weld HAZ. These welds were not repeatable and subsequent welds made with these parameters could differ significantly. These welds were not cross-sectioned. The variability observed with the bead geometry would also be present in root measurements and therefore a percent penetration measurement would not be representative of the entire weld.

The image in Figure 4.2f shows a weld that had excessive heat input and had melted completely through the sheet steel. This weld had been made using the TB60 weld parameters. These welds could not be measured for root penetration. The zinc isotherms can be seen in the image and show significant fluctuation.

From the 18 welds that were conducted during the Phase 1 trials, 11 welds were cross-sectioned and measured for root penetration. These 11 welds were used as the baseline data establish new welding parameters for Phase 2 trials. Most of the Phase 1 welds did not meet the root penetration requirement and only TB51 and TB81 were within 20% of the required 100% root penetration. The goal of Phase 2 welding trials was to refine the parameters from Phase 1 to achieve the root penetration requirement.

The weld parameters and measured root penetrations of welds made during Phase 2 welding trials are shown in Table 4.2. The weld parameters for Phase 2 used the parameters selected from Phase 1 trials with adjustments to travel speed in order to change the linear heat input. This increased or decreased the root penetration as required. Phase 1 welds that were used as baseline data for the Phase 2 parameters are shown in the table as ‘associated family welds’ with their respective Phase 2 weld. A weld ‘family’

represented welds that had the same power input, i.e., trim, WFS, and CTWD were held constant. In addition to using Phase 1 welds for baseline data, as Phase 2 welds were made and measured they were also used to create new weld parameters.

Table 4.2: The Phase 2 welding parameters. The shaded areas of the table indicate the weld parameters that were selected for use during DP600 welding trials.

Weld Code	Weld Family [Trim, WFS, CTWD]	Associated Family Weld(s)	TS [mm/s]	H_{rel} [J/mm]	Root Penetration [%]	Defect(s)
TB72	[1.00, 169 mm/s, 14.3 mm]	TB43, TB45	19.4	197	96.0%	-----
TB73	[1.00, 212 mm/s, 14.3 mm]	TB47, TB48	21.6	206	82.4%	-----
TB74	[1.00, 254 mm/s, 14.3 mm]	TB50, TB51	25.3	212	80.7%	-----
TB76	[1.25, 169 mm/s, 14.3 mm]	TB55	21.2	311	70.9%	-----
TB77	[1.25, 169 mm/s, 20 mm]	TB56	21.2	251	56.8%	-----
TB78	[1.25, 212 mm/s, 20 mm]	TB58	21.2	309	71.3%	-----
TB79	[1.25, 169 mm/s, 14.3 mm]	TB55, TB76	19.1	342	102.8%	-----
TB83	[1.15, 212 mm/s, 14.3 mm]	TB81	22.4	271	81.8%	-----
TB84	[1.00, 254 mm/s, 14.3 mm]	TB50, TB51, TB74	23.3	226	82.2%	-----
TB85	[1.25, 169 mm/s, 14.3 mm]	TB55, TB76, TB79	19.5	342	-----	-----
TB86	[1.00, 212 mm/s, 14.3 mm]	TB47, TB48, TB73	20.3	213	90.7%	-----
TB96	[1.15, 169 mm/s, 14.3 mm]	TB80	19.1	293	108.1%	-----
TB97	[1.15, 212 mm/s, 14.3 mm]	TB81, TB83	21.2	304	95.5%	-----
TB98	[1.15, 254 mm/s, 14.3 mm]	TB82	24.6	296	-----	Burn-through

There were three weld families established from Phase 1 and each included two welds. These were TB43/TB45, TB47/TB48, and TB50/TB51. A linear interpolation was used for each of these sets to estimate a new travel speed that would give 100% root penetration during Phase 2 welding. The linear interpolation was based on the Phase 1 travel speeds and root penetration measurements.

There were an additional five welds from Phase 1 that did not have an associated family weld. These welds could not use a linear interpolation to estimate a travel speed that would achieve 100% root penetration. Instead, an estimate based on the degree of root penetration for those welds was made. This meant that if the Phase 1 weld did not fully penetrate the sheet then a slower travel speed was required and if the Phase 1 weld gave greater than full penetration then a faster travel speed was required.

There were minimal external weld defects found during the Phase 2 welding trials and only TB85 and TB98 were excluded from root penetration measurements. The weld made with the TB98 parameters was excluded because it had the burn-through defect. The TB85 weld was not defective, but was excluded because observations based on the TB79 welded coupon suggested that the 100% root penetration requirement had already been met. These two welds were very similar and hence only one was selected.

After cross-sectioning and measuring for root penetration, nine welds were within 20% of the 100% root penetration requirement. Seven of these welds were selected for transfer to the 1.65 mm DP600 '16s' sheet steel. The welds that were selected were: TB72, TB79, TB83, TB84, TB86, TB96, and TB97; these welds are highlighted in the table with grey. These were selected because they were the nearest to 100% root penetration from their respective weld families. They each represented a different weld family and a different relative heat input. These seven welds created a range of heat input that spanned from approximately 197 J/mm to 342 J/mm.

Some sample images from the Phase 2 welds that were selected for the 1.65 mm DP600 '16s' weldability study are shown in Figure 4.3. The top surfaces show the weld bead width and the bottom surfaces show the root penetration. The zinc melting (420°C) isotherms are indicated on each image with white dashed lines.

The image in Figure 4.3a shows the lowest heat input weld, TB72. This weld represented a weld that was made with a trim of 1.00. This weld had a percent penetration of 96.0% and was made with a relative heat input of 197 J/mm. The image in Figure 4.3b shows a medium heat input weld that was made using the TB83 weld parameters. This weld was made with a trim of 1.15. The TB83 weld had a percent penetration of 81.8% and was made with a relative heat input of 271 J/mm. The image in Figure 4.3c shows the highest heat input weld that was made using the TB79 weld parameters. This weld was made with a trim of 1.25. The TB79 weld had a percent penetration of 102.8% and was made with a

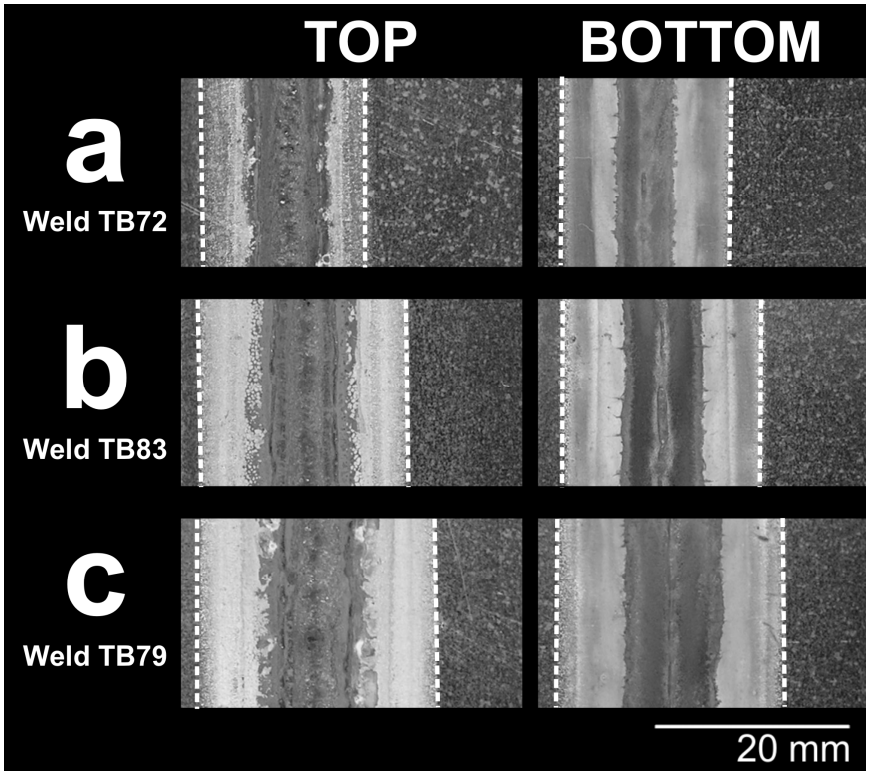

Figure 4.3: Sample images for the selected welds from Phase 2 welding trials. The image in a) shows the lowest heat input weld (TB72), the image in image b) shows a mid-range heat input weld (TB83), and the image in c) shows the highest heat input weld (TB79).

relative heat input of 342 J/mm. These images represent low, medium, and high heat input welds. The distance between the zinc melting (420°C) isotherms increased with higher heat input, while the root penetration for these welds remained similar. This was the main goal for Phase 2 welding experiments. A set of welds that had been made using a wide range of linear heat input and had similar weld bead geometry/root penetration had been created. After this point in the study, the focus was on welds made onto 1.65 mm thick DP600 '16s'sheet steel. A summary of the results and discussion related to welds made onto 1.80 mm thick HSLA '17s' sheet steel can be found in Appendix B.

4.1.1.1: DP600 '16s' Sheet Steel Weld Microstructure

The selected welding parameters from Phase 2 welding trials were used to make bead-on-plate welds in 254 mm × 76.2 mm 1.65 mm thick DP600 '16s' sheet steel coupons. These welds were then cross-sectioned to observe the weld HAZ microstructure and then to measure the HAZ width.

An overview of the different microstructural regions that were observed in the DP weld HAZ is shown in Figure 4.4. The chart in Figure 4.4a is the Fe-Fe_3C steel phase diagram. The microstructure that was found in the weld HAZ was relatable to the phase diagram and could be compared to the expected microstructural regions that were known to occur at different temperature and carbon weight percentage. Important microstructural regions are marked on the phase diagram, which include: the fusion zone (FZ), the supercritical grain growth (GG) region and grain refined (GR) region, the intercritical (IC) region, the subcritical (SC) region, and the base-metal (BM). The phase diagram is for a Fe-Fe_3C non-alloyed steel, so the agreement between the microstructure in the dual-phase steel welds and the phase diagram is only qualitative. The specified melting temperature [66] and the Ac_3 and Ac_1 temperatures [67] are based on calculations for an alloyed steel that correspond with the nominal DP600 '16s' steel composition. A DP600'16s' weld cross-section is shown in Figure 4.4b that has been labelled with the microstructural regions. The boundaries of these microstructural regions were used for the HAZ width measurements. The Ac_1 and Ac_3 lines are labelled on the image of the cross-section, which are the boundaries for the IC region. The suspect softened zone was located in the SC region immediately adjacent to the Ac_1 line.

An overview of the microstructures observed in the different microstructural regions in a DP weld and HAZ is shown in Figure 4.5. The base-metal, shown in Figure 4.5a, was found to have a slightly different microstructure than initially expected. The microstructure was comprised of the expected martensite islands within a ferrite matrix; however, there were also pockets of what is suspected to be bainite and other carbides. In the image martensite islands are labelled 'M' and bainite/carbide formations are labelled 'B/C'. These pockets are suspected to be caused by the dual-phase processing, where during the quenching step after intercritical annealing, some austenite islands did not form to martensite. This could have been caused by compositional differences between the various austenite islands. Manganese has been shown to segregate in past studies on DP steel processing [6]. Austenite

islands with lower manganese composition would have lower hardenability and during quenching could have formed bainite or other carbides.

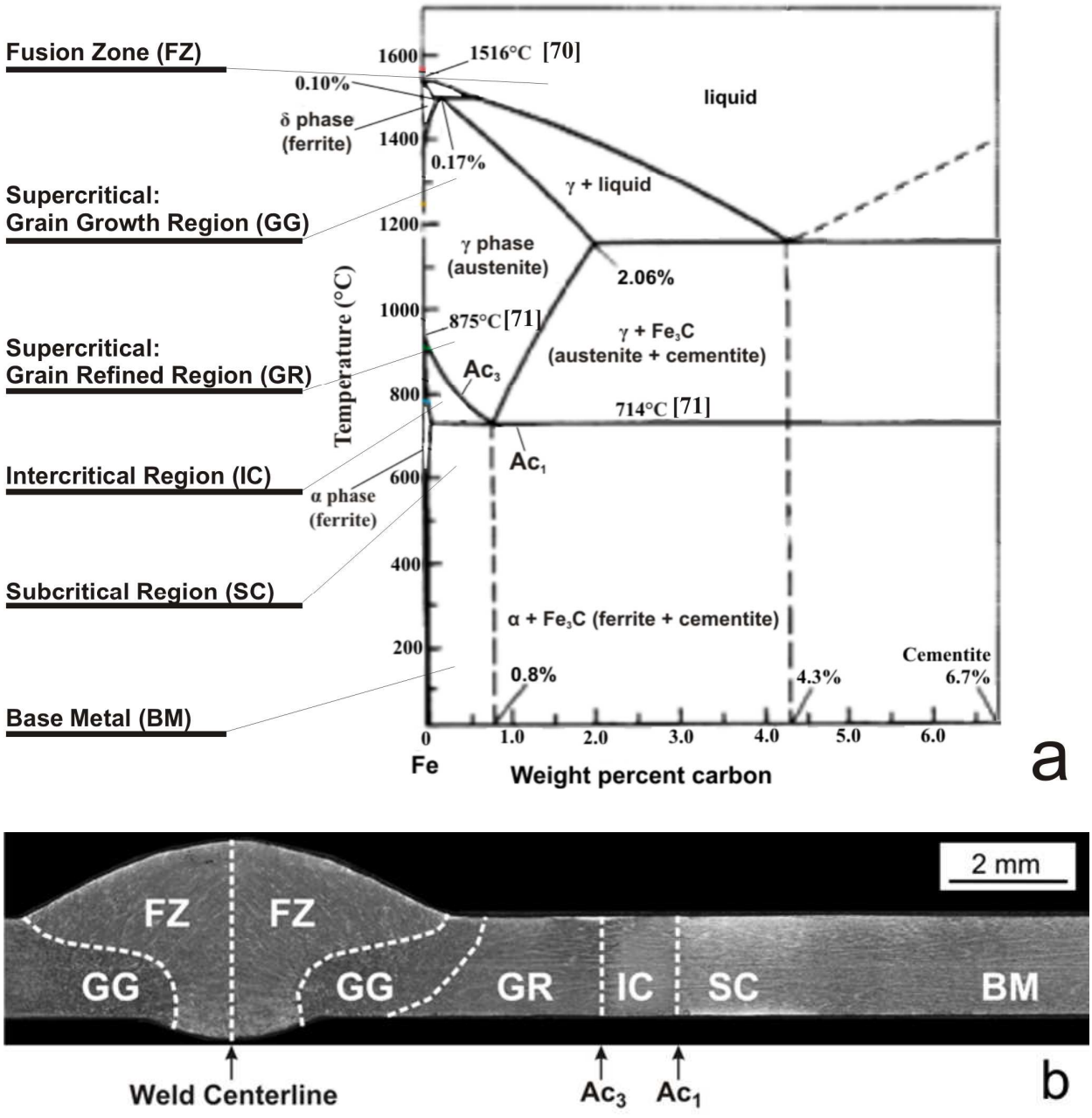

Figure 4.4: Overview of the DP weld HAZ. Image a) shows a typical Fe-Fe_3C binary phase diagram (with modified A_1, A_3, and TM temperature). Image b) shows a typical cross section from a GMAW-P DP600 weld. The suspect softened zone was located in the subcritical (SC) region of microstructure.

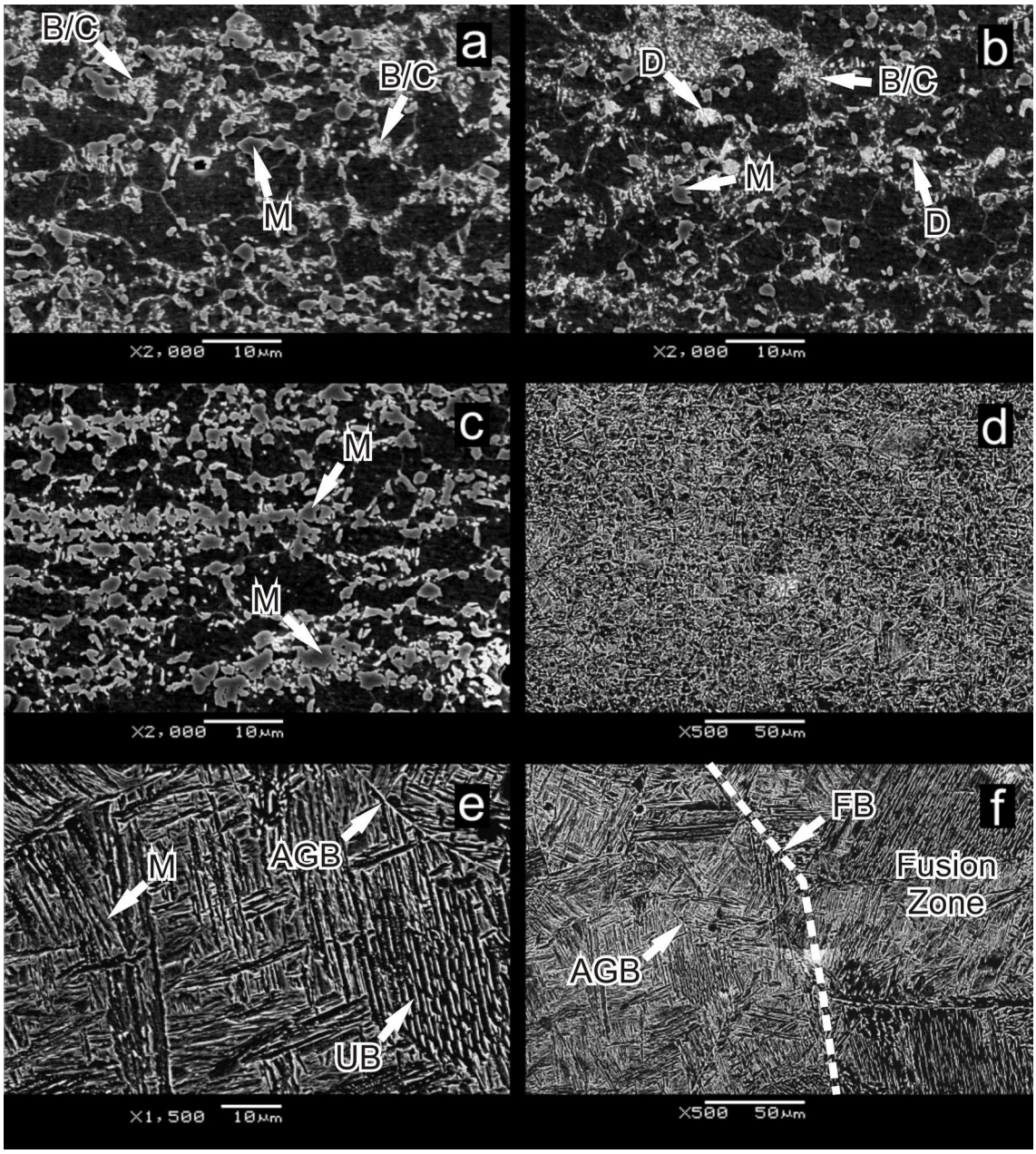

Figure 4.5: An overview of the 1.65 mm thick DP600 '16s' sheet steel weld microstructure. The image in a) was the base-metal, b) shows the subcritical region, c) shows the intercritical region, d) shows the grain refined region, e) shows the grain growth region, and f) shows the boundary between the grain growth region and the fusion zone.

The subcritical zone microstructure is shown in Figure 4.5b. In the image, the decomposed martensite islands are labelled 'D'. Material in this region was heated to just below the Ac_1 temperature during welding. The microstructure resembled the base-metal except that there were also islands of

decomposed (tempered) martensite found in the ferrite matrix. Unexpected formations that resembled martensite islands were also found that showed no signs of decomposition. Similar to the reasoning for the formation of bainite and carbide pockets, these formations suggest that martensite islands had differing compositions.

The microstructure of material heated into the intercritical zone during welding is shown in Figure 4.5c. The martensite islands from the base-metal had expanded in size and there was no evidence of the pockets of bainite/carbide formations. In this region, the martensite and bainite/carbide phases in the base-metal partially reformed to austenite and then re-quenched to martensite. The austenite phase had expanded into the surrounding ferrite, but otherwise the original ferrite matrix was unaffected. The absence of the bainite/carbide pockets suggests that the weld pass created a more rapid quench than during the original dual-phase process quenching step. Reformed ferrite was not detected; however, it may not have been resolved by the SEM and could have formed at the edges of martensite islands.

The microstructure of material heated into the austenitic temperature range that underwent grain refinement and grain growth is shown in Figure 4.5d and e, respectively. These two regions were found between the Ac_3 line and the fusion boundary. These represent the supercritical region of the steel phase diagram where, during the GMAW heating cycle, the steel was fully transformed to austenite. Growth of austenite grains in the grain refined region was prevented by aluminum and titanium inoculants in the base-metal [15, 68]. Upon cooling after welding austenite in this region transformed to massive martensite [10]. Above a certain peak temperature (an unknown temperature for this material) the inoculants dissolved in the austenite mix and the grains grew much larger than the grains in the GR region. The grains were largest immediately adjacent to the fusion boundary. The prior austenite grain boundaries can be seen in the region and are labelled ‘AGB’. The interior of these large grains transformed to massive martensite [10] and upper bainite [15] upon cooling after welding. Upper bainite is labelled ‘UB’ on the image. These regions were not examined in detail during the study but are included here for reference.

The location of the fusion boundary is shown in Figure 4.5f. On the image, large prior austenite grain boundaries are labelled 'AGB' and the fusion boundary is labelled 'FB'. At the boundary large columnar grains extended outwards from the large prior austenite grains (affected by a transformation to delta ferrite) to the central location of heat input. The composition of the material in the fusion zone was mostly ER70S-6 electrode material with a small amount of melted base-metal from the DP steel. The microstructure of the fusion zone grains was a mixture of martensite, and upper and lower bainite.

4.1.1.2: DP600 '16s' Weld HAZ Measurements

The weld parameters that were used to make full penetration welds in the 1.65 mm thick DP600 '16s' sheet steel, the resultant heat input, and average HAZ Ac_1 half-width measurements are given in Table 4.3. The average HAZ half-width was based on the distance from the weld centerline to the Ac_1 line on either side of the weld. In the table, the welds have been placed in order from the lowest relative heat input to the highest relative heat input. When placed in this order, the average HAZ Ac_1 half-width measurements followed an expected trend, with the smallest width occurring at the lowest heat input and the largest width occurring at the highest heat input. The table also shows the root penetration measurements. All of the DP600 welds attained the required full penetration, i.e., within 20% of full penetration. All of the welds were free from any defects, both external and internal.

Table 4.3: Welded DP600 '16s' sheet steel HAZ half-width measurements.

Weld Code	Weld Parameters [Trim, TS, WFS, CTWD]	H_{rel} [J/mm]	Root Penetration [%]	Average Ac_1 HAZ Half-Width [mm]	Average Ac_3 HAZ Half-Width [mm]
TB87	[1.00, 19.4 mm/s, 169 mm/s, 14.3 mm]	193	114.4%	5.12	4.25
TB95	[1.00, 20.3 mm/s, 212 mm/s, 14.3 mm]	215	118.3%	5.66	4.65
TB107	[1.00, 23.3 mm/s, 254 mm/s, 14.3 mm]	242	117.4%	5.85	4.78
TB94	[1.15, 22.4 mm/s, 212 mm/s, 14.3 mm]	274	112.9%	6.50	5.27
TB99	[1.15, 19.1 mm/s, 169 mm/s, 14.3 mm]	297	116.2%	6.87	5.53
TB100	[1.15, 21.2 mm/s, 212 mm/s, 14.3 mm]	307	120.3%	7.07	5.73
TB88	[1.25, 19.1 mm/s, 169 mm/s, 14.3 mm]	347	121.2%	7.44	6.16

The average HAZ Ac_1 half-width measurements are plotted against the relative linear heat input for each weld in Figure 4.6. The data points formed a linear trend. The variance that was seen for the half-width measurements of each weld was small and was likely caused by fluctuations of welding input power during processing, slight variations in clamping force along the weld, and slight variations in the clamp distance to the weld pool during processing.

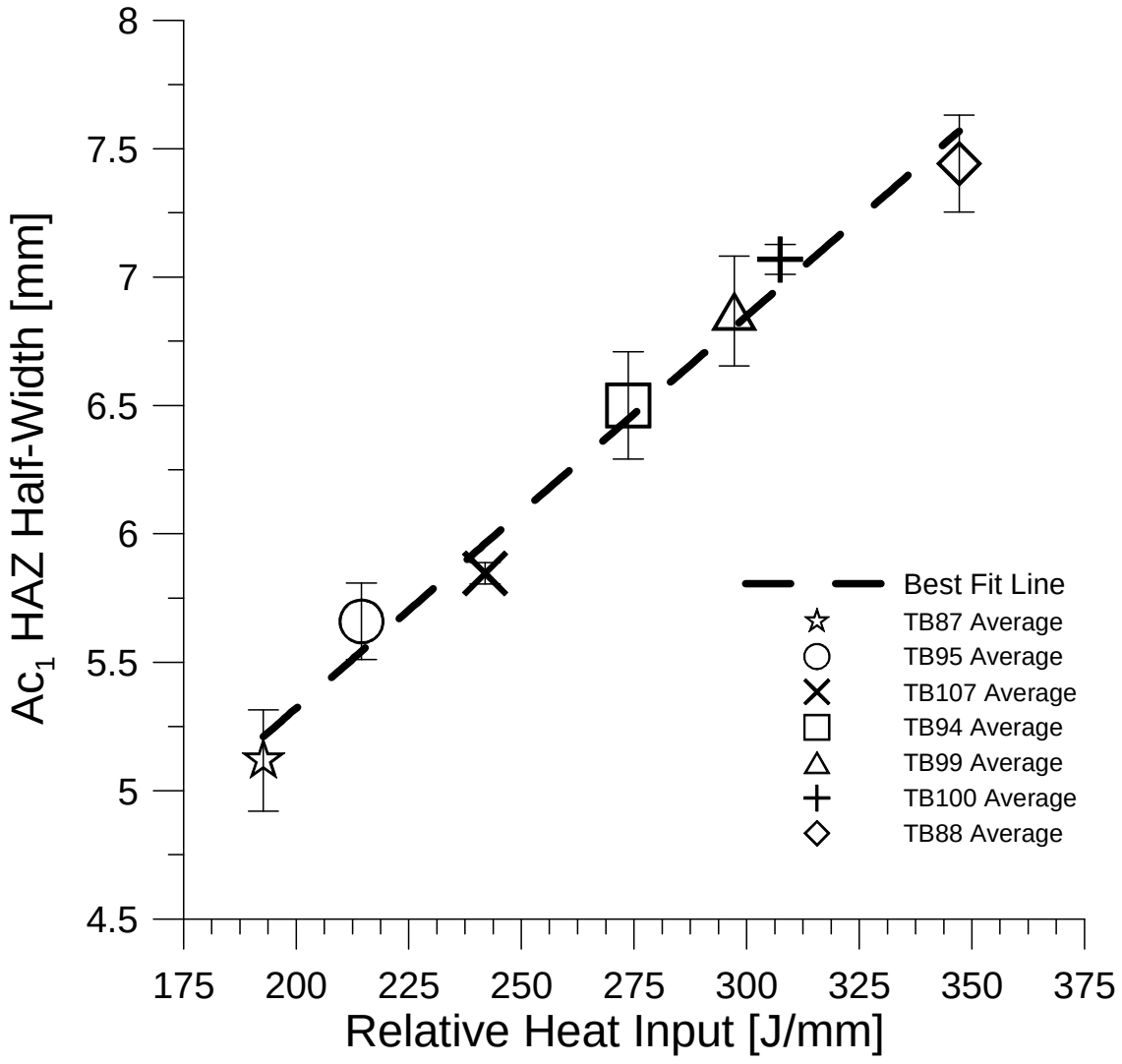

Figure 4.6: Plot of the Ac_1 HAZ half-width measurements against the measured relative heat input for each weld made in the 1.65 mm DP600 '16s' sheet steel.

Two example images of transverse weld sections that were used to measure HAZ half-width are shown in Figure 4.7. On the images, the weld centerline, Ac_3 line, and Ac_1 line are indicated with white dashed lines and an example measurement is shown. Both weld fusion zones fully penetrated the sheet thickness and had 'finger' penetration geometry. The 'finger' penetration weld fusion zone geometry is typical of a GMA weld made using spray transfer mode. Each image was taken at ×50 magnification with the optical microscope. At this low magnification, the Ac_1 line was difficult to locate. To identify the Ac_1 line, higher magnification (×500 and ×1000) images were observed with the optical microscope prior to measurement, which were similar to the images that are shown above in Figure 4.4b and c.

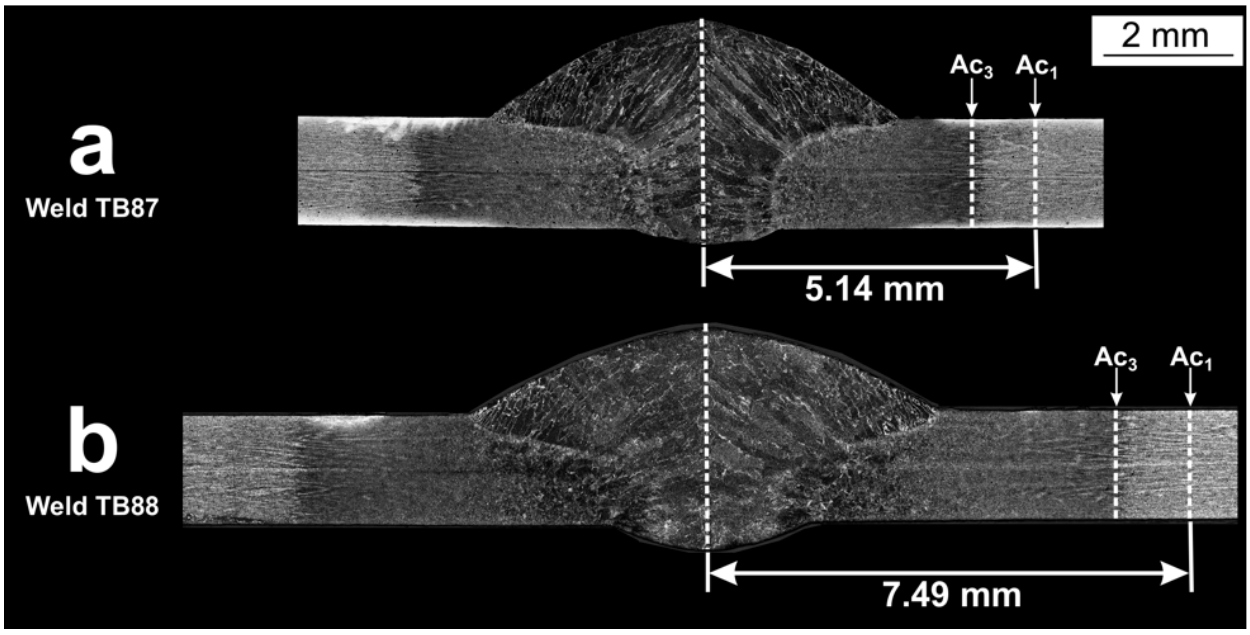

Figure 4.7: Example images that were used for the HAZ measurements of the half-width distances from the weld centerline to the Ac_1 and Ac_3 lines. Shown is a) the lowest heat input weld, TB87, and b) the highest heat input weld, TB88.

The image in Figure 4.7a shows a cross-section from a weld that was made with the TB87 welding parameters; this was the lowest heat input weld that had been selected for testing. An example Ac_1 HAZ half-width measurement is shown, which was 5.14 mm. The average Ac_1 HAZ half-width for the TB87 weld was 5.12 ± 0.20 mm. The image in Figure 4.7b shows a cross-section from a weld made with the TB88 welding parameters; this was the highest heat input weld that had been selected for testing.

An example Ac_1 HAZ half-width measurement is shown, which was 7.49 mm. The average Ac_1 HAZ half-width for the TB88 weld was 7.44 ± 0.19 mm.

4.1.1.3: DP600 '16s' Weld HAZ Microhardness Profile Results

Base-metal Microhardness

The 1.65 mm DP600 '16s' base-metal microhardness was characterized by using a 3 × 3 grid of indentations to measure Vickers microhardness. This grid was similar to a grid of indentations used by Biro [48] to characterize base-metal hardness at ArcelorMittal Dofasco, Inc. [48]. The grid of indentations gave an average hardness of 200 VHN with a standard deviation of 5.55 VHN. This hardness value was used to compare with the weld microhardness profiles in order to locate areas of hardening and softening.

Weld Microhardness Results

The seven selected welds from Phase 2 trials were cross-sectioned and brought to ArcelorMittal Dofasco, Inc. [48] for microhardness profiling. All of the profiles spanned from unaffected base-metal just outside the Ac_1 line on either side of the weld where the DP steel softened zone was expected to occur. An example Vickers microhardness profile that was compared to the weld macrostructure is shown in Figure 4.8; this profile was for the lowest heat input weld (TB87). The different microstructural regions are labelled on the image. Base-metal was observed at both ends of the profile and appeared to match the average BM hardness; however, this was not true for all of the welds, as will be explained later in this section. As the indentations approached the Ac_1 line, there was evidence of softened material; this was also not true for all of the welds and will also be explained later in this section. A division line between the SC region and the BM is marked; the division line indicated 'A' on the image. Indentations that were within the IC zone had a significant spike in hardness compared to the adjacent SC region; this spike in hardness is labelled 'B' at its minimum and 'C' at its peak. This was the location of the Ac_1 line; the hardness spike was common for all of the DP600 '16s' welds and was used to locate the Ac_1 for other

profiles. The hardness increased further upon entering the GR region and then reached a maximum hardness in the GG region of microstructure; high hardness in these regions was associated with the microstructure consisting of a mix of bainite, martensite, and small amounts of acicular ferrite. The FZ hardness decreased slightly compared to the hardened HAZ; however, it was significantly higher (+50 VHN) than the BM hardness.

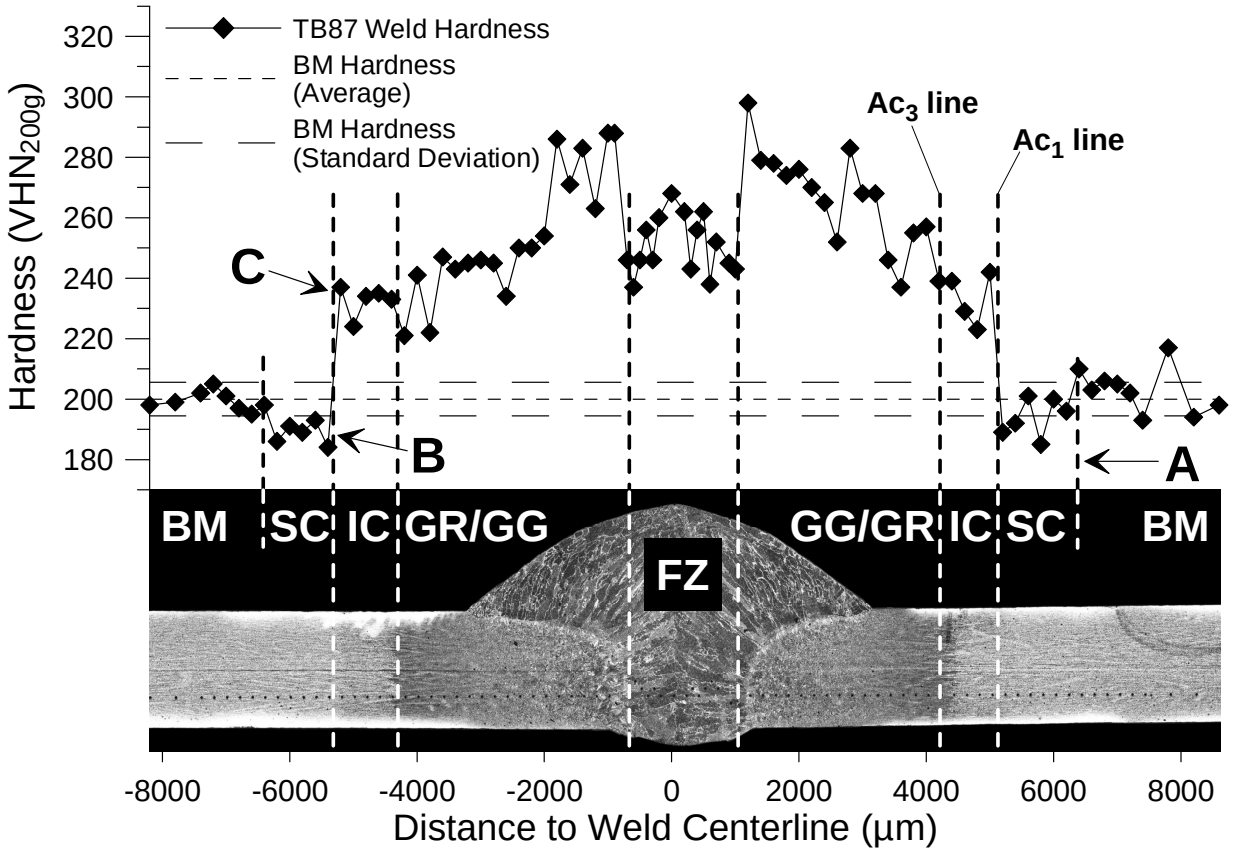

Figure 4.8: An example Vickers microhardness profile with weld cross-section to show the relative location of microstructural regions. The cross-section was for the TB87 weld (1.65 mm DP600 '16s' sheet steel).

A scanning electron microscope was used to examine the microstructure around the Ac_1 line, and some example images are shown in Figure 4.9. This was the area of interest during the course of the study, because it was at the location where martensite tempering occurred. The images that are shown

were taken between two adjacent microhardness indents that were 200 µm apart and were located on adjacent sides of the Ac_1 line.

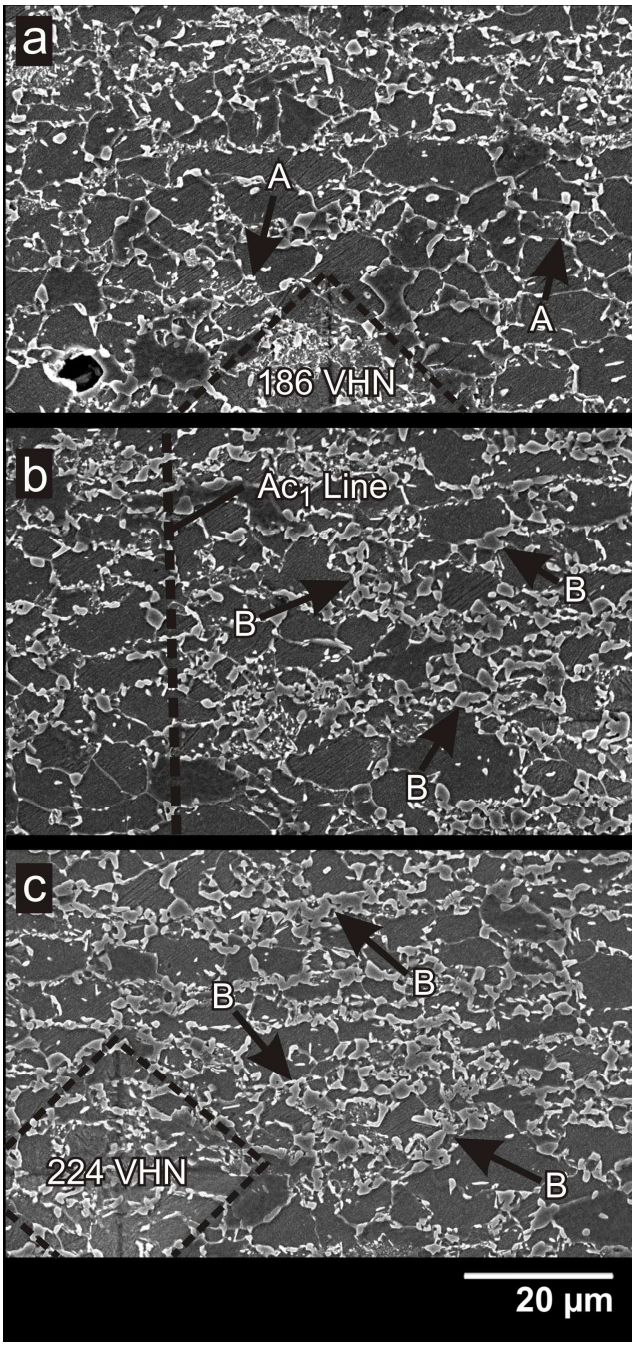

Figure 4.9: The dual-phase microstructure was compared with the Vickers microhardness results. Image a) shows an indent that was in the SC region adjacent to the Ac_1 line. Image b) shows the approximate location of the Ac_1. Image c) shows an indent that was in the IC region immediately adjacent to the Ac_1 line. (photographed with SEM).

The indent that was located in the SC region adjacent to the Ac_1 line is shown in Figure 4.9a. This indent measured a hardness of 186 VHN, i.e., 14 VHN softer than the base-metal. It was difficult to identify decomposed islands of martensite because the prior BM had non-martensitic carbides present, which were very similar in appearance; however, some example islands that resembled decomposed martensite are labelled 'A' on the image. The image in Figure 4.9b shows the approximate location of the Ac_1 line; the left side of the image was the SC region and the right side was the IC region. Renucleated martensite was present in the IC region, and some example islands are labelled 'B'. The indent that was located in the IC zone adjacent to the Ac_1 line is shown in Figure 4.9c. This indent measured a hardness of 224 VHN, i.e., 24 VHN harder than the base-metal. This increase in hardness is thought to be directly associated with the expansion of the martensite islands; the volume fraction of martensite had appeared to increase.

As mentioned above, there were some differences that were found when microhardness profiles for different welds were compared. For the majority of the microhardness profiles, the hardness data in the SC region and BM fluctuated so that it was difficult to measure the size of the softened SC region and the degree of softening. The location of the BM was also difficult to pinpoint on some profiles. This presented contradictory results when measurements from different welds were compared.

An example profile that illustrated some of the fluctuating hardness data is shown in Figure 4.10; this profile was for the TB94 weld (mid-range heat input). The different microstructural regions are indicated on the profile; these were identified from an etched weld cross-section after indentation (not shown). Measuring for maximum softening was not consistent. Some profiles did not exhibit a softened zone and on the example profile this is labelled 'A'; however, there did appear to be a drop in hardness at the edge of the IC region, but did not fall below BM properties. This was an issue that affected calculation of degree of softening, because some welds did not have obvious points to select for minimum hardness; in some cases (see Figure 4.11) minimum hardness was located more than 1 mm from the Ac_1 line. When the profiles for all of the welds were compared, there was no obvious trend that matched

similar studies found in the literature (high heat input welds did not appear to have greater softening); the only explanation from the literature was that DP600 did not exhibit significant softening in low heat input welds [36,45]. However, this explanation is insufficient, because some profiles had visible softening; an example of softening suggested by the value of only one indent is labelled 'B' on the profile.

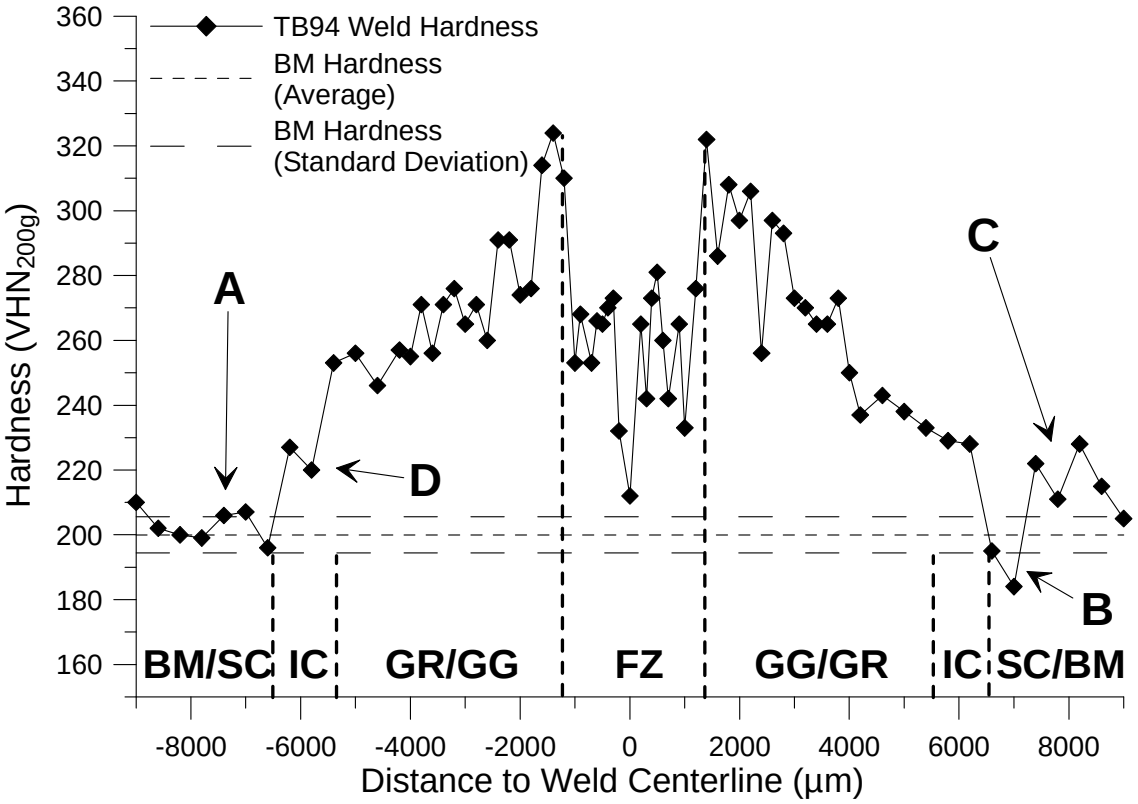

Figure 4.10: An example Vickers microhardness profile that was used to characterize the hardness across a weld HAZ. The profile that is shown is for the TB94 weld (1.65 mm DP600 '16s' sheet steel).

From the hardness profiles, it was difficult to measure for softened zone width because it was unclear if the microstructure at the edges of the profile were from the base-metal; hardness measurements did not consistently appear to match base-metal microhardness. There were also unexpected increases in hardness measured on some samples adjacent to the softened region where it had been expected that base-metal properties would occur. The location labelled 'C' on the profile shown in Figure 4.10 suggested that this region of microstructure had consistently higher hardness than the base-metal; this was observed

on several of the profiles, but no obvious trend was found. There was no visible explanation for this after an initial study of the microstructure.

A second example of a hardness profile is shown in Figure 4.11; this was from a high heat input weld (TB100). This profile is shown to illustrate that the hardness data in the SC and BM region had significant variance, which made measurement of the softened zone width difficult for some welds. The location that is labelled 'A' had both low and high hardness that did not match the average BM hardness. The location that is labelled 'B' shows that the BM hardness had not been achieved on this side of the weld. This region appeared to have hardened, which was not an expected result.

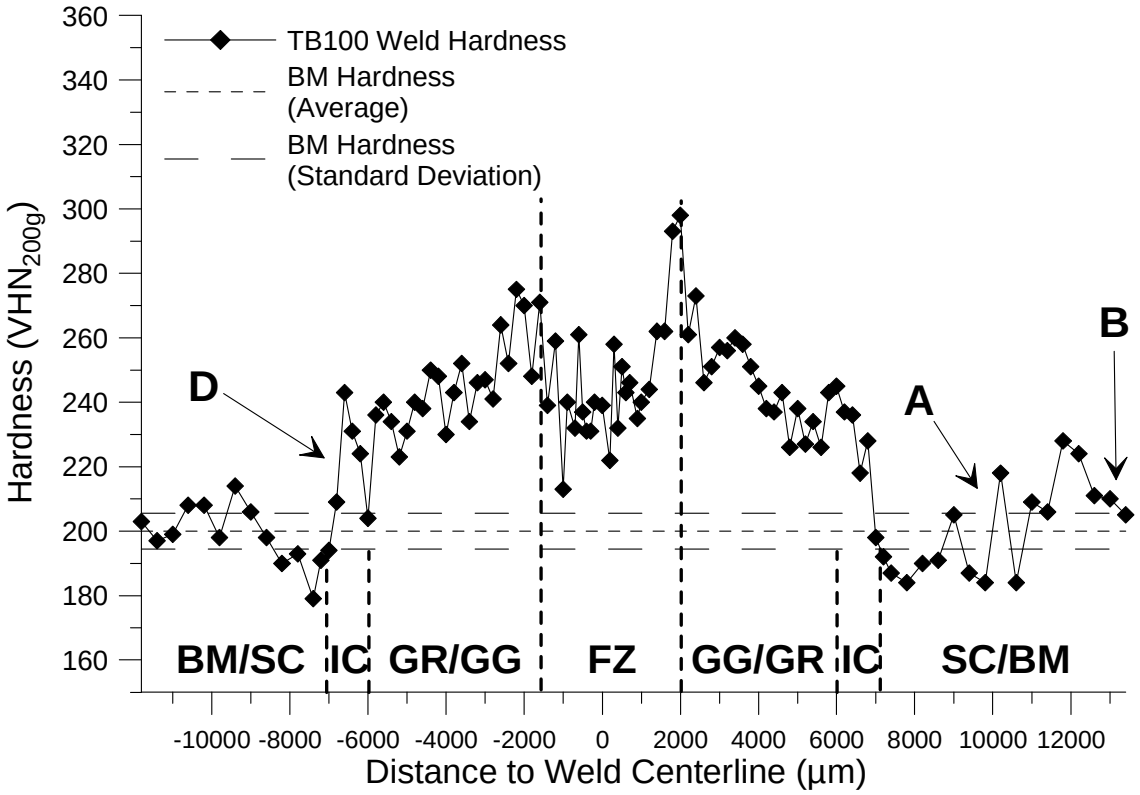

Figure 4.11: A microhardness profile that illustrates variability from hardness data taken from the SC region and BM.

The only consistent observation that was made from all of the microhardness profiles was that there was a significant increase in hardness that occurred adjacent to the Ac_1 line in the IC region of the microstructure; it is labelled 'D' on the profiles from Figure 4.10 and Figure 4.11.

Minimum hardness values that were measured for all of the welds are shown in Table 4.4; degree of softening is shown for both sides of each weld. Degree of softening calculations indicated that there was softening in the weld HAZ; however, a definitive value for softening was not established. There was no obvious trend across the range of weld heat inputs and softening did not increase as heat input increased; this is contrary to the results for DP steel softening reported by Biro and Lee [36] and Xia *et al.* [45]. Instead, the data suggested that the highest heat input weld (TB88) had the lowest degree of softening (8 VHN) and the lowest heat input weld (TB87) had among the highest degree of softening (16 VHN). It was believed that the method for calculating degree of softening as proposed by Xia *et al.* [45] was insufficient for this material because minimum points of hardness did not always occur immediately adjacent to the Ac_1 line.

Table 4.4: The degree of softening calculations for the Phase 2 welds.

Weld Code	H_{rel} [J/mm]	DP600 '16s' BM Hardness [VHN_{200gf}]	Minimum HAZ Hardness (Left Side) [VHN_{200gf}]	Minimum HAZ Hardness (Right Side) [VHN_{200gf}]	DOS_{Left} [VHN_{200gf}]	DOS_{Right} [VHN_{200gf}]
TB87	193	200	184	185	16	15
TB95	215	200	187	195	13	5
TB107	242	200	188	192	12	8
TB94	274	200	196	184	4	16
TB99	297	200	184	180	16	20
TB100	307	200	179	184	21	16
TB88	347	200	193	192	7	8

There was too much variability in the hardness measurements that were made in the SC region and the BM. The profiles did not provide a sufficient number of softening data points; this made comparison between different welds difficult. There was evidence of softening at the expected location just outside the Ac_1 line; however, it was not consistent. From the profiles, it was difficult to discern whether the unaffected base-metal had been reached; in some cases there was hardened material where the BM was expected.

Extended Weld Microhardness Samples

The microhardness profiles on symmetrical samples did not give definitive evidence of softening. There was also no definitive evidence that the base-metal had been reached with the indentation profiles. To support this belief, two new cross-sections were made that were extended asymmetric samples. A single microhardness indentation line was used on the lowest heat input weld, TB87, and on the highest heat input weld, TB88. The purpose was to re-evaluate the suspect softened zone on samples that assured that the base-metal was included in the profile.

The results for the two microhardness profiles are shown in Figure 4.12 and Figure 4.13. For both welds, it was evident that the indentation profiles had covered some of the base-metal; however, it showed that there was substantial variability in the hardness of the base-metal. The variability was suspected to be caused by the heterogeneous microstructure of the 1.65 mm DP600 '16s' sheet steel that included pockets of bainite and cementite instead of solely containing martensite and ferrite. It was also suspected that the weld heat input could have potentially affected the microstructure further into the base-metal than previously thought. Both samples had evidence of softening that occurred adjacent to the Ac_1 line; this is labelled 'A' on both profiles. However, the evidence was not entirely clear because the base-metal portion of the profile had significant variability. The base-metal included hardness measurements that were equivalent to the suspect softened zone; these points are labelled 'B' on both profiles. In Figure 4.13, the profile for the high heat input weld (TB88) had a point (labelled 'C') located in the BM (~10 mm away from the Ac_1 line) that was approximately 30 VHN softer than the average BM hardness; this point was approximately 10 – 15 VHN softer than the SC region. This further suggested that a degree of softening calculation was inappropriate to classify the welded samples. There was an unexpected increase in hardness in the SC region of the low heat input weld (TB87); this is labelled 'D' in Figure 4.12. The high heat input weld (TB88) did not show any definitive evidence of increased hardness in the SC region or the BM. Hardening in the SC region was not analysed further at this point in the study.

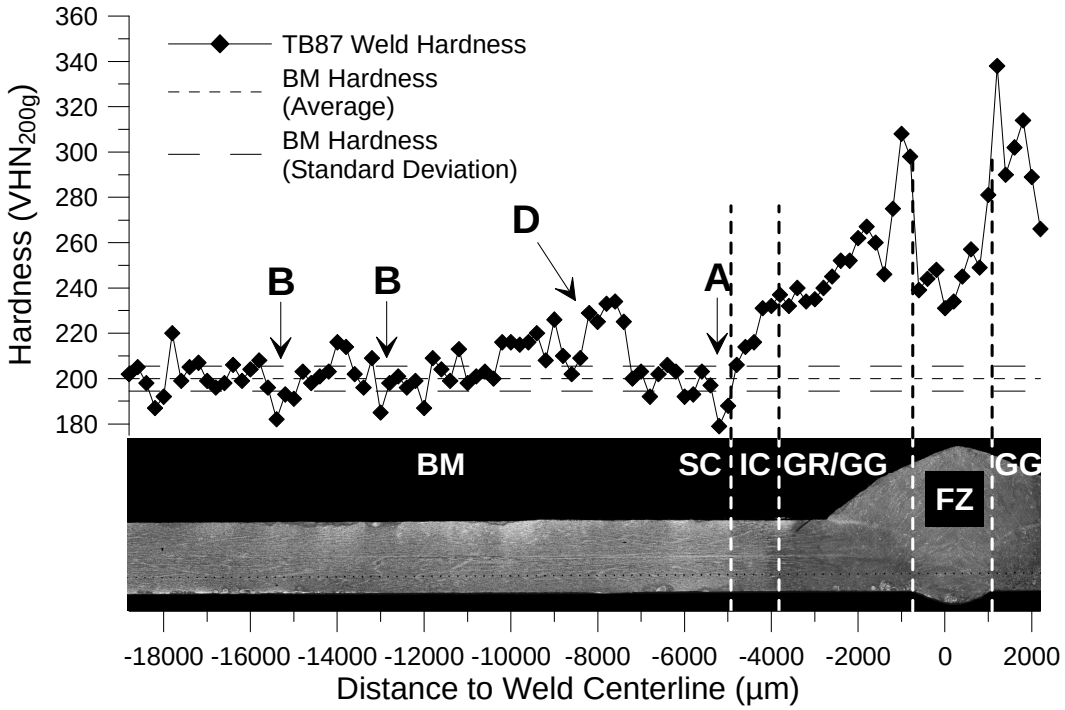

Figure 4.12: Vickers microhardness profile for an extended sample of TB87. A DP600 '16s' sheet steel weld.

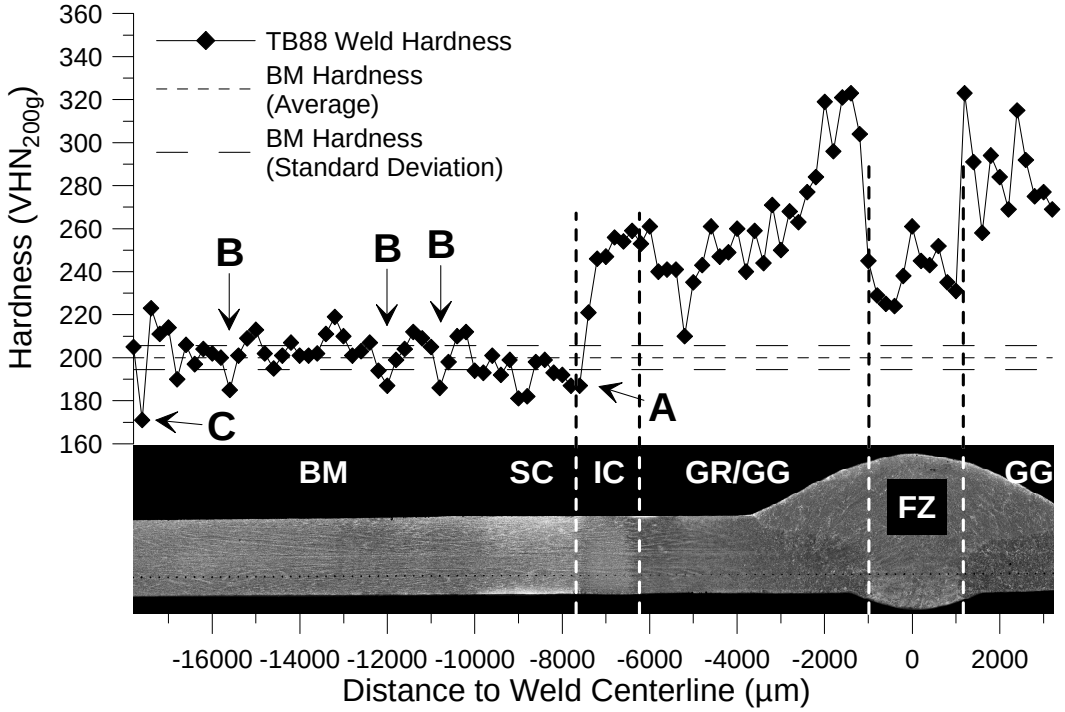

Figure 4.13: Vickers microhardness profile for an extended sample of TB88. A DP600 '16s' sheet steel weld.

The conclusions that were drawn from the microhardness profiles were as follows: the location of the suspect softened zone was in the SC region of the weld HAZ immediately adjacent to the Ac_1 line, there was a significant spike in hardness as measurements entered the IC zone, the spike in hardness was associated with renucleated martensite islands, the degree of softening within the SC region was not well defined when compared to the average BM hardness, and there was significant variability in the BM portion of the hardness profile that diminished the reliability of the softening data. No conclusions were drawn from the observations of increased hardness in the SC region of the HAZ.

4.1.1.4: DP600 '16s' Weld Specimen Transition of the Failure Location

The seven selected weld parameter sets from Phase 2 trials were used to weld onto 254 mm × 203 mm DP600 '16s' sheet steel coupons. These coupons were used to machine uniaxial transverse weld tensile specimens. Each weld was machined into at least five tensile specimens for full fracture uniaxial tensile testing.

A 100% BM failure set is shown in Figure 4.14a. This tensile specimen set had been machined from the low heat input (TB87) welded coupon. Each specimen fractured in the BM at the midway point between the weld fusion zone and the specimen grip. A fractured weld specimen set, made using the TB94 weld parameters, that had a mixed failure mode is shown in Figure 4.14b. There were three specimens that fractured in the HAZ and two specimens that fractured in the BM. A 100% HAZ failure is shown in Figure 4.14c. This tensile specimen set had been machined from the high heat input (TB88) welded coupon. Each fracture occurred in the HAZ at a relatively short distance from the weld fusion zone. From these images, it was not possible to determine what part of the HAZ had caused the fracture. The BM failure specimens had fracture planes that were typically perpendicular to the loading direction or to a maximum angle of approximately 25° offset from the specimen cross-sectional plane. All specimens that had fractured in the HAZ failure location had fracture planes that were perpendicular to the loading direction.

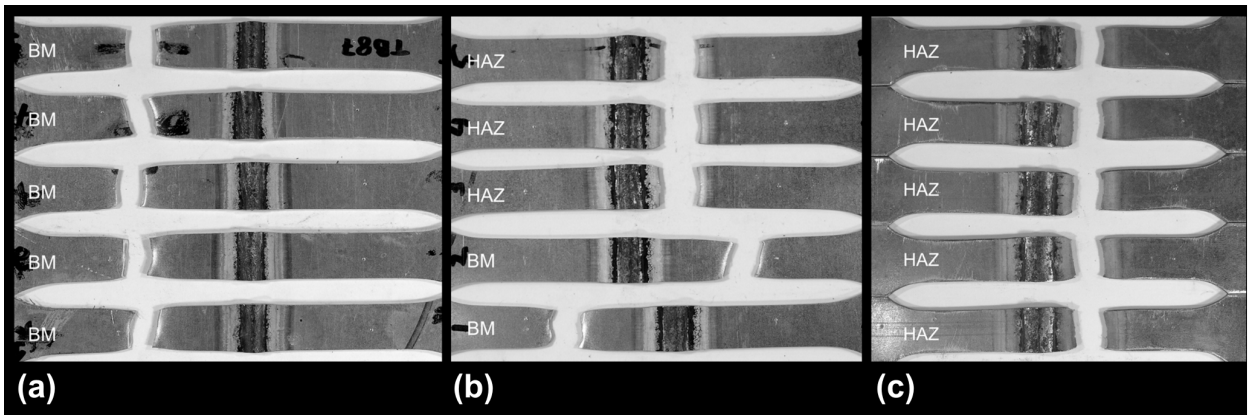

Figure 4.14: Transverse weld tensile test specimens: a) TB87 low heat input weld with 100% BM failure, b) TB94 medium heat input weld with mixed failure locations, and c) TB88 high heat input weld with 100% HAZ failure.

The failure locations for each transverse weld tensile specimen are summarized in Table 4.5. From these tests there were three welds that appeared to meet the requirement of a mono-type failure mode. All of the specimens from the lowest heat input weld (TB87) fractured in the BM while all of the specimens from two high heat input welds (TB88 and TB99) fractured in the HAZ. This provided the desired transition of failure mode. The remaining welds made using intermediate heat inputs exhibited mixed failure locations. Mixed failure occurred when a single weld had some tensile specimens fracture in the HAZ failure location and some fracture in the BM failure location. There were no fusion zone related fractures in any of the welded tensile specimens.

Table 4.5: Failure locations of the transverse weld tensile tests.

Weld Code	H_{rel} [J/mm]	Average HAZ Half-Width [mm]	Type of Failure Mode (Specimen #)					Failure Designation
			1	2	3	4	5	
TB87	193	5.09	BM	BM	BM	BM	BM	100% BM Failure
TB95	215	5.66	BM	BM	HAZ	BM	HAZ	Mixed Failure
TB107	242	5.85	HAZ	BM	BM	BM	BM	Mixed Failure
TB94	274	6.54	BM	BM	HAZ	HAZ	HAZ	Mixed Failure
TB99	297	6.91	HAZ	HAZ	HAZ	HAZ	HAZ	100% HAZ Failure
TB100	307	7.06	HAZ	BM	HAZ	HAZ	HAZ	Mixed Failure
TB88	347	7.48	HAZ	HAZ	HAZ	HAZ	HAZ	100% HAZ Failure

The tensile data for a HAZ failure specimen and BM failure specimen taken from the same weld sample, TB94, is shown in Figure 4.15. The tensile tests provided data for stress verses displacement; however, the tensile data from different welds could not be directly compared to each other or to the base-metal using these plots because the heat input from each weld had affected a different proportion of the base-metal. An approximate comparison could be made between two specimens that were taken from the same weld as shown in Figure 4.15. This would provide tensile specimens that had a similar proportion of affected material. This allows a comparison to be made between a HAZ failure specimen and a BM failure specimen by selecting specimens from a weld that had a mixed failure mode. The two sets of data shown in the figure were both taken from the TB94 weld.

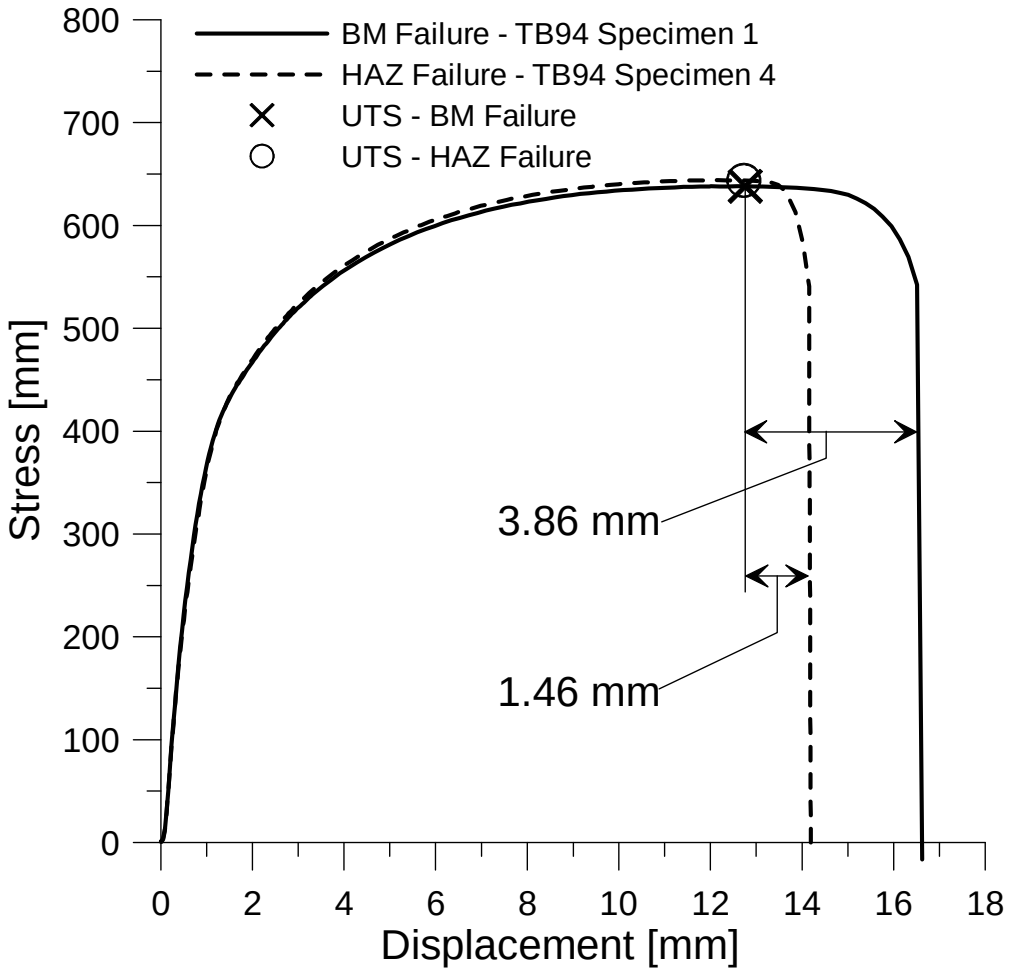

Figure 4.15: A comparison between stress-displacement curves from tensile specimens with a HAZ failure and BM failure.

The plot suggested that there was significant displacement prior to localized necking for both failure modes and that the UTS was similar for both failure modes; this suggested that DP steel had good weldability and 100% joint efficiency could be attained. The BM failure specimen appeared to have a more gradual change in curve slope after the UTS than the HAZ failure specimen. The displacement that occurred after the UTS had been reached is indicated on the chart. The BM failure specimen had displaced 3.86 mm after UTS and the HAZ failure specimen had displaced 1.46 mm. The BM failure mode had a significant increase in displacement during localized necking. This suggested that the BM failure mode was safer under loading conditions that could induce catastrophic failure. Otherwise the deformation that had occurred for both failure modes during uniaxial transverse weld tensile testing was mostly diffuse necking within the base-metal.

The tensile fracture results are also shown in Figure 4.16 to illustrate the transition of failure that occurred across the range of GMAW-P weld heat inputs. The lowest heat input weld (TB87) had all tensile specimens fail in the base-metal. The highest heat input weld (TB88) had all tensile specimens fail in the HAZ. Another relatively high heat input weld, TB99, also gave 100% HAZ failure. The weld TB99 was lower in heat input and average HAZ width in comparison to TB100. However, the result for TB100 included a specimen that gave a BM failure and hence it was a mixed failure mode weld. This suggested that TB99 was within a transitional zone of failure. For the purposes of this study, TB99 retained its designation as a 100% HAZ failure weld, but because it fell within the transitional zone, it was not used for tests to determine the differences between a HAZ failure and a BM failure. To pursue and determine the mechanism for achieving BM failure in GMAW-P DP sheet steel, welds TB87 and TB88 were selected for further study. These two welds were retested for uniaxial failure mode with an additional 5 tensile specimens each. The TB87 weld continued to show 100% BM failure and the TB88 weld continued to show 100% HAZ failure. After retesting and retaining consistent results, both welds were considered suitable for evaluating the DP sheet steel failure mechanism.

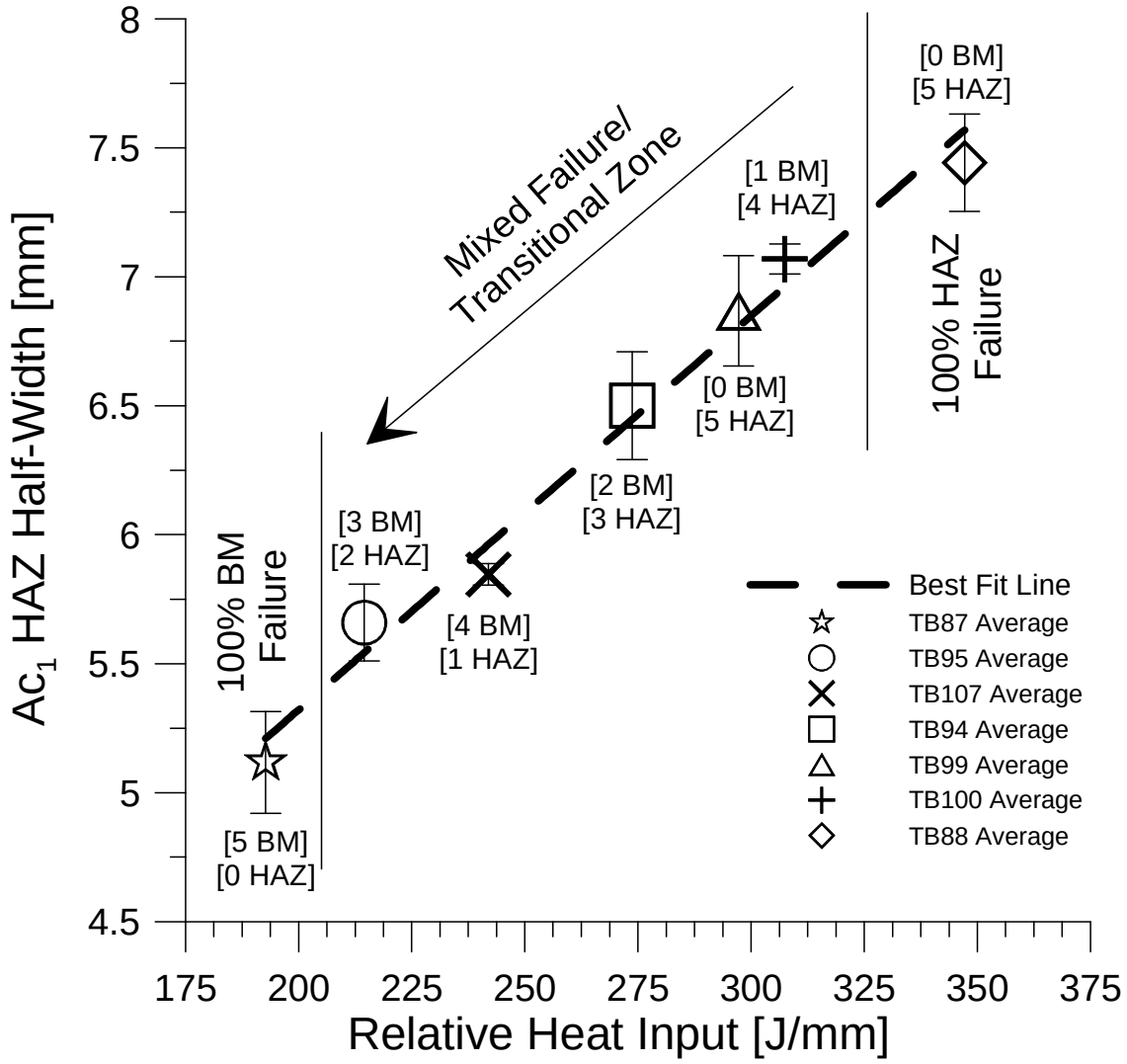

Figure 4.16: The fracture modes of the selected welds versus weld heat input and HAZ half-width.

Uniaxial transverse weld tensile testing of the welds that were selected from Phase 2 welding trials showed that the requirements for identifying welding conditions that would produce tensile specimens that would fracture in either the BM or the HAZ had been met. A 100% HAZ failure mode was established with welds TB99 and TB88, and a 100% BM failure mode was established with weld TB87. No further testing was required because the desired transition of failure mode had been achieved.

4.1.2: Determining Causes for Base-metal Failure in the Welded DP Sheet Steel

The following tests were performed on the low heat input weld (TB87) that had exhibited 100% BM failure during uniaxial tensile testing and the high heat input weld (TB88) that had 100% HAZ failure during testing. The testing that was used included: fracture analysis of complete fracture specimens, analysis of partially fractured specimens, martensite area fraction measurements, and microhardness mapping. The goal was to determine a reason for why the lower heat input welds always failed in the BM while all high heat input welds failed in the HAZ.

4.1.2.1: Full Uniaxial Tensile Test Fracture Analysis

The fractured specimens from the uniaxial transverse weld tensile tests were analysed to determine the micro-mechanism that occurred at the weld BM failure location and at the weld HAZ failure location. The fracture surfaces of unwelded BM and welded specimens that had failed in the BM and the HAZ were examined using the SEM. In addition, cross-sections of the welded specimen that fractured in the BM failure location and the welded specimen that failed in the HAZ failure location were examined using the SEM.

Base-metal Fractography

Prior to analysing the BM and HAZ weld failure locations in greater detail, the parent DP600 '16s' sheet steel was characterized with a fractographic analysis. Tensile specimens were loaded to complete fracture, the UTS and total elongation were measured for reference, and an analysis of a tensile specimen fracture surface was conducted.

The tensile test measurements for UTS and total elongation are given in Table 4.6. The values were slightly higher than the nominal values provided by ArcelorMittal Dofasco Inc. [48]. This was a significant amount of deformation that suggested ductile fracture.

Table 4.6: The DP600 '16s' base-metal mechanical properties derived from uniaxial tensile testing and the nominal values [48].

Specimen Number	UTS [MPa]	Total % Elongation [%]
1	653	27.30
2	658	25.71
Nominal [48]	638	23.7

A full image of a DP600 '16s' BM fracture surface that was examined with the SEM is shown in Figure 4.17. Crack formation for eventual fracture appeared to initiate from the half-way point between the central sheet and the sheet edge. This location is shown in the figure with a dashed white line. This produced a double slant fracture surface, which is typical for thin sheet [69]. This location was the central area of the tensile gauge width. Crack initiation appeared to be complex, where several relatively large micro-cracks had formed and expanded in the central area of the width. These expanding cracks would have connected by tearing (creation of a dimpled fracture plane between the crack tips) after the crack tips began to overlap on different planes [69]. The central area of the gauge width had the greatest amount of thickness reduction. The complete fracture extended away from the both sides of the initiation sites to the edge of the gauge width, shown in the figure with arrows pointing in the direction that fracture proceeded along. From the tensile tests, there were a number of different fracture planes. The angle of the fracture planes varied between very low angles (almost perpendicular to loading) to approximately 25° offset from the specimen cross-sectional plane.

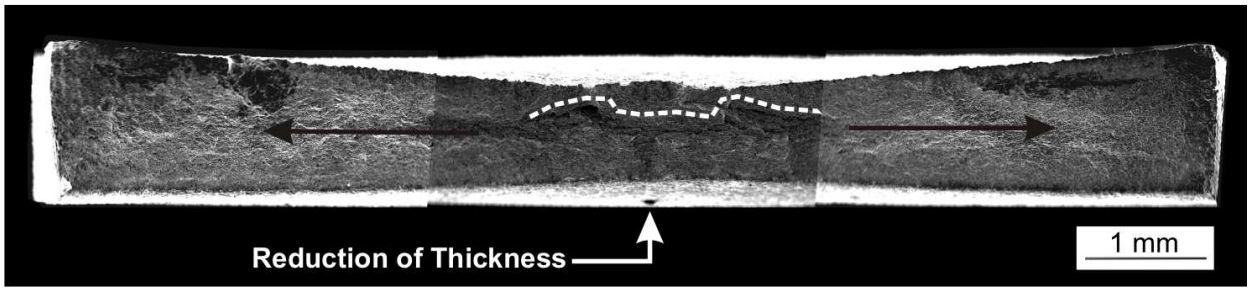

Figure 4.17: Top view of a typical fracture surface from a DP600 '16s' base-metal specimen.

A higher magnification analysis was also conducted and images are shown in Figure 4.18. The specimen had a ductile dimpled fracture surface and appeared to fail due to micro-void coalescence. There were no areas on the fracture surface that displayed brittle fracture. Crack initiation sites were typically associated with large voids. Cracking was also associated with micro-shearing away from the larger void sites. Most large voids were found to have formed around incoherent particles. In Figure 4.18a and f, the location of a connection between two coalesced void surfaces is shown. The surface has a drastic shift in elevation, indicated as location 'A' on the image. The void surfaces most likely extended from separate crack initiation sites and connected by tearing after the expanding planes overlapped [69]. This could be a grain boundary interface.

In Figure 4.18a, b, and c, suspected crack initiation sites are shown with a dashed line and labelled 'B'. Each of these sites had a line or string of voids that appeared to meet when they grew into each other. These void stings could have been located at grain boundaries. They were typically surrounded by a continuous shear lip, which indicated the formation of a crack [69].

Randomly distributed large voids had formed on the fracture surface. These appear in all of the figures with the label 'C'. Magnified images of these large voids are shown in Figure 4.18d, e, and f. Typically these voids contained a large incoherent particle [69]. An EDS analysis was performed on the particles and they were found to be aluminum-rich particles. These aluminum-rich inclusions were likely introduced during the steel killing process where aluminum is typically added to the melt to deoxidize the steel prior to casting. These normally innocuous Al_2O_3 inclusions normally retain their shape during hot rolling [70].

From the fracture surface analysis there was no definitive evidence of void nucleation between the ferrite and martensite interface; however, the size of the dimples/voids was associated with the volume fraction of martensite islands within the sheet steel. Other nucleation sites associated with the dimple size would have been the carbide/bainite interfaces with the ferrite matrix and along grain

boundaries. It was suspected that decohesion at these initiation sites would occur, but from the fracture surface analysis, it was not possible to determine if they occurred at final fracture or if decohesion was the dominant site for void nucleation early in loading.

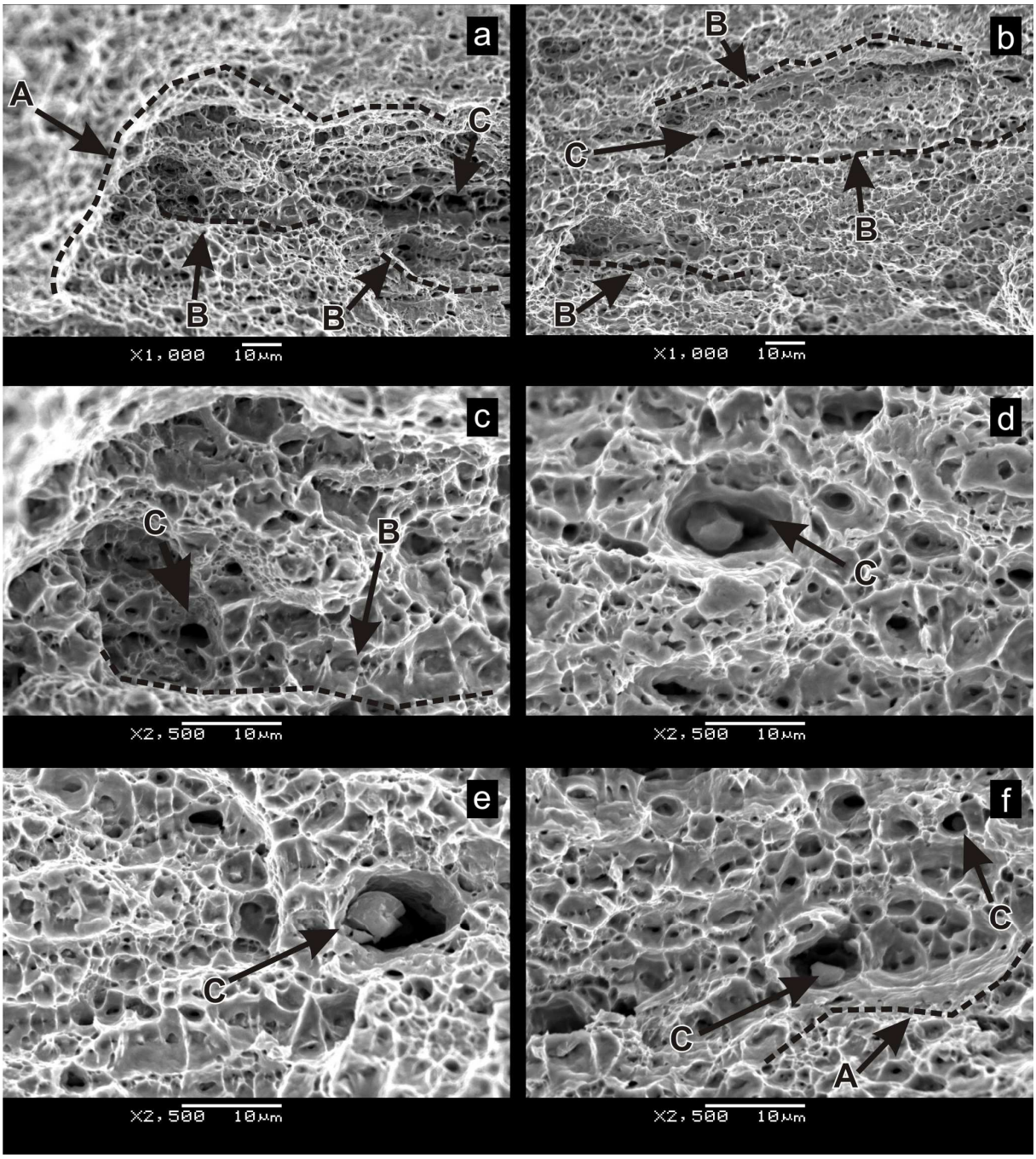

Figure 4.18: Analysis of DP600 '16s' sheet steel BM fracture surface. In image a),b), and c), suspected micro-crack initiation sites are shown, and in image d), e), and f) large micro-voids are shown, which had formed at incoherent particles.

Fractography of the Welded Specimens

The fracture surfaces of the welded tensile samples were analysed after fracture to determine the prominent failure mechanism and to determine probable sites of crack initiation. Prior to analysing the weld specimen fracture surfaces with the SEM, the location of fracture for both the BM failure and HAZ failure specimens were confirmed by examining a longitudinal section of the two types of fractured samples under the optical microscope. The longitudinal section for the weld that gave 100% BM failure is shown in Figure 4.19. The fracture location was confirmed to be far out into the base-metal. The fracture site was measured to be approximately 19.3 mm away from the Ac_1 line. The section of a HAZ failure mode specimen is shown in Figure 4.20. The section showed that the failure was not immediately adjacent to the Ac_1 line. The fracture was approximately 2.1 mm away from the Ac_1 line. In both fracture specimen sections, the hardened regions (IC, GR, GG, and FZ) had not undergone significant thinning due to the loading during the tensile tests. The sections also suggested that the HAZ failure had undergone more strain through the sheet thickness.

Figure 4.19: A longitudinal section of a fractured weld tensile specimen that had a BM failure location. (Low heat input weld).

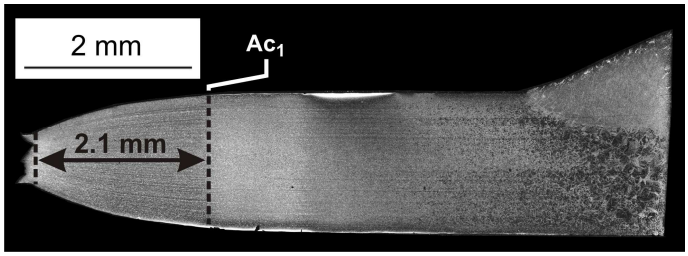

Figure 4.20: A longitudinal section of a weld tensile specimen that had a HAZ failure location. (High heat input weld).

A fracture surface from the set of welded specimens that were made with the TB87 weld parameters and had 100% BM failure is shown in Figure 4.21. The fracture surfaces were similar to unwelded BM specimen fracture surfaces. The specimens failed with double slant fracture surfaces and crack initiation sites appeared to be just above the midway point of the sheet thickness. Crack initiation appeared to be complex, with several crack initiation sites that connected by tearing between overlapping crack planes. Significant initial cracking was located in the area of greatest thickness reduction, which was located in the center of the specimen gauge width. This is labelled on the image with dashed white lines. A chevron pattern was observed on the surface, which suggested that some crack initiation occurred close to the edge of the specimen gauge width (labelled 'X' on the image) [69]. This suggested that although critical strain for significant crack formation was in the center of the specimen gauge width, there were also significant cracks forming at other locations throughout the gauge width. These areas would most likely only become dominant after there was significant cross-sectional area reduction over the entire gauge width. The edges did not show significant thickness reduction after fracture; however, the sheet edges typically incurred greater local strain during the onset of necking. This occurred because the sheet edges of the gauge width were free surfaces that did not have a stress normal to the sheet edge (along the gauge width axis). This caused greater local strain in these regions. If significant cracking in areas of reduced thickness had not already led to final fracture, then there was increased likelihood of cracks initiating and propagating from the sheet edges.

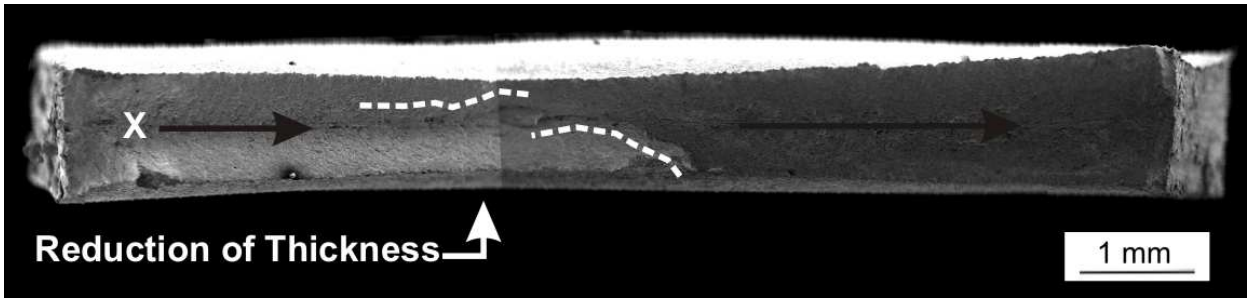

Figure 4.21: Top view of the fracture surface of a welded specimen that had a BM failure location.

Several fracture surface locations from a welded specimen that gave 100% BM failure are shown at higher magnification in Figure 4.22. The surface was similar to the unwelded BM specimen fracture surface. Fracture occurred due to micro-void coalescence and each image shown in the figure displays a typical dimpled rupture surface. In Figure 4.22a, two strings of voids with continuous shear lips that were most likely crack initiation sites are marked 'B'. These appeared to extend from the left of the image to right side where they ended in a series of shear tearing faces, which are marked 'A'. The dimpled rupture surface can be seen with a chevron pattern extended away from the cracks, indicated on the image with the direction of the dashed arrows. A similar pattern of crack initiation and shear tearing is shown in Figure 4.22b. This type of complex fracture was very similar to the unwelded BM fracture surface. The strings could be grain boundaries where there was decohesion between martensite and ferrite interfaces.

In Figure 4.22c, a shear tearing location is shown. The location where different planar cracks met and connected by tearing is marked 'A'. A crack with a large void formation is labelled 'D'. This crack appeared to initiate from a distance below the fracture plane before eventual rupture at the surface. This suggested that cracks were allowed to form for an extended duration of time, which suggested ductile fracture [69]. The dimples on the lower ledge of the tear appeared to be directed away from the formation as indicated by the dashed arrows. This suggested that initiation occurred at the location of the tear; this crack may have been a continuation of the upper ledge or was at a grain boundary [69].

In all of the figures, large voids that appeared to be the result of incoherent particles (inclusions) are marked 'C'. In Figure 4.22e, large voids were found that appeared to be at the initiation sites for strings of voids or continuous shear lips, which are marked as 'B'. The large voids did not contain evidence of inclusions; however, incoherent particles could have become dislodged during sample preparation [69]. Voids that did have inclusions can be seen in Figure 4.22d and f. The void shown in Figure 4.22f shows that dimpled rupture was directed away from the large void, indicated by the dashed arrows. This suggested that the large voids were effecting crack growth and initiation. The inclusions

were verified through EDS analysis to be rich in aluminum, which was similar to the unwelded BM fracture specimen.

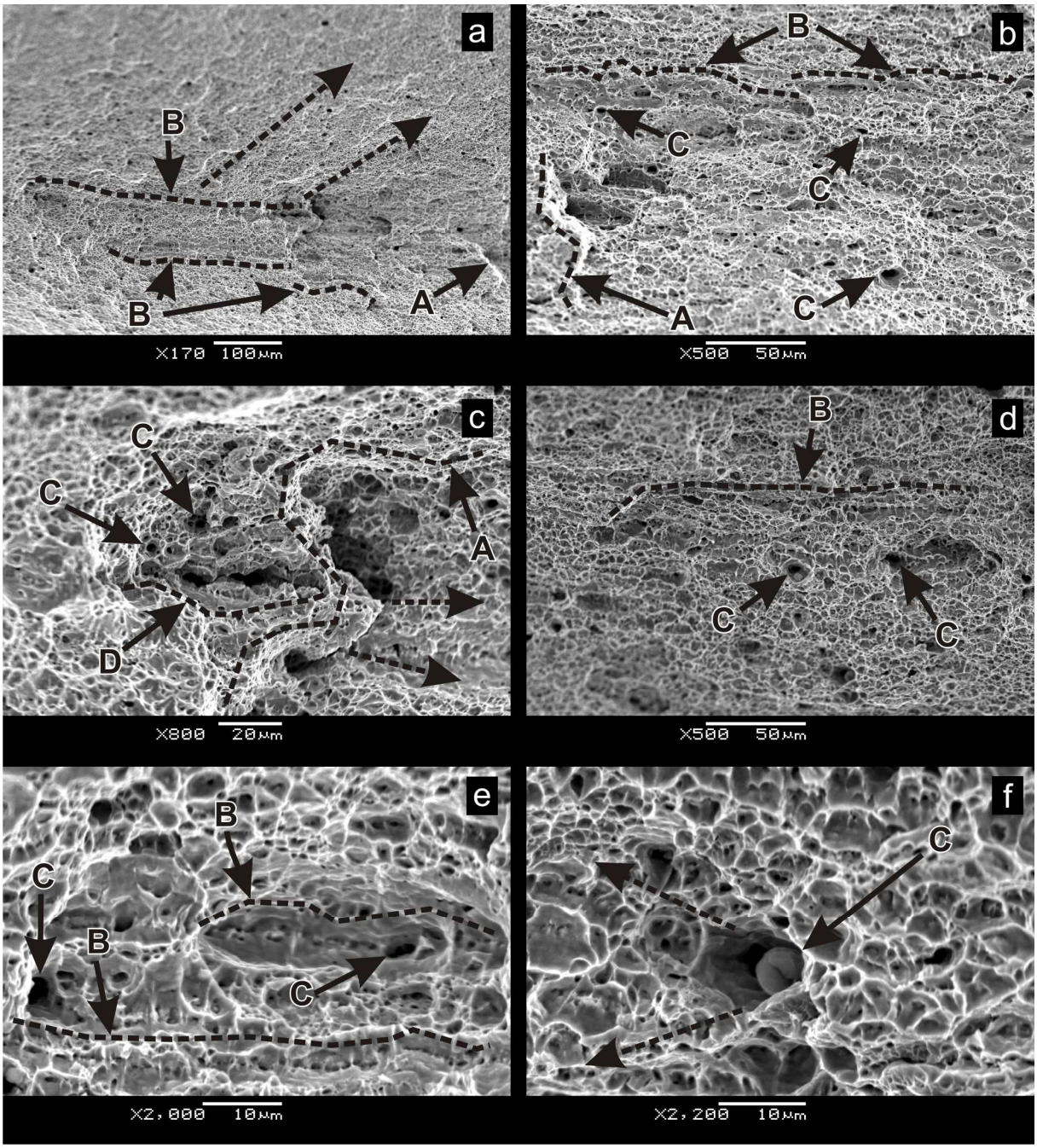

Figure 4.22: SEM Analysis of a welded DP600 '16s' sheet steel specimen that fractured in the BM. Image a), b), and d) show 'strings' of voids that were believed to be micro-crack initiation site, image c) shows a site of shear tearing, and image e) and f) show that large micro-voids had appeared to be located at initiation/termination sites for micro-cracks.

Generally, the fracture surfaces for a BM failure location did not definitively show the dominant mechanism for micro-void nucleation and crack formation; however, crack initiation leading to final fracture appeared to be caused by large void nucleation at inclusions and along strings of voids that had continuous shear lips. The strings were likely associated with the ferrite/carbide interfaces or grain boundaries and may have been affected by strain localization caused by the larger voids. The reasoning for final fracture could be described as a ductile failure by micro-void coalescence. From all of the evidence, it would appear that the welded specimen that gave BM failure was fracturing for the same reasons as the unwelded BM specimens.

To analyse the dominant mechanism for micro-void nucleation, the fracture cross-section from Figure 4.21 was examined with the SEM. Magnified images of the surface cross-section are shown in Figure 4.23. The images are labelled where there were large crack formations with an ‘A’ and are labelled where there was evidence of decohesion between the ferrite and martensite interface with a ‘B’. The microstructure displayed significant plastic deformation compared to unloaded BM microstructure images. From Figure 4.23a, it was found that cracks initiated and grew a significant distance away from the fracture surface. There were crack formations around inclusions found in the SC region of the HAZ; however, these sites did not have significant propagation.

In Figure 4.23b and c, there was evidence of micro-void nucleation due to decohesion. Decohesion appeared to be occurring between the ferrite matrix and the distributed martensite islands. Large cracks did not appear to have inclusions; however, initiation could have been caused by such particles on a different plane. From the images, the cracks appeared to shift and bypass the martensite and carbide islands. At these crack deflection points there was evidence of decohesion from the ferrite matrix. There was also evidence of martensite or carbide plastic deformation in this region. The deformation obscured the prior grain boundaries, which appeared to be aligned normal to the fracture surface.

At the location of decohesion in Figure 4.23d, the hardened island labelled ‘B’ appeared to have fractured. The martensite islands were coherent particles in the ferrite matrix and micro-cracks only formed due to decohesion or particle fracture [63]. This type of micro-void nucleation due to particle fracture was only seen in the region immediately adjacent to the fracture surface. It was suspected that this region adjacent to fracture incurred substantially higher local stresses than the remainder of the specimen and had entered into a tri-axial stress state. This suggested that these decohesion types only occurred during necking and immediately prior to fracture [63,70].

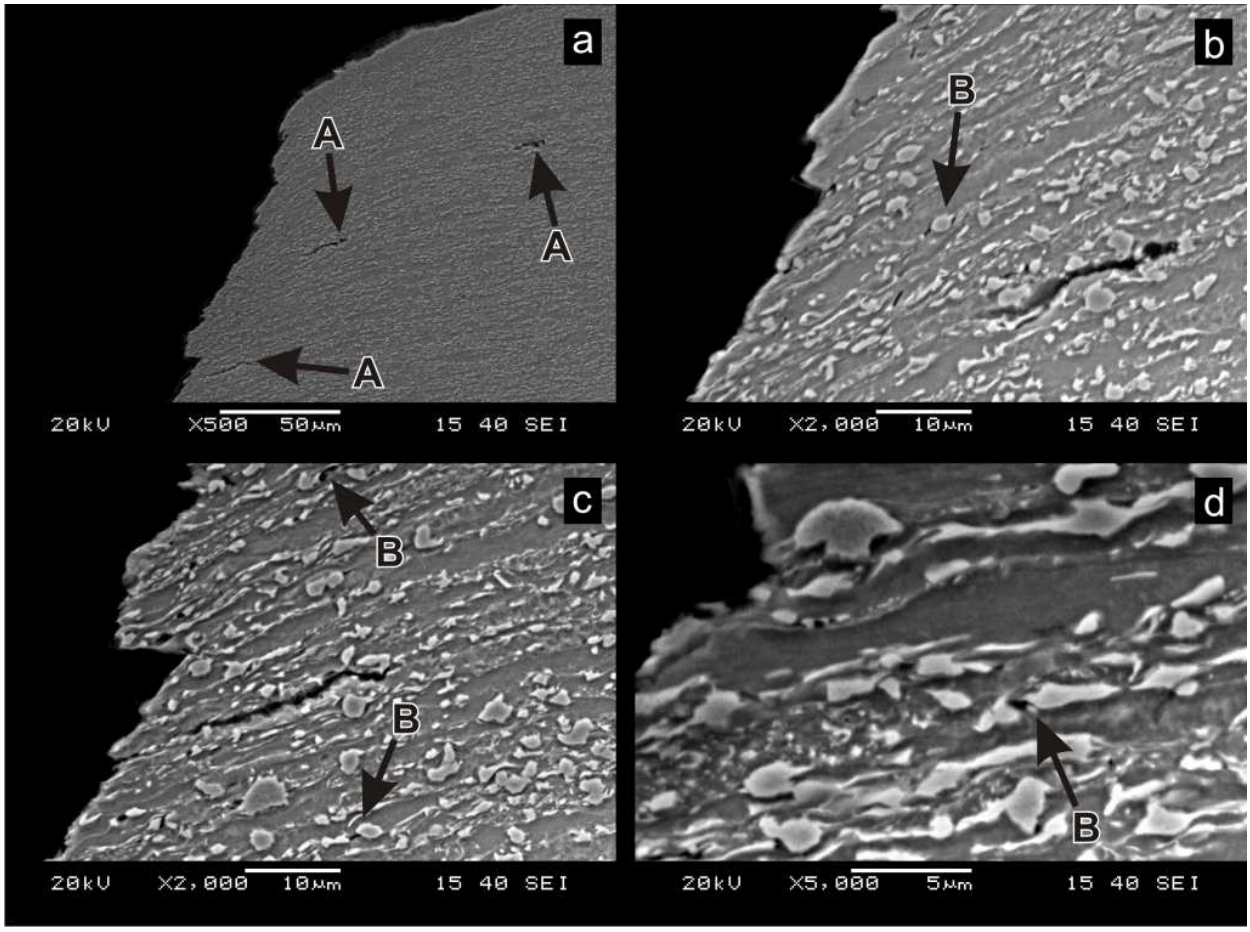

Figure 4.23: A longitudinal section at the fracture site of a welded specimen that had the BM failure location. Image a) shows large cracks that had initiated adjacent to fracture. Image b) and c) show locations where there was decohesion between ferrite-martensite interfaces. Image d) shows a martensite island that appeared to have fractured.

A similar fractographic analysis was conducted for the welded specimens that had produced 100% HAZ failure during uniaxial tensile loading. An image of a typical HAZ fracture longitudinal section is shown in Figure 4.24. The fracture surface showed double slant fracture. Numerous crack initiation sites and shear tears were found through the thickness of the sheet. These are shown on the image with a dashed white line. There was a noticeable reduction of thickness across the entire fracture surface compared to the BM fracture specimens. The center of the gauge width had the greatest amount of thickness reduction and in this region there was a complex arrangement of crack initiation sites and shear tearing. There was a significant reduction of thickness compared to the BM fracture specimens; however, after localized necking, specimens that fractured in the HAZ failure location had less localized necking across the length of the specimen, i.e., strain was concentrated through the sheet thickness. Decomposed martensite islands could have allowed for greater local deformation compared to the base-metal. Towards the edges of the gauge width, there were chevron patterns that suggested some crack growth at fracture had extended from the edges. It was found that shear planes existed at the sheet edges where crack initiation may have occurred. These cracks at the edges most likely did not occur until there was already significant crack growth from the central gauge width region.

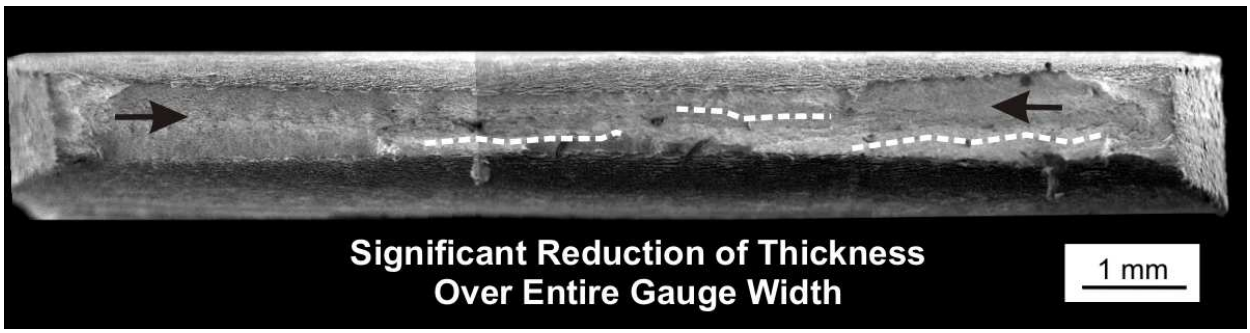

Figure 4.24: Top view of the fracture surface of a welded specimen that had a HAZ failure

The fracture surface was examined further at higher magnification and SEM images are shown in Figure 4.25. The surface had a dimpled rupture topography that suggested the cause of final fracture was micro-void coalescence. The central region of the gauge width is shown in Figure 4.25a. This area had

the greatest amount of thickness reduction after fracture. The surface appeared to be different than the BM fracture surfaces. There was a complex distribution of potential crack initiation sites and a greater proportion of shear tearing ledges than compared to BM fracture. On the image, large shear tearing faces are labelled 'A'. These fracture locations were most likely caused by cracks from separate planes that had overlapped during growth and then connected by shear tearing. These were similar to BM fracture except that they appeared to be more numerous. There were also smaller shear tearing locations that were more numerous than what had been observed on the BM fracture surfaces; these are labelled 'E' on the image. It was suspected that the increased reduction of thickness prior to fracture had caused a greater amount of crack initiation sites in this region. There was also less displacement in the loading direction compared to a BM fracture specimen and hence a shorter time span for cracks to propagate. These combined factors may have caused the relatively large population of small shear tearing ledges.

In Figure 4.25b and d, closer inspection of a shear tearing ledge are shown. In Figure 4.25b, crack formations were seen on the top and bottom of the ledge and are labelled 'B'. This resembled the same general mechanism as found in the BM fracture specimens. There was no definitive evidence from this formation that suggested that decomposed martensite had caused the failure. Large voids, like the one that is labelled 'C', were found across the entire surface of the gauge width. It was suspected that the void may have acted as either an initiation site or a termination site for the shear ledge that is labelled 'E'. The image was further magnified and is shown in Figure 4.25d. This was the upper ledge of the shear tearing formation where a crack initiation site was found. Its appearance resembled separation at a grain boundary [69]. The dashed arrows show the direction that the continuous shear lip had followed. The crack initiation site did not appear to have many voids along its central axis. This suggested that fast fracture occurred at this site. The appearance of fast fracture suggested that the duration of time between micro-void nucleation and crack formation was shortened when compared to instances where a string of voids were observed along the center of a set of shear lips. At the tip of this crack an aluminum-rich inclusion was found during EDS analysis and it is labelled 'C'. There did not appear to be a large void

associated with that inclusion; however, it may have been an important micro-void initiation site at that ledge.

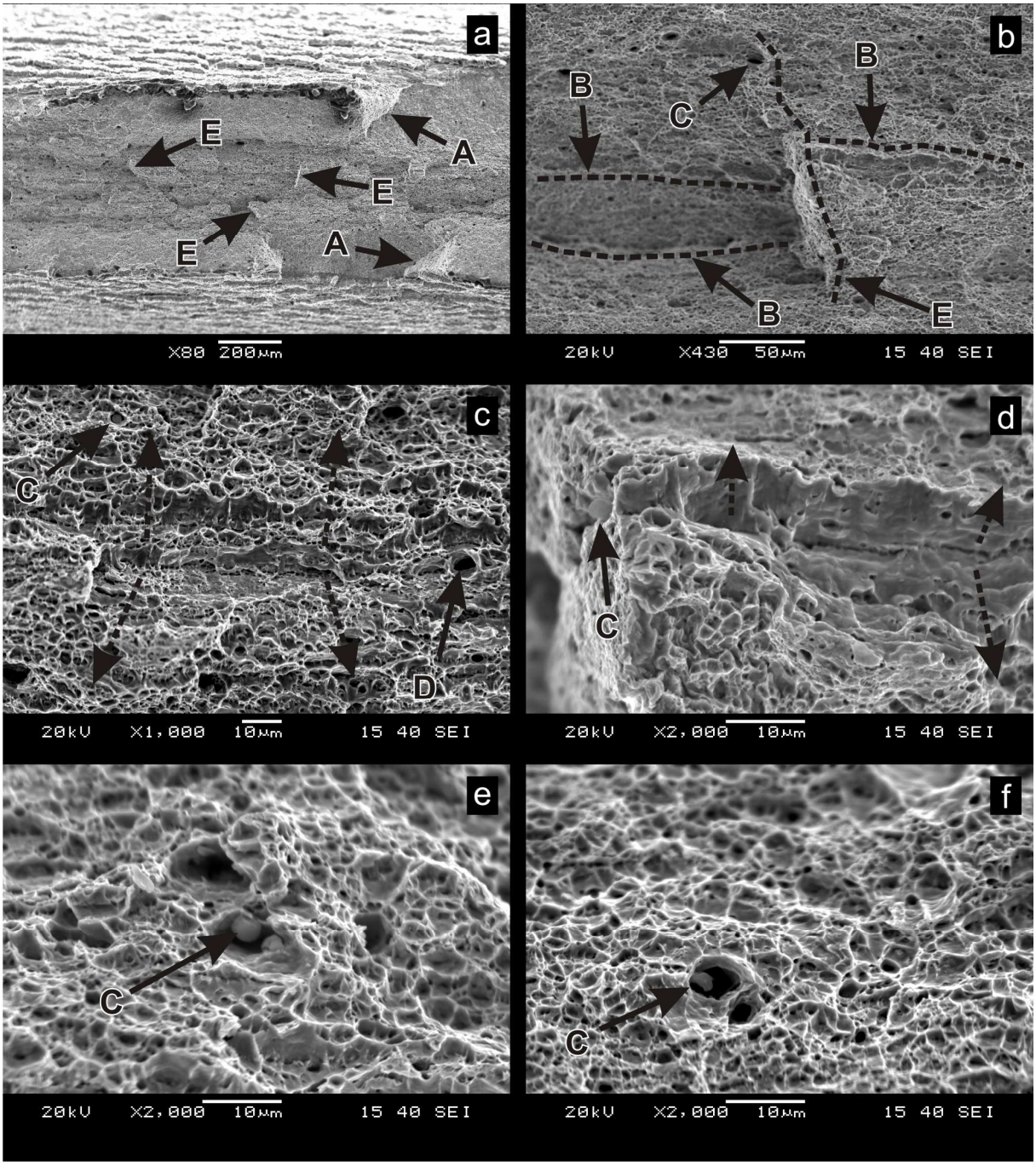

Figure 4.25: SEM analysis of a welded DP600 '16s' sheet steel specimen that fractured in the HAZ. Image a) shows numerous shear tearing sites and b) and d) are magnified images of a shear tearing ledge. Image c) shows a crack initiation site that consisted of a string of voids and shear lips. Images e) and f) show that large micro-voids were associated with incoherent particles (similar to BM fracture).

The image in Figure 4.25c shows a crack initiation site where there was a large void located at the tip of it. The large void is labelled 'D' and the direction of crack propagation is shown with dashed arrows. The large void may have acted as a nucleation site for the crack or alternatively it may have acted as a termination site. This formation appeared to be similar to crack formations found in the BM fracture surfaces.

In Figure 4.25c, e, and f, large void locations are shown that had aluminum-rich inclusions within them. These void locations appeared to have nucleated as a result of the inclusions [69]. It was suspected that all large voids were most likely directly related to inclusions within the sheet steel.

Generally, the micro-mechanisms for HAZ fracture appeared to be similar to the BM fracture specimens. There was no definitive evidence to show the dominant mechanism for micro-void nucleation. There was no evidence that definitively showed that decomposed martensite was causing early onset for crack initiation; however, the reduction of sheet thickness may have been as a result of the HAZ softened zone. The similarities were a dimpled rupture surface that suggested micro-void coalescence at fracture, large voids formed around aluminum-rich inclusions, and shear tearing between suspected crack propagation fronts appeared to form in a similar manner. The major differences of a HAZ fracture specimen compared to a BM fracture were found at the macroscopic scale, which included: a greater reduction of thickness across the gauge width and smaller, more numerous shear tearing formations.

To analyse the dominant mechanism for micro-void nucleation in a HAZ fracture, the fracture cross-section from Figure 4.20 was examined with the SEM. Magnified images of the surface longitudinal section are shown in Figure 4.26. In Figure 4.26a the longitudinal section revealed that there was a significant amount of damage immediately adjacent to the fracture surface. A large crack is labelled 'A', areas where there was substantial micro-void nucleation are labelled 'B', and a large void site is labelled 'D'. There appeared to be more micro-void nucleation sites in the HAZ fracture than in a

BM fracture and significant damage (large cracks) were more likely to form. The image in Figure 4.26b gives another example of a large crack formation (labelled 'A') and the image in Figure 4.26c shows an area that had an abundance of micro-void nucleation sites.

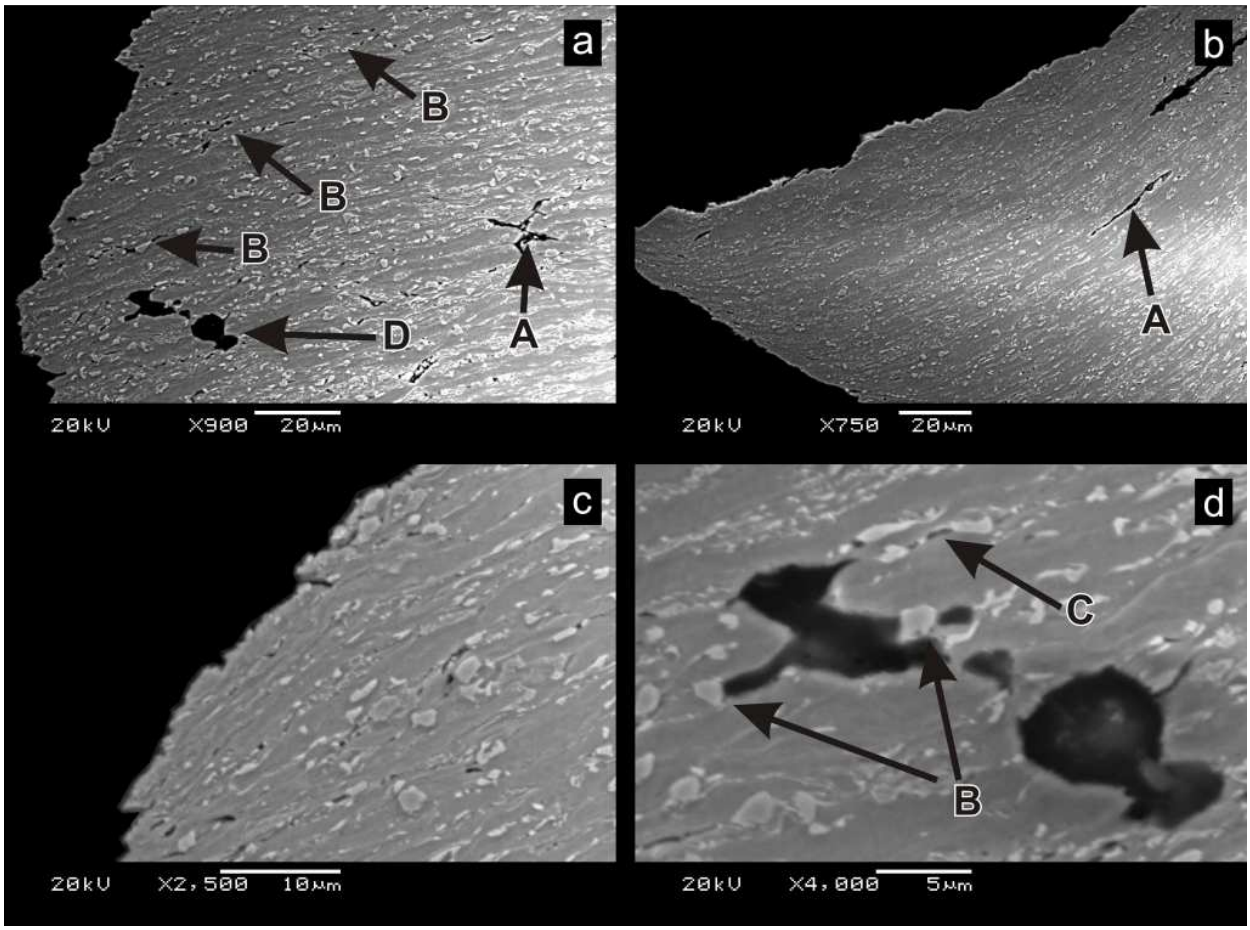

Figure 4.26: A longitudinal section at the fracture site of a welded specimen that had the HAZ failure location. Images a) and b) show an abundance of micro-cracks adjacent to the fracture. Image c) shows that martensite/carbide particles were aligned normal to the fracture surface. Image d) shows a large void formation and sites of decohesion at ferrite-martensite interfaces.

The large void site that is labelled 'D' is shown at higher magnification in Figure 4.26d. Two locations where there was decohesion between a hardened martensite island (or other carbide) and the ferrite matrix are labelled 'B'. These were sites that were directly linked to the large void; however, from this image it was not possible to determine if they caused the void to form. These islands appeared to

have disrupted the void from propagating further. There was also evidence that micro-void nucleation had occurred due to the micro-fracture of a hardened island, which is labelled 'C' on the image.

4.1.2.2: Partial Uniaxial Fracture Analysis

It had been suggested by Steinbrunner *et al.* [24] that erroneous conclusions could be derived by solely analysing the longitudinal section adjacent to the fracture surface. To determine the dominant mechanism for micro-void nucleation, partial tensile tests were conducted and then longitudinal sections were examined to locate sites where void or crack nucleation had occurred. For this test, the literature suggested that noticeable damage and micro-void nucleation was not expected until after the onset of necking [63,70]. The specimens were, therefore, plastically deformed past the onset of localized necking and allowed to displace until the level of stress began to rapidly decrease but was stopped before final fracture occurred. The full fracture data was used to judge the slope of the stress-displacement curve, specifically after necking; this provided an indication of the rate at which fracture would occur. From the stress-displacement curve for a BM fracture, it was known that the slope of the curve after necking changed gradually and that there was a significant duration of time before fracture. For the HAZ failure location, the duration of time after necking was much shorter and the change of slope was rapid.

It was difficult to directly compare the BM and HAZ failure locations because the degree of necking was only a qualitative estimate. Both specimens appeared to be rapidly approaching final fracture when the loading was stopped, but it was assumed that there was a difference between the specimens and one was most likely closer to fracture than the other. Another difficulty with direct comparison was that the cross-sections were not necessarily cut along the same plane, i.e., the same distance from the edge of the gauge width; this could affect the amount of visible nucleation sites.

The longitudinal section of a partial uniaxial fracture test that necked at a BM failure location is shown in Figure 4.27. The specimen had been machined from a weld made with the low heat input TB87 weld parameters. The specimen necked at a significant distance from the weld fusion zone and hence the

weld bead was not included with the cross-section. An image of a partially fractured specimen that began to neck in the HAZ failure location is shown in Figure 4.28. The specimen had been machined from a weld made with the high heat input TB88 weld parameters. Both of these specimens were observed with the SEM to locate micro-void nucleation sites and significant damage was only found in the necked area, relatively close to the location of greatest thickness reduction. It was found that although there was a greater reduction of area in the HAZ failure location, the span of localized necking was shorter in the HAZ when compared to the BM failure location.

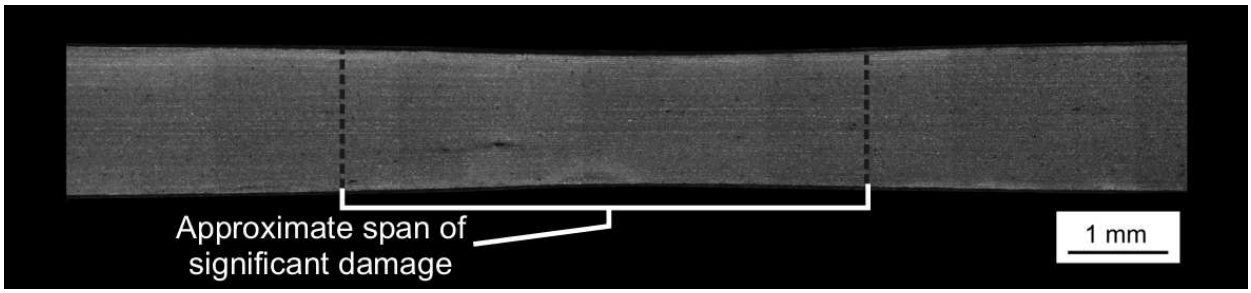

Figure 4.27: Longitudinal section from a partial fracture test of a TB87 welded sample that necked in the BM failure location.

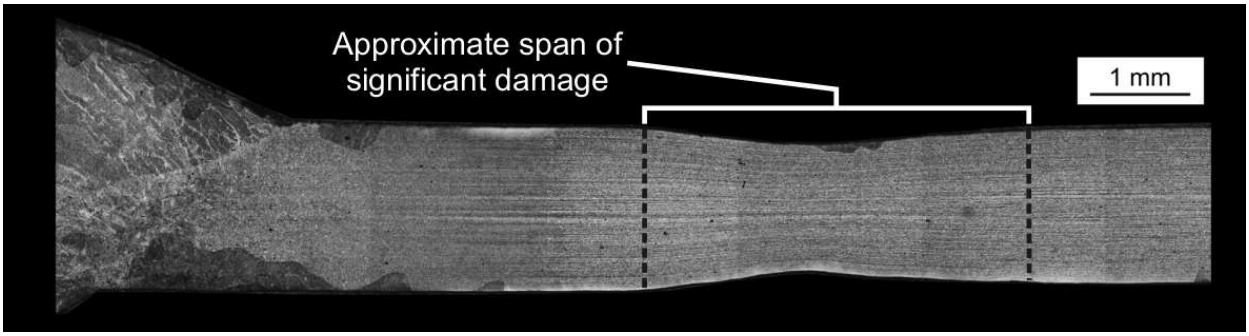

Figure 4.28: Longitudinal section from a partial fracture test of a TB88 welded sample that necked in the HAZ failure location.

The SEM images from the specimen that necked in the BM failure location are shown in Figure 4.29. Damage was found predominantly in the form of large cracks. There was very little evidence of decohesion between ferrite-martensite interfaces. Locations where EDS analysis determined that a

particle was an aluminum-rich inclusion are labelled ‘A’, particles that were found to be close to the nominal steel composition are labelled ‘B’, and sites where there was decohesion are labelled ‘C’.

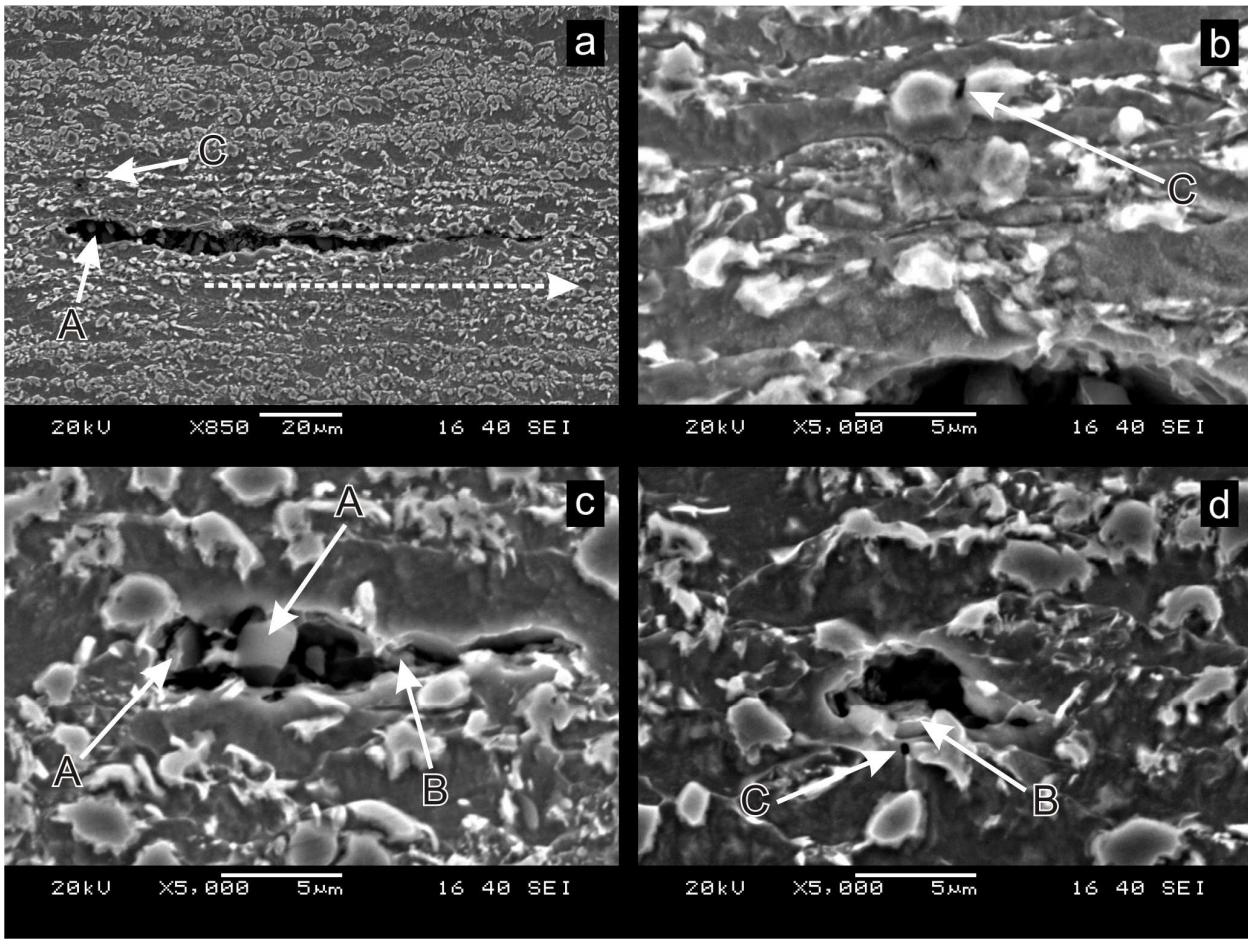

Figure 4.29: Damage found in the necked region of a welded specimen that had the BM failure location. Images a) and c) show large cracking that had formed as a result of incoherent particles. Image b) shows a site decohesion between two martensite islands. Image d) shows a micro-void that was adjacent to a larger dominant void site.

The image in Figure 4.29a shows a relatively large crack that had formed in the necked region. The crack was adjacent to the location of greatest thickness reduction and was approximately half-way between the center of the sheet and the sheet edge. The crack had propagated towards the location of greatest thickness reduction as indicated by the dashed arrow. The crack had formed in the direction of the uniaxial load and therefore propagated due to a difference in shear stress throughout the sheet thickness that was caused by the diffuse necking deformation (a tri-axial stress state had developed). The

predominant factor for nucleation appeared to be the presence of second phase particles, as indicated by 'A'. The small area adjacent to the crack site that is labelled 'C' had evidence of decohesion. This location is magnified in Figure 4.29b. This site appeared to be decohesion at a fractured particle, which was most likely martensite. The only evidence of decohesion was in areas that were relatively close to larger crack formations. This suggested that the local stress in regions that had large cracks was higher than the surrounding material.

A similar site that had significant damage is shown in Figure 4.29c. This was another site that had formed and propagated along the uniaxial tensile direction. Some second-phase particles were identified as aluminum-rich inclusions and are labelled 'A'. Some particles within the crack were analysed and found to be close to the nominal steel composition. One such particle is labelled 'B'. These were most likely martensite islands, but could also have been bainite or other carbides. The image in Figure 4.29d shows a crack that did not have an aluminum-rich inclusion present. It was suspected that this site most likely initiated due to a second-phase particle, like the aluminum-rich inclusions, but that evidence had been removed during grinding and polishing. The particle that is labelled 'B' was found to be close to the nominal steel composition and was most likely martensite. It appeared to disrupt the crack formation. Although the crack had been disrupted/pinned by the particle, there was evidence that the crack would expand around the particle and connect to the micro-void that was nucleating adjacent to it, which is labelled 'C'.

Micro-voids that had nucleated by decohesion between the ferrite/martensite interfaces and had been found close to the fracture surface in Figure 4.23 were not predominant during necking. If decohesion had been the dominant mechanism for nucleation of micro-voids/cracks then there should have been a larger distribution of decohesion nucleation sites. Significant damage that was found suggested that the dominant mechanism for micro-void nucleation and significant internal cracking was caused by second-phase particles, such as aluminum-rich inclusions.

The SEM was used to examine the partially fractured specimen that had a HAZ failure location and images are shown in Figure 4.30. Locations where EDS analysis determined that a particle was an aluminum-rich inclusion are labelled ‘A’, particles that were found to be close to the nominal steel composition are labelled ‘B’, sites where there was decohesion are labelled ‘C’, and decomposed martensite islands are labelled ‘D’.

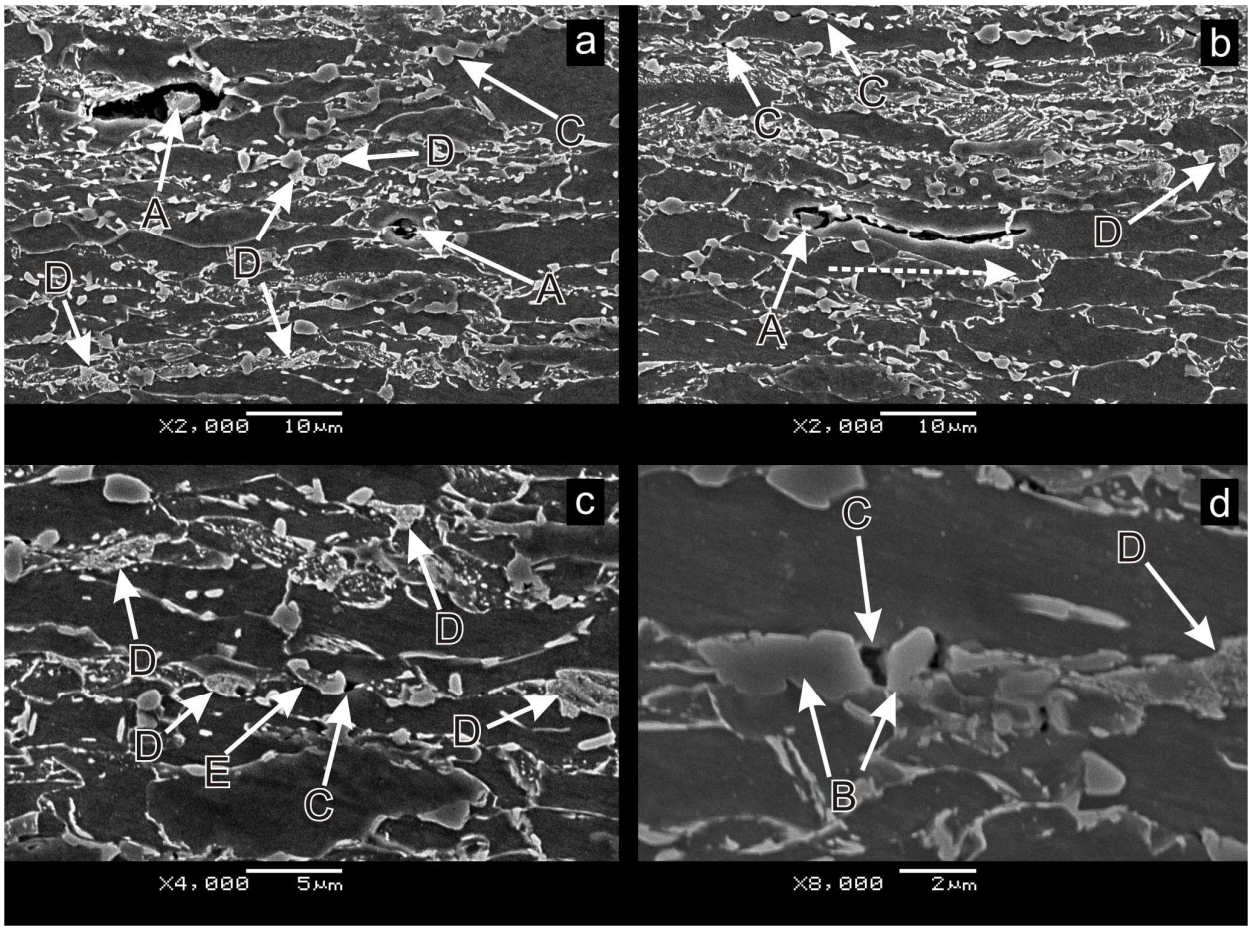

Figure 4.30: Damage found in the necked region of a welded specimen that had the HAZ failure location. Images a) and b) show that large cracking had formed as a result of incoherent particles. Image c) shows that there was evidence of decohesion between ferrite-martensite interface and that decohesion did not occur at sites of decomposed martensite. Image d) shows what appeared to be a fractured martensite island.

In Figure 4.30a the image shows two locations where micro-voids had nucleated and grown around an inclusion. These two sites are labelled ‘A’. There were no sites that had attained the size of

these voids on the cross-section that were not associated with an inclusion. An example of this was a micro-void that had nucleated by decohesion and is labelled ‘C’ on the image. This nucleation site was several orders of magnitude smaller than the voids that formed around the inclusions. In the image, several decomposed martensite islands are labelled ‘D’. Decohesion did not appear to form at any of those sites. This suggested that decohesion only occurred between solid particles and the ferrite matrix; it was suspected that the decomposed martensite islands, which had broken down to spheroidal carbides, were free to move and hence did not resist the flow of stress in the ferrite matrix. Spheroidal carbides were most likely firmly bonded with the ferrite matrix and would require excessive plastic strain to nucleate a micro-void by decohesion [70].

In Figure 4.30b, a large crack is shown that had nucleated at an aluminum-rich particle, labelled ‘A’, and had propagated in the direction of the axial load, as indicated by the dashed arrow. This was very similar to BM fracture and further suggested that the most significant damage was caused by second phase particles, which were mainly aluminum-rich inclusions. The HAZ failure location differed from the BM failure location by the presence of decomposed martensite, but also by a noticeable increase in the amount of micro-void nucleation due to decohesion between the ferrite matrix and hardened particles. Two sites that had evidence of micro-void nucleation due to decohesion are labelled ‘C’ and more evidence of decomposed martensite that was found is labelled ‘D’.

The increased population of micro-voids may have meant that the HAZ partial fracture specimen had an increased degree of necking compared to the BM partial fracture specimen and was closer to final fracture. This did not explain why the largest cracks in the HAZ sample were relatively similar to the BM sample. It was assumed that because both samples had similar large cracking, the increased population of micro-voids due to decohesion was a trait of the HAZ failure location and not just caused by an increased degree of necking. This trait for a larger population of micro-voids was also seen on the fully fractured sample from Figure 4.26.

A micro-void that had nucleated at an interface between a solid particle and the ferrite matrix is shown in Figure 4.30c. The particle appeared to be a martensite island that had partially decomposed at its center, which is labelled 'E'. This suggested that the martensite island (and others like it) may have had significant alloy micro-segregation. The region that is shown had a large distribution of decomposed martensite islands that are labelled 'D'. It is suspected that the decomposed martensite islands allowed for a greater amount of material flow in a direction that was normal to the axial load direction. This appeared to be the main difference between the HAZ failure location and the BM failure location. The increased flow due to decomposed martensite islands caused a significant tri-axial stress state to evolve during necking and increase the amount of material that attained a critical strain that could nucleate micro-voids [70].

A site that had micro-void nucleation that was not associated with an inclusion is shown in Figure 4.30d and is labelled 'C'. The void appeared to have nucleated due to a fractured martensite island. The EDS analysis of the island found that both locations labelled 'B' were close to the nominal steel composition. This suggested that it was a hardened particle and not an inclusion. The image also shows a magnified image of a decomposed martensite island that is labelled 'D'.

The dominant mechanism for micro-void nucleation was at large second-phase particles. This result was similar to the BM failure location and large cracks were found at incoherent aluminum-rich inclusions; however, there was also a larger population of micro-voids that had nucleated due to decohesion of ferrite-martensite interfaces.

The HAZ failure location appeared to have more nucleation sites that were related to decohesion than the BM failure location. These sites were not the dominant mechanism for micro-void nucleation; however, the larger population of micro-voids could explain the increased number of shear tearing ledges that had been found in Figure 4.25a. A greater population of micro-voids was suspected to have led to a more numerous distribution of cracks that propagated and met during a later stage of necking immediately

prior to final fracture. An increased distribution of cracks would have decreased the length of propagation before a propagating crack overlapped and connected with other cracks by shear tearing. Decomposed martensite islands did not appear to have direct decohesion with the ferrite matrix; decohesion only appeared to occur at large solid particles. Decomposed martensite islands were free to move with the deforming material and most likely increased material flow in this region; this would have caused a tri-axial stress state and localized necking to occur in the HAZ.

4.1.2.3: Percent Area of Martensite Measurements

A study to quantify the depletion of martensite in the suspected softened zone of the HAZ was conducted on the low heat input (TB87) and the high heat input (TB88) welds. This study determined the amount of martensite at different locations across the HAZ of the weld that had failed in the HAZ and compared the results with the weld that had fractured in the BM. It was suspected that the high heat input weld would have a greater decrease in martensite and that tempering/decomposition would be found further away from the Ac_1 line when compared to the low heat input weld. The weld HAZ profiles were also compared to the nominal base-metal value for percent area of martensite. This allowed an approximate measurement of the distance from the Ac_1 line to where martensite decomposition first emerged in the HAZ.

Decomposed Martensite in the Weld Subcritical Region

Prior to making the percent area of martensite profiles, both welds were examined using the SEM to confirm that there was decomposed martensite in the subcritical region adjacent to the Ac_1 Line. An image that was taken from the SC region of the low heat input weld (TB87) is shown in Figure 4.31. Decomposed martensite was found in the microstructure of this weld. An island of decomposed martensite is labelled on the image with an ‘A’. There were also islands that had not decomposed in that area. Examples of these carbide islands are labelled on the image with a ‘B’; the nature of these carbides were unknown.

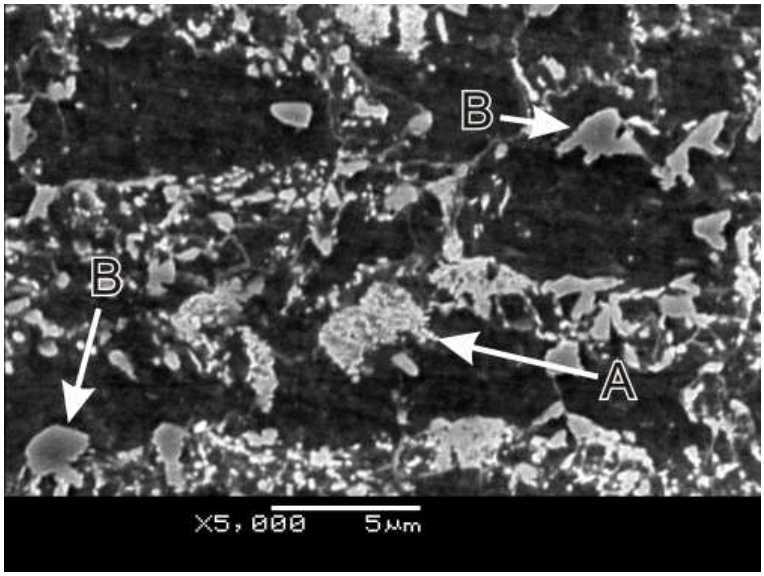

Figure 4.31: The lowest heat input weld (TB87) had evidence of decomposed martensite located in the subcritical region.

The SC region of the high heat input weld (TB88) is shown in Figure 4.32. Decomposed martensite was also found in the microstructure of this weld. In the image, decomposed martensite is labelled with an 'A'. A similar observation compared to the low heat input weld was that there were islands that had not decomposed. Examples of these carbide islands are labelled on the image with a 'B'.

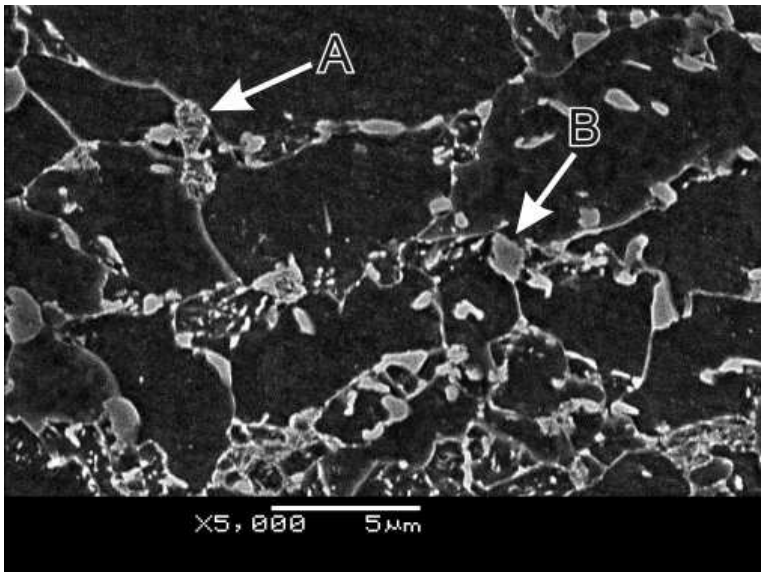

Figure 4.32: The highest heat input weld (TB88) had evidence of decomposed martensite located in the suspect softened zone.

The confirmation of decomposed martensite in the weld that had consistently fractured in the BM failure location during uniaxial tensile testing was significant because this meant that decomposed martensite could be present in a weld HAZ and yet maintain BM fracture. Islands that had not decomposed may have been low carbon martensite or could have been bainite, cementite, and/or austenite; these would have been less susceptible to decomposition.

Base-metal Martensite Measurements

Prior to conducting the HAZ profiles, the percent area of martensite in the DP600 '16s' base-metal was measured. The result of the test is shown in Figure 4.33. The figure shows the BM cross-section at the location where the profile was made. The specimen was etched with the Lepera's tint [7] and the 16 locations through the thickness of the sheet that were measured for percent area of martensite are indicated with black circular markers. The profile result suggested that the sheet steel was inhomogeneous. Areas near the edge of the sheet appeared to have a decrease in the percent area of martensite and the lower half of the sheet appeared to have lower martensite content than the upper half. This suggested that there was macro-segregation of alloying elements throughout the sheet thickness or that there had been cooling rate differences throughout the sheet during quenching/cooling. At the center of the sheet, a band of hardened martensite was found that was continuous across the entire central axis of the sheet. This band caused the spike that was in the profile. The central band was not included in the average percent area of martensite calculation. The average percent area of martensite for the base-metal was $7.8 \pm 1.4\%$.

In the region immediately adjacent to the central band there was an area that appeared to be depleted of martensite. This suggested that the area was depleted of alloying elements that promote steel hardenability, such as C, Mn, Cr, Si, and Mo, which were all present in the nominal steel composition [33]. This suggested that there was significant macro-segregation at the center of the sheet. The central martensite band likely formed due to the continuous casting process [48]. Macro-segregation of the solute elements normally occurs during solidification of the continuous cast ingot. This solute is

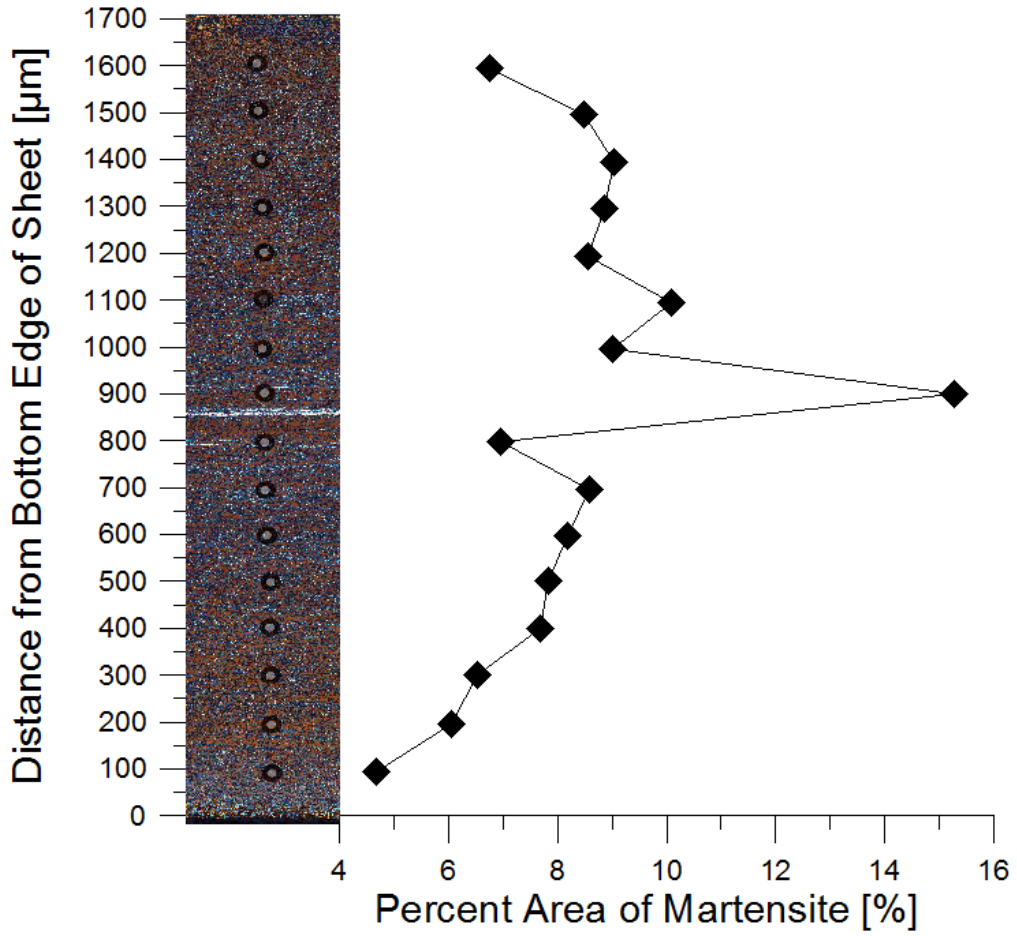

Figure 4.33: The DP600 '16s' base-metal percent area of martensite profile. The spike at the center of the profile contained was caused by the central band of martensite and was not included in the average calculation for the BM percent area of martensite.

pushed into the liquid ahead of the solidifying solid and creates a build up of alloying elements that solidify when the columnar fronts meet at the center to form the band of solute-rich material [6,48]. The band macro-segregation is retained during hot rolling. This solute-rich band in the centre of the rolled sheet is fully austenitized during intercritical annealing and most likely has higher hardenability than other regions due to the increase in alloying elements [33]. The depleted region adjacent to the spike was suspected to be caused by a build up of equiaxed grains that had formed during continuous casting by dendrite tips breaking off during solidification and by nucleation off of unmelted particles in the molten zone. These grains would have settled on top of the advancing columnar front and so in the region below the central band there would have been a build up of alloy depleted grains [48]. There was also potential

for pockets of insoluble rejected solute elements to get trapped between the dendrite arms. This likely caused the macro-segregation through the sheet thickness that was suggested by the percent area of martensite profile.

Some of the images that were used for measurement are shown in Figure 4.34. The Lepera's tint [7] had caused martensite islands to appear white, bainite/carbides to appear blackish-blue, and the ferrite matrix to appear brown. The image in Figure 4.34a was located approximately 200 µm from the bottom edge. It appeared to have a significant amount of bainite/carbides, which were measured to occupy a percent area of 16.1%. The carbide pockets had not formed to martensite and hence the percent area of martensite had been low, at 6.1%. The area between the dashed white lines appeared to be lower in percent martensite than the adjacent regions. Regions like this were found across the sheet and tended to extend for a significant distance. The large central band of martensite is shown in Figure 4.34b. This area was measured to have 15.3% martensite. Other banding, indicated by the arrow, was known to be caused by macro-segregation that produced Mn-rich regions of microstructure that became elongated during hot-rolling [6]. The image in Figure 4.34c was located approximately 200 µm away from the top edge. It was measured to have a percent area of martensite of 8.5%. This region appeared to have a relatively uniform distribution of martensite islands and had less bainite/carbide formation (10.3%) than the image in Figure 4.34a.

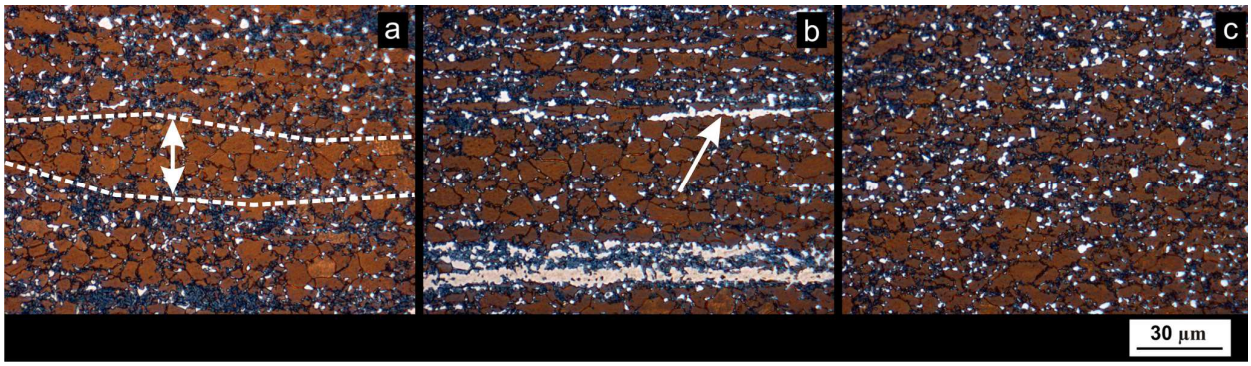

Figure 4.34: Examples of the DP600 '16s' BM images that were used to measure the percent area of martensite. Images a) and c) were taken at opposite edges of the sheet steel thickness and image b) was taken at the center of the sheet where there was a large band of martensite.

Area Fraction of Martensite in Welded Specimens

The percent area of martensite in the low heat input and high heat input welds were measured at stepwise locations through their respective HAZ's. The results for the low heat input weld (TB87) that had fractured in the BM is shown in Figure 4.35. The longitudinal section that was used for this study was the same one used for the extended microhardness profile from Figure 4.12. The locations where the percent area of martensite was measured are indicated on the cross-section image with black circular markers. The profile was approximately 580 µm away from the sheet edge.

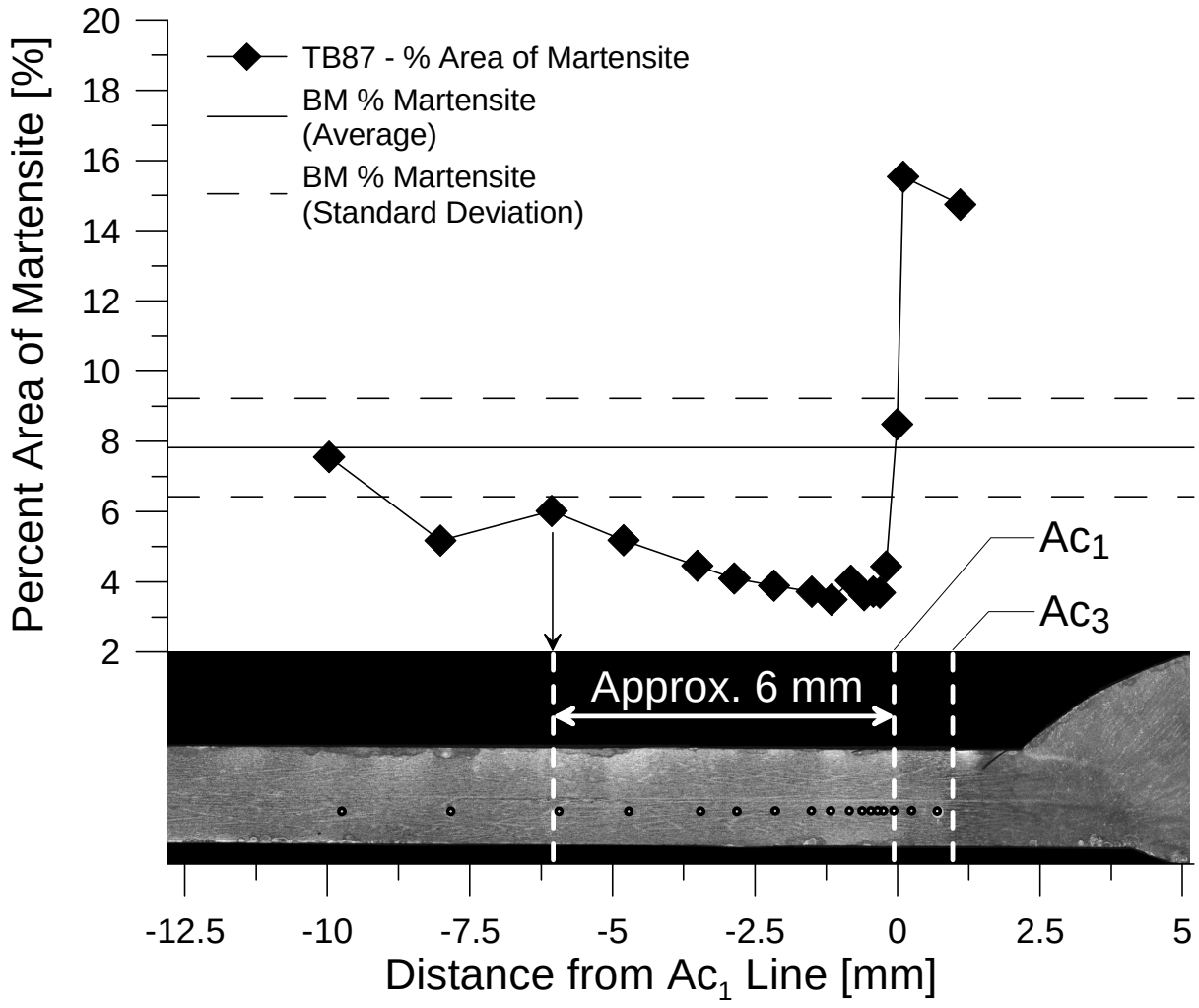

Figure 4.35: The percent area of martensite profile for the low heat input weld (TB87) that had 100% BM fracture during testing.

The percent area of martensite curve shown in Figure 4.35 suggests that decomposition/tempering of martensite occurred at a distance of approximately 6 mm from the Ac_1 line. This location was selected because it was the point along the curve where the BM nominal value was first attained. The curve was generally well below the BM nominal value, which suggested that the axis along which the profile had been made may have coincided with a band that had a lower percent area of martensite than adjacent regions. The percent area of martensite spiked above the BM nominal value at locations that were above the Ac_1 line and within the IC region; this was due to the presence of renucleated martensite.

Example images that were used for the percent area of martensite measurements are shown in Figure 4.36. The sample was etched with the Lepera's tint [7] and martensite islands appeared white, bainite/carbides appeared black, and ferrite appeared as tan; decomposed martensite islands, which were broken down into ferrite and spheroidal carbides, appeared brown and black. An image that represented the base-metal is shown in Figure 4.36a. This image was measured and found to have a percent area of martensite of 7.6%. The image in Figure 4.36b was taken immediately adjacent to the Ac_1 line in the SC region. The majority of carbides found in this area appeared to be retained from the original BM microstructure; decomposed martensite islands are indicated by the arrows. This image was measured and found to have a percent area of martensite of 4.4%. The image in Figure 4.36c was taken within the intercritical zone. There was a visible increase in the size of the renucleated martensite islands. The image was measured and found to have a percent area of martensite of 15.5%.

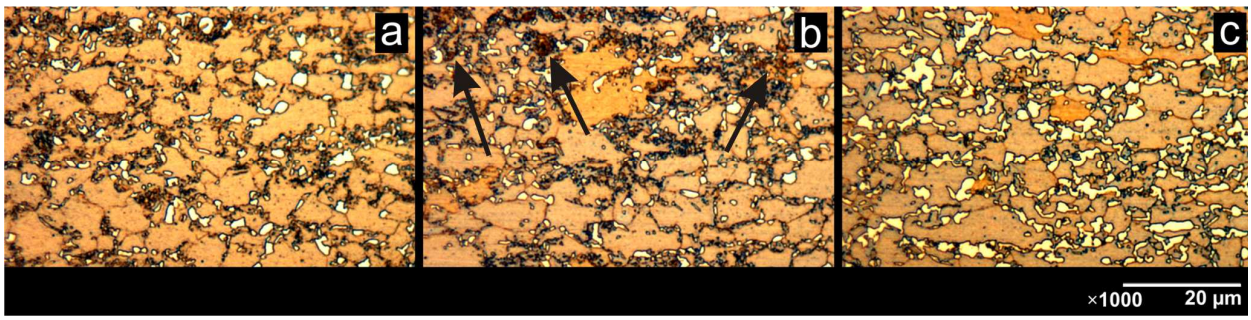

Figure 4.36: Locations that were used for the percent area of martensite profile of the low heat input weld (TB87) that had fractured in the BM failure location 100% during testing. Image a) was from the BM, image b) was from the SC region, and image c) was from the IC zone.

A similar study was performed with the high heat input weld (TB88) that had fractured in the HAZ failure location during uniaxial tensile testing. The resulting profile for percent area of martensite is shown in Figure 4.37. The cross-section is included in the figure and the locations used to take percent area of martensite measurements are indicated with black circular markers. This was the same cross-section used to make the extended microhardness profile from Figure 4.13. The profile was made approximately 480 µm away from the sheet edge.

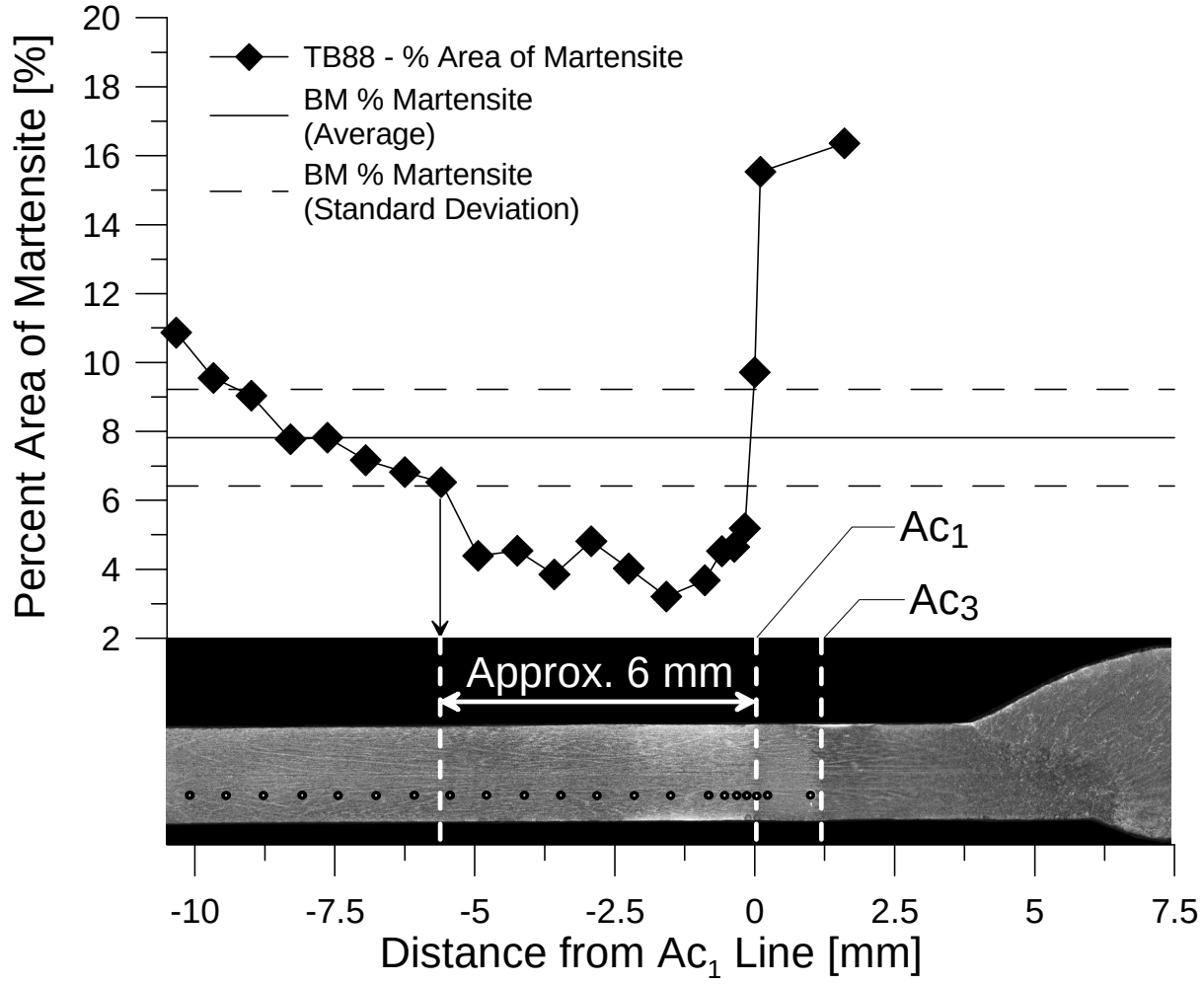

Figure 4.37: The percent area of martensite profile for the high heat input weld (TB88) that had 100% HAZ fracture during testing.

The profile suggested that decomposition/tempering existed at approximately 6 mm away from the Ac_1 line. This was the same distance that had been found for the low heat input weld; however, this

profile was more easily definable. The profile had a very drastic transition from depleted martensite into a region that resembled the BM nominal percent area of martensite. The profile appeared to show that significant decomposition/tempering had occurred further into the BM, i.e., the drastic transition was the point that was selected and measured to be 6 mm. The prior base-metal along the axis that was used to measure the high heat input weld profile most likely had a higher percent area of martensite than the prior base-metal for the low heat input weld profile. This further suggested that macro-segregation was present throughout the sheet steel thickness.

Example images that were used to measure percent area of martensite are shown in Figure 4.38. The sample was etched with the Lepera's tint [7] and martensite islands appeared white, bainite/carbides appeared black, and ferrite appeared as tan; decomposed martensite islands, which were broken down into ferrite and spheroidal carbides, appeared brown and black. The image in Figure 4.38a was found in the base-metal. It had a noticeably higher percentage of martensite than the base-metal locations from the low heat input weld sample. This image was measured and found to have a percent area of martensite of 10.9%. The image in Figure 4.38b was from the SC region immediately adjacent to the Ac_1 line. There were a significant portion of decomposed martensite islands and some have been indicated by the arrows on the image; however, there were also martensite islands that had not decomposed. This image was measured and found to have a percent area of martensite of 4.5%. The image in Figure 4.38c was taken

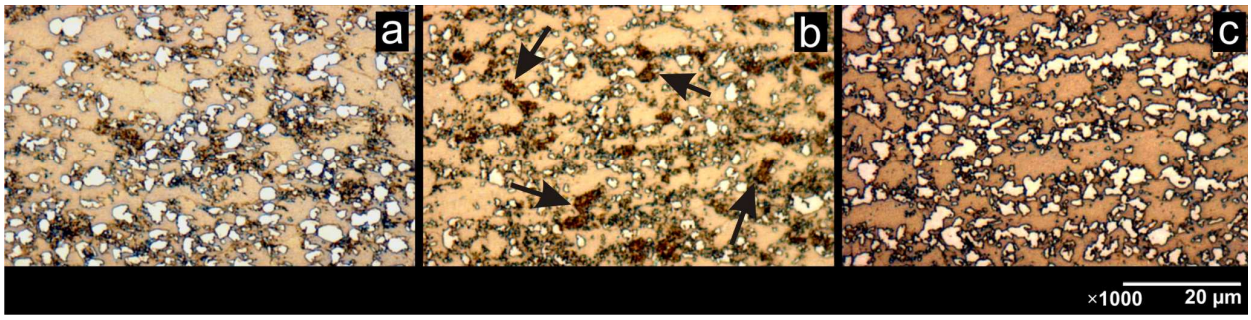

Figure 4.38: Locations where images were taken to measure percent area of martensite for the high heat input weld (TB88). Image a) was from the BM, image b) was from the SC region, and image c) was from the IC zone.

within the intercritical region. The martensite islands were noticeably larger. The area was measured to have a martensite percentage of 15.5%.

Generally, the profiles suggested that there was depletion of martensite in both the low heat input weld HAZ and the high heat input weld HAZ. It was suspected that HAZ failure in welded DP sheet steel was caused by increased material flow in the SC region when compared to the BM; this was due to the presence of decomposed martensite islands. Increased material flow likely caused localized necking to occur in the SC region. The SC region of the low heat input (TB87) weld HAZ had decomposed martensite, but this weld did not fracture in the HAZ. During uniaxial transverse weld tensile testing, the low heat input (TB87) weld was instead fracturing in the BM, which was a region that had a higher percent area of martensite.

The expectation that there was significant decomposition of martensite in the 100% HAZ failure weld was confirmed. The comparison with the 100% BM failure weld suggested that there was no major difference in martensite decomposition in the HAZ; however, the high heat input (TB88) weld had a more distinct difference between the martensite fractions from the BM and SC regions.

The base-metal microstructure was inhomogeneous through the thickness of the sheet; this is believed to cause the difference between the two welds. This was because the prior base-metal along the axis of the HAZ profile was only loosely based on the average BM value; i.e., if the profile axis used for measurement landed on a banded region. To properly define the weld HAZ for an inhomogeous base-metal like the DP600 ‘16s’ sheet steel, a percent area of martensite study that covered the entire thickness could have been made. However, mapping of the area fraction of martensite in the HAZ was not performed. Instead, microhardness mapping was used to cover the entire thickness of the sheet and minimize the difficulties of comparison that the inhomogeneous structure had on the results.

4.1.2.4: Microhardness Mapping of the DP600 ‘16s’ Sheet Steel

The same weld cross-sections that were used for the martensite profiles were taken to ArcelorMittal Dofasco, Inc. [48] and were mapped for Vickers microhardness throughout the weld HAZ and through the entire thickness of the sheet steel. This portion of the study was meant to clarify the findings from the microhardness profiles, provide definitive evidence of softening in the weld HAZ suspect softened zone of both welds, and provide a better measurement for the relative size of the softened zone in the 100% BM failure weld and the 100% HAZ failure weld.

Base-metal Mircohardness Mapping

Prior to evaluating the weld microhardness maps, a Vickers microhardness map was used to characterize the DP600 ‘16s’ base-metal hardness. The colour contour map of microhardness was generated from a regular grid of hardness measurements consisting of 32 × 15 hardness measurements. The results of the hardness mapping plot are shown in Figure 4.39. From the map it was immediately clear that the hardness varied significantly throughout the sheet thickness. There was lower hardness (~195 VHN) surrounding the central band of hard martensite and the edges of the sheet appeared to have different average hardness (bottom edge ~214 VHN / top edge ~207 VHN). This result confirmed that the hardness varied through the sheet thickness. This data agreed with the results from the percent area of martensite profile from Figure 4.33.

The sheet steel hardness appeared to vary significantly. For a single column of indents, one standard deviation of the average through-thickness hardness (ATTH) was 8.5 VHN. This suggested that the previous calculation for average hardness, which was based on a 3 × 3 indentation grid, was not sufficient for this steel. The ATTH for the DP600 ‘16s’ sheet steel was calculated and was found to be 201 ± 1.5 VHN. This calculation was the average value for all of the indentation columns that were used to create the hardness map. The sheet thickness was measured using the optical microscope and was

found to be approximately 1.68 mm thick. This was slightly different than the nominal value of 1.65 mm thick.

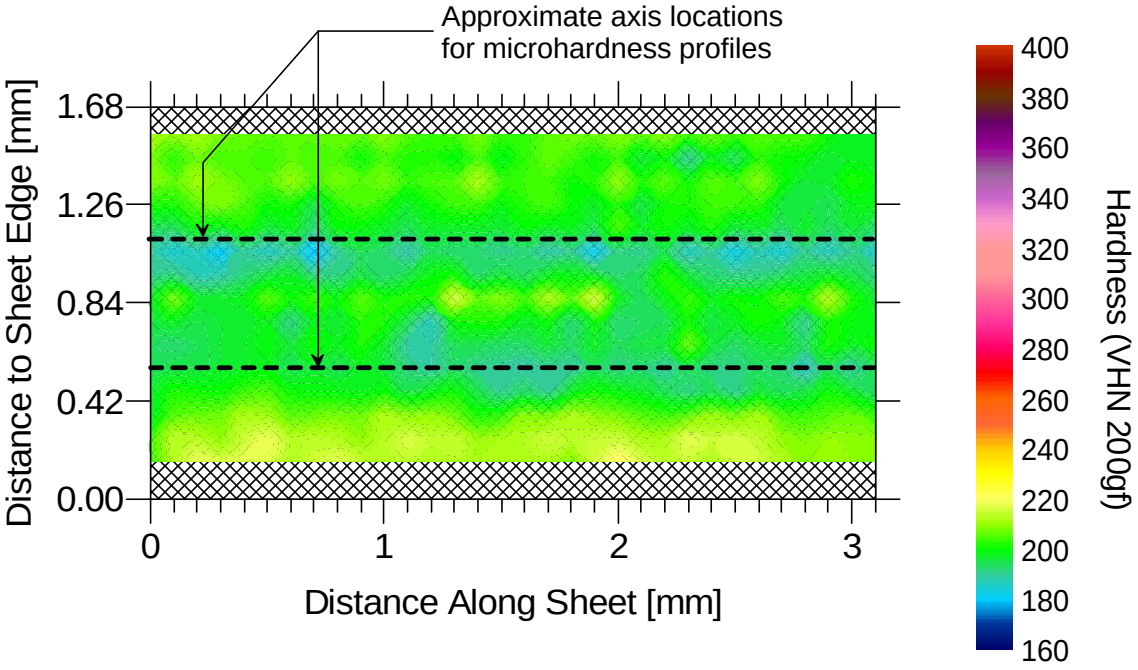

Figure 4.39: A Vickers microhardness map for the DP600 '16s' base-metal.

The map provided an image of the hardness through the entire sheet thickness. This also provided a series of microhardness indentation profiles that could be compared with the DP600 '16s' microhardness line profiles shown in Figure 4.10 – Figure 4.13. The profiles had been made at an approximate distance of 560 µm from the sheet edge and are indicated on the map with dashed lines. This meant that the profiles were made along axes that were relatively non-uniform. The axes appeared to border on an area of the sheet that was significantly lower in hardness but could potentially fluctuate to higher hardness values. This helped to explain the discrepancies from the previous HAZ microhardness profiles.

The image in Figure 4.40 shows how the microhardness mapping indentation grid was aligned on the unwelded BM cross-section. The grid was parallel to the sheet edges and was symmetrical between

the two sheet edges. The image was measured with the optical microscope software and it was found that the distance from the edge of the sheet to the first line of indents was very similar at both edges; distances of approximately 160 µm and 154 µm were measured. This difference was minimal and suggested that the grid had a desired alignment. From examining the microstructure, it was found that the central line of indentations had been made along the central band of hardened martensite. This is labelled 'A' on the image. This confirmed that the central martensite band was present in the hardness mapping data. The average hardness along the line of indents that had been located at the central band of martensite was 206 ± 6.5 VHN. The central band of hardened martensite was included in the ATTH calculation. If this line of indents was removed from the calculation, the ATTH became 201 ± 1.2 VHN; this difference was negligible.

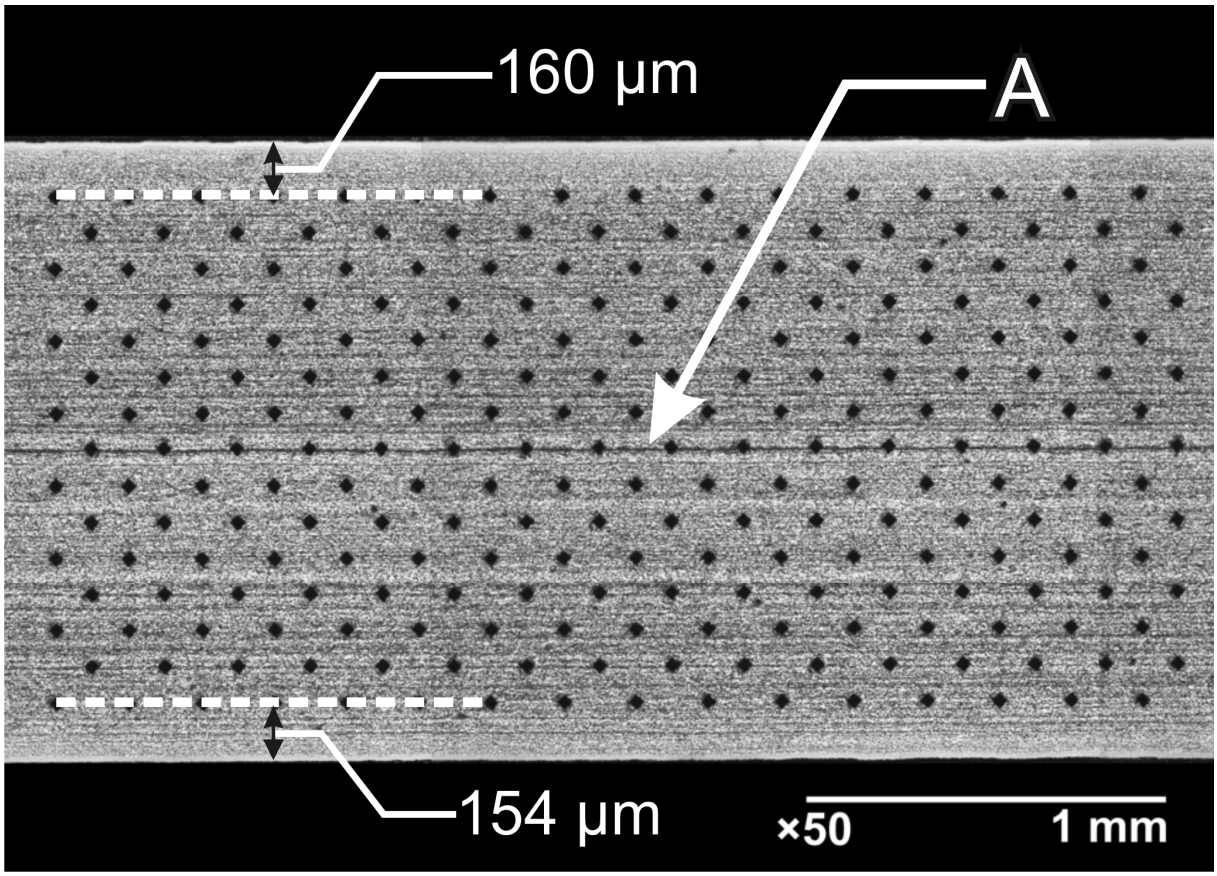

Figure 4.40: The unwelded BM cross-section for the DP600 '16s' sheet steel that shows the alignment of the indentation grid used for microhardness mapping.

The hardness of the DP600 '16s' sheet steel was slightly asymmetrical. The bottom edge of the steel, which lay between 0.00-0.42 mm on the map, had higher average hardness (~214 VHN) than the opposite edge of the sheet (~207 VHN). This was the edge of the steel where the first indentation line was at a distance of 154 µm as shown in Figure 4.40. If the grid of indentations had been aligned closer to the bottom edge it could have caused more significant asymmetry. This meant that it was important to have good grid alignment that was centered between both sheet edges.

Weld HAZ Microhardness Mapping

The low heat input weld (TB87) and the high heat input weld (TB88) were mapped using a similar grid pattern to the one that was used for the 1.65 mm DP600 '16s' BM specimen. The only differences between the indentation grids were a greater surface area that was covered and there were alignment differences that were inherent with the equipment.

The result for the low heat input weld (TB87) that had provided 100% BM failure during uniaxial tensile testing is shown in Figure 4.41. The weld cross-section is shown in Figure 4.41a. This was the same cross-section that had been used for the extended microhardness profile and the percent area of martensite profile. The indentation grid covered from just above the Ac_3 line to the BM. The grid orientation was relatively parallel to the sheet edges.

The hardness map is shown in Figure 4.41b. There was significant evidence that a softened zone did exist in the weld HAZ from the map. It was located in the subcritical region in the location where decomposed martensite had been found, immediately adjacent to the Ac_1 line. The softened zone was measured from the map to be approximately 2 mm in width. The measurement was taken from the Ac_1 line to the location where uniform softening appeared to begin. The measurement was contrary to the percent area of martensite profiles, which had appeared to show that tempered/decomposed martensite had existed further away from the Ac_1 line. The area adjacent to the softened zone appeared to have hardened in the subcritical zone; the area is labelled 'A' on the map. This suggested that some areas that

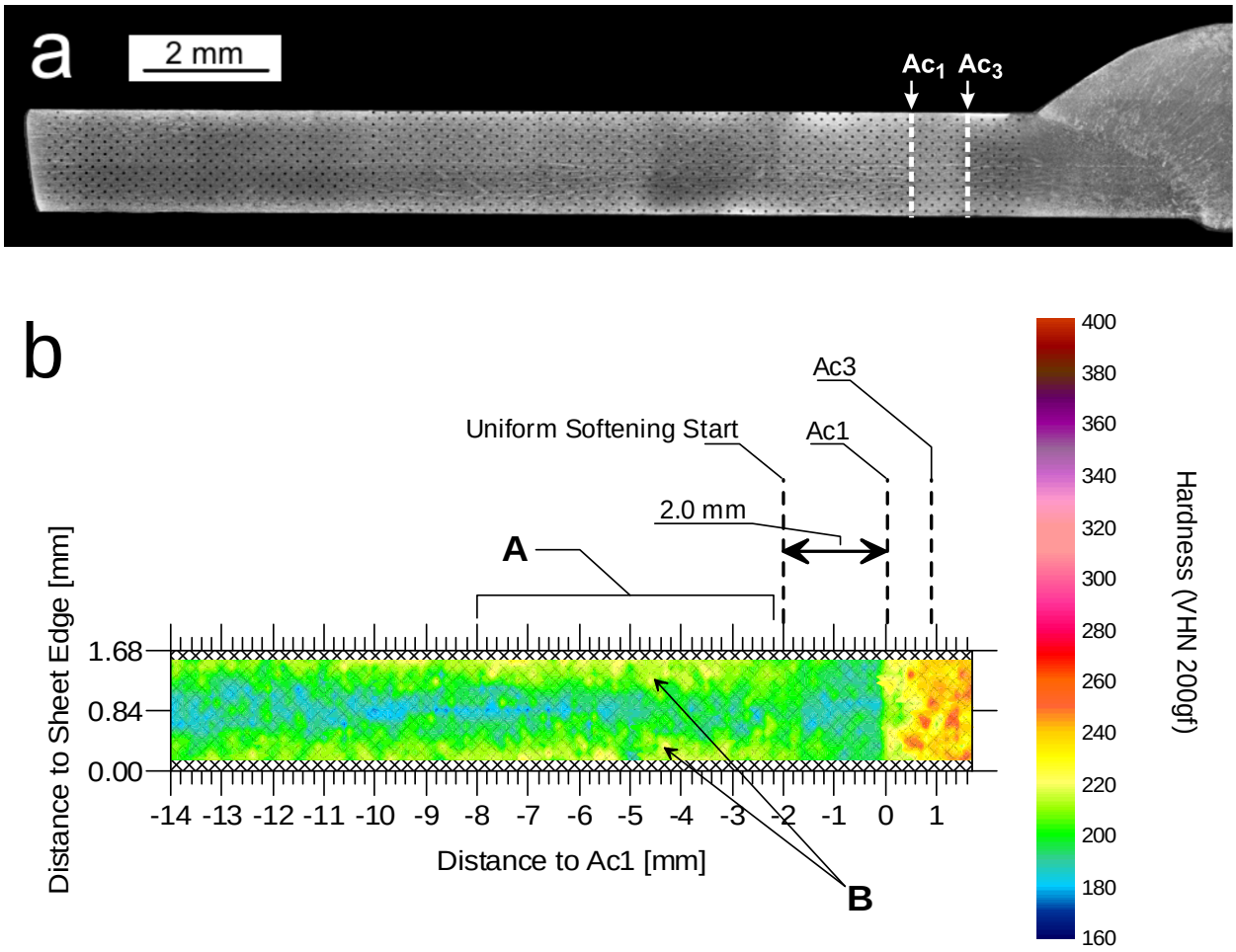

Figure 4.41: The microhardness map for the lowest heat input (TB87) DP600 '16s' weld HAZ. The image in a) shows the grid of indentations on the TB87 weld cross-section and b) shows the mapped microhardness.

had tempered martensite may have increased in hardness. The suspect hardening in the subcritical region appeared to occur at both edges, which is indicated with a 'B' on the map image. This did not match the map from the unwelded BM sample, which was slightly asymmetrical and one edge had appeared to have a higher hardness.

There was significant hardening in the intercritical and supercritical regions. This result agreed with the microhardness line profiles from Figure 4.10 – Figure 4.13. It also agreed with microstructural interpretation, showing that the significant increase in the percent area of martensite in the IC zone had caused the region to increase in hardness.

Generally, the map appeared to show the emergence of BM hardness properties past the area of suspect hardening; however, it did not include a hardened band down the central axis of the sheet. This suggested that indentations had not landed on the hardened band of martensite. The sample was examined with an optical microscope and it was found that indentations had not in fact landed on the hardened central band, as shown in Figure 4.42. The indents are indicated as 'A' and the hardened band is indicated as 'B' on the image. This suggested that the alignment of the grid was different than the BM sample. It was unclear how much effect this had on the mapping image and the value for average hardness through the thickness.

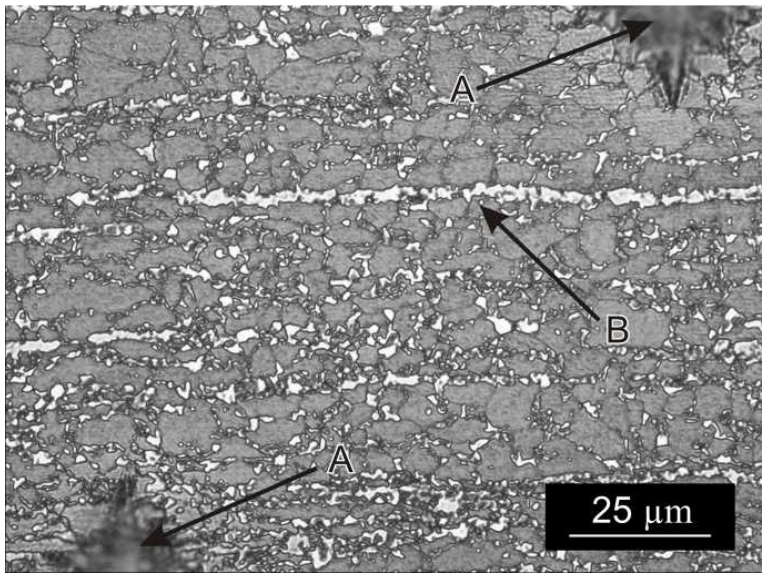

Figure 4.42: Image shows that indents did not land on the central band of hardened martensite. This was from the grid of indentations used to map the TB87 weld hardness.

A profile of the average through-thickness hardness (ATTH, see Figure 3.17) for the TB87 weld map is shown in Figure 4.43. This provided a quantitative comparison between the unwelded BM map and the map of the TB87 weld specimen. A curve was fit to the profile to show the general trend that was associated with hardness throughout the weld HAZ. Four regions of hardness were observed along the profile: the base-metal (BM), the hardened subcritical region (H-SC), the softened subcritical region (S-SC), and the intercritical region (IC). These regions are labelled on the chart.

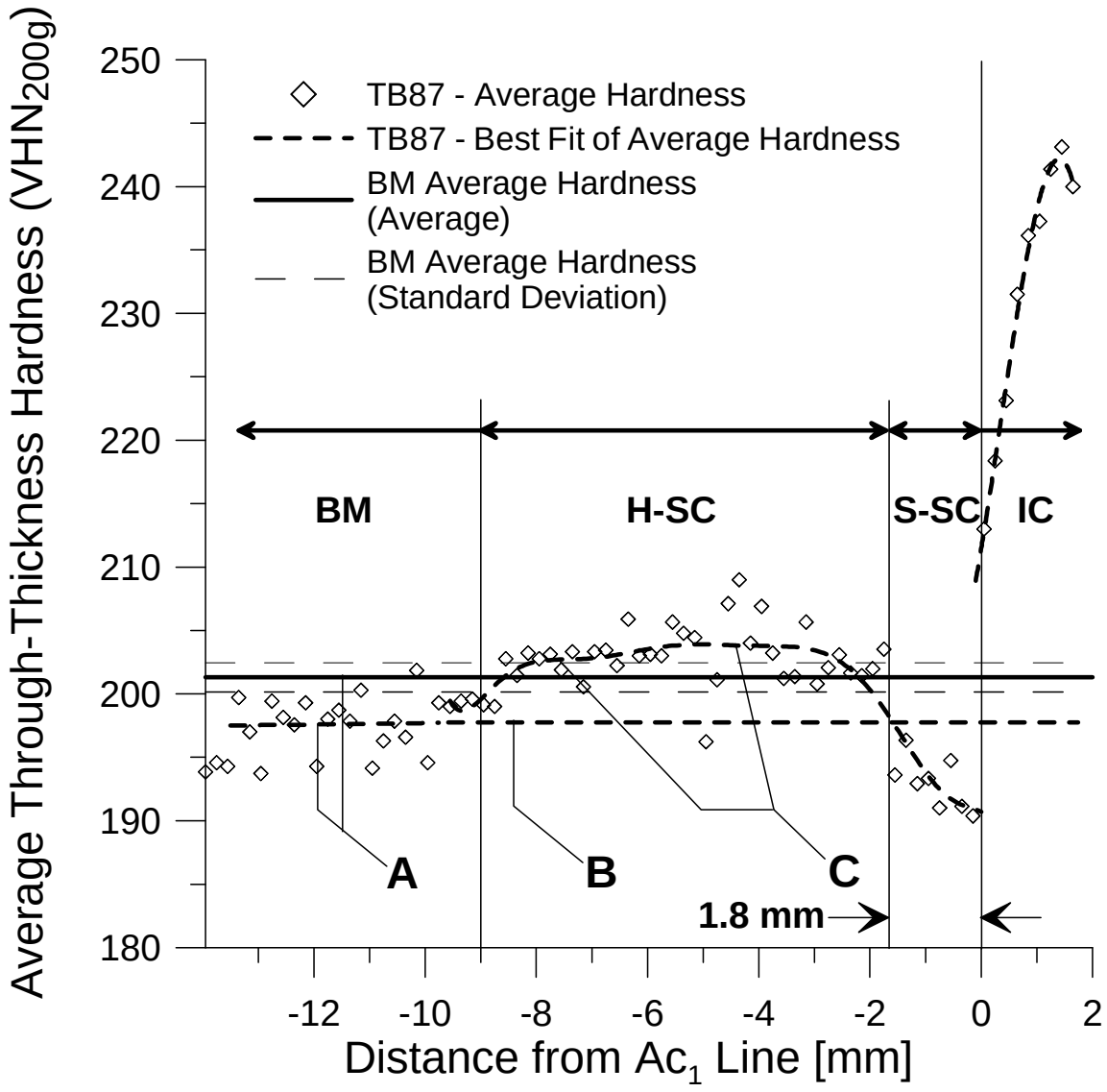

Figure 4.43: The average through-thickness hardness profile for the low heat input weld (TB87). The profile shows the four regions of differing hardness that were observed.

The BM region was defined as the region where the fitted curve on the weld average hardness profile was relatively parallel to the unwelded BM ATTH. This location on the chart was located approximately 9 - 10 mm away from the Ac_1 line. There was a difference between the unwelded BM ATTH and the weld BM ATTH, which is marked 'A' on the chart. The BM hardness value in the welded specimen was lower than the unwelded BM. The difference in hardness was approximately 4 – 5 VHN. This difference was small; however, it suggested that there was a discrepancy between the unwelded BM

and the BM from the welded specimen. This discrepancy could have been from the mapping grid orientation or it could have been caused by a microstrucutural difference that had been caused by the weld heat input. The welded BM ATTH was approximately 198 VHN.

The H-SC region was observed to have an increase in hardness relative to the unwelded and welded BM hardness. This region had a peak average hardness that was approximately 5 – 10 VHN higher than the welded BM region. The ATTH from the welded specimen BM was extended across the profile and is labelled 'B' on the chart. The H-SC region was approximately 7 – 8 mm in width. From the curve fit, the H-SC region appeared to have two hardness plateaus. These plateaus are labelled 'C' on the chart. The plateau with the higher ATTH was located adjacent to the S-SC region.

The presence of hardness plateaus suggested that there were different microstructural changes at different peak temperatures throughout the weld HAZ. Additions of Cr, Mo, and Si, were known to retard the softening effects of martensite tempering and potentially increase hardness due to secondary hardening of alloyed martensite [10]. However, it could also have been caused by plastic deformation of the weld coupon; sheet steel coupons were heavily clamped down during welding and would have resisted thermal expansion.

The S-SC region had a definitive decrease in hardness compared with the unwelded and welded BM hardness. There was a sharp drop in the ATTH at an approximate distance of 1.8 mm away from the Ac_1 line; this was the width of the softened zone. This measurement was more accurate than the estimated measurement that was made directly on the hardness map from Figure 4.41. The location of the sharp drop in hardness was defined as the boundary between the H-SC and the S-SC regions. The profile allowed for a quantitative measurement of softening. The degree of softening was approximately 6 VHN relative to the welded BM ATTH value and was approximately 10 VHN compared to the unwelded BM ATTH value. The difference in average hardness between the H-SC and the S-SC was approximately 15 VHN.

The IC region had the same result as found in the hardness profiles. The material hardness in this region was substantially higher than the BM ATTH. The degree of hardening was measured off of the profile and was found to be approximately 44 VHN.

The result for the hardness map that was made on the high heat input weld (TB88) that had provided 100% HAZ failure during uniaxial tensile testing is shown in Figure 4.44. The weld cross-section is shown in Figure 4.44a. This was the same cross-section that had been used to make the extended microhardness profile and the percent area of martensite profile. The grid of indentations was located from just below the Ac_3 line to out towards the BM. The grid orientation was parallel to the sheet edges and approximately equidistant from each sheet edge. The grid had an extra row of indentations compared to the grid that was used to map the uwelded BM sample.

The hardness map image is shown in Figure 4.44b. It gave a similar image as the low heat input weld. A definitive softened zone was observed in the expected location of decomposed martensite adjacent to the Ac_1 line. The intercritical region was also found to have a significant increase in hardness. The softened zone was measured off of the image and was found to extend approximately 2.8 mm away from the Ac_1 line. This indicated that there was a more significant amount of softening occurring in the high heat input weld. This may have contributed to local necking in the high heat input weld HAZ during uniaxial tensile testing.

There was evidence that hardening may have occurred in the subcritical zone. This suspected area of hardening is labelled ‘A’ on the map image. Significant regions of hardening appeared to have emerged at both the top and bottom edges of the sheet thickness. These are labelled ‘B’ on the map image. This hardening did not appear further out towards the BM. This result was very similar to the hardness map from the low heat input weld (TB87).

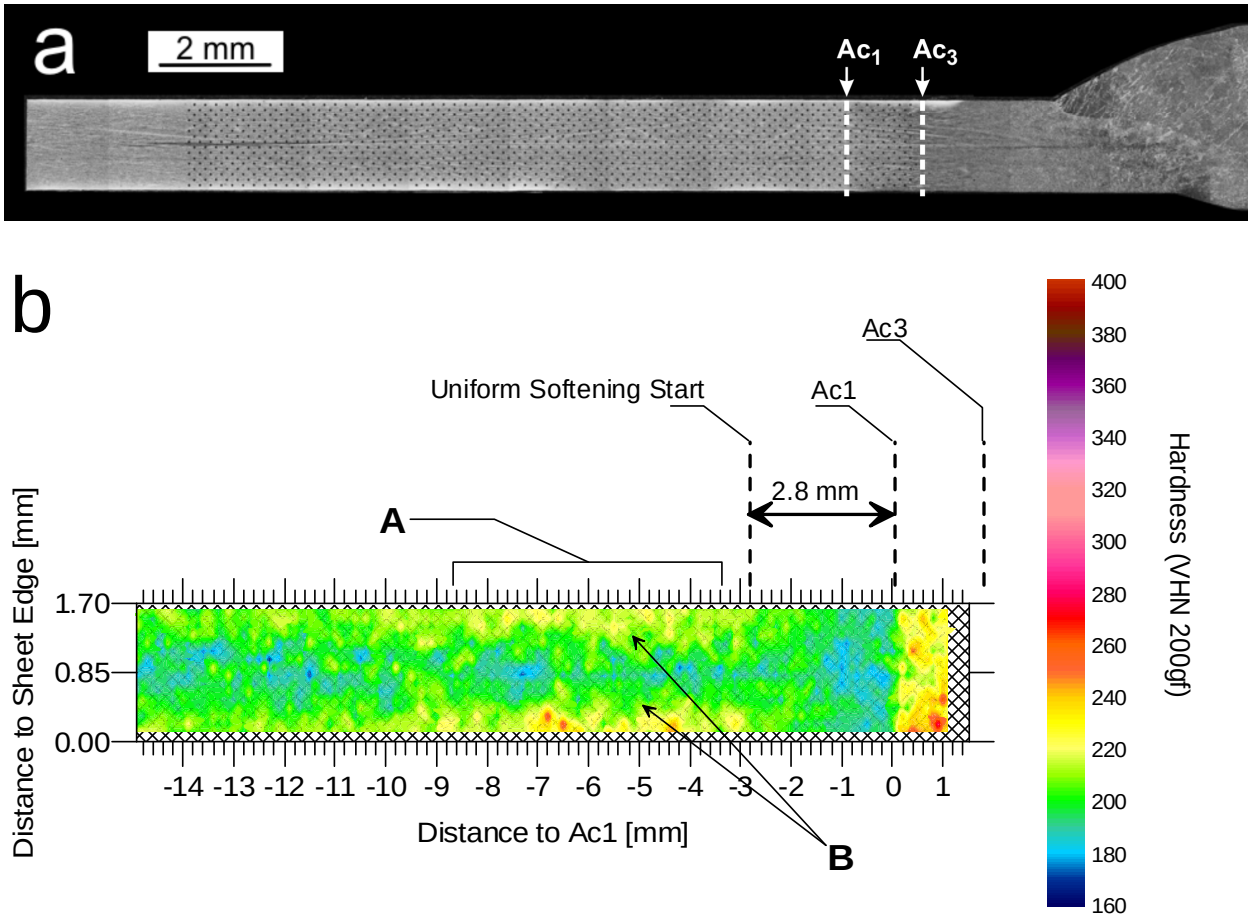

Figure 4.44: The microhardness map for the high heat input (TB88) DP600 '16s' weld HAZ. The image in a) shows the grid of indentations on the TB88 weld cross-section and b) shows the mapped microhardness.

An ATTH profile was created for the high heat input (TB88) weld and is shown in Figure 4.45. The profile allowed for the same type of quantitative measurements that were used to classify the low heat input weld (TB87). A curve was fitted to the profile in order to observe the general trend of the average hardness data. The four regions of hardness that were identified on the average through-thickness profile for the low heat input weld (TB87) were also found on the profile for the high heat input weld (TB88). The BM, H-SC, S-SC, and IC regions are labelled on the chart.

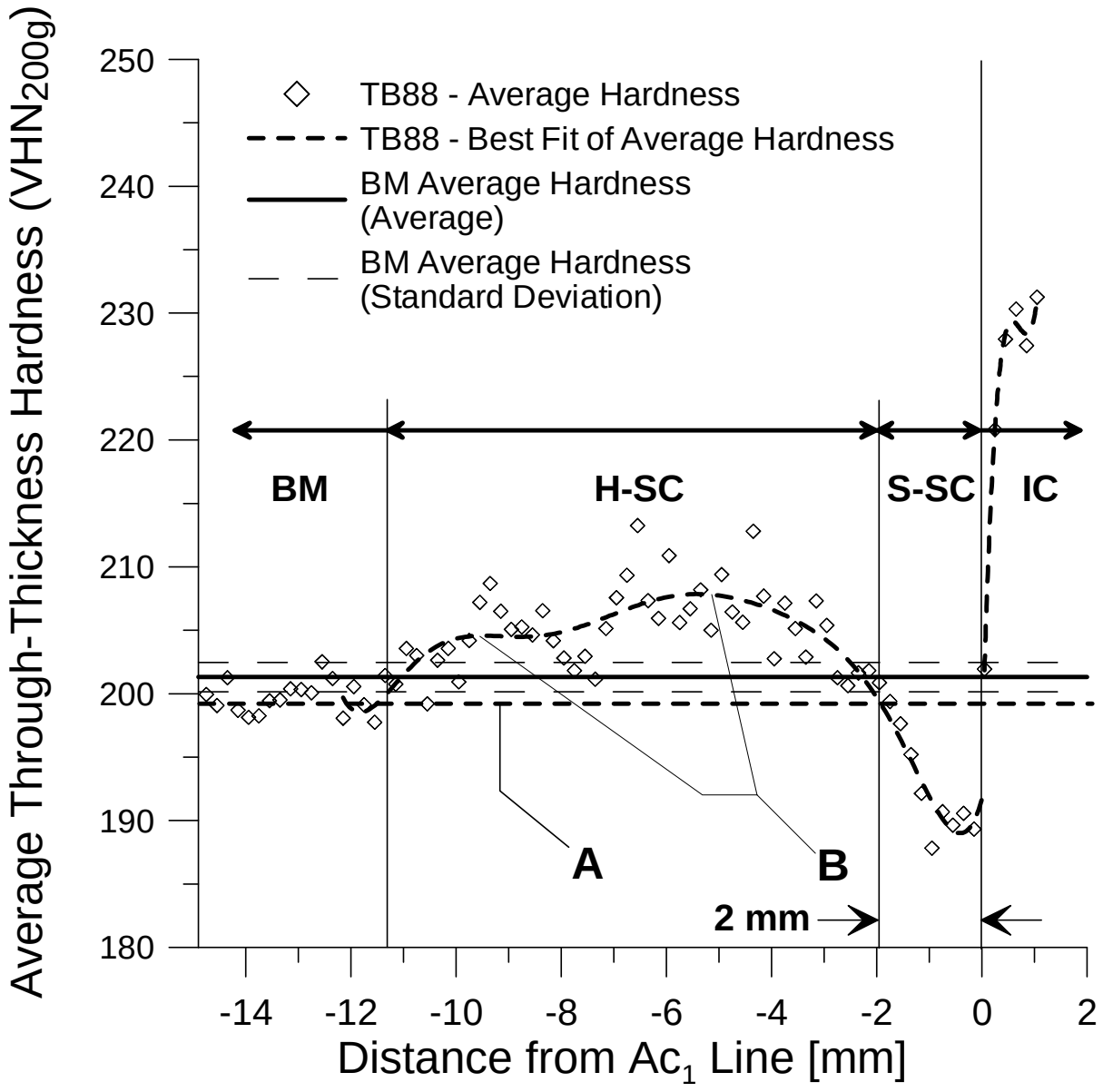

Figure 4.45: The average through-thickness hardness profile for the high heat input weld (TB88). The profile shows the four regions of differing hardness that were observed.

The boundary between the BM and the H-SC regions was estimated to be at an approximate distance of 11 mm away from the Ac_1 line. The welded BM ATTH was approximately 200 VHN. This was the point on the profile where the fitted curve dropped below the unwelded BM ATTH. The BM region for the high heat input weld (TB88) specimen appeared to have lower average hardness than the unwelded BM. The difference in hardness was approximately 1 – 2 VHN; this discrepancy was minimal.

The H-SC region for the high heat input weld (TB88) was very similar to the H-SC region that had been observed on the low heat input weld (TB87) average hardness profile. In this region, the average hardness had increased above the unwelded BM average hardness and above the welded BM average hardness. The ATTH for the welded BM was extended across the entire profile and is labelled 'A' on the chart. The increase in hardness was measured to be approximately 5 - 14 VHN above the welded BM ATTH; this was higher than the low heat input weld. The width of the H-SC region was measured to be approximately 8 – 9 mm; this was wider than the low heat input weld. Two hardness plateaus were observed in the H-SC region on the high heat input weld average hardness profile, which are labelled 'B' on the chart. The plateau with the higher hardness was located adjacent to the S-SC region; this was the same observation that was made on the low heat input weld average hardness profile.

The S-SC region showed definite evidence that softening had occurred in the region immediately adjacent and below the Ac_1 line. The S-SC region began to decrease in hardness at an approximate distance of 2 mm away from the Ac_1 line; this S-SC width was slightly larger than the S-SC width of 1.8 mm in the low heat input weld profile. The maximum decrease in hardness for this region was measured to be approximately 10 VHN below the welded BM ATTH. The decrease in average hardness compared to the unwelded BM was approximately 12 VHN.

The IC region had a substantially higher hardness than the BM average hardness. This was similar to the findings from the microhardness profiles. The approximate increase in average hardness within the IC region was measured to be 30 VHN.

To directly compare the low heat input weld (TB87) to the high input weld (TB88), the profile curve fits for the H-SC and S-SC regions were superimposed onto each other and are shown in Figure 4.46. From this comparison, it appeared that the high heat input weld (TB88) was more significantly affected by the GMAW-P heat input in all aspects across the weld subcritical HAZ. It had a more

substantial decrease in hardness within the S-SC and a more substantial increase in hardness within the H-SC. The H-SC was also observed to extend further away from the Ac_1 line in the high heat input weld.

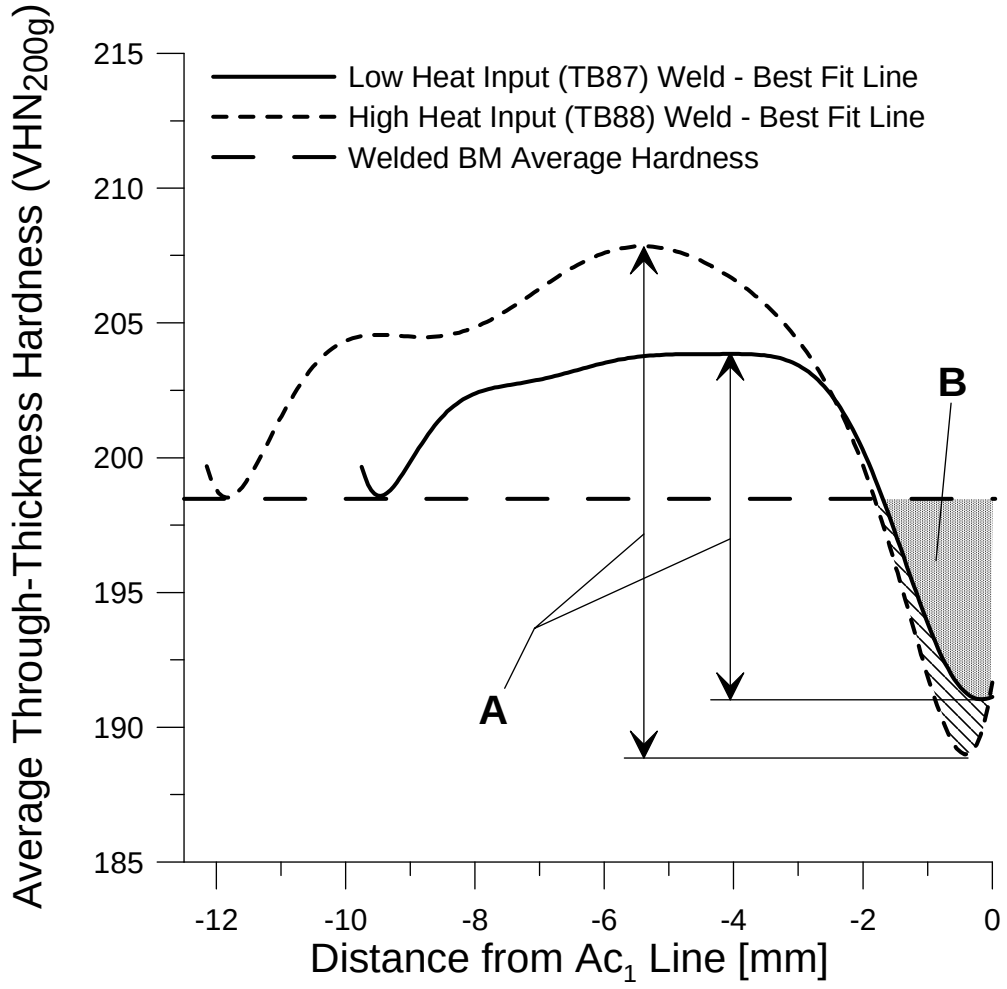

Figure 4.46: A direct comparison between the average through-thickness hardness profiles for the low heat input weld (TB87) and the high heat input weld (TB88).

The presence of a higher hardness region that extended further into the welded specimen BM could have increased the likeliness for a HAZ failure location to occur during uniaxial tensile testing. A greater difference between the BM/H-SC hardness compared to the S-SC hardness would have limited the amount of diffuse necking in the BM and promoted localized necking within the S-SC HAZ. The total difference between the H-SC peak and the S-SC trough is indicated on the chart with an 'A' for both curves. This difference in hardness was approximately 13 VHN for the low heat input weld and was

approximately 20 VHN for the high heat input weld. This suggested that higher heat input during welding had caused the identified regions of hardness to reach extremes in both the degree of hardening and the degree of softening. This would have been related to an increase in the time duration for diffusion to occur within the microstructure of the weld SC HAZ.

A greater amount of softening within the S-SC was observed in the high heat input weld (TB88) when it was compared to the low heat input weld (TB87). This is shown on the chart in the shaded regions, which are labelled 'B'. The area under the welded BM ATT hardness was larger for the high heat input weld (TB88). This direct comparison had shown a clear difference between the two welds. This suggested that the degree of softening in the high heat input weld had been an important factor for a HAZ failure location during uniaxial tensile testing; however, the difference between the S-SC regions did not appear to be substantial. This appeared to match the transition of failure that had been identified in Figure 4.16; the transition from a HAZ failure to a BM failure had been gradual.

Subcritical hardening of the H-SC was not an expectation during the study. There were no reports in the literature that had observed hardening in the subcritical zone of a DP steel weld HAZ; however, the potential for hardening did exist and had been observed during studies where martensite was tempered over prolonged periods at low isothermal temperatures [10].

Generally, the hardness mapping suggested that a softened zone did exist in the GMAW-P HAZ of the DP600 16s sheet. This was an expectation of the study; however, because there were BM failures during uniaxial tensile testing, it was unexpected to find significant softening in the 100% BM failure weld. This definitive evidence of softening helped to explain why local necking had occurred in the HAZ for welds that had the HAZ failure location. The softened zone most likely allowed for a higher amount of local strain compared to the BM and therefore reached a critical strain for micro-void nucleation before the BM [70]. It was suspected that this level of strain could only be attained once the tensile sample had necked and entered into a state of tri-axial stress. This occurred because decomposed martensite islands

did not resist plastic deformation like the solid martensite particles found in the BM and instead flowed with the deforming ferrite matrix. Indents landing on areas of decomposed martensite would also be subject to an increase in plastic flow during loading and hence would measure lower levels of hardness.

The high uniform hardness found in the IC zone was suspected to cause a substantial decrease in plastic flow. This was seen in the HAZ fracture cross-section from Figure 4.20. The high hardness found in the IC zone would have supported the adjacent softened zone to resist plastic flow through the sheet thickness. The area of greatest softening was the area that had the most martensite decomposition, which was immediately adjacent to the Ac_1 line; however, this area was observed to have minimal deformation. The effect of the intercritical zone was measured to extend approximately 2.1 mm out from the Ac_1 line. This value could not directly correspond to the softening measurement of 2 mm because there was significant deformation in the sample; however, these values were of the same magnitude and suggested that the 100% HAZ failure weld softened zone extended far enough away from the support given by the rigid intercritical zone to cause localized necking in the SC region.

4.1.3: The Welded Dual-Phase Sheet Steel Fracture Mechanism

Reasoning for why there was a transition from a HAZ failure location to a BM failure location was also developed based on the mapping data. Welds that were within the transition zone shown in Figure 4.16 most likely had softened zones that followed a similar linear trend as the Ac_1 half-width measurements, i.e., as heat input was decreased the softened zone width was decreased.

The presence of the H-SC could help to explain why a BM failure mode had occurred in the lower heat input welds. The S-SC may have been supported by the adjacent regions of high hardness (H-SC and IC regions) just enough to prevent strain localization. A smaller S-SC required a greater amount of diffuse necking before strain localization could occur. This was analogous to a brazed joint under uniaxial loading. In a brazed joint, increased strength can occur with narrow joint fit up. As joint gap is increased, the brazed joint strength decreased [71,72]. In the case of DP steels, the S-SC region of

microstructure may act in a similar fashion as the soft brazing filler metal and a wider S-SC could be more likely to neck locally at lower levels of stress.

A schematic diagram that illustrates the general theory for why BM fracture can occur in pulsed-GMA welded Cr-Mo thick DP600 sheet steel, which has a HAZ softened zone, is shown in Figure 4.47. The illustration depicts a longitudinal section of a weld joint during loading past the yield point, at constant load *P*, where appreciable diffuse necking has already occurred; this is the state just before localized necking occurred.

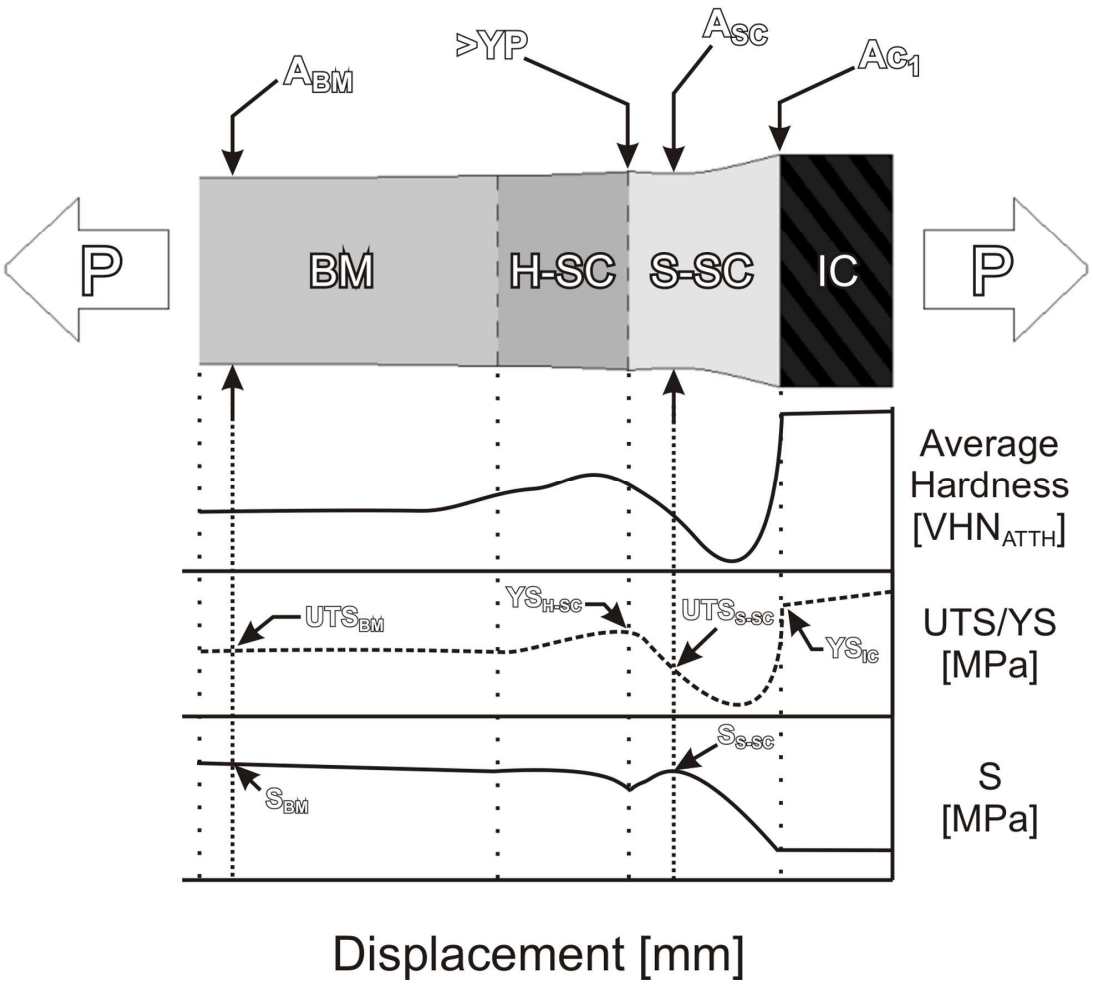

Figure 4.47: The general mechanism during diffuse necking that occurred during uniaxial transverse weld tensile testing of pulsed-GMA welded 1.65 mm thick Cr-Mo DP600 sheet steel. The schematic drawing depicts a typical longitudinal section of a weld from the IC region to the BM.

The drawing is an exaggeration of thinning that actually takes place during a uniaxial transverse weld tensile test. The four regions of microstructure that were identified from the average though-thickness hardness (ATTH) plots are labelled on the image. The intercritical (IC) region did not have visible thinning in either of the fracture longitudinal sections from Figure 4.19 and Figure 4.20, and had been found to have significant hardening. In the drawing, therefore, it is shown as being rigid. The tensile specimen grip is not shown (off to left of image), but it too was assumed to be a rigid area. Beneath the drawing there are two generalized profiles of the local mechanical properties. The trend for local ATTH was known from microhardness mapping and is depicted as the solid line in the figure; the hardness has not been adjusted to include strain hardening. The trends for local ultimate tensile strength (UTS) and yield strength (YS) are also included; however, because these local values have not been measured, the trend that is shown is only inferred from the ATTH curve and observations made from full and partial fracture tests performed in Sections 4.1.2.1 and 4.1.2.2 , respectively. A profile for the local true stress (S) is also included, which is inversely proportional to the cross-sectional area (A) at a given displacement; cross-sectional area varies along the length of the section due to diffuse necking.

A BM fracture occurred, even though there was appreciable softening in the S-SC, because the level of local stress in the BM reached the BM ultimate tensile strength (UTS_{BM}) before the local stress in the S-SC reached $UTS_{S\text{-}SC}$. An illustration of BM fracture is shown in Figure 4.48. A simplified relationship to illustrate this is:

$$\frac{S_{BM}}{UTS_{BM}} = \frac{P}{A_{BM} \cdot UTS_{BM}} > \frac{P}{A_{S-SC} \cdot UTS_{S-SC}} = \frac{S_{S-SC}}{UTS_{S-SC}} \qquad \textbf{(4.1)}$$

where fracture occurred when:

$$\frac{S_{BM}}{UTS_{BM}} = 1 \qquad \textbf{(4.2)}$$

Here, P is the applied load in Newton's (N), S_{BM} and $S_{S\text{-}SC}$ are the maximum local stresses in the BM and S-SC regions of microstructure, respectively, in megapascals (MPa), A_{BM} and $A_{S\text{-}SC}$ are the minimum cross-sectional areas, for their respective regions, in square millimetres (mm^2), UTS_{BM} is the ultimate tensile strength of the BM in megapascals (MPa), and $UTS_{S\text{-}SC}$ is the local ultimate tensile strength at the location in the S-SC at the location of $A_{S\text{-}SC}$ in megapascals (MPa).

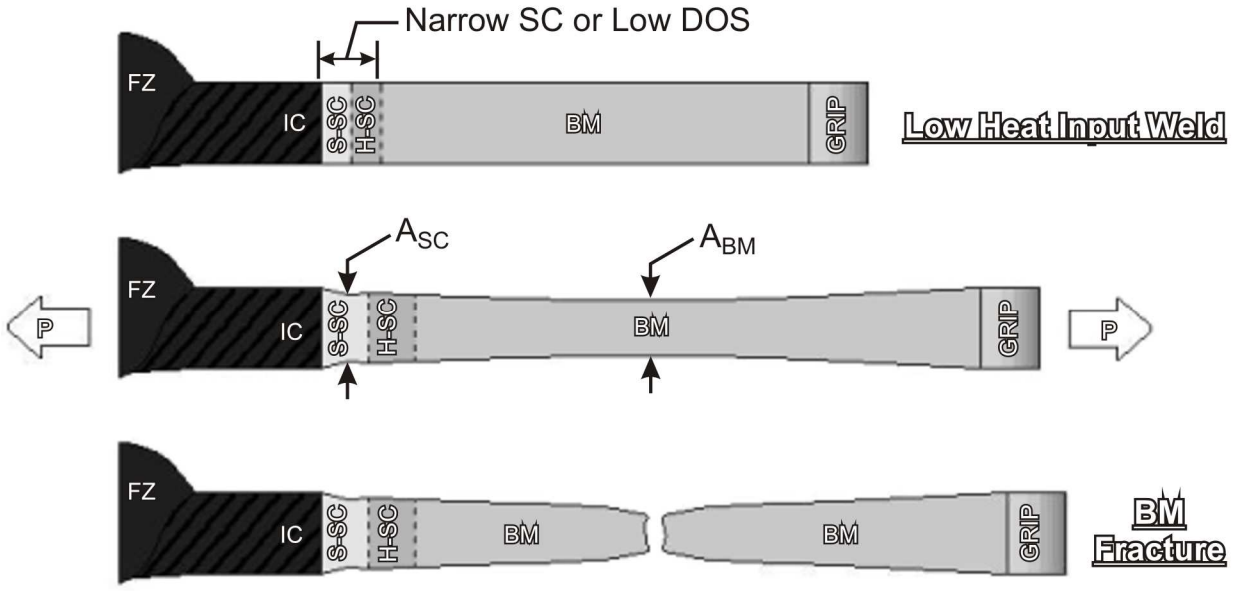

Figure 4.48: An illustration of base-metal fracture that occurred during uniaxial transverse weld tensile testing of Cr-Mo DP600 steel. Top image: A low heat input weld cross-section, which depicts a narrow HAZ with low DOS. Middle image: The weld in tension at maximum diffuse necking prior to strain localization. Bottom image: the resulting BM fracture location.

The relations in Equations (4.1) and (4.2) are based on the assumption that the location of minimum cross-section in the S-SC was the location of fracture for specimens that failed in the HAZ fracture location. Consider that the cross-sectional area of the S-SC immediately adjacent to the Ac_1 line was at a maximum and that this was also the location of maximum softening. This location will never fail by ductile fracture because the other regions of microstructure (BM, H-SC, and remainder of the S-SC) experienced more thinning due to diffuse necking and had reduced cross-sectional area and hence were experiencing greater local stress. However, a weld tensile specimen could fail by brittle fracture at this

location if the degree of softening was substantial; and hence the local stress S_{Ac1} surpassed a substantially low UTS_{Ac1}.

During diffuse necking, the following relation always existed:

$$A_{BM} < A_{S-SC} \quad \textbf{(4.3)}$$

This was because there was significant constraint surrounding the S-SC, which was supported by the adjacent hard intercritical (IC) and hardened subcritical (H-SC) regions. These points, at adjacent edges of the S-SC, were suspected to be locations where peak local YS occurred. It has been reported in the literature that discontinuous yielding, accompanied with an increase in YS, occurred at certain ranges of isothermal tempering temperature for various alloyed DP steels [23,25,27,29,30]. Therefore, the local YS in the diagram are shown to increase within the H-SC region of microstructure. During a study by Biro *et al.* [40], using non-isothermal Gleeble simulations to mimic welding tempering cycles, they found that discontinuous yielding returned but that YS only increased for prestrained DP steel. However, in their study, they had tested for a thermal cycle that would have occurred in the S-SC during an actual welding process. Therefore, the local YS that are shown in the S-SC are low; however, it is not known if the local $YS_{S\text{-}SC}$ would actually drop significantly lower than YS_{BM}. It is suspected that Biro *et al.* [40] would have found evidence of an increase in YS if the peak temperature that they had used was slightly lower. Therefore, the following general relationship between local YS was proposed:

$$YS_{IC} >> YS_{H-SC} > YS_{BM} > YS_{S-SC} \quad \textbf{(4.4)}$$

During the study, the IC region was found to be very hard and had minimal deformation after full fracture had occurred in both the HAZ or BM fracture locations. This support limited diffuse necking in the S-SC so that critical strain to induce localized necking did not occur. The effect of the H-SC constraint was likely less significant than the constraint from the IC region; however, it would still help to limit the reduction of $A_{S\text{-}SC}$. Then, based on the inferred UTS curve, as the S-SC width increases or as the

DOS increases, the likelihood to have HAZ fracture will increase. The same principle will also decrease the resulting UTS of the weld joint during uniaxial transverse weld tensile testing because, as the S-SC width increases, the location of minimum cross-sectional area within the S-SC will have a lower local $UTS_{S\text{-}SC}$.

An illustration of a HAZ fracture location is shown in Figure 4.49. A shift in failure location from BM fracture to HAZ fracture occurred because the width of the softened subcritical (S-SC) region had been increased by using a higher heat input and in part due to a lower local $UTS_{S\text{-}SC}$; the lower $UTS_{S\text{-}SC}$ was inferred by the greater DOS in a high heat input welded DP HAZ.

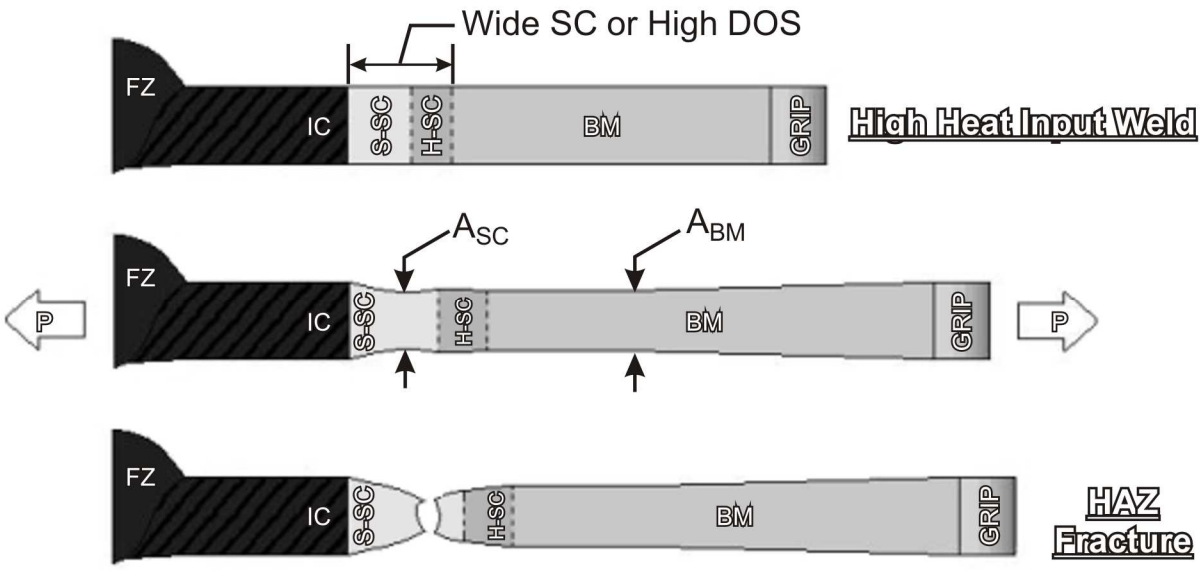

Figure 4.49: An illustration of heat affected zone fracture that occurred during uniaxial transverse weld tensile testing of Cr-Mo DP600 steel. Top image: A high heat input weld cross-section, which depicts a wide HAZ with high DOS. Middle image: The weld in tension at maximum diffuse necking prior to strain localization. Bottom image: the resulting HAZ fracture location.

A HAZ fracture occurs when the relation in Equation (4.1) is reversed so that local stress in the S-SC ($S_{S\text{-}SC}$) region reaches $UTS_{S\text{-}SC}$ before local stress in the BM (S_{BM}) has reached UTS_{BM}, i.e., fracture occurs when:

$$\frac{S_{S-SC}}{UTS_{S-SC}} = 1 \qquad \textbf{(4.5)}$$

This may be an obvious relation, but its importance is that it provides reasoning for why joint efficiency was found to approach 100% for a DP600 weld joint that had fractured in the HAZ. From the literature, Hsu *et al.* [38] found that there was minimal (<5%) loss of joint efficiency for pulsed-GMA welded DP600 sheet steel during HAZ fracture, Conrardy *et al.* [39] found 10-15% reduction of joint efficiency for GMA welded DP780 steel, which had HAZ fracture, and Xia *et al.* [44] found that DP980 steel had a reduction of 22% for a high heat input LBW process, but only had a 5% reduction for a low heat input LBW process. This suggested that the degree of softening was of most importance when trying to improve joint efficiency, because it had also been shown that the degree of softening increased as base-metal volume fraction of martensite increased [40,45].

An illustration of how the joint efficiency was affected during HAZ fracture is shown in Figure 4.50. In the diagram, the local stress, S, has been superimposed on the inferred local UTS curve. The UTS curve depicts two different degrees of softening (low and high DOS) for the same S-SC width. The two relations from Equation (4.1) are indicated on the diagram and it is shown that $UTS_{S\text{-}SC} = S_{S\text{-}SC}$ for low and high DOS, and that $UTS_{BM} > S_{BM}$. As shown, the curve for local stress intersects with the curve high DOS UTS curve at a significant reduction in joint efficiency. For the lower DOS, the local stress curve intersects at a higher local UTS and the joint efficiency increases accordingly.

For the range of heat input that had been created during this study, the transition of failure had produced minimal loss of joint efficiency and initially, loss of strength had been overlooked as being a transient variance. However, after creating this formal evaluation for joint efficiency, re-evaluating the weld specimen for ultimate tensile strength showed the same argument. The welds that had been within the transition of failure depicted in Figure 4.16, which had mixed fracture locations, had near 100% joint efficiency regardless of the fracture location. Whereas, the highest heat input (TB88) weld had dropped

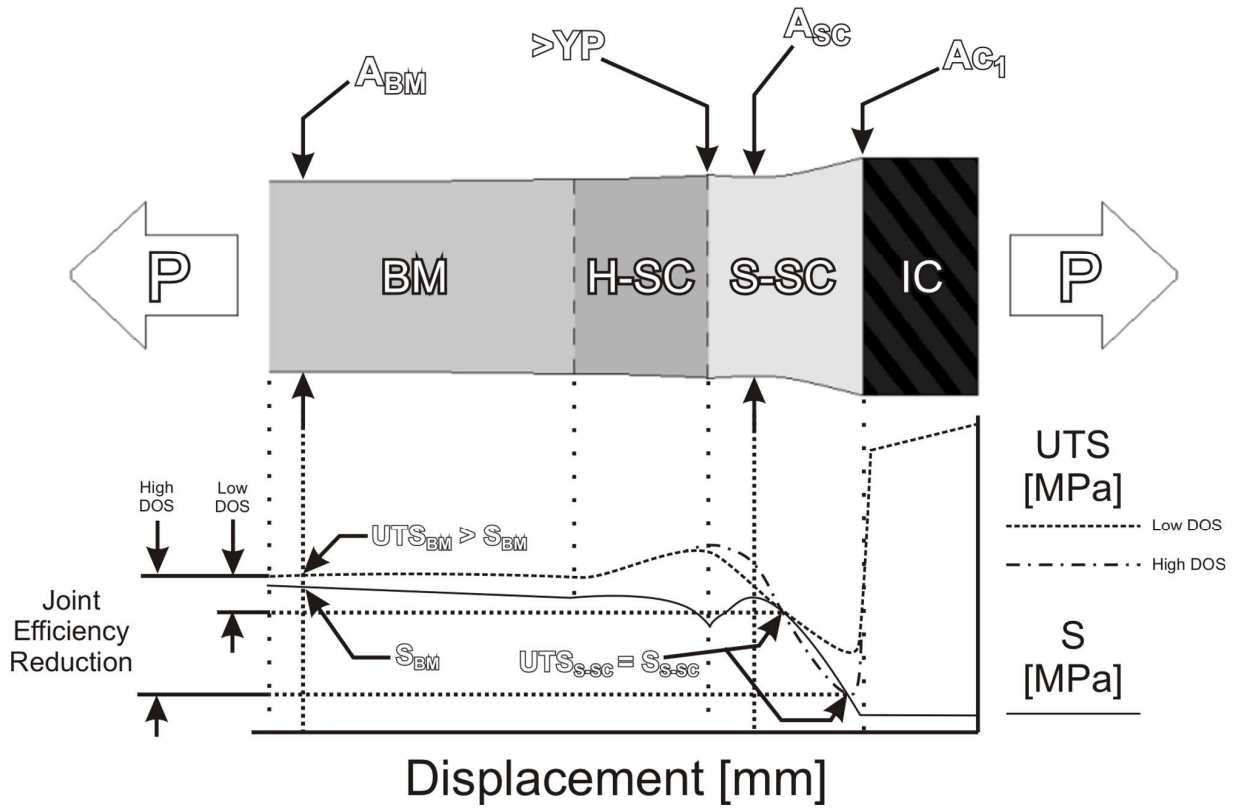

Figure 4.50: A general schematic depicting how HAZ fracture can cause the joint efficiency in welded DP sheet steel to decrease.

in UTS and had a re-evaluated joint efficiency of 98%, which although minor, was a sign that the weld trials had created a near perfect fit on either side of the transition of failure operating window.

With a formal definition in tow, the path to achieve improved joint efficiency for pulsed GMA welding of all grades of DP sheet steel strength could be explored. In the following section, this knowledge was used to evaluate different methods of shifting failure mode from the HAZ and into the more desirable BM fracture location, which in turn would show improvement of DP sheet steel joint efficiency.

4.2: **Experimental Series 2 – Shifting GMAW-P Welded Dual-phase Sheet Steel Failure Location**

During Experimental Series 2, using the knowledge base that was developed during Experimental Series 1, different methods to shift failure location were assessed. Shifting failure location from the HAZ to the BM was achieved by increasing sheet thickness. By increasing the sheet thickness, it was hoped that the degree of softening would decrease because a more favourable path for heat transfer would be introduced; for a similar reason, it was hoped that the width of the S-SC would be decreased. These were two methods that were believed to be significant factors for making a DP sheet steel that would fracture in the BM failure location (as described in Section 4.1.3). Shifting from a BM failure location to the HAZ was achieved by decreasing sheet thickness and/or increasing the strength grade of the DP sheet steel; this assumption was also based on Section 4.1.3 . The results and discussion for Experimental Series 2 are presented in Appendix A. A summary of the findings from all of the work from this study is provided in Appendix C.

Chapter 5: Conclusions and Recommendations

In the automotive industry, autobody structural components that have traditionally been made with conventional plain carbon and high strength low alloy (HSLA) sheet steels are being fabricated increasingly from materials that reduce the components weight and hence improve the vehicle fuel economy. Materials like aluminum, magnesium, and advanced high strength steel (AHSS) alloys are being used because they offer better strength-to-weight ratios over the conventional materials. The AHSS steels, such as dual-phase (DP) and transformation induced plasticity (TRIP), are being used to reduce weight because they retain a comparable formability to HSLA steel at a higher strength and therefore the sheet steel gauge thickness can be reduced while maintaining the required design strength. The reduction in thickness provides a reduction in vehicle weight.

In the present study, the weldability of various coated HSLA and DP sheet steels by the pulsed gas metal arc welding (GMAW-P) process has been examined. Conventional HSLA steels can be welded with relative ease, whereas DP steels, which have a two-phase microstructure comprised of hardened martensite islands in a soft ferrite matrix, tend to soften due to welding heat input. The softening is caused by martensite tempering in the subcritical region of the weld heat affected zone (HAZ). The softened region can lead to a loss of the required design strength at the joint. In the literature, DP sheet steel softening has been regarded as the primary cause of failure in the HAZ of welded DP sheet steels; however, the mechanisms responsible for the more desirable failure in the base-metal (BM) of these welded DP sheet steels has not been studied.

Using full-penetration bead-on-plate GMAW-P welds made onto coated DP600 sheet steel, a wide range of heat input was developed so that the two types of uniaxial transverse weld tensile failure locations occurred at the extremes of the heat input range, i.e., low heat input welds consistently fractured in the BM failure location, high heat input welds consistently fractured in the HAZ failure location, and welds made with intermediate heat input had mixed fracture. The fracture mechanisms that cause a HAZ

failure location during uniaxial transverse weld tensile tests were compared with the more desirable BM failure location to determine why BM fracture can occur when there is a softened zone present in the weld HAZ. This was predominantly studied using 1.65 mm thick DP600 galvanized sheet steel; however, supporting data was studied from welds that were made onto 1.80 mm DP600, 1.20 mm DP600, 1.20 mm DP780, and 1.20 mm DP980 sheet steels. A 1.80 mm thick HSLA galvanized sheet steel was used to develop a welding procedure required to make full-penetration bead-on-plate GMAW-P welds in the DP sheet steels. Subsequent metallurgical analysis of the different welded DP sheet steels was performed to gain insight into how the fracture and fracture mechanism changed based on sheet gauge thickness and BM strength (prior BM percent area of martensite).

From this study, the following conclusions can be made:

- ☑ A transition of failure from a HAZ failure location to a BM failure location during uniaxial transverse weld tensile testing can be achieved for the 1.65 mm thick DP600 sheet steel by varying the GMAW-P heat input. A weld that failed 100% of uniaxial tests in the BM was observed at low heat input and a weld that failed 100% of uniaxial tests in the HAZ was observed at high heat input. Mixed failure during uniaxial transverse weld tensile testing occurred within this range of heat input. This showed that a sufficiently low heat input can be achieved with GMAW-P so that welds made in DP600 sheet steel attain 100% joint efficiency. DP600 has good weldability with a GMAW-P process.
- ☑ For GMAW-P welds that were made in 1.65 mm thick Cr-Mo DP600 galvanized sheet steel, the shift in failure location from HAZ fracture to BM fracture occurred because the width of the softened subcritical (S-SC) region had been reduced by using a lower heat input. A narrow S-SC was supported by the adjacent hard intercritical (IC) and hardened subcritical (H-SC) regions. This support limited diffuse necking in the S-SC so that critical strain to induce localized necking did not occur. By limiting diffuse necking in the S-SC, the BM region incurred greater reduction

in cross-sectional area (only prior to localized necking) and, therefore, the BM entered a state of higher stress than the S-SC and failed once it reached the BM UTS.

- ☑ A HAZ failure location was believed to occur when diffuse necking was sufficient to reach a critical strain in the S-SC and initiate void nucleation around second-phase particles in the steel. A wider S-SC was believed to achieve this critical strain during diffuse necking, whereas a narrow S-SC was believed to be supported by adjacent hardened regions and, therefore, was prevented from reaching this critical strain.
- ☑ A similar mechanism, that had caused BM fracture in DP600 steel, can cause high joint efficiency in pulsed-GMA welded 1.20 mm thick Cr-Mo DP780 sheet steel. Supporting regions of high hardness adjacent to the S-SC region can limit diffuse necking, while diffuse necking occurred to a greater extent in the BM (thus reducing the cross-sectional area of the BM). However, unlike the DP600 welds, the degree of softening is more substantial in DP780 welds and, therefore, diffuse necking in the BM region does not likely reduce cross-sectional area enough to cause localised necking, i.e., the stress in the S-SC would reach UTS first. This could also improve joint efficiency in DP980 steel; however, the high degree of improvement would be limited due to significant losses of strength in the S-SC.
- ☑ Visualization of the BM welded HAZ non-homogeneous microhardness distributions in these DP steels are best achieved by using a microhardness map in conjunction with an ATTH profile. The profiles were used to identify the H-SC and provide visualization of the welded BM region, which was not consistently identified with conventional microhardness profiles during this study due to the non-homogeneous microstructure characteristic of these materials.
- ☑ The 1.80 mm thick HSLA sheet steel could be welded with a full penetration bead-on-plate weld from a GMAW-P welding process and achieve 100% BM failure during uniaxial transverse weld tensile testing and retain the HSLA design UTS, i.e., it attained 100% joint efficiency and hence good weldability with a GMAW-P process.

Recommendations for further research:

- ☑ DP steels tend to have non-homogeneous microstructures such that standard microhardness profile measurements can provide misleading results. A Study of how indentation grid orientation and grid resolution affects ATTH measurements should be done. A finer grid of indentations at lower indentation load could be used to achieve better resolution. However, this would be time costly, so it would be beneficial to determine an optimal grid resolution that is efficient and does not incur significant variability.
- ☑ The nature and morphology of the H-SC region should be examined to determine if fine alloy carbide precipitation plays a role in the hardness increase that is observed in that region of microstructure, i.e., determine if secondary hardening of martensite occurs within the HAZ of a GMAW-P welded DP sheet steel.
- ☑ Measurements for the degree of softening in the S-SC region should be calculated by using area-under-the-curve for curve fitted data from an ATTH profile. Then study how this measurement affects the resolution of the degree of softening plots proposed by Xia *et al.* [45], which describes the threshold time duration for preventing HAZ softening.
- ☑ A fracture analysis of higher strength grades of pulsed-GMA welded DP780 and DP980 should be performed to determine the dominant mechanism for void nucleation and to verify that the mechanism for preventing DP600 HAZ fracture is also a mechanism that improves joint efficiency in these materials.
- ☑ Tests should be performed on DP600 welds that have varying softened zone width and a hardened IC region, but do not exhibit an H-SC region of hardness; this would provide evidence to show whether an adjacent H-SC region is a reason for preventing a HAZ or a BM fracture from occurring.
- ☑ Similarly, tests should be performed on DP600 welds that have varying softened zone width, but do not have intercritical (IC) and supercritical (SP) hardening; this would provide evidence to

show that the significant hardened region that was found adjacent to the weld softened zone supports the softened zone during loading and prevents localized necking. This could be accomplished with post-weld local tempering of the IC and SP or could be a with welds in age-hardened aluminum)

- ☑ Welds should be made onto varying sheet thicknesses of higher strength grades of DP sheet steel; specifically DP780, which had a minimal reduction of UTS. Increased sheet thickness should improve joint efficiency and could potentially shift fracture to the BM. Although increasing sheet thickness is contrary to the goal of using DP sheet steel for weight reduction, if joint efficiency does improve, then in future it may be beneficial to tailor components so that joints have a higher local thickness than the bulk of the sheet, e.g., the sheet edges could be plastically deformed prior to welding to increase thickness at the edges where welds will be made. This would create a more favourable path for heat transfer and would reduce stress in this area.

References

[1] Doggett, S. (2009, May 19). *Green Car Advisor*. Retrieved November 8, 2009, from Edmunds.com: http://blogs.edmunds.com/greencaradvisor/2009/05/obama-proposes-bold-dual-standards-for-automotive-fuel-economy-and-emissions.html

[2] Hyatt, D., & Cyrill, C. (2009, March 27). *National Automobile Dealers Association News: Press Release: Obama Fuel Economy Standard Set Higher Than California Rule.* Retrieved November 8, 2009, from nada.org: http://www.nada.org/MediaCenter/News+Releases/Obama+Fuel +Economy+Standard +Set+Higher+Than+California+Rule.htm

[3] Keeler, S., & Opbroek, E. G. (2009, June 08). *Advanced High Strength Steel Application Guidelines: Version 4.1*. Retrieved October 27, 2009, from World Auto Steel Web Site: http://www.worldautosteel.org

[4] Brown, L. R. (2001). Designing a New Materials Economy. In *Eco-Economy: Building an Economy for the Earth* (pp. 121-143). New York: Earth Policy Institute.

[5] Davies, R. (1978). Influence of Martensite Composition and Content on the Properties of Dual-phase Steels. *Metallurgical Transactions A* , Vol 9A, No. 5, 671-679.

[6] Park, Y., Coldren, A., & Morrow, J. (1981). Effect of Marteniste Bands and Elongated Manganese Sulfide Inclusions on the Formability of Dual-Phase Steels. *Fundamentals of dual-phase steels: Proceedings of a symposium* (pp. 485-497). Warrendale, PA: Metallurgical Society of AIME.

[7] LePera, F. (1979). Improved Etching Technique for the Determination of Percent Martensite in High-Strength Dual-Phase Steels. *Metallography* , 263-268.

[8] Askeland, D., & Phule, P. (2003). *The Science and Engineering of Materials: Fourth Edition.* Pacific Grove, CA: Brooks/Cole, a division of Thomson Learning, Inc.

[9] Brooks, C. R. (1996). *Principles of the Heat Treatment of Plain Carbon and Low Alloy Steels.* Materials Park, OH: ASM International.

[10] Petty, E. R. (1970). *Martensite: Fundamentals and Technology*. London: Longman Group Ltd.

[11] Gould, J., Khurana, S., & Li, T. (2004, May 11-14). Calculations of Cooling Rate for a Range of Automotive Welding Processes and their Relationship to the Hardenability of Advanced High-Strength Sheet Steels. *Sheet Metal Welding Conference XI* , Detroit, MI, pp. 1-10.

[12] Lancaster, J. (1986). *The Physics of Welding, 2nd Edition.* Oxford, UK: Pergamon Press.

[13] AWS Committee on Arc Welding and Cutting, Subcommittee on Gas Metal Arc Welding. (1989). *ANSI/AWS C5.6-89: An American National Standard: Recommended Practices for Gas Metal Arc Welding.* Miami, FL: American Welding Society.

[14] ASM Handbook Online – *Volume 6, Welding, Brazing, and Soldering: Fundamentals of Welding: Transfer of Heat and Mass to the Base-metal in Gas-Metal Arc Welding: Mass Transfer*, ASM International®, Materials Park, OH, 2002, from the website ASM Handbooks Online: http://products.asminternational.org/hbk/index.jsp

[15] Lancaster, J. (1980). *Metallurgy of Welding: Third Edition.* London, UK: George Allen & Unwin Ltd.

[16] ASM Handbook Online – *Volume 6, Welding, Brazing, and Soldering: Fusion Welding Processes: Gas-Metal Arc Welding: Process Fundamentals*, ASM International®, Materials Park,

OH, 2002, from the website ASM Handbooks Online: http://products.asminternational.org/hbk/index.jsp

[17] ASM Handbook Online – *Volume 6, Welding, Brazing, and Soldering: Fundamentals of Welding: Shielding Gases for Welding: Shielding Gas Selection*, ASM International®, Materials Park, OH, 2002, from the website ASM Handbooks Online: http://products.asminternational.org/hbk/index.jsp

[18] Lawson, R., Matlock, D., & Krauss, G. (1981). The Effect of Microstructure on the Deformation Behavior and Mechanical Properties of a Dual-Phase Steel. The fundamentals of dual-phase steels: Proceedings of a symposium (pp. 347-381). Warrendale, PA: Metallurgical Society of AIME.

[19] Okamoto, A., & Takahashi, M. (1981). Control of Strength and R-Value in Box-Annealed Dual-Phase Steel Sheet. *Fundamentals of dual-phase steels: Proceedings of a symposium* (pp. 427-445). Warrendale, PA: Metallurgical Society of AIME.

[20] Avtar, R., Jha, B., & Dwivedi, V. S. (1986). Effect of transformed ferrite on fracture behaviour of a dual-phase steel. *Journal of Materials Science Letters* , 725-727.

[21] Ahmad, E., Manzoor, T., Ali, K., & Akhter, J. (2000). Effect of Micro-void Formation on the Tensile Properties of Dual-Phase Steel. *Journal of Materials Engineering and Performance* , Vol. 9, No. 3, pgs 306-310.

[22] Chen, H.-C., & Cheng, G.-H. (1989). Effect of martensite strength on the tensile strength of dual-phase steels. *Journal of Materials Science* , Vol. 24, pp. 1991-1994.

[23] Davies, R. (1981). Tempering of Dual-Phase Steels. *The fundamentals of dual-phase steels: Proceedings of a symposium* (pp. 265-277). Warrendale, PA: Metallurgical Society of AIME.

[24] Steinbrunner, D., Matlock, D., & Krauss, G. (1988). Void Formation during Tensile Testing of Dual-phase Steels. *Metallurgical Transactions A* , Vol. 19A, pp. 579-589.

[25] Speich, G., & Miller, R. (1981). Tempering of Ferrite-Martensite Steels. *Fundamentals of dual-phase steels: Proceedings of a symposium* (pp. 279-303). Warrendale, PA: The Metallurgical Society of AIME.

[26] Grange, R., Hribal, C., & Porter, L. (1977). Hardness of Tempered Martensite in Carbon and Low-Alloy Steels. *Metallurgical Transactions A* , Vol. 8A, pp. 1775-1785.

[27] Jha, B. K., Avtar, R., Dwivedi, V. S., & Mishra, N. S. (1993). Tempering characteristics of a Cr-Mo dual-phase steel . *Steel Research* , Vol. 64, No. 3, pp. 171-177.

[28] Joarder, A., Jha, J., Ojha, S., & Sarma, D. (1990). The Tempering Behavior of a Plain Carbon Dual-Phase Steel. *Materials Characterization* , Vol. 25, pp. 199-209.

[29] Speich, G., Schwoeble, A., & Huffman, G. (1983). Tempering of Mn and Mn-Si-V Dual-Phase Steels. *Metallurgical Transactions A* , Vol. 14A, pp. 1079-1087.

[30] Rashid, M., & Rao, B. (1982). Tempering Characteristics of a Vanadium Containing Dual-phase Steel. *Metallurgical Transactions A* , Vol. 13A, pp. 1679-1686.

[31] Panda, A., Sarma, D., Ganguly, R., & Misra, S. (1993). Tempering behaviour of a dual-phase low-alloy steel. *Steel Research* , Vol. 64, No. 10, pp. 513-516.

[32] Zhu, C., Xiong, X., Cerezo, A., Hardwicke, R., Krauss, G., & Smith, G. (2007). Three-dimensional atom probe characterization of alloy element partitioning in cementite during tempering of alloy steel. *Ultramicroscopy* , Vol. 107, pp. 808-812.

[33] Krauss, G. (1990). *Steels: Heat Treatment and Processing Principles.* Materials Park, OH: ASM International.

[34] Ghosh, P. (1990). Thermal Cycle and Microstructure of Heat Affected Zone (HAZ) of Flash Butt Welded Mn-Cr-Mo Dual-phase Steel. *ISIJ International* , Vol. 30, No. 4, pp. 317-324.

[35] Ghosh, P., Gupta, P., Pal, O., Avtar, R., Jha, B., & Dwivedi, V. (1993). Influence of Weld Thermal Cycle on Properties of Flash Butt Welded Mn-Cr-Mo Dual-phase Steel. *ISIJ International* , Vol. 33, No. 7, pp. 807-815.

[36] Biro, E., & Lee, A. (May 11-14, 2004). Welded Properties of Various DP600 Chemistries. *Sheet Metal Welding Conference XI*, Sterling Heights, MI (Paper 5-2). American Welding Society, Miami, FL.

[37] Yurioka, N., Suzuki, H., Ohshita, S., & Saito, S. (1983). Determination of Necessary Preheating Temperature in Steel Welding. *Welding Journal* , Vol. 62, No. 6, pp. 147-153.

[38] Hsu, C., Soltis, P., Carroscia, M., Barton, D., & Occhialini, C. (May 11-14, 2004). Weldability of Dual-Phase Steel with Arc Welding Processes. *Sheet Metal Welding Conference XI*, Sterling Heights, MI (Paper 5-1). American Welding Society, Miami, FL.

[39] Conrardy, C., Kapustka, N., & Albright, C. (May 9-12, 2006). Effect of Material and GMAW Process Conditions on AHSS Welds. *Sheet Metal Welding Conference XII*, Livonia, MI (Paper 5-2). American Welding Society, Miami, FL.

[40] Biro, E., & Lee, A. (May 9-12, 2006). Tensile Properties of Gleeble-Simulated HAZ from Various Dual-Phase Steels. *Sheet Metal Welding Conference XII*, Livonia, MI (Paper 7-1). American Welding Society, Miami, FL.

[41] Khan, M., Kuntz, M., & Zhou, Y. (2008). Effects of weld microstructure on static and impact performance of resistance spot welded joints in advanced high strength steels. *Science and Technology of Welding and Joining* , Vol. 13, No. 1, pp. 49-59.

[42] Hernandez, V., Kuntz, M., Khan, M., & Zhou, Y. (2008). Influence of microstructure and weld size on the mechanical behaviour of dissimilar AHSS resistance spot welds. *Science and Technology of Welding and Joining* , Vol. 13, No. 8, pp. 769-776.

[43] Xia, M., Screenivasan, N., Lawson, S., Zhou, Y., & Tian, Z. (2007). An Initial Comparative Study of Formability of Diode Laser Welds in DP980 and HSLA Steels. *Journal of Engineering Materials and Technology* , Vol. 129, pp. 446-452.

[44] Xia, M., Kuntz, M., Tian, Z., & Zhou, Y. (2008). Failure study on laser welds of dual-phase steel in formability testing. *Institute of Materials, Minerals and Mining* , Vol. 13, No. 4, pp. 378-387.

[45] Xia, M., Biro, E., Tian, Z., & Zhou, Y. (2008). Effects of Heat Input and Martensite on HAZ Softening in Laser Welding of Dual-phase Steels. *ISIJ International* , Vol. 48, No. 6, pp. 809-814.

[46] O'Brien, R. (1991). Testing for Evaluation of Welded Joints: Tension Tests. In *AWS Handbook: Eighth Edition - Volume 1: Welding Technology* (pp. 387-397). Miami, FL: American Welding Society.

[47] Biro, E., Jiang, C., & Lyttle, K. (May 14-16, 2008). Correlation between Failure Location and Tensile Strength of AHSS GMAW Lap Joint. *Sheet Metal Welding Conference XIII*, Livonia, MI (pp. 1-13). American Welding Society, Miami, FL.

[48] E. Biro, personal communications, ArcelorMittal Dofasco Inc., Hamilton, ON, 2007-2009.

[49] *ASM Handbook Online – Volume 1, Properties and Selection: Irons, Steels, and High Performance Alloys: Carbon and Low-Alloy Steels: High-Strength Structural and High-Strength Low-Alloy Steels: HSLA Steels*, ASM International®, Materials Park, OH, 2002, from the website ASM Handbooks Online: http://products.asminternational.org/hbk/index.jsp

[50] ASTM Standard E 8-04M, (2007), "Standard Test Methods for Tension Testing of Metallic Materials [Metric]". In V. A. Mayer, *Annual Book of ASTM Standards 2007: Section 3 - Metals Test Methods and Analytical Procedures: Volume 03.01 - Metals-Mechanical Testing; Elevated and Low-Temperature Tests; Metallography* (pp. 89-113). ASTM International, West Conshohocken, PA, www.astm.org.

[51] ASM Handbook Online – *Volume 6, Welding, Brazing, and Soldering: Practice Considerations for Arc Welding: Arc Welding of Carbon Steels: Welding Consumables Selection and Procedure Development*, ASM International®, Materials Park, OH, 2002, from the website ASM Handbooks Online: http://products.asminternational.org/hbk/index.jsp

[52] Gases & Blends, Argon-Carbon Dioxide Mixtures – Praxair's *StarGold*™ and *Mig Mix Gold*™ Blends, Praxair Technology, Inc. 2009. From*: http://www.praxair.com/praxair.nsf/7a1106cc 7ce1c54e85256a9c005accd7/5fd4386080b482bc85256e75004faff2?OpenDocument*

[53] *PowerWave™ 455/R Operator's Manual*, Lincoln Electric, Cleveland, OH, USA.

[54] *Current and Voltage Transducers for Industrial Applications: Industrial Transducers Catalogue, Edition 1998/99*, LEM Corporate Communications, LEM Geneva, Switzerland, 1998.

[55] *NuDAQ® PCI-9114(A) DG/HG Enhanced Multi-Functions Data Acquisition Card User's Guide*, ADLINK Technology Inc., Chungho City, Taipei, Taiwan, 2003.

[56] Lee Upshall, personal communications, University of Waterloo: CAMJ, Waterloo, ON, 2007.

[57] Microsoft Visual Basic 6.0 (SP5) For 32-bit Windows Development. (1987-2000). Microsoft Corp.

[58] Microsof(R) Office Excel(R) 2007 (12.0.6514.5000) SP2 MSO (12.0.6425.1000): Part of Microsoft Office Professional Plus 2007. (2006). Microsoft Corporation.

[59] Nguyen, T. C. (2005). *Weld Defects in High-Speed Gas Metal Arc Welding.* Waterloo, ON: PhD Thesis, University of Waterloo, Waterloo, ON.

[60] ASM Handbook Online – *Volume 1, Properties and Selection: Irons, Steels, and High Performance Alloys: Carbon and Low-Alloy Steels: Precoated Steel Sheet: Zinc Coatings,* ASM International®, Materials Park, OH, 2002, from the website ASM Handbooks Online: http://products.asminternational.org/hbk/index.jsp

[61] Image-Pro Plus: Version 6.3.0.512 for Windows XP/Vista. (1993-2008). Media Cybernetics, Inc.

[62] Jorge Cruz, personal communications, University of Waterloo: Engineering Machine Shop - Stores, Waterloo, ON, 2009.

[63] Mathy, H., Gouzou, J., & Greday, T. (1981). A study of the early stages of plastic deformation of dual-phase sttels, including microplasticity. *Fundamentals of dual-phase steels: Proceedings of a symposium* (pp. 413-425). Warrendale, PA: Metallurgical Society of AIME.

[64] ASTM Standard E 92-82, (2007), "Standard Test Method for Vickers Hardness of Metallic Materials". In V. A. Mayer, *Annual Book of ASTM Standards 2007: Section 3 - Metals Test Methods and Analytical Procedures: Volume 03.01 - Metals-Mechanical Testing; Elevated and Low-Temperature Tests; Metallography* (pp. 291-299). ASTM International, West Conshohocken, PA, www.astm.org.

[65] Surfur - Version 8.00: Surfer Mapping System. (2002, February 11). Golden, CO, USA: Golden Software, Inc.

[66] Schurmann, E., Djurdjevic, M., & Nedeljkovic, L. (1997). Calculation of liquidus temperature of low and high alloyed iron base melts from their chemical composition by means of the equivalence factors. *Steel Research 68*, No. 3, pp. 101-106.

[67] K.W. Andrews, D. (July 1965). Empirical formulae for the calculation of some transformation temperatures. *Journal of the Iron and Steel Institute* , pp. 721-727.

[68] ASM Handbook Online – *Volume 6, Welding, Brazing, and Soldering: Selection of Carbon and Low-Alloy Steels: Influence of Welding on Steel Weldment Properties: Heat-Affected Zone,* ASM International®, Materials Park, OH, 2002, from the website ASM Handbooks Online: http://products.asminternational.org/hbk/index.jsp

[69] Brooks, C. R., & Choudhury, A. (2002). Failure Analysis of Engineering Materials. New York, NY: The McGraw-Hill Companies, Inc.

[70] Thomason, P. (1990). *Ductile Fracture of Metals.* Oxford, UK: Pergamon Press.

[71] Taie, A., & Ateia, A. (n.d.). An Experimental Study of Clearance Width Effects on the Strength of a Carbon Steel Brazed Joint. 57-71.

[72] *AWS Bazing Handbook: 4th Edition.* (1991). American Welding Society, Miami, FL.

[73] ASM Handbook Online – *Volume 6, Welding, Brazing, and Soldering: Fundamentals of Welding: Solid-State Transformations in Weldments: Fusion Zone of a Single-Pass Weld*, ASM International®, Materials Park, OH, 2002, from the website ASM Handbooks Online: http://products.asminternational.org/hbk/index.jsp

Appendix A

Experimental Series 2:

Shifting Dual-phase Steel Failure Location

Experimental Procedure

A second series of welds was created to compliment the 1.65 mm DP600 ‘16s’ sheet steel welds and give an extra point of comparison for the differing modes of uniaxial tensile failure. The purpose of these extra welds was to create different conditions for a HAZ fracture and a BM fracture to occur during uniaxial transverse weld tensile testing. This second series was made in differing DP sheet steel thicknesses and differing DP sheet steel strength grades. These included the 1.20 mm DP600 ‘22s’ and 1.80 mm DP600 ‘24s’, the 1.20 mm DP780 ‘21s’, and the 1.20 mm DP980 ‘23s’ sheet steels. By taking similar strength grades of DP steel and varying the sheet thickness, the expected size of the softened region would be increased on smaller thicknesses and decreased on larger thicknesses. An increase in the size of the softened region was expected to increase the likeliness of HAZ failure and a decrease in the softened region size was expected to increase the likeliness of BM failure. A comparison was also made between the steels with a thickness of 1.20 mm by observing the failure mode in the differing steel strength grades. The differing DP sheet steel strength grades were included in the study because ultimately a mechanism for preventing a HAZ fracture and/or improving joint efficiency in the higher strength grades was desired.

For the DP600 ‘24s’ sheet steel, the DP600 ‘16s’ Phase 2 weld parameters were used to make bead-on-plate welds in 254 mm × 203 mm sized coupons for tensile testing. There were no modifications to the Phase 2 weld parameters. These welds were cross-sectioned to measure HAZ width with a minimum of 2 cross-sections per weld. They were then tensile tested using 3 transverse weld tensile specimens to determine failure location and relative UTS. For this series of welds, if no weld gave HAZ fracture, then a higher heat input weld would be added to the study in an attempt to induce a HAZ fracture. The only other testing conducted was a hardness map of the highest heat input weld from the weld set.

For the DP600 ‘22s’ sheet steel, a new set of GMAW-P weld parameters was created and used to make bead-on-plate welds in 254 mm × 203 mm sized coupons for tensile testing. There was minimal

optimization conducted for this study and only six sets of weld parameters were developed. This was done because there was no requirement for a transition of failure within this sample set. The weld development process was as follows: the weld Trim, WFS, and CTWD were setup prior to the study, and the TS was selected during the study based on the observed root penetration of the previous weld. Initial TS was set to 25.4 mm/min (60 ipm). Full root penetration through the bottom of the sheet was desirable. For the DP780 '21s' and DP980 '23s' sheet steels, welds were made using the same weld parameters that had been used to make the DP600 '22s' sheet steel welds. The lowest and highest heat input welds that were also free from defects were selected from each grade of steel for further study. These six welds were cross-sectioned for HAZ measurement with a minimum of 2 cross-sections per weld. Each weld was tested for uniaxial transverse weld tensile fracture location and relative UTS with a minimum of 3 tensile specimens per weld. The lowest heat input weld from each steel grade was used to create a microhardness map.

For each sheet steel in this series, the base-metal was characterized as follows: a uniaxial transverse weld tensile test using 3 tensile specimens was conducted to compare with the weld UTS, a martensite through-thickness profile was conducted to compare the volume fraction of martensite between different grades and calculate the estimated martensite island carbon content, and a hardness map was made to observe the base-metal hardness as it existed through the entire thickness of the sheet steel. The base-metal characterization was used for comparisons between all of the sheet steels, specifically to relate back to the 1.65 mm DP600 '16s' sheet steel measurements from Experimental Series 1.

Results and Discussion

The goal of this experimental series was to make welds onto DP sheet steels that had different sheet thicknesses and onto DP sheet steels that had different nominal strengths and to compare uniaxial transverse weld tensile test failure location to the welds from Experimental Series 1.

Base-metal Characterization

Prior to welding, the base-metal for the 1.77 mm DP600 ‘24s’, the 1.20 mm DP600 ‘22s’, the 1.20 mm DP780 ‘21s’, and the 1.20 mm DP980 ‘23s’ were characterized by measuring the percent area of martensite through-thickness profile and with a Vickers microhardness map. These were made in order to compare these results with the 1.65 mm DP600 ‘16s’ sheet steel from Experimental Series 1. Each of these steels was also tested to complete failure with uniaxial tensile tests.

The percent area of martensite through-thickness profile for the 1.80 mm DP600 ‘24s’ sheet steel is shown in Figure A.1. The locations for the images that were used for percent area analysis are marked on the cross-section with black circles. The result for this steel was similar to the profile from Experimental Series 1. The percent area of martensite profile varied through the thickness of the sheet. The profile was asymmetric, and as shown in the figure, the lower half had a higher average martensite percentage than the upper half. There was a peak found at the center of the thickness; however, unlike the 1.65 mm DP600 ‘16s’ sheet steel, there was no visible evidence of a continuous band of hardened martensite at this location. This suggested that during continuous casting, this steel did not have as much macro-segregation of rejected solute at the advancing fronts of the solidifying steel during casting or that the cooling rate from intercritical annealing was not as high as the DP600 ‘16s’ sheet steel. The peak in the profile that was at this location meant that solute build up existed, but was not as pronounced as in the DP600 ‘16s’ sheet steel. This result meant that there was some macro-segregation present through the sheet thickness. The average martensite percentage that was calculated for the DP600 ‘24s’ BM was $7.4 \pm 1.5\%$. The sheet thickness was measured with the optical microscope and found to be approximately 1.75 mm.

Two example images that were used to measure the percent area of martensite for the 1.80 mm DP600 ‘24s’ sheet steel are shown in Figure A.2. The base-metal was comprised of martensite islands that were dispersed within a ferrite matrix. On the images, martensite appears white and ferrite appears

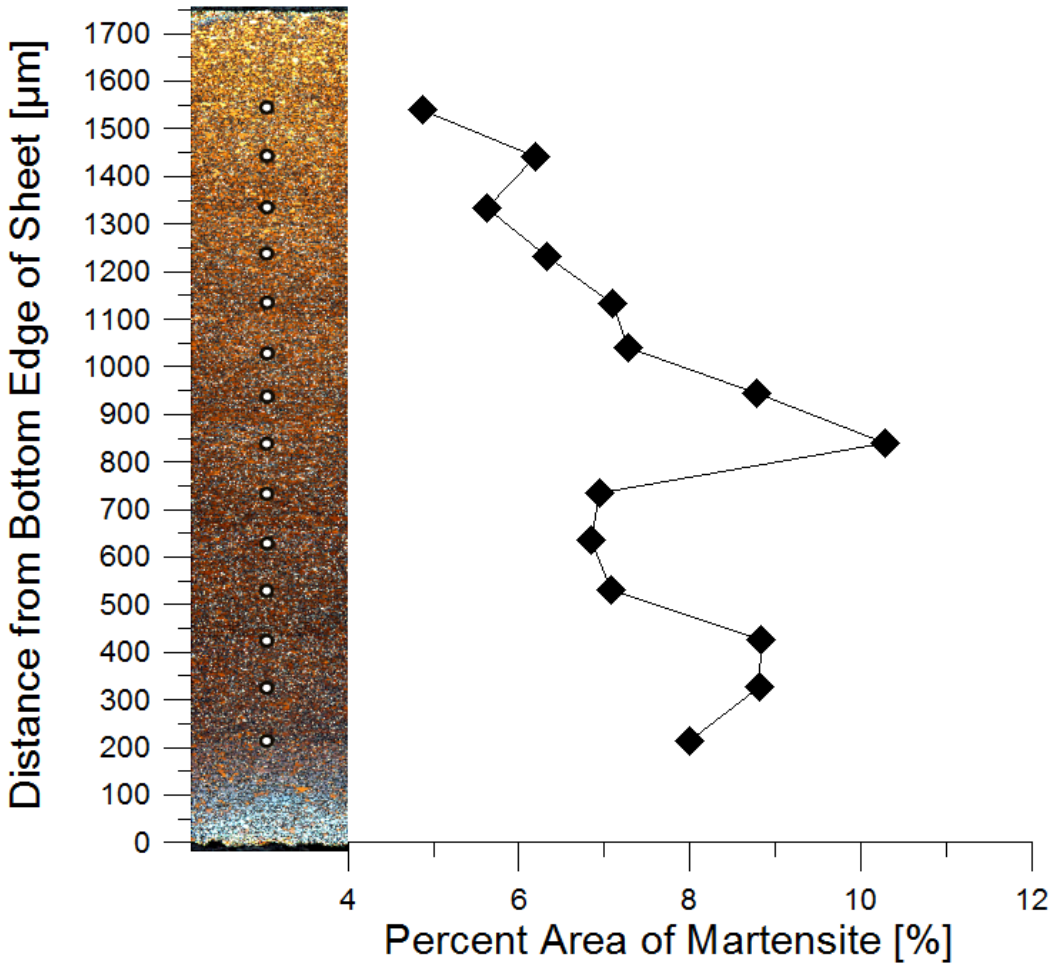

Figure A.1: The percent area of martensite through-thickness profile for the 1.80 mm DP600 '24s' sheet steel.

tan/brown. There was no evidence of the bainite/carbide pockets that had been found in the DP600 '16s' sheet steel. The image in Figure A.2a was located on the upper half of the sheet thickness at the 1550 µm location. This image was measured and found to have a martensite percentage of 4.9%. The image in Figure A.2b was located at the center of the sheet thickness at the 850 µm location. This was the location of the peak value from in the through-thickness profile. This image verified that there was no central band of hardened martensite. The image was measured and found to have a percent area of martensite of 10.3%.

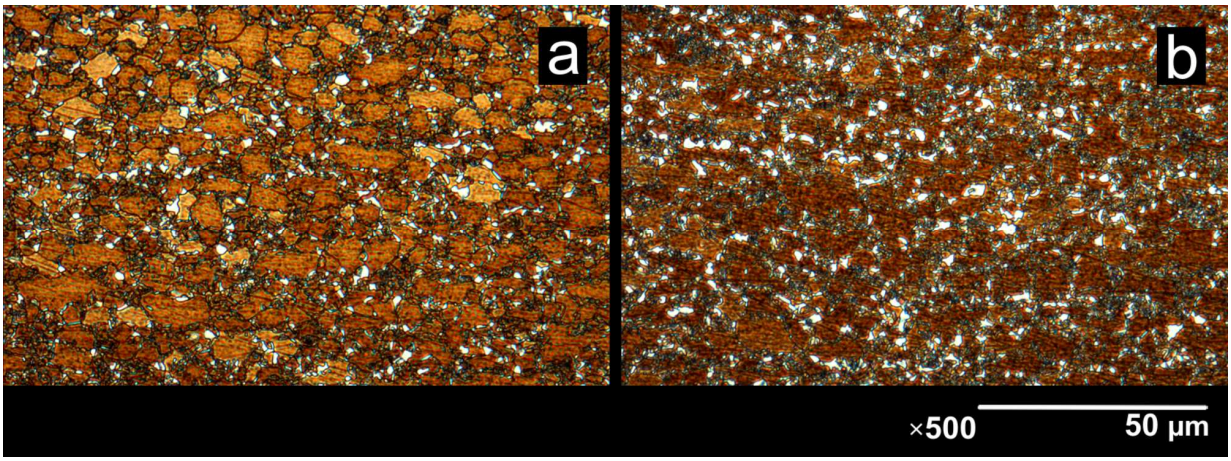

Figure A.2: Examples of the DP600 '24s' BM images that were used to measure the percent area of martensite. Image a) was taken at 1550 µm from the bottom surface and b) at 850 µm.

The Vickers microhardness map for the 1.80 mm DP600 '24s' sheet steel is shown in Figure A.3. The sheet steel showed highest hardness values at the sheet edges. The softest area was located along the center of the sheet thickness. There was no evidence of high hardness along the center of the sheet that could correspond to the peak of martensite percentage that had been shown by the martensite percentage profile. The ATTH was 201 ± 0.5 VHN.

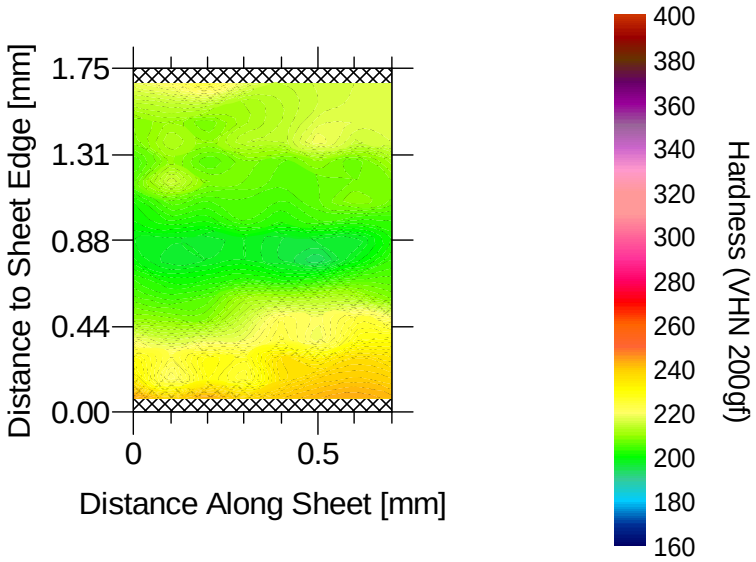

Figure A.3: The microhardness map for the 1.80 mm DP600 '24s' BM.

The through-thickness percent area of martensite profile for the 1.20 mm DP600 '22s' sheet steel is shown in Figure A.4. The profile showed that the upper half of the sheet had a higher martensite percentage than the lower half of the sheet; this result was similar to the BM profile for the 1.65 mm DP600 '16s' sheet steel from Experimental Series 1. There was a peak in the profile at the center of the sheet thickness; this peak corresponded with a central band of martensite that was continuous along the central axis of the sheet steel. The Lepera's tint etch [7] that was used to establish the contrast between martensite islands and the ferrite matrix was non-uniform; the lower half of the sheet was lightly etched compared to the upper half. During analysis it was difficult to achieve images with similar contrasts and the percent area of martensite values could have been affected. This issue was investigated with higher magnification optical images and are shown below. The average through-thickness martensite percentage that was calculated for the DP600 '22s' BM was 7.7 ± 2.0%. The sheet thickness was measured with the optical microscope and found to be approximately 1.16 mm.

Two example images that were analysed to measure the percent area of martensite for the profile in Figure A.4 are shown in Figure A.5. The images were from opposite edges of the sheet thickness. Both images had minimal evidence of bainite/carbide formations, and during image analysis dark regions were included in ferrite measurements. The image in Figure A.5a was on the lower half of the sheet, where the profile had shown a lower percent area of martensite. This image was located at 200 µm from the bottom edge of the sheet. There was good contrast between martensite and ferrite. This image was measured and found to have a martensite percentage of 5.0%. The image in Figure A.5b was located on the upper half of the sheet, where the profile had shown a high percent area of martensite. This image was located at a distance of 950 µm from the bottom edge of the sheet. This image had good contrast between martensite and ferrite, and it visually appeared to contain more martensite than the location in Figure A.5a. This suggested that contrast at different sheet locations was not causing the differences in martensite percentage. This image was measured and found to have a martensite percentage of 9.1%.

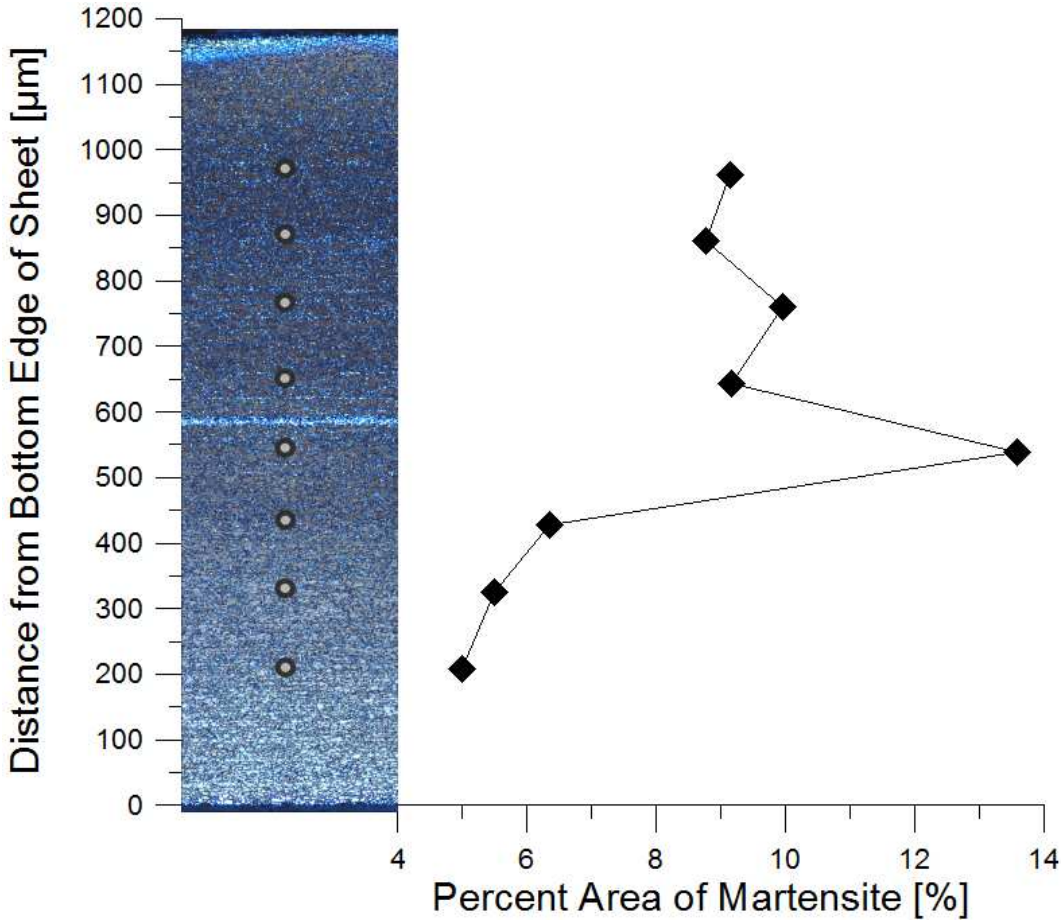

Figure A.4: The percent area of martensite through-thickness profile for the 1.20 mm DP600 '22s' sheet steel.

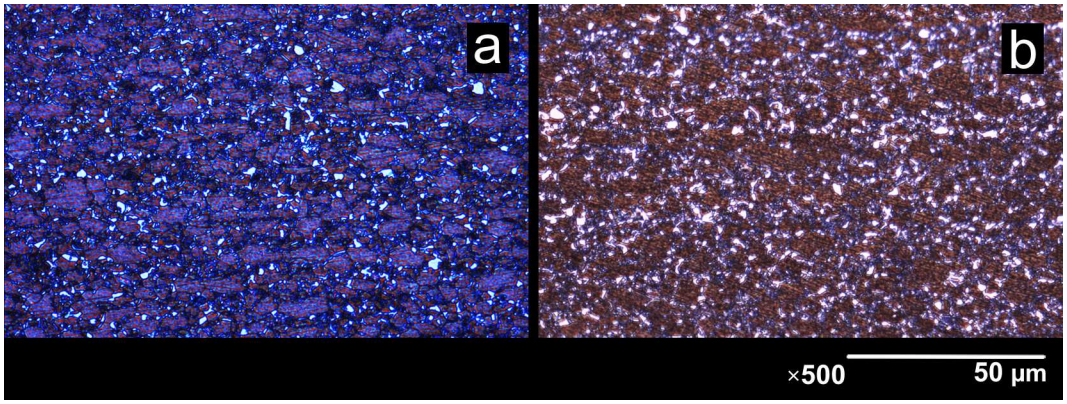

Figure A.5: Examples of the DP600 '22s' BM images that were used to measure the percent area of martensite; a) at 200 µm from the bottom surface and b) at the top surface, 950 µm from the bottom surface.

The Vickers microhardness map for the DP600 ‘22s’ sheet steel is shown in Figure A.6. The result showed similarities to the DP600 ‘16s’ map. The map followed similar trends that were observed from the percent area of martensite profile. The sheet was harder at locations close to the edges when compared to the locations that were surrounding the central band of martensite. The central band was present on the map and represented the hardest region in the sheet steel. The sheet appeared to have asymmetrical through-thickness hardness, and the upper half of the map appeared to contain larger regions of hard material than the lower half. The ATTH was 214 ± 3.1 VHN. This average included the hardened band of martensite that was located along the central axis of the sheet thickness.

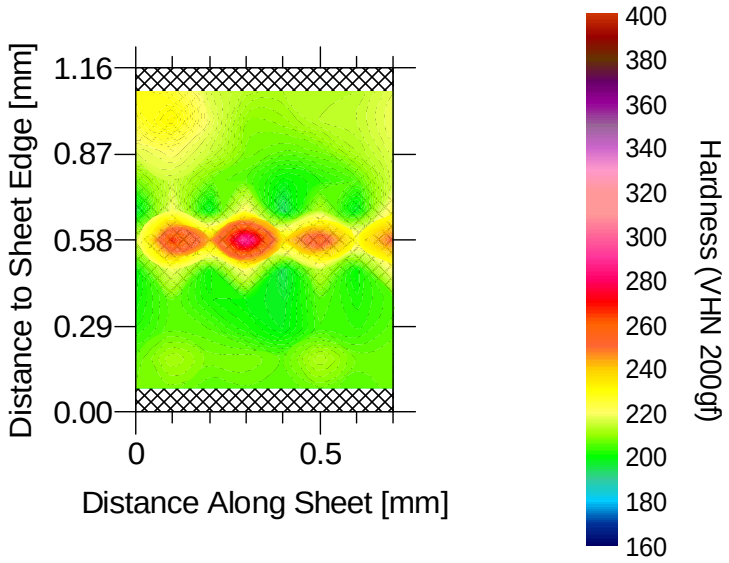

Figure A.6: The microhardness map for the 1.20 mm DP600 ‘22s’ BM.

The percent area of martensite profile for the 1.20 mm DP780 ‘21s’ sheet steel is shown in Figure A.7. The profile was slightly asymmetric, and the upper half showed a slightly higher percent area of martensite than the lower half. Observations of the cross-section showed that the sheet was heavily banded. The majority of the banding was caused by Mn-rich regions that became highly elongated during hot rolling [6]. During intercritical annealing, locations that were Mn-rich had high hardenability and during quenching had formed as martensite bands [6]. There was also evidence of a significant central

band of martensite that had formed during continuous casting. The highest martensite percentage (~25 VHN) was located at the central band of martensite. The average through-thickness for percent area of martensite that was calculated for the DP780 '21s' BM was 20.2 ± 1.9%. The sheet thickness was measured with the optical microscope and found to be approximately 1.24 mm.

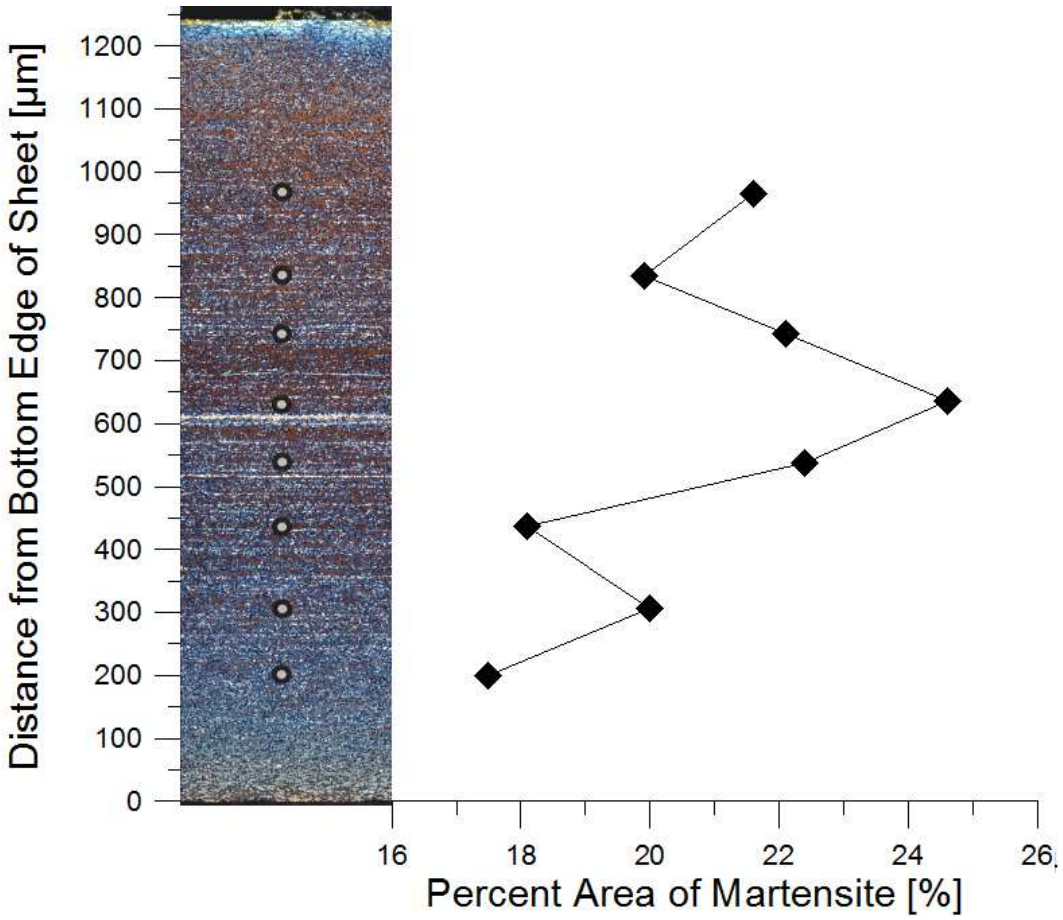

Figure A.7: The percent area of martensite through-thickness profile for the 1.20 mm DP780 '21s' sheet steel.

Example images that were used to measure the percent area of martensite for the DP780 '21s' sheet steel are shown in Figure A.8. The images that were used to measure martensite percentage for the profile had similar contrast. Martensite islands appeared white and the ferrite matrix appeared brown; there was no evidence of bainite/carbide pockets. The image in Figure A.8a was located 970 µm away

from the bottom edge of the sheet. In the image, a band of martensite that had formed due to a prior Mn-rich region is labelled 'A' and indicated with a parallel black dashed line. This image was measured and found to have a martensite percentage of 21.6%. The image in Figure A.8b shows the location of the central band of hardened martensite. The band was continuous along the central axis of the sheet and was much larger than any other bands throughout the sheet thickness. This image was measured and found to have a percent area of martensite of 24.6%.

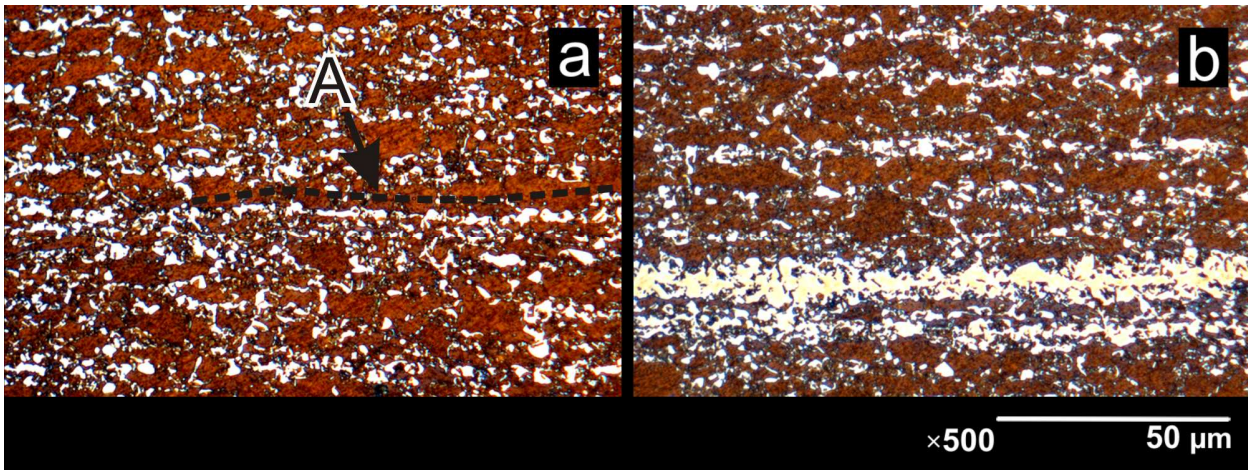

Figure A.8: Examples of the DP780 '21s' BM images that were used to measure the percent area of martensite. a) point 8 at 970 µm from the bottom surface and b) point 5, at the sheet center.

The Vickers microhardness map for the 1.20 mm DP780 '21s' sheet steel is shown in Figure A.9. The resulting map was relatively uniform; although some regions on the upper half appeared softer than regions on the lower half. The map did not have a spike in hardness located along the central axis. The map is shown next to the cross-section with the indentation grid. The cross-section shows that the indents that were located along the central axis had not covered the central band of martensite; the central band is marked 'A'. This was why there was no spike in hardness observed on the map. The ATTH was 254 ± 3.8 VHN.

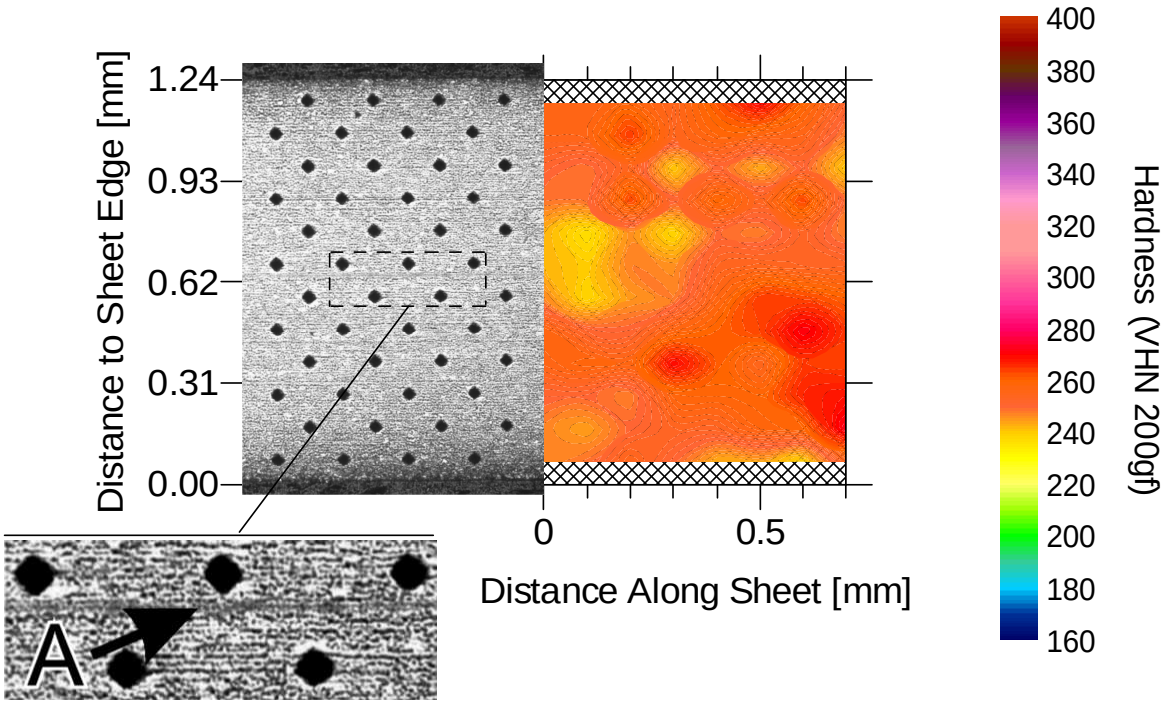

Figure A.9: The microhardness map for the 1.20 mm DP780 '21s' BM.

The percent area of martensite profile for the 1.20 mm DP980 '23s' sheet steel is shown Figure A.10. The locations that were used to measure the martensite percentage are shown on the figure with black circles. The profile was asymmetrical across the thickness of the sheet; this was trend that had appeared on each martensite profile for all of the steels that were tested. For this profile, there was no evidence of a spike in the martensite percentage along the central axis that had been observed in all of the other steels that were tested. The percent area of martensite for the DP980 '23s' sheet steel was significantly higher than for the other steels that were tested. The average through-thickness martensite percentage was 45.6 ± 3.5%. The sheet thickness was measured using the optical microscope and was found to be 1.18 mm.

Example images that were used to measure the percent area of martensite for the DP980 '23s' sheet steel are shown in Figure A.11. The contrast between the images that were used for the percent area analysis was very similar. Martensite appeared white and ferrite/bainite/carbides appeared dark blue and

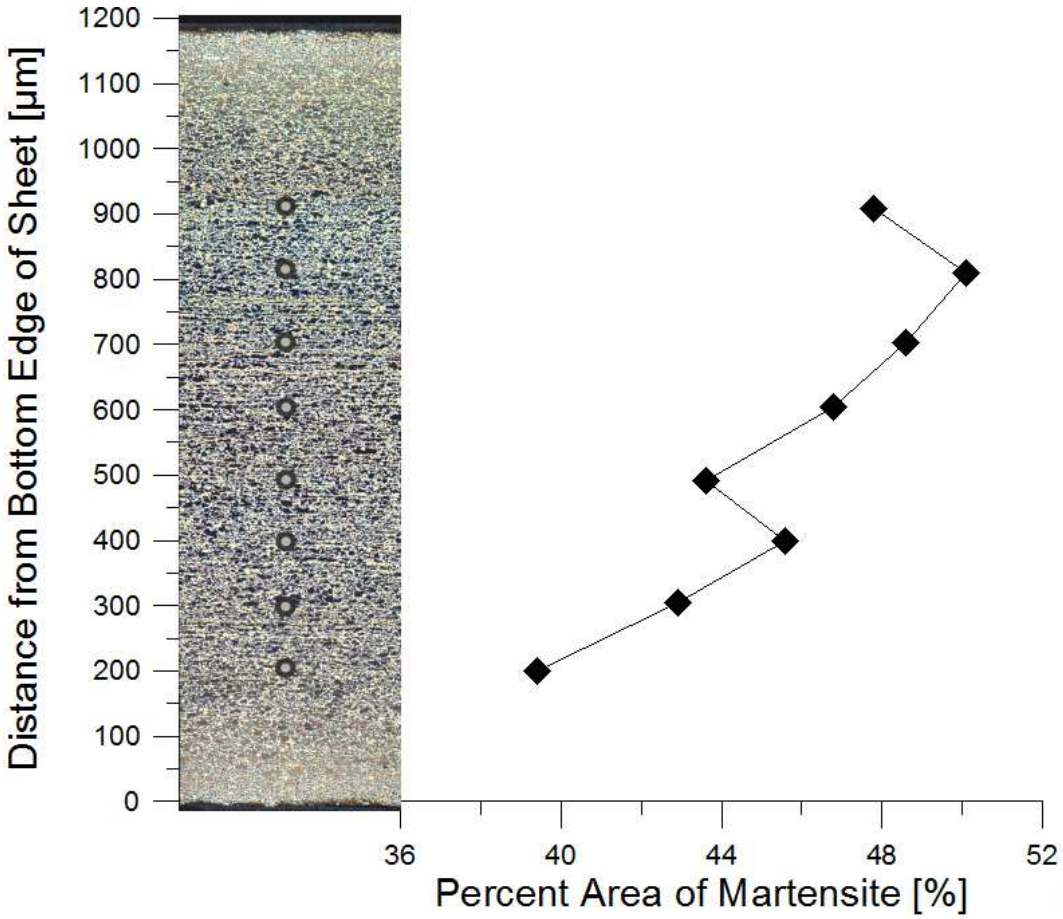

Figure A.10: The percent area of martensite through-thickness profile for the 1.20 mm DP980 '23s' sheet steel.

brown. It was difficult to differentiate between ferrite and bainite/carbides and so these phases were grouped as one. The microstructure that is shown in Figure A.11a was located 200 µm away from the bottom edge of the sheet. It was measured and found to have a martensite percentage of 39.4%. The microstructure that is shown in Figure A.11b was located 700 µm away from the bottom edge of the sheet, above the central axis of the sheet. This image showed that the steel had a severely banded microstructure. The band that is marked 'A' was most likely associated with an Mn-rich region that had elongated during hot rolling [6]. The microstructure from this image was measured and found to have a martensite percentage of 48.6%.

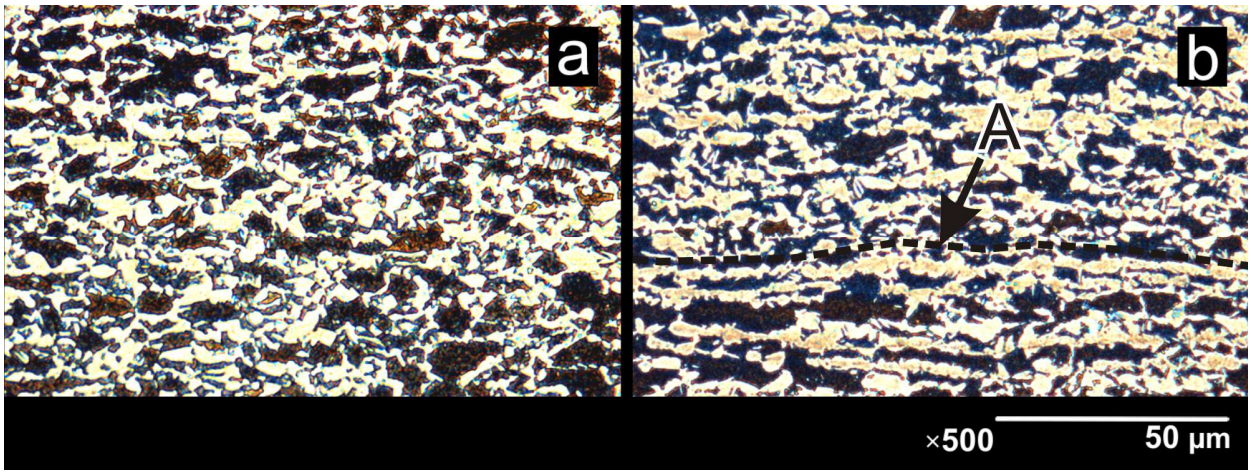

Figure A.11: Examples of the DP980 '23s' BM images that were used to measure the percent area of martensite. Image a) was 200 µm up from the bottom surface and b) was 700 µm.

The Vickers microhardness map for the DP980 '23s' sheet steel is shown in Figure A.12. The result was similar to the DP780 '21s' map; the sheet steel appeared to be relatively uniform and locations of differing hardness were randomly distributed through the thickness of the sheet. There was no evidence of increased hardness along the central axis of the sheet thickness. The ATTH was 330 ± 4.6 VHN.

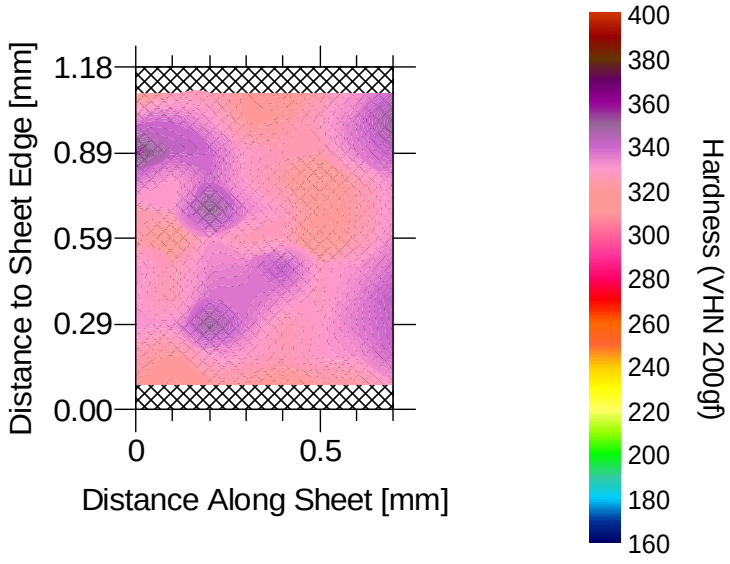

Figure A.12: The microhardness map for the 1.20 mm DP980 '23s' BM.

A summary of the BM properties that were established from the tests found in this section is shown in Table A.1. The table includes the measured sheet thicknesses, which differed from the nominal values. It was important to know the actual sheet thickness because changing the DP sheet steel thickness was suspected to be a method of affecting the fracture location for welded DP sheet steels, and now it was known that the nominal sheet difference of 0.15 mm between the DP600 '16s' and '24s' sheet steels was actually a smaller difference of 0.08 mm. It was also shown that the nominal 1.20 mm thick DP sheet steels varied in thickness, which would affect heat transfer during welding and hence welds made in these steels may have differing weld dimensions. The base metal hardness and area fraction of martensite appeared to follow an expected trend from the literature [5], and the hardness increased as the amount of martensite increased. Lastly, the estimated martensite carbon content is shown, which was calculated using Equation (3.10) from Section 3.4.4:. It appeared that the DP600 '24s' and DP780 '21s' sheet steels had above average martensite hardness, and that the DP980 '23s' had the lowest martensite carbon content. It is unclear in the literature [5,22] if martensite carbon content has a significant effect on DP steel strength, but it has been included here for reference. These properties are in addition to the BM properties found in Table 3.1 and Table 3.2 in Section 3.1 .

Table A.1: Summary of the measured BM properties for the different strength grades of DP sheet steel.

Steel Grade	Measured Sheet Thickness [mm]	Average Martensite Percentage [%]	Average TT Hardness [VHN]	Estimated Martensite C%
1.65 mm DP600 '16s'	1.68	7.8 ± 1.4	201 ± 1.5	0.42
1.80 mm DP600 '24s'	1.75	7.4 ± 1.5	201 ± 0.5	>0.70
1.20 mm DP600 '22s'	1.16	7.7 ± 2.0	214 ± 3.1	0.39
1.20 mm DP780 '21s'	1.24	20.2 ± 1.9	254 ± 3.8	0.64
1.20 mm DP980 '23s'	1.18	45.6 ± 3.5	330 ± 4.6	0.31

Shift in Failure Location: Differing DP600 Sheet Steel Thickness

A comparison to the welds made on 1.65 mm DP600 '16s' sheet steel was made with welds that had similar weld bead geometry but different DP600 sheet steel thicknesses. The 1.80 mm DP600 '24s'

sheet steel was similar to the thickness of the 1.80 mm HSLA '17s' sheet steel, and so the seven selected weld parameter sets from the Phase 2 welding trials could be used to make full penetration bead-on-plate welds for this study. Using these welding parameters, a new group of full penetration bead-on-plate welds was created using the 1.80 mm DP600 '24s' sheet steel.

During this study, the DP600 welding operating window (weldability) was adjusted by increasing the steel sheet thickness to create a more favourable path for heat dissipation away from GMAW-P weld heat input. This method for improving weldability was counter-productive to the main goal of AHSS in automotive, which attempts to lower vehicle weight by decreasing sheet thickness; however, it was suspected that this would improve DP steel weldability.

All of the welds that were made onto the 1.80 mm DP600 '24s' sheet steel are listed in Table A.2. The relative heat input, the weld root penetration, and the Ac_1 and Ac_3 HAZ half-width measurements are listed. All of the welds were full penetration, except for the lowest heat input weld (TB110). This weld was measured and found to have a percent penetration of 93.8%, which was acceptable for the study because the Ac_1 and Ac_3 lines were linear and perpendicular to the sheet edges. The welds have been placed in order from the lowest relative heat input to the highest relative heat input. When the welds were ordered in terms of relative heat input, the HAZ half-width increased in size as the heat input was increased; this was the expected trend for the HAZ width measurements and reflected the results found from welding trials in Experimental Series 1. The weld TB136 was an additional weld that was made at a higher heat input than the welds from the 1.65 mm DP600 '16s' sheet steel study. This weld extended the range of the HAZ half-width measurements so that there was a weld that had similar HAZ width to the highest heat input weld (TB88) from Experimental Series 1. The basis for comparison for this study was between the HAZ width and the sheet thickness for the two different DP600 sheet steels.

Although the weld parameters that were used during this study were the same as those used for the Phase 2 welding trials, there were some discrepancies that were found in the power input data when compared to the observations that had been made during the welding of the 1.65 mm DP600 '16s' sheet

Table A.2: The weld parameter sets that were used to make bead-on-plate welds onto the 1.80 mm DP600 '24s' sheet steel.

Weld Code	Weld Parameters [Trim, TS, WFS, CTWD]	H_{rel} [J/mm]	Root Penetration [%]	Average Ac_1 HAZ Half-Width [mm]	Average Ac_3 HAZ Half-Width [mm]
TB110	[1.00, 19.4 mm/s, 169 mm/s, 14.3 mm]	186	93.8%	4.59	3.84
TB112	[1.00, 23.3 mm/s, 254 mm/s, 14.3 mm]	218	114.7%	5.33	4.43
TB111	[1.00, 20.3 mm/s, 212 mm/s, 14.3 mm]	226	115.7%	5.52	4.55
TB115	[1.15, 22.4 mm/s, 212 mm/s, 14.3 mm]	----	102.4%	5.59	4.63
TB114	[1.15, 21.2 mm/s, 212 mm/s, 14.3 mm]	261	102.8%	5.93	4.95
TB113	[1.15, 19.1 mm/s, 169 mm/s, 14.3 mm]	288	114.5%	6.39	5.57
TB116	[1.25, 19.1 mm/s, 169 mm/s, 14.3 mm]	324	108.1%	6.87	5.79
TB136	[1.25, 21.1 mm/s, 212 mm/s, 14.3 mm]	366	117.7%	7.31	6.19

steel. The relative heat input that was calculated for weld TB112 was approximately 20 J/mm lower than weld TB107, which had been made with the same weld parameters during trials Experimental Series 1. A similar difference was observed between weld TB114 and weld TB94 and between weld TB116 and weld TB88. These differences caused the order of the welds to change from what had been observed during the 1.65 mm DP600 '16s' sheet steel welding trials, when they were placed in order of relative heat input. These discrepancies were not investigated further because the HAZ half-width measurements retained the expected linear trend when compared with relative heat input and, therefore, met the initial goal and the desired basis for comparison.

The average Ac_1 HAZ half-width measurements are plotted against the calculated relative heat inputs from all of the welds that were made onto the 1.80 mm DP600 '24s' sheet steel, and they exhibited the linear trend that is shown in Figure A.13. The chart includes the curve fit that represents the linear trend that had been observed in the 1.65 mm DP600 '16s' sheet steel welding trials. The difference in the HAZ half-width between the two sheet steels was approximately 0.5 mm. The expectation was that a higher relative heat input would be required for the thicker 1.80 mm DP600 '24s' sheet steel to cause a HAZ failure location during uniaxial tensile testing. The difference between the two linear curve fits was relatively small and it was expected that there would be HAZ failure in the higher heat input welds.

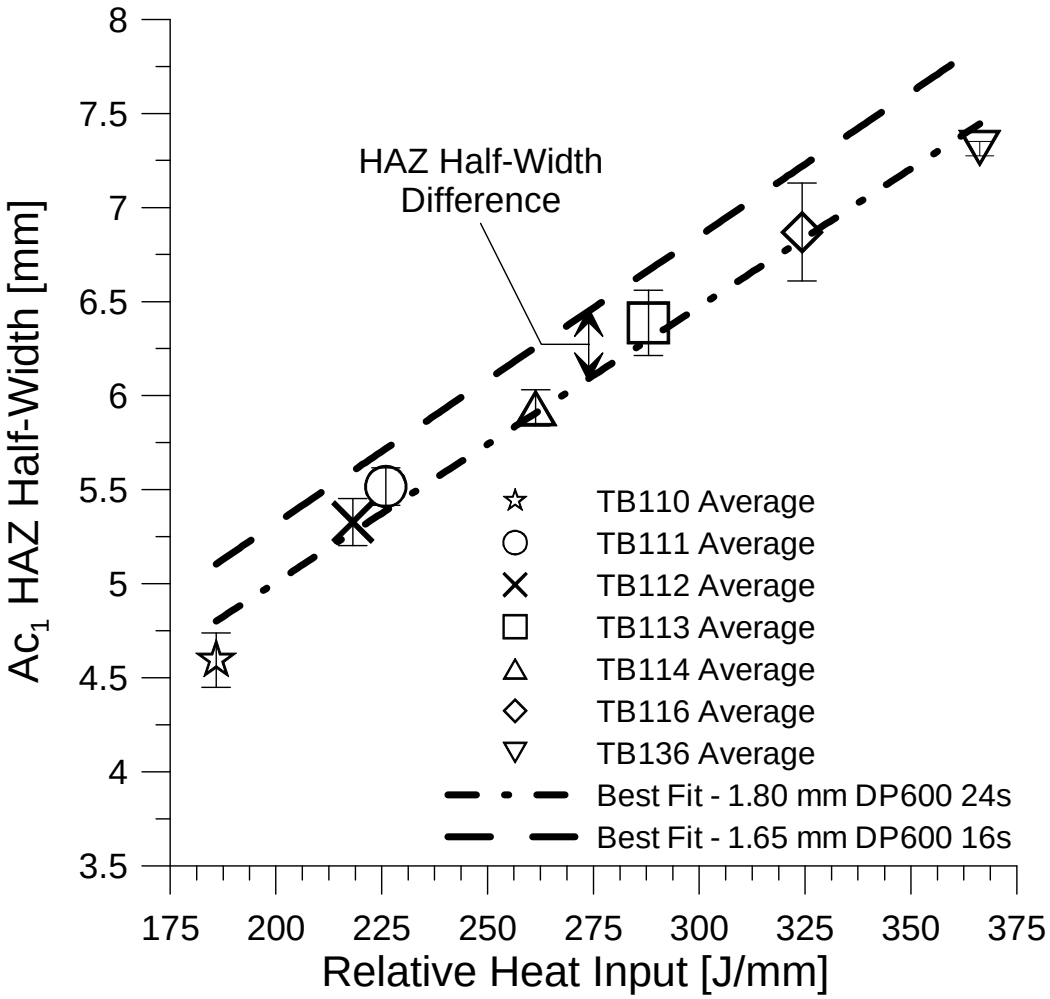

Figure A.13: The plot shows how the Ac_1 HAZ half-width was related to the relative weld heat input. An expected linear trend was observed.

An example image that was used to measure the weld HAZ half-width is shown in Figure A.14a. A detailed microstructural analysis of the 1.80 mm DP600 '24s' weld HAZ was not conducted. The HAZ half-widths were measured from samples that had been ground to 1200 fine grit paper and then etched with 2% Nital to attain a macro etch that was suitable for measuring the weld HAZ. This was done to eliminate the time required for polishing. The accuracy of the HAZ half-width measurements was comparable to welds that had been polished and then etched; however, discrepancies could not be evaluated at optical microscope magnifications greater than ×50. The weld that is shown was the highest heat input weld (TB136) from the study. An example measurement is shown, which was found to be

7.30 mm. The weld was measured to have an average Ac_1 HAZ half-width of 7.31 ± 0.04 mm. The image that is shown in Figure A.14b is from the highest heat input weld (TB88) from Experimental Series 1. This weld had been etched with 2% Nital after being polished with 1 µm diamond polish and a visual comparison between the two weld images shows that identification of the Ac_1 and Ac_3 lines was similar for both preparation techniques. An example measurement is shown, which was found to be 7.49 mm. The weld was measured to have an average Ac_1 HAZ half-width of 7.44 ± 0.19 mm. This weld had provided 100% HAZ failure during uniaxial tensile testing. The two welds had relatively similar weld geometry, and only differed by 0.07 mm in the measured sheet thickness and by approximately 0.14 mm in Ac_1 HAZ half-width. The expectation was that the TB136 weld would provide a similar HAZ failure during uniaxial tensile testing; however, because the sheet steel was slightly thicker, it was thought that there was potential for tensile specimens to fracture in the BM failure location.

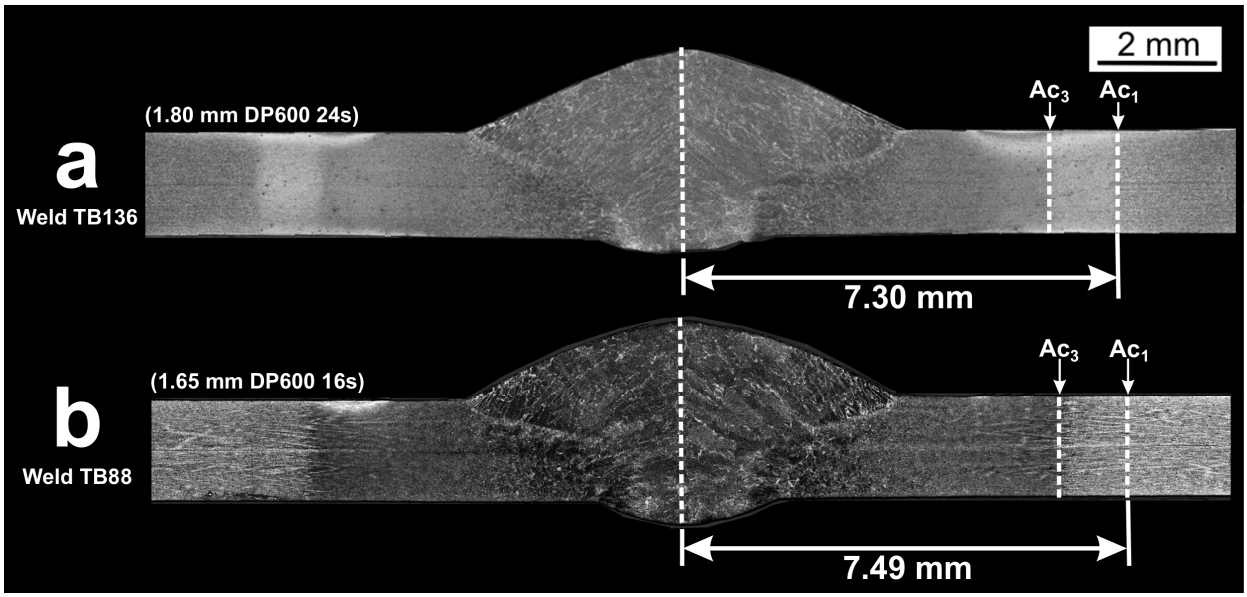

Figure A.14: A comparison between two welds that were measured to have similar average Ac_1 HAZ half-widths but were from different sheet thicknesses. The image in a) was etched after grinding with 1200 fine grit paper and the image in b) was etched after polishing with 1 µm diamond polish; both were etched with a 2% Nital etchant.

The images in Figure A.15 show a comparison between the top and bottom surfaces of two welds that were made with the same weld parameters. The weld parameters that were used for both of the welds

were: 1.15 trim, 22.4 mm/s TS, 212 mm/s WFS, and 14.3 mm CTWD. From the images, the welds appeared to be similar. The zinc melting (420°C) isotherms, which are marked with white dashed lines, showed similar width for both weld HAZ's. The root penetration for both welds was visible at the bottom surface of the sheet steel coupons. The weld that is shown in Figure A.15a was made onto the 1.80 mm DP600 '24s' sheet steel. It had a calculated relative heat input of 288 J/mm. The average Ac_1 HAZ half-width for this weld was 6.39 mm. The weld that is shown in Figure A.15b was made onto the thinner 1.65 mm DP600 '16s' sheet steel during Experimental Series 1. It had a calculated relative heat input of 297 J/mm. The average Ac_1 HAZ half-width for this weld was 6.87 mm. For these welds, there was a difference in relative heat input of 9 J/mm, a measured sheet thickness difference of 0.07 mm (from the base-metal characterization), and a difference in Ac_1 HAZ half-width of 0.48 mm. The welds had similar relative heat input, but were each made on a different sheet thickness of DP600 steel. The difference in sheet thickness affected the rate of heat transfer away from the weld during welding. The thicker

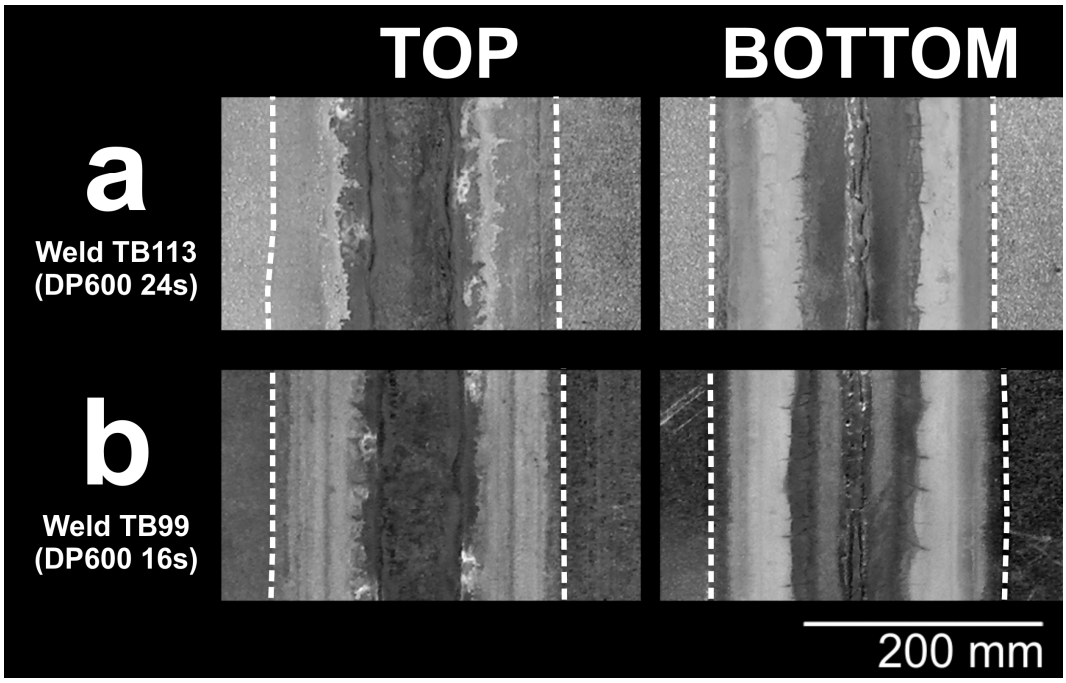

Figure A.15: Example images that show a comparison between two welds that were made using the same welding parameters but were on different thickness DP600 sheet steels. The two welds had similar relative heat input.

1.80 mm DP600 ‘24s’ sheet steel acted as a more effective heat sink and hence its measured HAZ width was smaller than HAZ width measured on the thinner 1.65 mm DP600 ‘16s’ sheet steel. This was observed for other welds in the study; however, this comparison could not be made directly between all of the welds and the original welds from Experimental Series 1, because the calculated values for relative heat input showed too much fluctuation.

The average width of the IC zone was observed to be larger in the thinner 1.65 mm DP600 ‘16s’ sheet steel when it was compared to the IC zone width of a weld made at a similar relative heat input on the 1.80 mm DP600 ‘24s’ sheet steel; this general trend is shown in Figure A.16. On the chart the

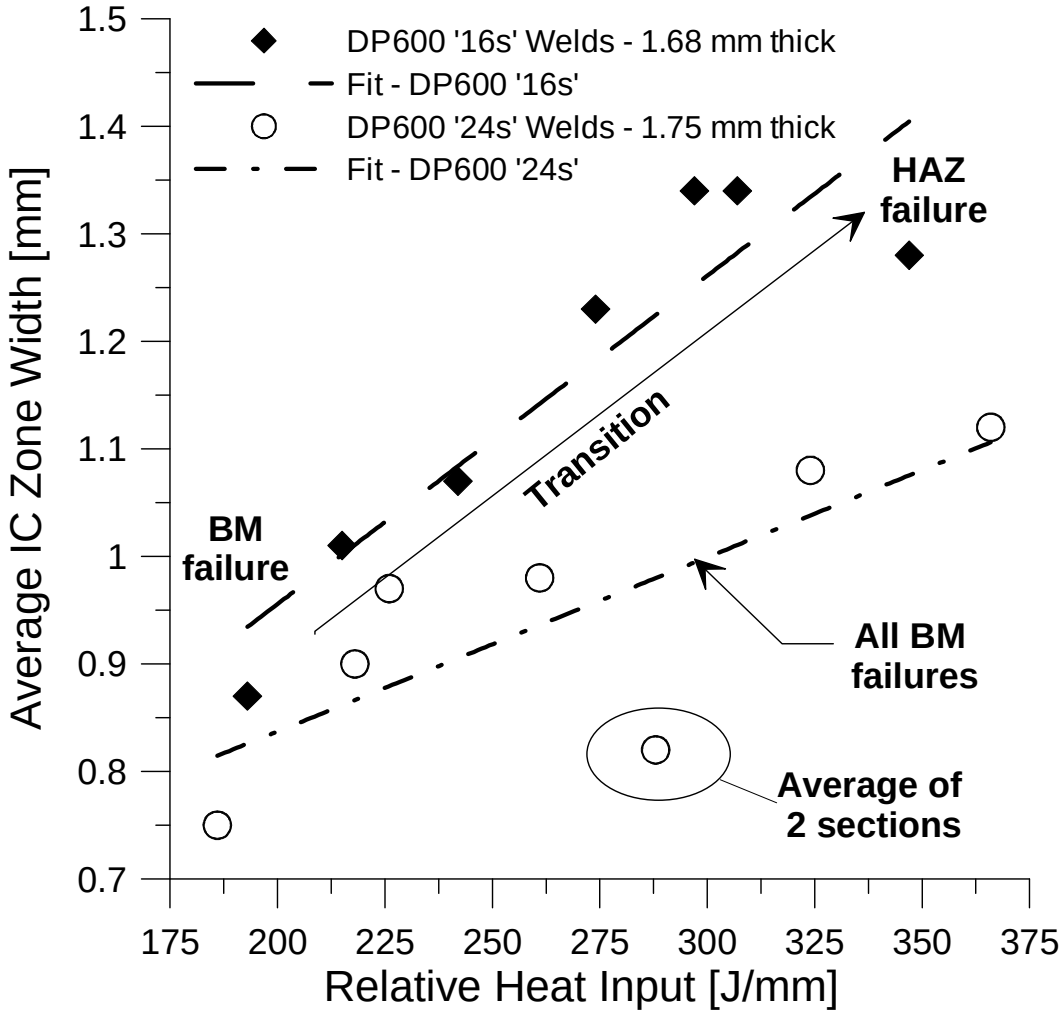

Figure A.16: The general trend of the IC zone width that was observed for both the 1.65 mm DP600 ‘16s’ welds and the 1.80 mm DP600 ‘24s’ welds.

average IC HAZ widths of individual welds are shown for both sheet steels and linear curve fits are shown. The difference in IC zone width increased with increased relative heat input. This was a goal of the study, which showed that microstructural regions were reduced in width due to an increase in sheet steel thickness. It was suspected that this trend would also be reflected in the width of other microstructural regions within the weld HAZ. It was suspected that the subcritical softened zone width would be reduced in the 1.80 mm DP600 '24s' welds and that this reduction in width could shift the failure location from a HAZ failure into the BM failure location during uniaxial transverse weld tensile testing.

The welds were machined into uniaxial transverse weld tensile specimens and were loaded to failure to observe the failure location. An example image of a set of specimens that had been loaded to failure is shown in Figure A.17. Three specimens were tested for each weld. The uniaxial transverse weld tensile tests for all of the transverse welded tensile specimens in the study had fractured in the BM failure location, i.e., there were no HAZ failure locations observed in any of the tensile tests. This was an unexpected result. The weld that is shown in the figure had the second largest HAZ width. This weld (TB116) had been made using the same weld parameters as the highest heat input weld (TB88) from Experimental Series 1. After observing that the TB116 weld had fractured in the BM failure location

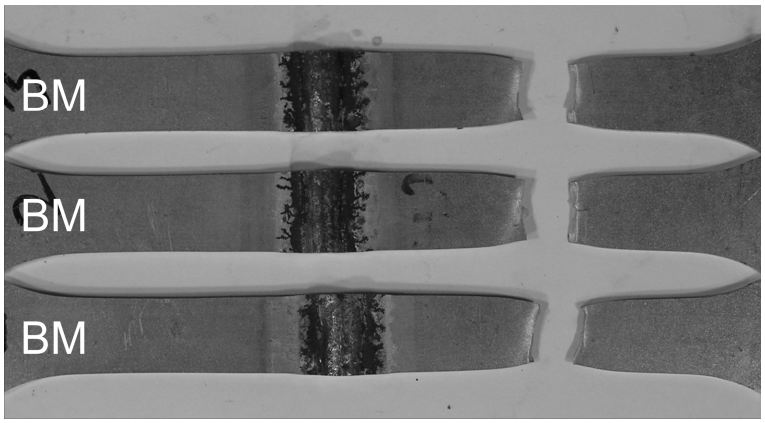

Figure A.17: An example image showing the 100% BM failure location that was observed for all of the uniaxial transverse weld tensile specimens. This weld (TB116) was made the highest heat input weld parameters from Experimental Series 1 onto the 1.80 mm DP600 '24s' sheet steel.

through 100% of uniaxial tensile tests, the weld TB136 was made to include a higher heat input weld in attempt to cause a HAZ failure location; however, the TB136 weld also fractured in the BM failure location through 100% of testing. The uniaxial tensile tests were not continued after TB136 had shown 100% BM failure.

Although there was no transition of failure location within the set of 1.80 mm DP600 '24s' sheet steel welds, the failure location appeared to have shifted away from the HAZ and into the BM when compared with the thinner 1.65 mm DP600 '16s' sheet. This was the general result that had been expected, which suggested that the increase in sheet thickness had prevented a HAZ failure. The increase in sheet thickness represented a more favourable path for heat dissipation during welding that was reflected in narrowed microstructural zones within the weld HAZ. It was important to note that this shift in failure location appeared to have been caused by relatively small difference in sheet thickness, which was measured to be 0.07 mm or approximately 4%.

To complete this portion of the study, the highest heat input weld (TB136) was cross-sectioned and used to create a Vickers microhardness map, which is shown in Figure A.18. The weld cross-section is shown in Figure A.18a. The indentation grid covered from just below the Ac_3 line to the BM. The grid orientation was relatively parallel to the sheet edges. The microhardness map is shown in Figure A.18b. There was definite evidence of softening in the subcritical zone immediately adjacent and below the Ac_1 line. Uniform softening was measured on the map to be approximately 2.3 mm away from the Ac_1 line. There was some evidence of subcritical hardening, which is labelled 'A' on the map. This suggested that the steel had been affected by the weld heat input in a similar fashion as the welds made onto the 1.65 mm DP600 '16s' sheet steel from Experimental Series 1. It further supported the evidence that subcritical hardening was occurring in the GMAW-P DP600 weld HAZ. An unexpected increase in hardness was observed out towards the BM at the location that is labelled 'B'. This increase in hardness was isolated and was non-uniform through the sheet thickness. It was suspected that this was not a result of weld heat input, and was rather a spike in hardness due to the initial steel processing or handling during weld

preparation. A microstructural analysis was not made for this area because it appeared to be a 'random' occurrence. There was also a significant increase in hardness observed in the IC region of the HAZ. This was the same observation that had been made from Experimental Series 1 for the 1.65 mm DP600 '16s' sheet steel.

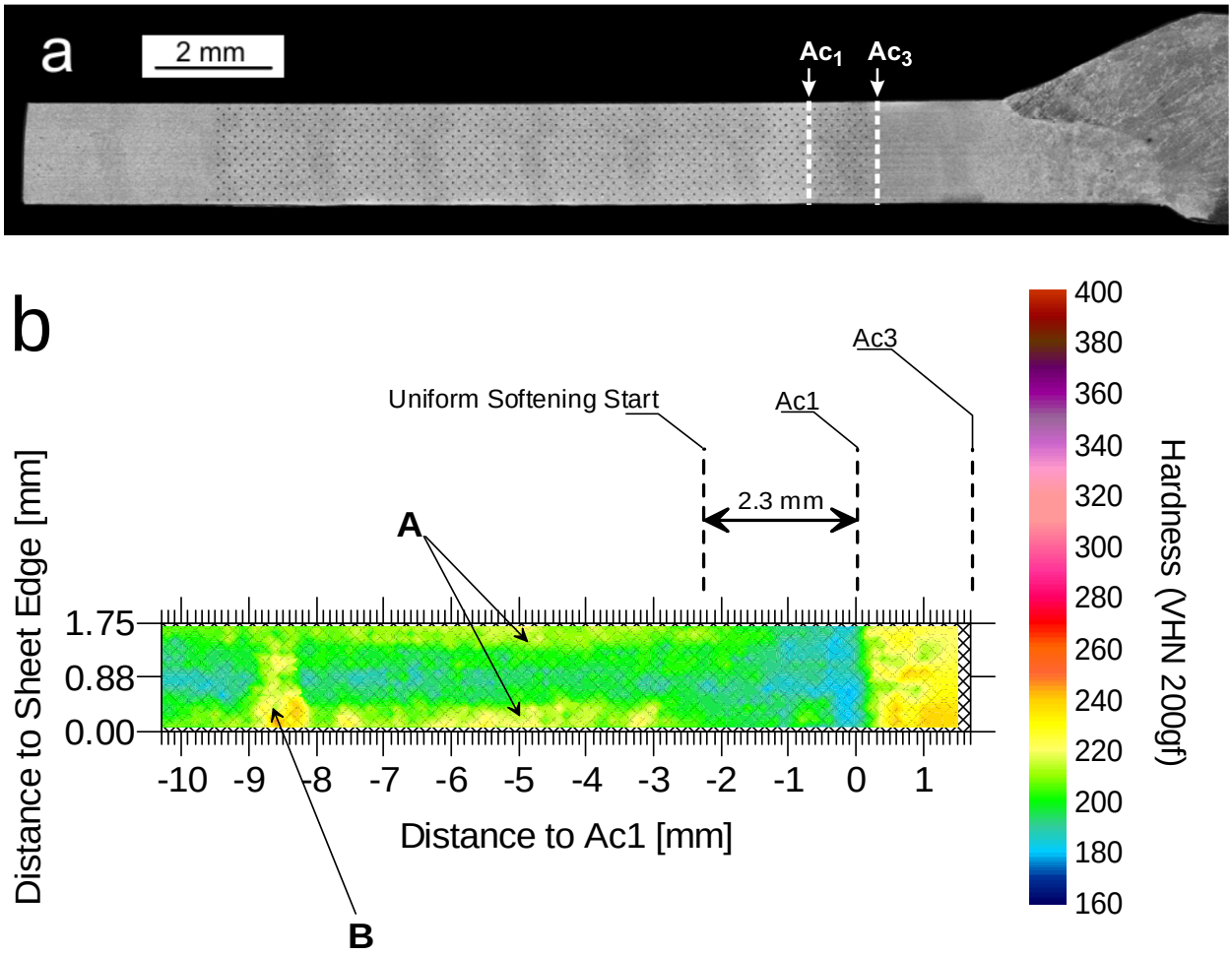

Figure A.18: The microhardness map for the TB136 1.80 mm DP600 '24s' weld HAZ. The image in a) shows the grid of indentations on the TB136 weld cross-section and b) shows the mapped microhardness.

The ATTH was calculated for the TB136 weld HAZ using the data from the microhardness map and the profile is shown in Figure A.19. A curve was fitted to the data to create a general trend that the ATTH had followed. This profile was very similar to the profiles from Experimental Series 1 and the

same general trend was observed as had been found for the low heat input (TB87) weld and the high heat input (TB88) weld. The regions that were identified from the profiles in Experimental Series 1 could also be identified on the TB136 profile, and the BM, H-SC, S-SC, and the IC zones are labelled on the profile.

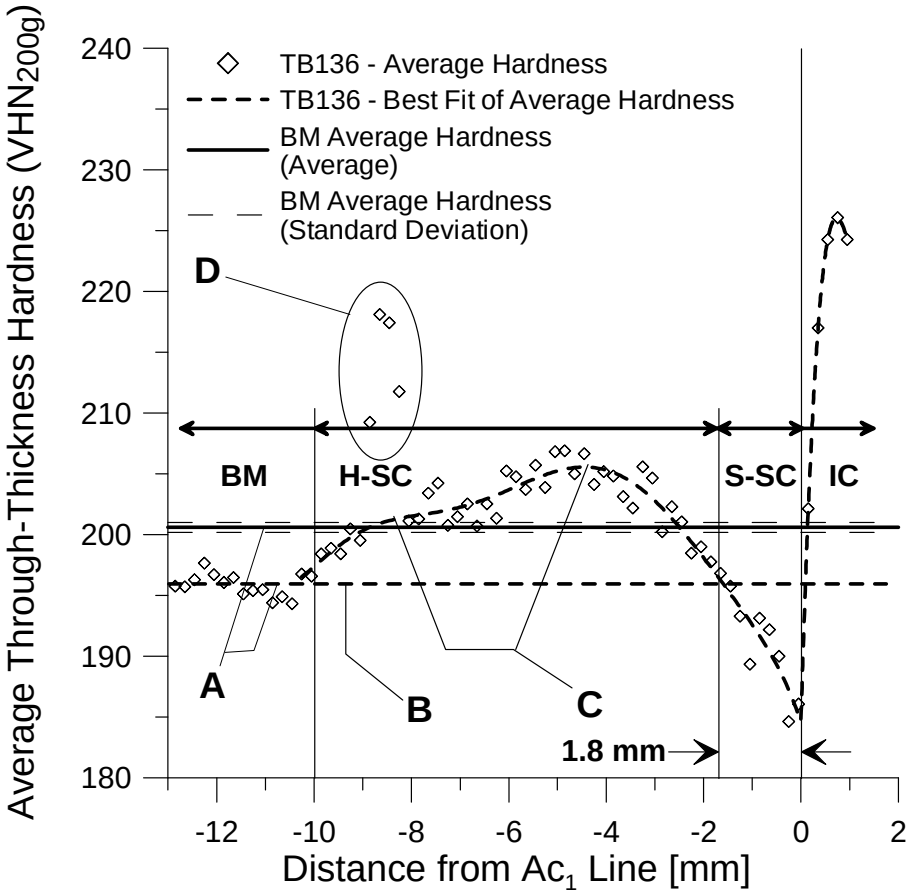

Figure A.19: The average through-thickness hardness profile for the highest heat input (TB136) weld that was made onto the 1.80 mm DP600 '24s' sheet steel. Four characteristic regions of hardness (IC, S-SC, H-SC, and BM) were identified and are marked on the profile.

There was a discrepancy in the average through-thickness BM hardness from the unwelded BM microhardness map when compared to the TB136 average through-thickness profile. This discrepancy is marked on the chart with an 'A'. The unwelded BM ATTH had been found to be 201 ± 0.5 VHN. The approximate BM hardness value that was observed for the TB136 ATTH profile was 197 VHN, which is labelled with a 'B' on the profile. This was a minimal difference of 4 VHN in the average hardness. From the BM characterization, the microhardness map for the unwelded BM had appeared to have higher

hardness on one edge of the sheet thickness, and so it was believed that the indent grid orientation may have caused this discrepancy. If the indentation grid had covered a greater portion of the edge that had higher hardness then the ATTH would have appeared harder. The approximate welded average BM hardness value of 196 VHN was used as the value for comparison with other regions across the TB136 weld HAZ profile. This region was located approximately 10 mm away from the Ac_1 line.

There was further evidence that a hardened subcritical region did exist in the TB136 weld HAZ of the 1.80 mm DP600 '24s' sheet steel. This region appeared to have two plateaus of peak hardness, which are labelled 'C'. These plateaus had also been observed in the TB87 and TB88 profiles from Experimental Series 1 and so this new profile supported the observations that had been made. From the TB136 H-SC region, there appeared to be an approximate increase in ATTH of 9 VHN when compared to the welded BM hardness value. The spike in hardness that had been observed on the TB136 microhardness map is labelled 'D'. These ATTH data points were not used to create the curve fit and were not used for further analysis.

There was significant evidence that subcritical softening had occurred immediately adjacent to the Ac_1 line. This was significant because the weld had not failed in the softened zone. The width of the TB136 S-SC region was measured using the profile and was found to be approximately 1.8 mm wide; this measurement was made from the Ac_1 line to the location where the profile curve fit dropped below the welded BM ATTH. This was smaller than the softened zone width from the highest heat input (TB88) weld from Experimental Series 1. This supported the belief that the microstructural regions were narrower for similar relative heat input welds that were made onto the thicker 1.80 mm DP600 '16s' sheet steel. From the profile, a decrease in ATTH was measured and found to be approximately 12 VHN when compared to the welded BM average hardness; this was similar to the highest heat input (TB88) weld from Experimental Series 1.

The IC region showed a significant spike in hardness. This was similar to the welds from Experimental Series 1 and was most likely due to an increase in martensite percentage. The peak hardness in this region was measured and found to be approximately 30 VHN higher than the weld BM average hardness.

From the observations that were made for this study, the welds that were made onto the 1.80 mm DP600 '24s' sheet steel appeared to be very similar to the welds made onto the 1.65 mm DP600 '16s' sheet steel from Experimental Series 1. The nominal BM composition of both steels was similar, the measured BM martensite percentages were similar, and the Vickers microhardness maps and average through-thickness profiles were similar. These similarities suggested that the failure mechanism during uniaxial transverse weld tensile testing was most likely similar and that a combination of a high hardness in the IC region and support from the H-SC region could have prevented failure within the S-SC. This study also provided evidence that a relatively small increase in sheet thickness had increased the likelihood for a BM failure location to occur during uniaxial transverse weld tensile testing. The increase in sheet thickness represented a more favourable path for heat dissipation away from the weld zone.

Shift in Failure Location: Differing DP Sheet Steel Strength

In this study, the failure mode of three DP sheet steels with similar thickness and differing grades of strength were compared in order to examine whether or not a shift of failure location would occur from a BM failure location to HAZ failure location during uniaxial tensile testing due to an increase in the percentage of martensite in the BM. The steels that were used during this study were: the 1.20 mm thick DP600 '22s' sheet steel, 1.20 mm DP780 '21s' sheet steel, and 1.20 mm DP980 '23s' sheet steel. Although the nominal thickness of these sheet steels was 1.20 mm, the actual measured thicknesses were found to be different. The DP600 '22s' sheet steel had a measured thickness of 1.16 mm, the DP780 '21s' sheet steel had a measured thickness of 1.24 mm, and the DP980 '23s' sheet steel had a measured thickness of 1.18 mm. These differences in sheet steel thickness were not ideal for the study;

however, this difference was not considered significant when compared to the significant differences in the percent area of martensite in the sheet steel BM.

During this study, a shift in the DP welding operating window (weldability) was observed by comparing the failure mode of welded DP steel sheets that had similar sheet thickness and different grades of strength. There was no expectation to prevent a HAZ failure mode in the high strength DP780 or DP980 sheet steels; however, by comparison to the DP600 failure mechanism and weld HAZ hardness properties, it was believed that some insight into preventing higher strength DP steel HAZ fracture could be established. The concepts developed during Experimental Series 1 for a DP600 weld failure, specifically the failure mechanism (brazed joint analogy) that was suggested, were compared with the higher strength grades of DP steel. The different grades of strength were associated with differing percentages of BM martensite. Steel with a higher area fraction of martensite in the BM had a higher strength. Individual martensite islands from each grade of steel most likely had different chemical compositions and potentially different morphology and mechanical properties; however, there was no attempt to determine the mechanical properties of individual martensite islands.

The goal of this study was to create S-SC regions of similar size and geometry that had different prior BM percentages of martensite. This would create different physical metallurgical conditions for martensite tempering by increasing the percentage of martensite (from steel to steel); this was the mechanism that was used to shift failure location from the BM to the HAZ. The geometry and size of the S-SC was suspected to be a significant factor for causing HAZ fracture during uniaxial tensile testing, and it was expected that an S-SC region with a higher prior BM martensite percentage would incur more significant local softening and, therefore, be more likely to fracture in the S-SC region.

The 1.20 mm DP600 ‘22s’ sheet steel was also used to compare with the 1.65 mm DP600 ‘16s’ sheet steel from Experimental Series 1 to observe a shift of failure due to the difference in sheet thickness (similar to the study of the previous section); this comparison was used to observe a shift of failure

location from BM to the HAZ due to a decrease in sheet thickness. The 1.20 mm DP600 ‘22s’ sheet steel had a significant difference in sheet thickness when compared to the 1.65 mm DP600 ‘16s’ sheet steel. The 1.20 mm DP600 ‘22s’ sheet steel required a new set of welding parameters in order to make full penetration bead-on-plate welds.

The new weld parameters that were used to make full penetration bead-on-plate welds onto 254 mm × 203 mm 1.20 mm DP600 ‘22s’ sheet steel coupons are shown in Table A.3. There were a total of 6 bead-on-plate welds made. The weld parameters for these 6 welds are shown along with the calculated relative heat input, the percent root penetration measurement, and the Ac_1 and Ac_3 HAZ half-width measurements. Only two of the welds were cross-sectioned to measure the root penetration and the HAZ half-widths. These two welds represented a low heat input (TB117) weld and a high heat input (TB120) weld. The low heat input (TB117) weld had a relative heat input of 119 J/mm and was measured and found to have a percent root penetration of 91.9%, which satisfied the requirement for full root penetration. This weld had an average Ac_1 HAZ half-width of 4.05 ± 0.55 mm. The high heat input (TB120) weld had a relative heat input of 132 J/mm and a measured root penetration of 119.4%. The measured average Ac_1 HAZ half-width was 4.85 ± 0.10 mm. The relative heat input difference between these two welds was approximately 13 J/mm and the average Ac_1 HAZ half-width difference was approximately 0.80 mm. The two welds (TB117 and TB120) that were cross-sectioned and measured for HAZ width were the only welds made onto 1.20 mm DP600 ‘22s’ sheet steel that were tested with an uniaxial transverse weld tensile test.

The weld parameters that were established from the 1.20 mm DP600 ‘22s’ sheet steel bead-on-plate welds were used without modification to make similar welds onto 1.20 mm DP780 ‘21s’ sheet steel coupons and onto 1.20 mm DP980 ‘23s’ sheet steel coupons. The results for the 1.20 mm DP780 ‘21s’ sheet steel welds are shown in Table A.4 and the results for the 1.20 mm DP980 ‘23s’ sheet steel welds are shown in Table A.5. The weld parameters and the calculated relative heat input are shown for all of

Table A.3: The weld parameter sets that were used to make bead-on-plate welds onto the 1.20 mm DP600 '22s' sheet steel.

Weld Code	Weld Parameters [Trim, TS, WFS, CTWD]	H_{rel} [J/mm]	Root Penetration [%]	Average Ac_1 HAZ Half-Width [mm]	Average Ac_3 HAZ Half-Width [mm]
TB117	[1.00, 25.4 mm/s, 127 mm/s, 14.3 mm]	119	91.9%	4.05	3.41
TB118	[1.05, 27.5 mm/s, 127 mm/s, 14.3 mm]	122	----	----	----
TB119	[1.10, 29.6 mm/s, 127 mm/s, 14.3 mm]	125	----	----	----
TB120	[1.00, 28.8 mm/s, 169 mm/s, 14.3 mm]	132	119.4%	4.85	4.02
TB121	[1.05, 31.8 mm/s, 169 mm/s, 14.3 mm]	133	----	----	----
TB122	[1.10, 34.7 mm/s, 169 mm/s, 14.3 mm]	134	----	----	----

the welds. Only two welds were selected to be cross-sectioned and measured for root penetration and Ac_1 and Ac_3 HAZ half-width for each set of welds on the two different DP sheet steels; these selected welds were made with the same weld parameters as the selected welds (TB117 and TB120) from the 1.20 mm DP600 '22s' sheet steel. This selection provided a high and low heat input weld to be used for comparison during the study. For the 1.20 mm DP780 '21s' sheet steel, the low heat input (TB130) weld had a heat input of 116 J/mm. It was measured and found to have a root penetration of 68.0% and an average Ac_1 HAZ half-width of 3.74 ± 0.11 mm. The root penetration was lower than the TB117 weld because there was an increase in the measured sheet thickness of approximately 0.08 mm. The high heat input (TB133) weld had a relative heat input of 133 J/mm. It was measured and found to have a root penetration of 100.2% and an average Ac_1 HAZ half-width of 4.51 ± 0.01 mm. For the 1.20 mm DP980 '23s' sheet steel, the low heat input (TB123) weld had a heat input of 114 J/mm. It was measured and found to have a root penetration of 67.8% and an average Ac_1 HAZ half-width of 4.13 ± 0.12 mm. The high heat input (TB126) weld had a heat input of 130 J/mm. It was measured and found to have a root penetration of 101.4% and an average Ac_1 HAZ half-width of 4.28 ± 0.07 mm. The TB126 weld had an Ac1 HAZ half-width that was lower than expected; this could have due to BM chemistry or this could have been due to improper measurement, which is explained later in this section.

Table A.4: The weld parameter sets that were used to make bead-on-plate welds onto the 1.20 mm DP780 '21s' sheet steel.

Weld Code	Weld Parameters [Trim, TS, WFS, CTWD]	H_{rel} [J/mm]	Root Penetration [%]	Average Ac_1 HAZ Half-Width [mm]	Average Ac_3 HAZ Half-Width [mm]
TB130	[1.00, 25.4 mm/s, 127 mm/s, 14.3 mm]	116	68.0%	3.74	3.17
TB131	[1.05, 27.5 mm/s, 127 mm/s, 14.3 mm]	122	----	----	----
TB132	[1.10, 29.6 mm/s, 127 mm/s, 14.3 mm]	122	----	----	----
TB133	[1.00, 28.8 mm/s, 169 mm/s, 14.3 mm]	133	100.2%	4.51	3.86
TB134	[1.05, 31.8 mm/s, 169 mm/s, 14.3 mm]	134	----	----	----
TB135	[1.10, 34.7 mm/s, 169 mm/s, 14.3 mm]	136	----	----	----

Table A.5: The weld parameter sets that were used to make bead-on-plate welds onto the 1.20 mm DP980 '23s' sheet steel.

Weld Code	Weld Parameters [Trim, TS, WFS, CTWD]	H_{rel} [J/mm]	Root Penetration [%]	Average Ac_1 HAZ Half-Width [mm]	Average Ac_3 HAZ Half-Width [mm]
TB123	[1.00, 25.4 mm/s, 127 mm/s, 14.3 mm]	114	67.8%	4.13	----
TB124	[1.05, 27.5 mm/s, 127 mm/s, 14.3 mm]	118	----	----	----
TB125	[1.10, 29.6 mm/s, 127 mm/s, 14.3 mm]	123	----	----	----
TB126	[1.00, 28.8 mm/s, 169 mm/s, 14.3 mm]	130	101.4%	4.28	----
TB128	[1.05, 31.8 mm/s, 169 mm/s, 14.3 mm]	136	----	----	----

Example images that were used to measure the HAZ dimensions for the welds TB117, TB130, and TB123 are shown in Figure A.20. There was no detailed microscopic analysis performed on the microstructure in the HAZ's of these welds; the macrostructure was only required for HAZ measurement. The Ac_1 line and Ac_3 line are labelled for each cross-section. The image in Figure A.20a was the low heat input (TB117) weld that had been made onto the 1.20 mm DP600 '22s' sheet steel. A sample measurement is shown for the Ac_1 HAZ half-width, which was found to be 4.34 mm. The image in Figure A.20b was the low heat input (TB130) weld that had been made onto the 1.20 mm DP780 '21s' sheet steel. A sample measurement is shown for the Ac_1 HAZ half-width, which was found to be

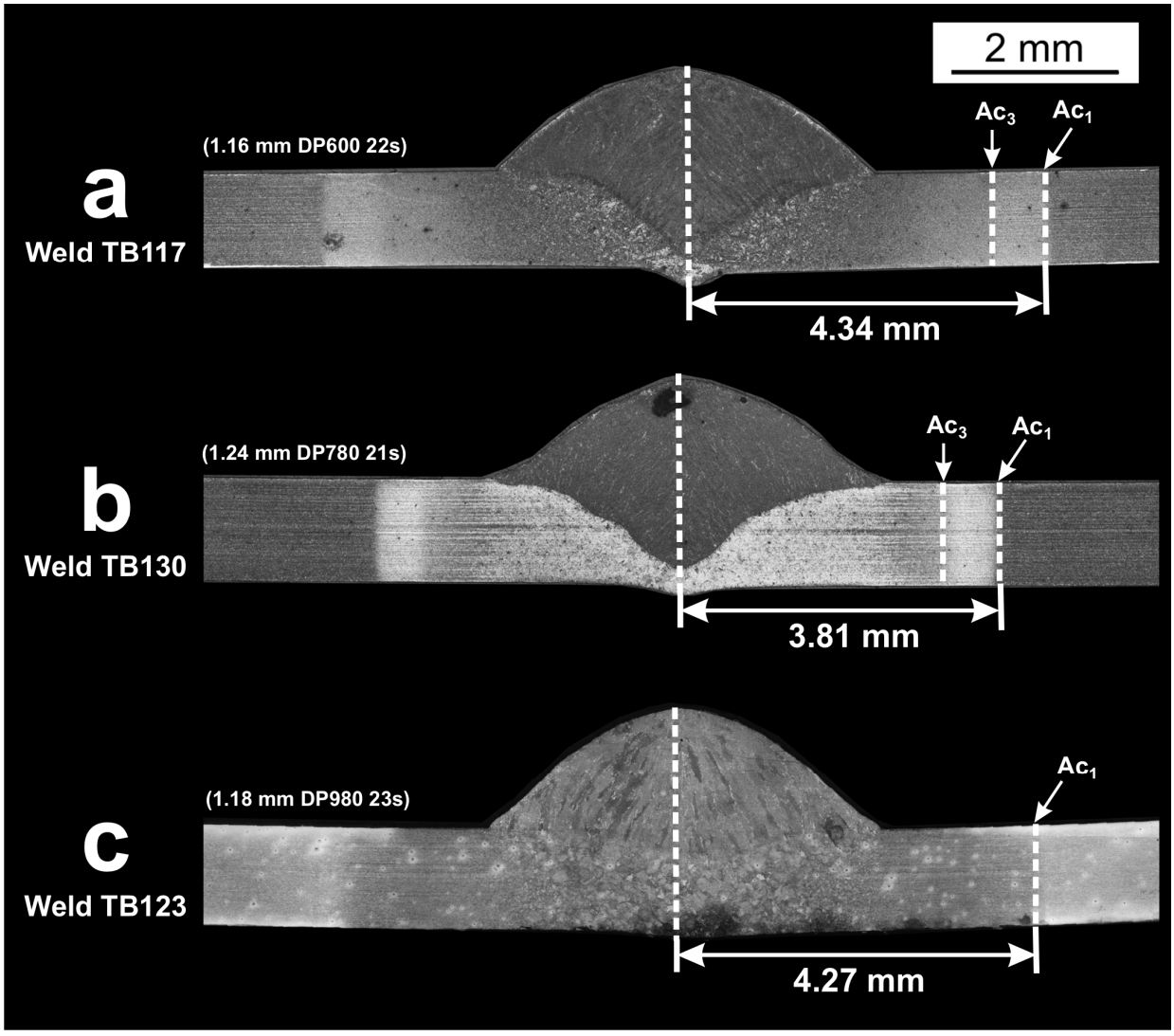

Figure A.20: A comparison between three welds that were made with the same weld parameters but were on different sheet steels. The weld in a) was made on DP600 '22s' sheet steel (1.16 mm thick), the weld in b) was made on DP780 '21s' sheet steel (1.24 mm thick), and the weld in c) was made on DP980 '23s' sheet steel (1.18 mm thick). (2% Nital etch).

3.81 mm. A visual comparison between TB117 and TB130 suggested that the TB117 weld HAZ was wider. These two welds had been made with the same weld parameters and had a similar calculated heat input; however, the TB130 weld was made on a thicker sheet steel and therefore had a more effective path for heat dissipation that resulted in a narrower HAZ. It was also observed that the TB130 weld had an internal pore within the FZ. There was no optimization stage during the weld development for this study

and so the TB130 weld was retained for further analysis. The image in Figure A.20c was the low heat input (TB123) weld that had been made onto the 1.20 mm DP980 ‘23s’ sheet steel. The weld HAZ macrostructure for this sheet steel was difficult to identify and two distinct locations for the Ac_1 and Ac_3 lines were not established. The prominent division seen on the macrocrostructure was considered to be the Ac_1 line. A sample measurement is shown for the Ac_1 HAZ half-width, which was found to be 4.27 mm.

The six welds that were cross-sectioned and measured for weld HAZ dimensions were also used to machine three uniaxial transverse weld tensile specimens. These specimens were loaded to complete fracture and the failure location was observed. For the 1.20 mm DP600 ‘22s’ sheet steel, the TB117 and TB120 weld were used to make tensile specimens. The low heat input (TB117) weld had one uniaxial tensile specimen fracture in the BM failure location and two fractures in the HAZ failure location, and the specimens are shown in Figure A.21; this weld was the only weld in this study that had a BM fracture. From the image, all of the DP600 ‘22s’ tensile specimens typically fractured at an approximate angle of 24° to the specimen gauge width. The high heat input (TB120) weld uniaxial tensile specimen failed 100% of testing in the HAZ failure location. For the 1.20 DP780 ‘21s’ sheet steel, the TB130 and TB133 weld were used to make tensile specimens. All of the specimens that were machined from both of these welds fractured in the HAZ failure location, and the specimens from the low heat input (TB130) weld are shown in Figure A.22. From the image, the DP780 ‘21s’ tensile specimens appeared to fracture parallel to the specimen gauge width. For the 1.20 DP980 ‘23s’ sheet steel, the TB123 and TB126 weld were used to make tensile specimens. All of the specimens that were machined from both of these welds fractured in the HAZ failure location, and the specimens from the low heat input (TB123) weld are shown in Figure A.23. From the image, the DP980 ‘23s’ tensile specimens appeared to fracture parallel to the specimen gauge width.

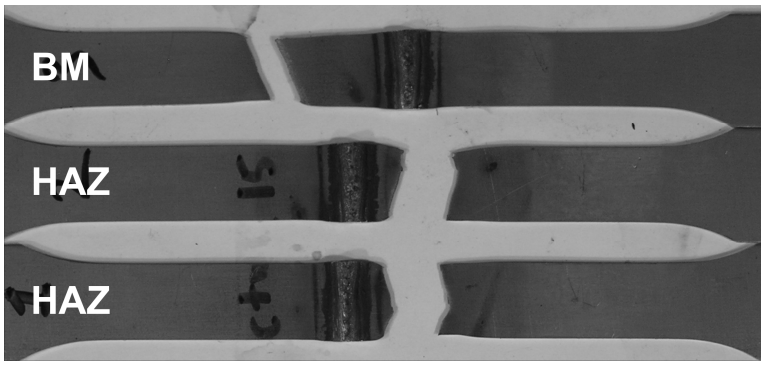

Figure A.21: The low heat input (TB117) weld tensile specimens from the 1.20 mm DP600 '22s' sheet steel are shown after they were loaded to fracture. The weld was observed to have a mixed failure mode.

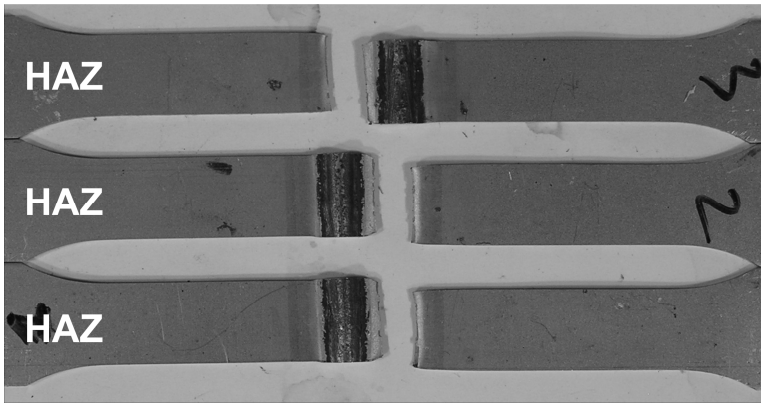

Figure A.22: The low heat input (TB130) weld tensile specimens from the 1.20 mm DP780 '21s' sheet steel are shown after they were loaded to fracture. The weld was observed to have 100% HAZ failure.

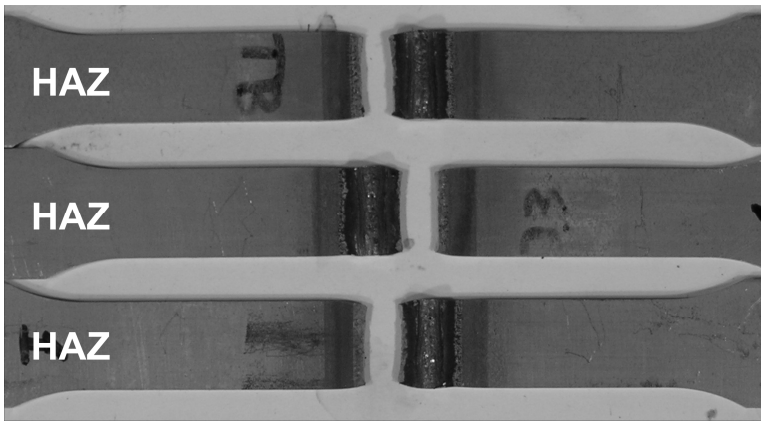

Figure A.23: The low heat input (TB123) weld tensile specimens from the 1.20 mm DP980 '23s' sheet steel are shown after they were loaded to fracture. The weld was observed to have 100% HAZ failure.

The uniaxial transverse weld tensile ‘stress vs. displacement’ results for the low heat input (TB117, TB130, and TB123) welds for each of the sheet steels are plotted in Figure A.24. The ‘stress vs. displacement’ results for unwelded BM uniaxial tensile specimens are also shown. There was very little change between the UTS of the welded and unwelded 1.20 mm DP600 ‘22s’ sheet steel uniaxial tensile specimens. The curve that is shown was from a specimen that fractured in the HAZ failure location. Similarly, there was very little change between the UTS of the welded and unwelded 1.20 mm DP780 ‘21s’ sheet steel uniaxial tensile specimens; this was unexpected and it suggested that a BM failure location may be possible by adjusting the geometry of the welded DP780 ‘21s’ S-SC region. The

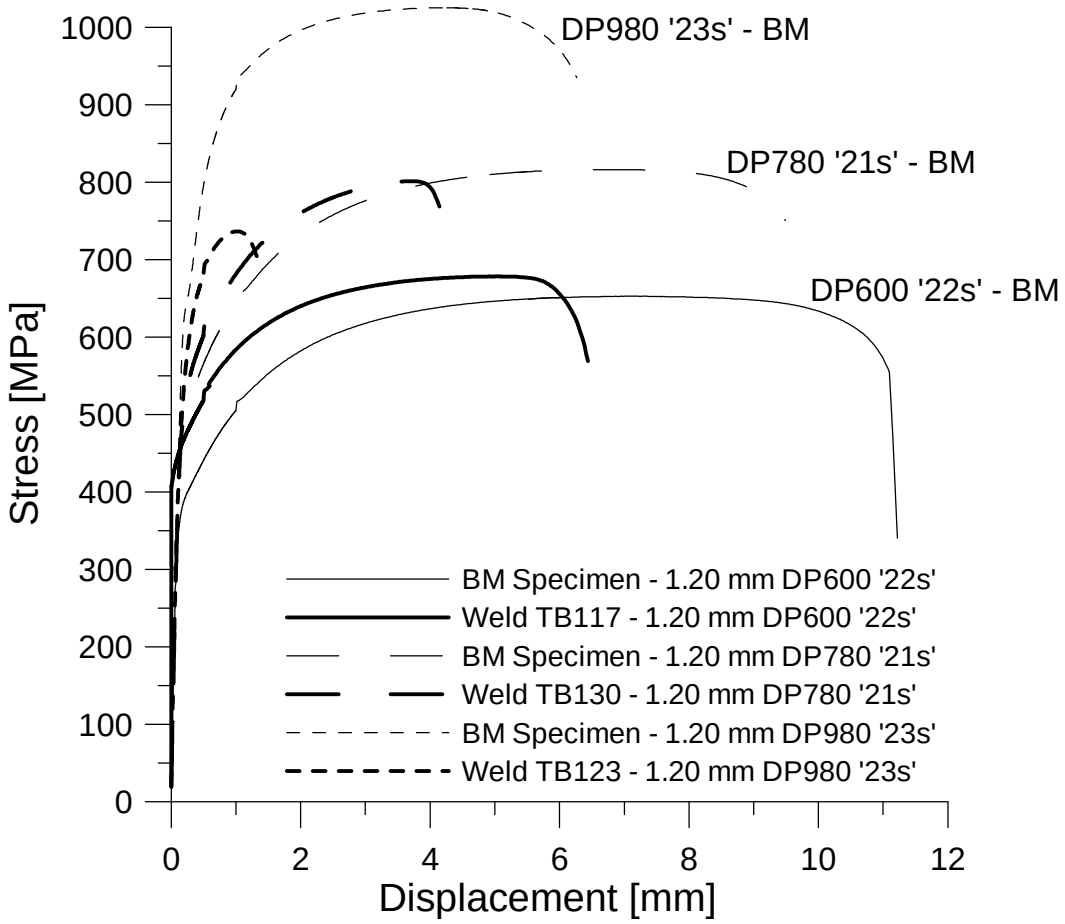

Figure A.24: A comparison between the uniaxial tensile specimen stress vs. displacement results for the low heat input welds and their corresponding unwelded BM uniaxial tensile specimen stress vs. displacement results.

1.20 mm DP980 ‘23s’ sheet steel was observed to have a significant loss of strength. The UTS that was measured from welded tensile specimens was well below (~28%) the UTS of the parent steel. All of the welded specimens appeared to have decreased ductility; there was less diffuse necking prior to strain localization. The amount of diffuse necking decreased as the strength grade of DP steel increased; this was true for both welded and unwelded tensile specimens.

Extended cross-sections were cut from the low heat input (TB117, TB130, and TB123) welds. These cross-sections were taken to ArcelorMittal Dofasco, Inc. [48] and were tested with a Vickers microhardness map. These maps were meant to support the data and trends that were observed on the microhardness maps from Experimental Series 1.

The Vickers microhardness map for the low heat input (TB117) weld that was made onto the 1.20 mm DP600 ‘22s’ sheet steel is shown in Figure A.25. The image that is shown in Figure A.25a shows the extended weld cross-section, the location of the Ac_1 and Ac_3 lines, and the indentation grid orientation. The grid orientation was not ideal and it was found that the cross-sectioned weld sample had a slight bend across its length. This bend had most likely formed when the sheet steel was sheared in order to obtain the sample. Generally, weld samples were not taken at a close proximity to a shearing location; however, there was limited weld zone available on the welded coupon to be used for cross-sectioning and hence this sample had been relatively close to a shearing location. The grid of indentations did not follow the path of the bend in the sample and hence the grid was not parallel to the sheet edges. The top line of the indentation grid was discontinued at the location that is marked ‘B’ on the image, which was approximately 4 mm away from the Ac_1 line; further along the sample, this top line of indents would have been too close to the sheet edge to obtain a valid measurement. This misalignment was present in all of the indentation lines within the grid. There was no attempt to identify what the effect of a misaligned grid would have on the microhardness map.

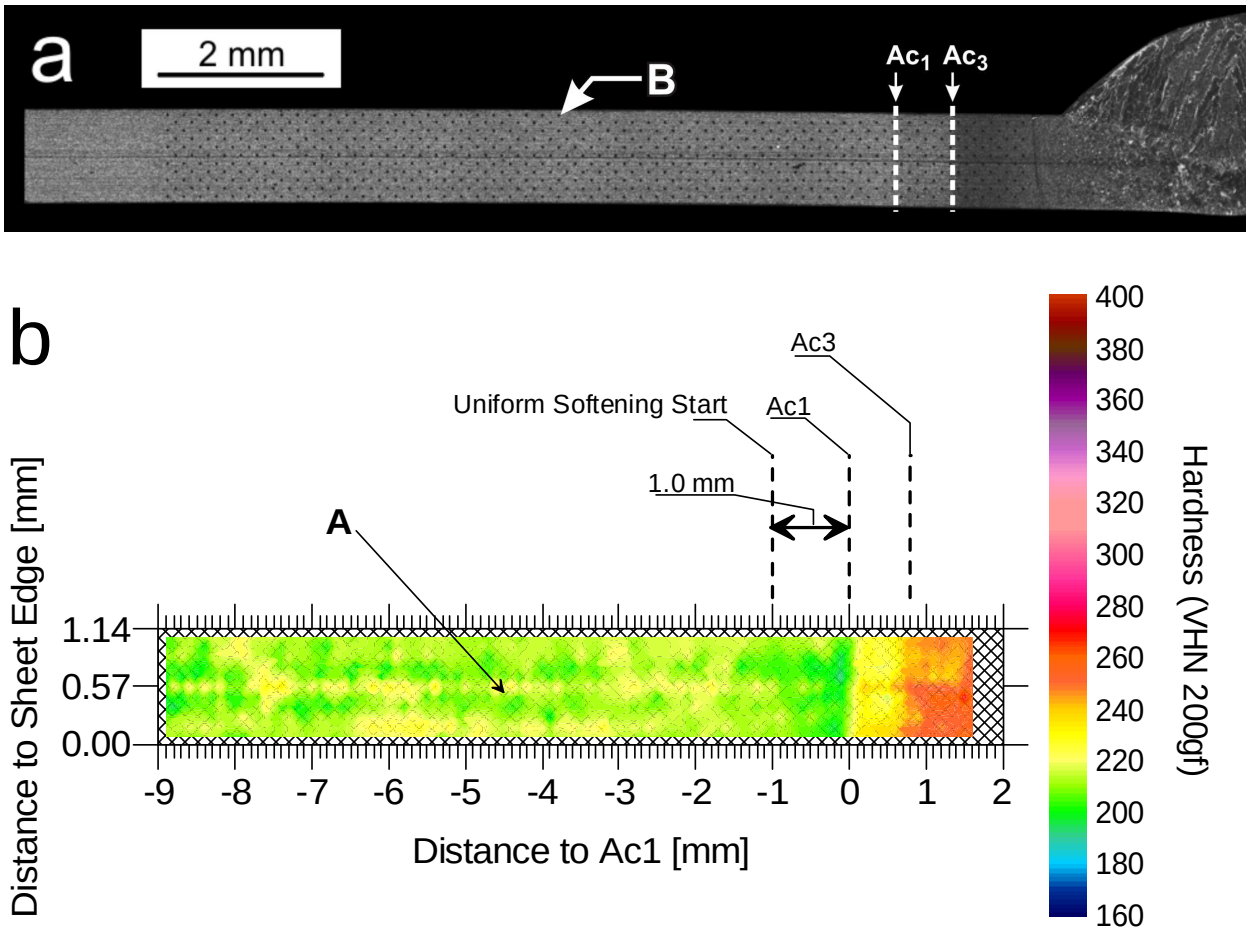

Figure A.25: The microhardness map for the low heat input (TB117) 1.20 mm DP600 '22s' weld HAZ. The image in a) shows the grid of indentations on the TB117 weld cross-section and b) shows the mapped microhardness.

The image of the microhardness map for the TB117 weld is shown in Figure A.25b. There was significant evidence that softening had occurred adjacent to and below the Ac_1 line. From the map, the softened zone was measured to be approximately 1 mm in width; this distance was from the location where uniform softening emerged to the Ac_1 line. There was no visual evidence that subcritical hardening was present in the weld sample. There was evidence that the weld HAZ above the Ac_1 line had significantly increased in hardness. This increase in hardness was suspected to have a similar effect during uniaxial tensile loading that had been considered from Experimental Series 1. The hardened zone in the IC microstructural region could have supported the softened zone and limited diffuse necking

around the S-SC region; this could have potentially prevented localized necking in the S-SC and shifted failure to the BM. There was no visual evidence that suggested that the misaligned grid of indentations had affected the map result, i.e., the map was qualitatively similar to the maps from Experimental Series 1. Also, the indentation grid appeared to have overlapped the central band of hardened martensite, which is labelled 'A' on the map.

The ATTH was calculated for the TB117 weld HAZ using the data from the microhardness map and the profile is shown in Figure A.26. The profile was fitted with a curve to visualize the general trend that existed throughout the weld HAZ. The different regions of hardness (IC, S-SC, H-SC, and BM) that were identified on the average through-thickness weld profiles from Experimental Series 1 are indicated on the TB117 weld profile. The unwelded BM average hardness is also shown on the chart. The welded BM region that was identified on the profile had lower ATTH (~7 VHN) than the unwelded BM; this is indicated as 'A' on the chart. The welded BM, labelled 'B', had an approximate average hardness of 206 VHN. However, the hardness appeared to decrease from approximately 208 VHN, at 9 – 10 mm away from the Ac_1 line, down to 203 VHN, at 11 - 12.5 mm from the Ac_1 line. This could have been caused by grid misalignment that had been observed. The distance from the Ac_1 line to the BM region was measured and found to be approximately 9 mm.

There was evidence of hardening in the H-SC region of the TB117 weld HAZ; it appeared to correspond to unwelded BM average hardness. There was a significant decrease in variance of the H-SC ATTH at the location that is labelled 'C'. This section of the TB117 weld HAZ appeared to be consistently above the average BM hardness. The location where the top indentation line had been discontinued was approximately 4 mm from the Ac_1 line, and so it was within the H-SC region. The consistency of the profile data that is labelled 'C' on the profile appeared to change at approximately 4 mm away from the Ac_1 line, and so the grid misalignment could potentially have caused a difference of hardness in the H-SC region. The ATTH data that was relatively consistent at the location 'C' was approximately 10 VHN higher than the welded BM ATTH.

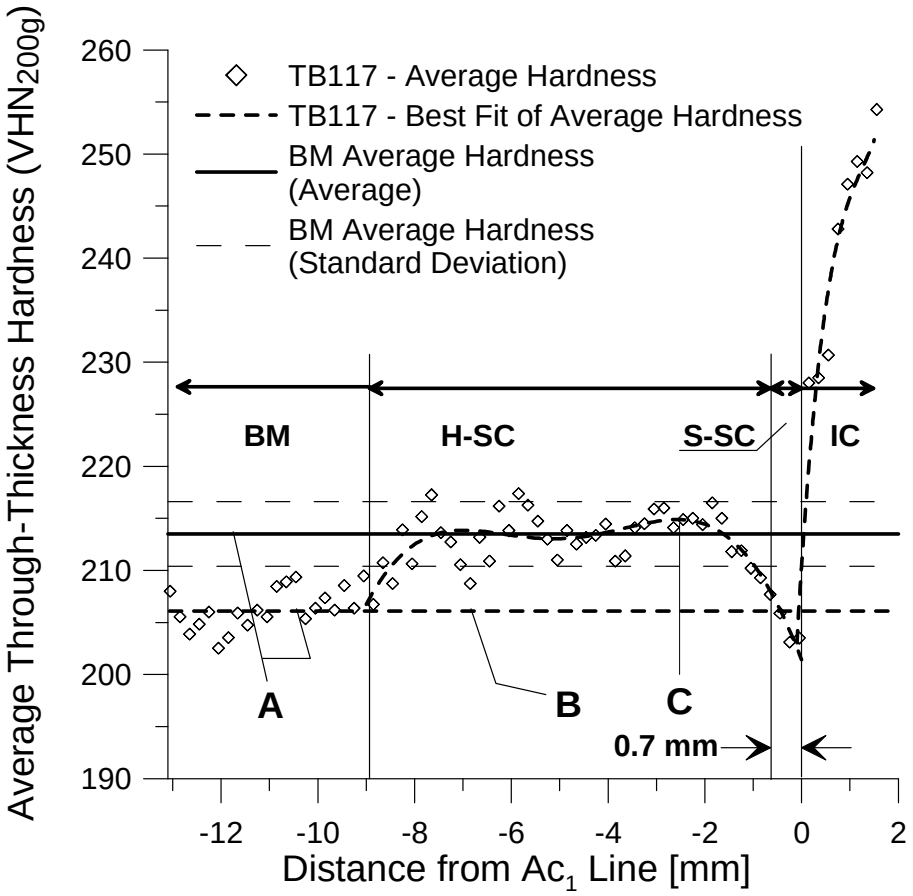

Figure A.26: The average through-thickness hardness profile for the lowest heat input (TB117) weld that had been made onto the 1.20 mm DP600 '22s' sheet steel. Four characteristic regions of hardness (IC, S-SC, H-SC, and BM) were identified and are marked on the profile.

Compared to the welded BM average hardness, there was minimal evidence of softening in the S-SC region of the TB117 weld HAZ; however, a distinct drop in average hardness was visible. This was unexpected because during uniaxial transverse weld tensile testing there were HAZ fractures; this suggested that the welded BM average hardness was measured to be lower than it actually was and that grid misalignment had likely skewed average hardness measurements. The minimum average hardness was approximately 203 VHN. The S-SC region was measured to be approximately 0.7 mm in width compared to the welded BM hardness and was 1.3 mm in width compared to the unweled BM hardness; the true S-SC width likely fell within these limits. Similarly, a range for the degree of softening was

defined and the true value likely fell somewhere in between; the S-SC was 3 VHN softer than the welded BM average hardness and was 11 VHN softer than the unwelded BM hardness.

The IC region was observed to have a significant increase in hardness, which was similar to all previous Vickers microhardness results. From the profile, an increase in hardness compared to the welded BM ATTH was measured to be greater than approximately 40 VHN.

The microhardness mapping result for the low heat input (TB130) weld that had been made onto 1.20 mm DP780 '21s' sheet steel is shown in Figure A.27. An image of the extended cross-section that was used to create the microhardness map is shown in Figure A.27a. On the image, the grid of indentations can be seen and the location of the Ac_1 and AC_3 lines are indicated. Similarly to the grid orientation that had been observed on the TB117 weld sample, the TB130 weld was also misaligned. The misalignment was caused by a slight bend in the weld sample cross-section. The bend was most likely associated with the shearing step required to obtain the sample. The location that is labelled 'A' indicates where the top line of indentations was discontinued. The internal pore that had been observed while taking the HAZ measurements was also present on this cross-section, and is labelled 'B' on the image.

The image of the microhardness map is shown in Figure A.27b. From the image there was significant evidence that softening had occurred in the S-SC region immediately adjacent to the Ac_1 line. This region was measured using the map image to be approximately 1.5 mm.. This was larger than the width measured for the TB117 weld. Both of these welds had similar relative heat input, but because the TB130 weld had been made on thicker sheet steel (approximately 0.08 mm) it had been expected that there would be a decrease in the width of the S-SC region. This suggested that the DP780 '21s' sheet steel composition or its higher martensite percentage had caused a larger S-SC region to form. From the image there was some evidence of hardening in the approximate location of the H-SC region, which is labelled 'C'. This location is also labelled on the image of the cross-section, which shows that the top line of indentations were discontinued approximately 2 mm away from this location. This was important

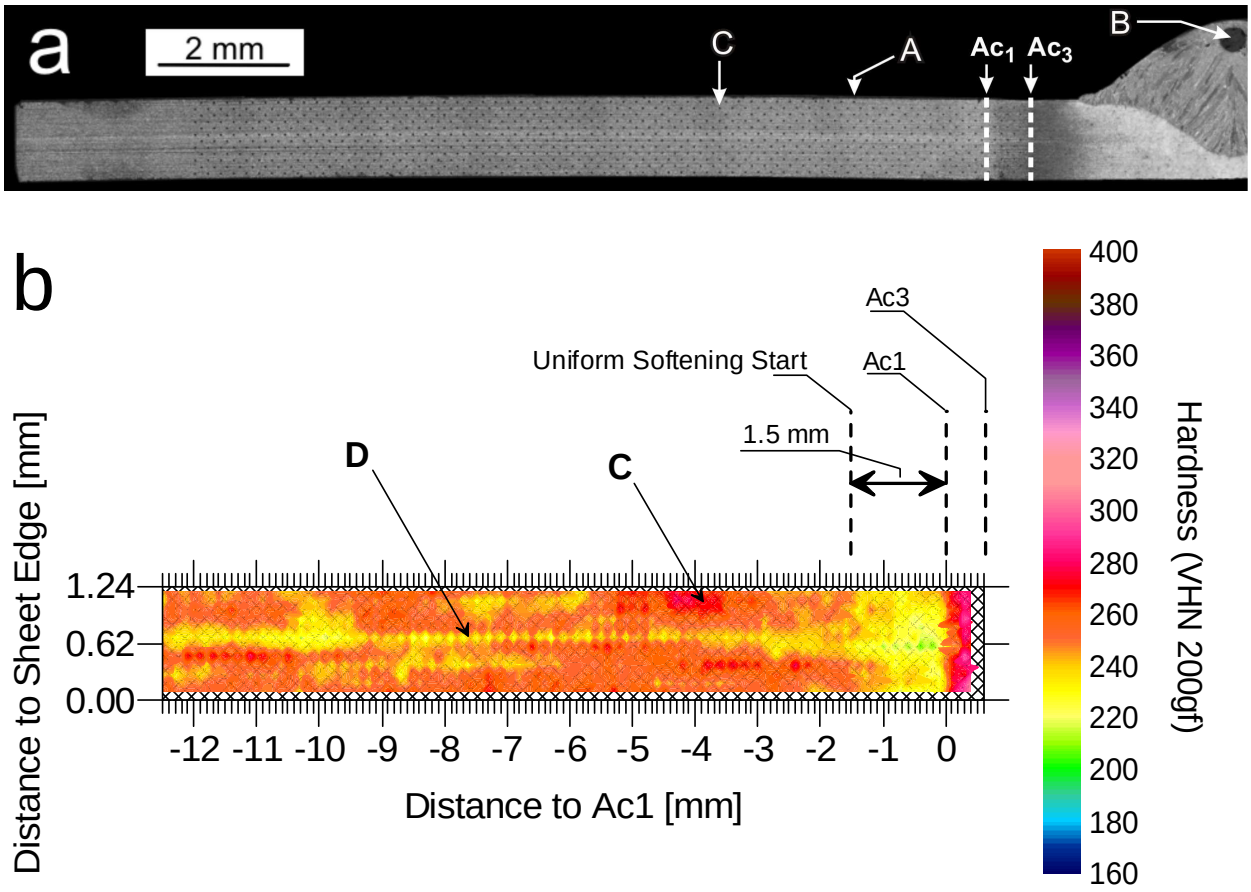

Figure A.27: The microhardness map for the low heat input (TB130) 1.20 mm DP780 '21s' weld HAZ. The image in a) shows the grid of indentations on the TB130 weld cross-section and b) shows the mapped microhardness.

because it suggested that the discontinuation of the top line of indentations was not associated with the increase in hardness at this location in the HAZ. The grid of indentations appeared to have overlapped with bands of hard and soft phases along the center of the sheet thickness as indicated by 'D'. There was also a small section from the IC region of the microstructure that was represented on the map image. This region was observed to have a significant increase in hardness, which was similar to the previous microhardness results that had been observed on all of the DP600 sheet steels.

The ATTH profile for the TB130 weld is shown in Figure A.28. The same four regions of hardness were identified in the TB130 weld HAZ. The ATTH in the welded BM region was observed to

have significant variability; grid misalignment may have caused variability of ATTH in the BM region. There appeared to be a difference between the unwelded BM ATTH and the welded BM region average hardness as indicated by 'A'. The welded BM hardness was estimated to be approximately 246 VHN and is labelled 'B' on the chart. The difference between the unwelded BM average hardness and the welded BM region average hardness was approximately 8 VHN. The welded BM region ATTH was used for comparisons to the other HAZ hardness regions. From the profile, the location of the BM region was measured to be approximately 7.5 mm to 9 mm away from the Ac_1 line.

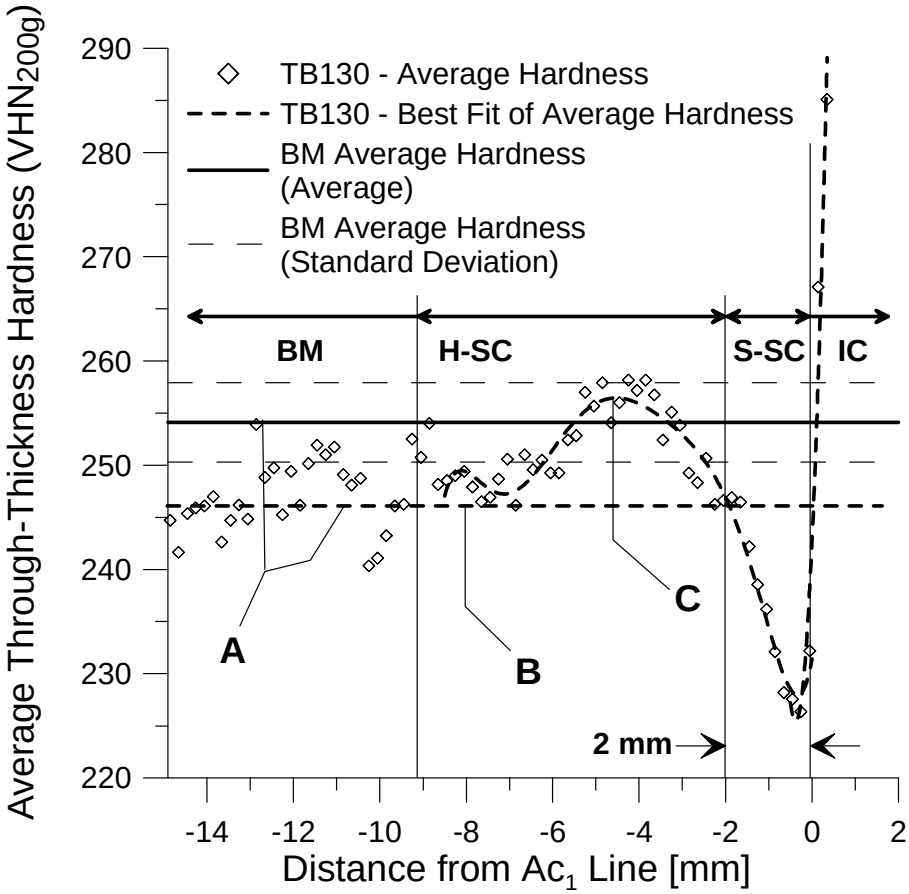

Figure A.28: The average through-thickness hardness profile for the lowest heat input (TB130) weld that had been made onto the 1.20 mm DP780 '21s' sheet steel. Four characteristic regions of hardness (IC, S-SC, H-SC, and BM) were identified and are marked on the profile.

There was significant evidence of hardening in the H-SC region of the TB130 weld HAZ. There was a consistent peak of hardening that was observed, which is labelled 'C' on the profile. This peak was

measured from the profile to have an average hardness that was approximately 11 VHN above the welded BM ATTH. This further suggested that an H-SC region was common in the weld HAZ of DP sheet steels. The low heat input (TB130) weld had consistently fractured in the S-SC region (100% HAZ failure) and hence the presence of an H-SC region did not prevent a HAZ failure location during uniaxial transverse weld tensile testing; however, the H-SC region may have helped support the S-SC during loading and prevented a significant reduction of the UTS. The belief was that the H-SC could prevent HAZ fracture and/or improve joint efficiency if the S-SC was narrow enough to limit diffuse necking across the boundary of these two regions of hardness. The presence of the H-SC region suggested that there was potential to prevent a HAZ failure location for welds onto the 1.20 mm DP780 '22s' sheet steel.

There was significant evidence of softening in the S-SC region immediately adjacent to the Ac_1 microstructural line. The region was measured from the profile to be approximately 2 mm in width. The degree of softening was measured to be approximately 20 VHN; this value was the difference in average hardness between the welded BM and the lowest point on the S-SC trough. This degree of softening was approximately 8 VHN higher than the highest heat input (TB88) weld that had been tested during Experimental Series 1, which had also consistently fractured in the HAZ. This was a significant difference of softening when the welded DP780 '21s' sheet steel was compared to the DP600 steels (degree of softening within range of 8 – 12 VHN). This suggested that welds that were made onto the 1.20 mm DP780 '21s' sheet steel would require a much narrower S-SC region in order to prevent a HAZ failure during uniaxial transverse weld tensile testing. The more significant softening value was most likely associated with the higher percent area of martensite that was present in the prior BM microstructure.

There was a significant increase in ATTH within the IC region. This was similar to all of the previous microhardness results and was most likely associated with an increased martensite percentage within this region. The entire IC region was not covered by the indentation grid and therefore it was

difficult to measure a value for the increase in hardness. From the profile, the increase in ATTH was measured to be at least 40 VHN.

The microhardness map for the low heat input (TB123) weld that had been made onto the 1.20 mm DP980 '23s' sheet steel is shown in Figure A.29. The location of the Ac_1 line and the Ac_3 line are indicated on the image. The grid of indentations was observed to overlap with a section of the weld FZ, which is labelled 'A' on the image. The extended cross-section was observed to have a slight bend that was most likely associated with a shearing step that had been used to cut a section of the weld out from the welded coupon. This bend caused a misalignment of the microhardness indentation grid and so indentation lines through the weld HAZ were not parallel to the sheet edges.

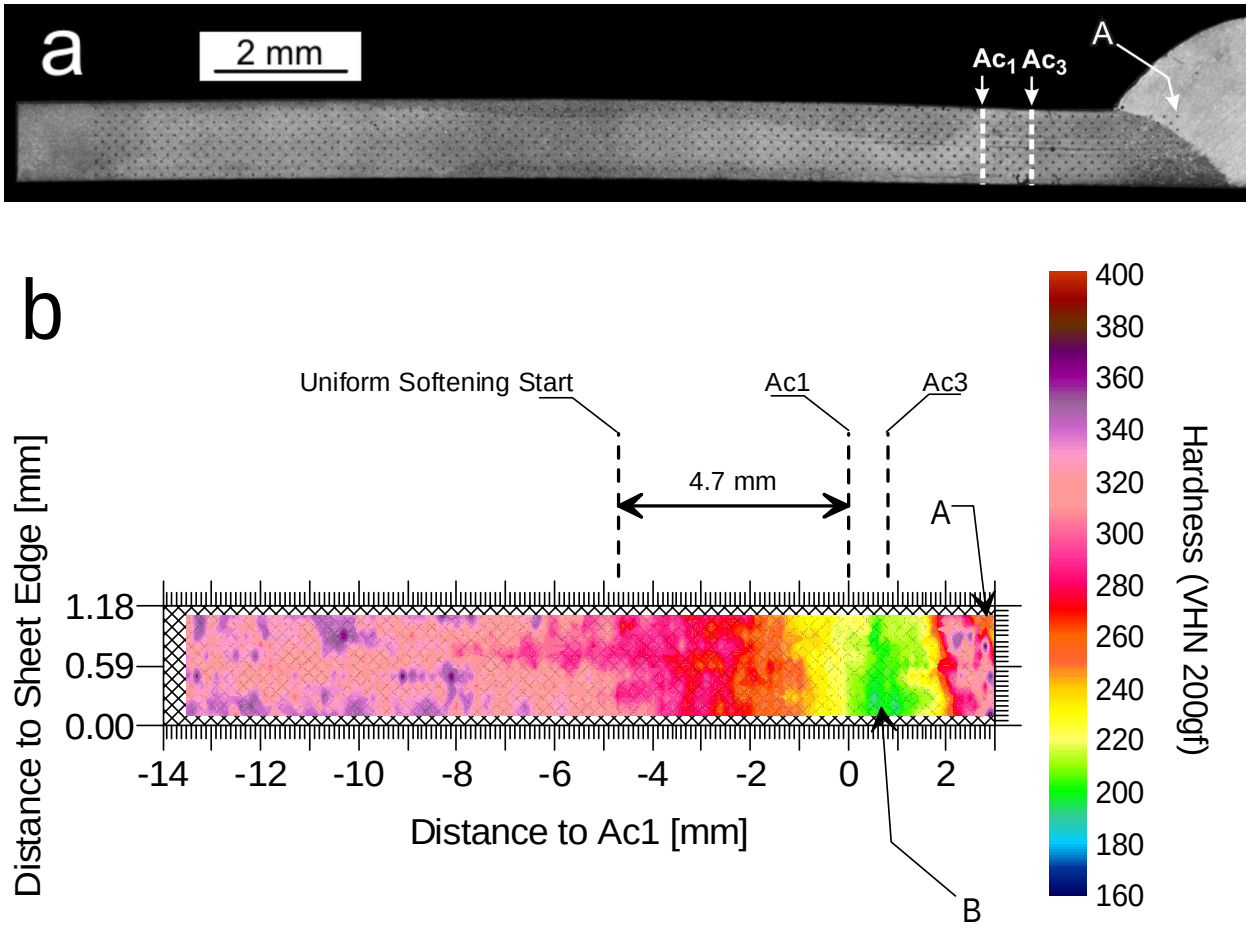

Figure A.29: The microhardness map for the low heat input (TB123) 1.20 mm DP980 '23s' weld HAZ.

The image of the microhardness map is shown in Figure A.29b. The indentation grid had covered from the weld FZ, through the weld HAZ, and into the welded BM. The section of the map that had covered the FZ is labelled 'A'. The FZ was observed to have a hardness that was lower than the adjacent material in the weld HAZ and was lower than the BM hardness. There was significant evidence of softening in the weld HAZ; however, the lowest hardness appeared to be located within the IC region of the weld. This area of lowest hardness is labelled 'B' on the map image. This was unexpected because all previous DP steel weld HAZ's had exclusively been observed to have softening in the S-SC and had significantly hardened in the IC region. The location of where uniform softening emerged was measured to be approximately 4.7 mm from the Ac_1 line.

An analysis of the IC region microstructure from the TB123 weld was made and an image of the transition from the IC region into the supercritical GR region is shown in Figure A.30. On the image, the approximate location of the Ac_3 line is shown. The Ac_3 line did not appear to be perpendicular to the sheet edges; it appeared to be aligned with the FZ boundary. The IC region had minimal evidence of the martensite islands that had existed in the prior BM. The majority of the IC region microstructure appeared to be a ferrite matrix with small islands of carbides, which was potentially renucleated martensite; it could also have been martensite that had been autotempered during cooling. This could explain the lower hardness that was observed in the microhardness map. The 1.20 mm DP980 '23s' sheet steel did not have significant additions of strong carbide-forming alloying elements (Cr-Mo-V) that were known to retard martensite decomposition [10]. This may have caused martensite decomposition to occur in the IC region of the weld HAZ before the peak IC temperature was reached at that same location, i.e., the heat input from the front end of the welding heating curve was sufficient to cause significant martensite decomposition. Then, once peak IC temperature had been reached, austenite nucleation would occur around much smaller carbide islands instead of at the larger martensite islands of the prior BM. The GR region was located by observing the emergence of refined ferrite grains. Some refined ferrite grains are labelled 'A' on the image. This region of the weld HAZ microstructure helped to locate the

approximate location of the Ac_3 line. An indent that was used for the microhardness map is labelled 'B' on the image.

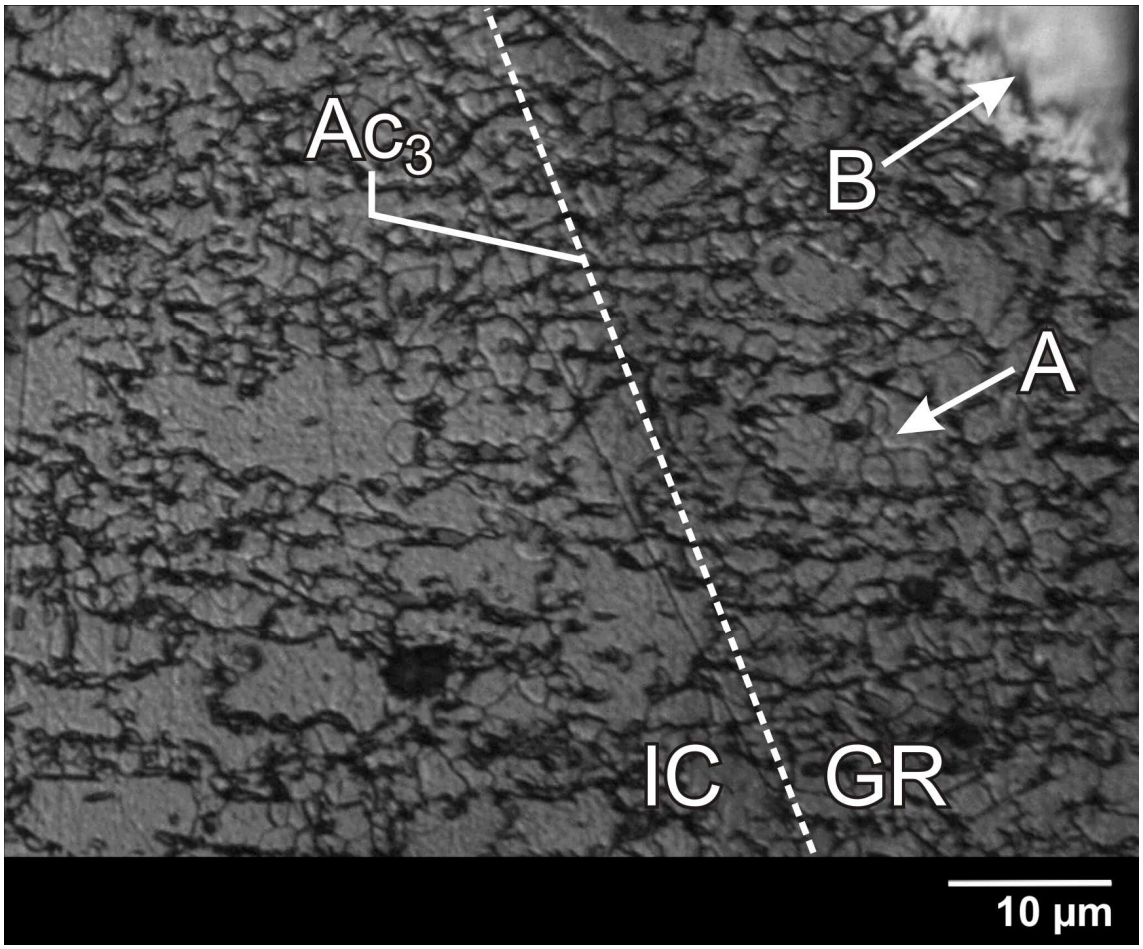

Figure A.30: Location of the transition from the IC region into the supercritical GR region that was observed in the TB123 weld HAZ. This weld had been made onto the 1.20 mm DP980 '23s' sheet steel.

The ATTH profile for the low heat input (TB123) weld that had been made onto the 1.20 mm DP980 '23s' sheet steel is shown in Figure A.31. A curve was fitted to the ATTH profile. Based on the curve, five characteristic regions of average hardness were observed, which were: the FZ, the supercritical (SP) region, the IC region, the S-SC region, and the BM region. There was no evidence of an H-SC region.

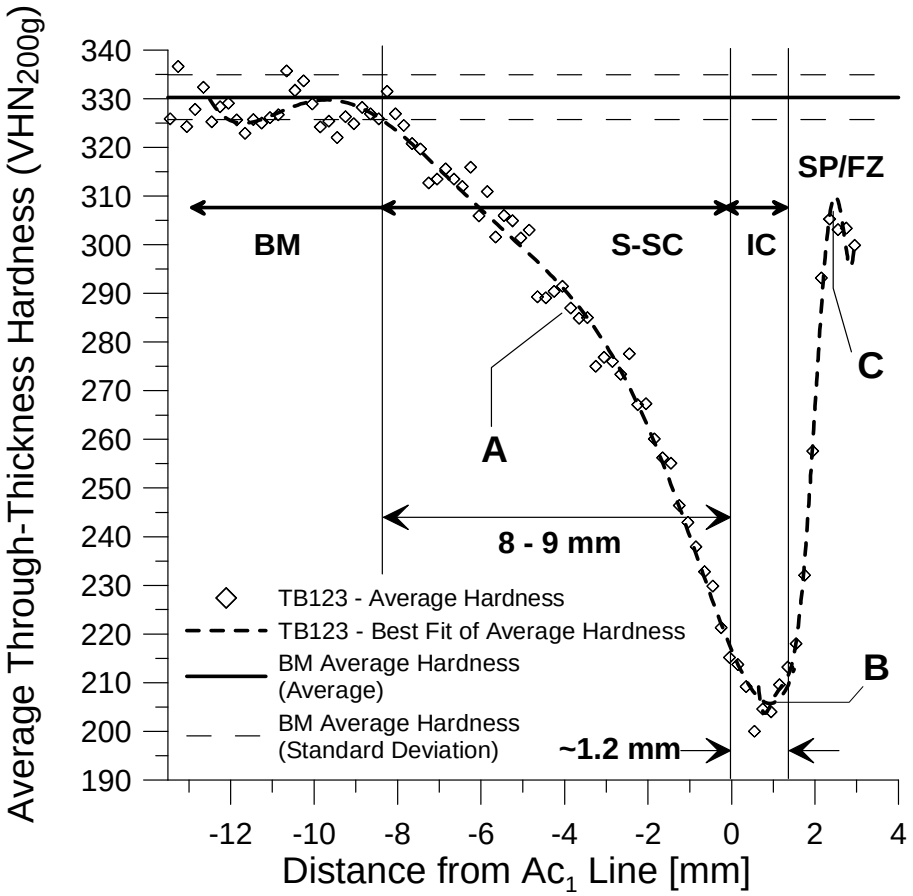

Figure A.31: The average through-thickness hardness profile for the lowest heat input (TB123) weld that had been made onto the 1.20 mm DP980 '23s' sheet steel. Three characteristic regions of hardness (IC, S-SC, and BM) were identified and are marked on the profile.

The welded BM region that was observed had an ATTH that was similar to the unwelded BM average hardness that was measured during the BM characterization. For comparisons to the other characteristic regions of hardness in the TB123 weld HAZ, the uwelded BM region ATTH was used. The location of the welded BM region was measured to be at a distance of approximately 8 – 9 mm away from the Ac_1 line. This was similar to the measurements that were observed in the DP600 '22s' and DP780 '21s' sheet steels.

There was significant evidence of softening in the S-SC region of the TB123 weld HAZ. The S-SC region extended from the Ac_1 line to the BM region, and there was no H-SC region observed. With no evidence of an H-SC region, the width of the S-SC region was uninterrupted out to the BM region.

The S-SC region was measured to be approximately 8 – 9 mm in width. This was larger than the measurement of 4.7 mm that had been made using the image of the microhardness map; however, the location where uniform softening emerged was present on the curve at approximately 4.7 mm; it appeared on the curve as an inflection point and is labelled 'A'. The wider S-SC region was believed to be caused by the removal of alloying elements (Cr-Mo-V) from the BM composition; similar to the reasoning for softening in the IC region mentioned above. The lack of an H-SC region in the TB123 weld HAZ suggested that these alloying elements could have caused the emergence of the H-SC regions that were observed in the other DP steels that did have these alloying elements in their nominal composition. The degree of softening in the S-SC region was measured from the chart to be approximately 115 VHN. The minimum ATTH that was measured in the S-SC region (at the Ac_1 line) was approximately 215 VHN; however, this was not the softest region of the TB123 weld HAZ.

The IC region of the TB123 weld HAZ was observed to have lower ATTH than the S-SC region, and it had the lowest average HAZ hardness. The IC region trough is marked 'B' on the plot. Softening in the IC region had been observed by Biro and Lee [36] for a similar lean chemistry DP sheet steel. This region was measured to have a minimum ATTH of approximately 200 VHN and therefore the absolute degree of softening for the TB123 weld HAZ was approximately 130 VHN. This also extended the width of the softened region of the weld HAZ to approximately 9 – 10.5 mm. This suggested that the softened region of the low heat input (TB123) weld made onto the 1.20 mm DP980 '23s' sheet steel was approximately 8 mm wider and over 100 VHN softer than either of the welds that were tested for the DP600 '22s' or DP780 '21s' sheet steels. These substantial differences suggested it would be difficult to create a narrowed softened region using the GMAW-P weld process (due to its relatively high heat input) and that a narrowed softened region would most likely be insufficient to eliminate a HAZ failure in the 1.20 mm DP980 '23s' sheet steel (due to the substantial degree of softening).

The SP and FZ regions were grouped as a single region on the plot. The point that is labelled 'C' was the location where the grid of indentations entered into the upper section of the FZ. Generally, these

two regions were observed to have increased ATTH when compared to the S-SC and the softened-IC regions. The peak ATTH was measured to be approximately 305 VHN. This value was below the unwelded BM average hardness, and the difference in ATTH was approximately 25 VHN.

In general, this study confirmed that an increase in DP sheet steel strength shifted the failure location during uniaxial transverse weld tensile testing from a BM failure mode to a HAZ failure. The increase in sheet strength was associated with an increase in the prior BM percent area of martensite. The 1.20 mm DP600 '22s' sheet steel was observed to have a BM failure location during uniaxial transverse weld tensile testing, and for the same weld heat input and similar HAZ geometry and size, the higher strength 1.20 mm DP780 '21s' and 1.20 mm DP980 '23s' sheet steels failed 100% of uniaxial tests in the HAZ. A higher degree of softening was measured as the percent area of martensite increased. This was an expected result of the study. The DP600 '22s' and DP780 '21s' sheet steels were Cr-Mo DP sheet steels and had narrow S-SC regions of microstructure based on analysis from microhardness mapping; both of these steels also had evidence that an H-SC region existed in the DP weld HAZ. The DP980 '23s' sheet steel had no strong carbide-forming alloying additions of Cr or Mo and was observed to have a wide S-SC region; this sheet steel had no evidence of an H-SC region within the weld HAZ. This was the only weld that had no evidence of an H-SC region and had the widest S-SC region of all of the welds that were tested. This was also the only weld made onto a DP sheet steel that was not a Cr-Mo DP sheet steel. This suggested that the Cr-Mo DP sheet steel composition had been a factor in reducing the size of the S-SC region and creating an H-SC region in the weld HAZ.

A summary of the data from weld HAZ microhardness maps is shown in

Table A.6. The table includes all of the welds that were analysed by using a microhardness map. The DP steel grade and the measured sheet thickness for each weld are given, along with the relative heat input, volume fraction of martensite (VFM) for the base-metal, and the fracture location from uniaxial transverse weld tensile tests. The following microhardness data is listed in the table: the BM ATTH

(ATTH), the minimum ATTH from the HAZ, the degree of softening, the softened zone width, the degree of H-SC hardening, and the width of the SC region. The following is a general summary of the trends that were observed. The degree of softening increased as the DP strength grade increased; this was directly related to higher area fractions of martensite in the prior BM. The DP600 welds, which all had

Table A.6: Summary of the measured weld HAZ properties for the different strength grades of DP sheet steel that were assessed using the microhardness maps and average through-thickness hardness (ATTH) profiles.

Weld Code	**TB87**	**TB88**	**TB136**	**TB117**	**TB130**	**TB123**
Measured Sheet Thickness [mm]	1.68	1.68	1.75	1.16	1.24	1.18
Steel Grade	DP600 ‘16s’	DP600 ‘16s’	DP600 ‘24s’	DP600 ‘22s’	DP780 ‘21s’	DP980 ‘23s’
Volume Fraction of Martensite [%]	7.8 ± 1.4	7.8 ± 1.4	7.4 ± 1.5	7.7 ± 2.0	20.2 ± 1.9	45.6 ± 3.5
H_{rel} [J/mm]	193	347	366	119	116	114
Uniaxial Tensile Failure Mode	100% BM	100% HAZ	100% BM	1 BM, 2 HAZ	100% HAZ	100% HAZ
Welded BM ATTH [VHN]	198	198	196	206 - 214	246	330
Minimum HAZ ATTH [VHN]	192	188	185	203	226	200
Degree of Softening [VHN_{ATTH}]	6	10	11	3 - 11	20	130
Softened Zone Width [mm]	1.8	2.0	1.8	0.7 - 1.3	2	9 - 10.5
Degree of H-SC Hardening [VHN_{ATTH}]	5 - 10	6 - 15	9	2 - 14	11	N/A
Subcritical Zone Width [mm]	9 - 10	10 - 11	9.5 - 11	8 - 9	7.5 - 9	8 - 9

approximately 7.5 – 8% martensite, had the lowest degree of softening, at approximately 6 - 10 VHN. When the area fraction of martensite was increased to 20% by welding onto DP780 '21s' sheet steel, softening increased to approximately 20 VHN. Welding DP980 sheet steel, which had the highest percentage of martensite at approximately 46%, increased the degree of softening dramatically to 130 VHN. The degree of softening also increased as the relative heat input increased. The low heat input (TB87) weld, which had been made with a weld heat input of 193 J/mm, had softened by approximately 6 VHN. When the heat input was increased to 347 J/mm for the high heat input TB88 weld or to 366 J/mm for the TB136 weld, the DP600 material softened by approximately 10 VHN. The minimum hardness for the TB123 weld HAZ, which was a DP980 sheet steel weld, was lower than the minimum average hardness both for the TB117 DP600 '22s' weld HAZ and the TB130 DP780 '21s' weld HAZ. These welds were made with similar relative heat input on similar sheet gauge thickness. This suggested that after GMAW-P welding heat input, the 1.20 mm DP980 '23s' sheet steel was a weaker joint than the welded DP780 '21s' sheet steel and became a comparable joint to the welded DP600 '22s' sheet steel.

A direct comparison between the SC width for the TB117, TB130, and TB123 welds showed that BM hardness emerged at approximately the same distance from the Ac_1 line. These welds had been made with similar heat input and they each had similar sheet thickness, therefore, this met with the expectation that the relative width of the HAZ would also be similar.

As mentioned above, only the Cr-Mo DP sheet steel welds had an H-SC region, i.e., all of the welds except for weld TB123. There did not appear to be any difference between the amounts of hardening that existed in these welds. There were two explanations developed for why the H-SC region had emerged in the HAZ. The first explanation was that secondary hardening had occurred due to martensite tempering. As mentioned in the sections above, it was believed that hardening may have been caused by strong carbide-forming alloys like Cr or Mo. From the literature, tempering has been shown to increase the YS of alloyed DP steels [23,25,27,29,30] and that increased YS was potentially related to carbide precipitation within a martensite body. During tempering, DP steels that contain these alloys

have been shown to have secondary hardening at moderate elevated temperature [10]; temperature ranges depend on the alloy addition. This could have caused the formation of the H-SC. However, the degree of H-SC hardening for each weld was similar. It was suspected that if tempering was the cause of the H-SC, then there should have been more significant hardening in the DP780 '21s' sheet steel. This steel had a higher area fraction of martensite and, therefore, there would have been more islands of martensite that had hardened; this should have caused a higher degree of hardening. Likewise, welds on DP780 had a higher degree of softening for the same reason. The second explanation was that thermal expansion during welding had plastically deformed the material that was adjacent to the weld; the coupons had been heavily clamped and would have resisted. This explanation had not been considered further, but could be tested by measuring the hardness of an HSLA weld from Phase 2 welding trials with a microhardness map. If an HSLA weld did not have an H-SC, then it could be concluded that plastic deformation had not caused hardening in the DP sheet steel welds.

Appendix B

HSLA ‘17s’ Joint Efficiency Study

To conclude the weld procedure development, the joint efficiency of the selected welds from Phase 2 welding trials that had been made onto 1.80 mm HSLA ‘17s’ sheet steel was evaluated. The welds were cross-sectioned and the HAZ microstructure was analysed. The cross-sections were measured for HAZ half-width and then were taken to ArcelorMittal Dofasco, Inc. [48] and were tested with microhardness profiles to determine the nature of mechanical properties within the weld HAZ. The weld parameters were then used to make bead-on-plate welds onto 254 mm × 203 mm HSLA ‘17s’ sheet steel coupons. These welds were used to create tensile specimens for complete fracture testing.

An image of a typical cross-section from a GMAW-P bead-on-plate welded HSLA ‘17s’ sheet steel is shown in Figure B.1. The microstructural regions that were observed in the HSLA ‘17s’ HAZ cross-section are labelled on the image. The labels are similar to the DP600 ‘16s’ welded cross-section from Figure 4.4b, which included: the fusion zone (FZ), the grain growth (GG) region, the grain refined (GR) region, the intercritical (IC) region, and the base-metal (BM) region. The nature of the microstructure in each region was different than the DP600 ‘16s’ HAZ; however, the regions were based on the same principle that the steel had reached different peak temperatures throughout the HAZ and the resulting microstructure could be to the binary steel phase diagram in Figure 4.4a. The image shown in Figure B.1 was from a full penetration weld cross-section. The weld FZ had a ‘finger’ penetration profile, which was typical of GMAW-P streaming spray metal transfer. Large columnar grains were visible in the FZ that had extended from the fusion boundary (FB) towards the weld centerline. The Ac_3 and Ac_1 lines are marked at the approximate location where the microstructure had appeared to change. These boundaries were difficult to identify on macroscopic images. At the approximate center of the IC region, there was a macroscopically visible transition from newly formed refined grains into larger grains of the BM. This line was visible on all of the welded cross-sections, and is marked on the image as the ‘central IC region’.

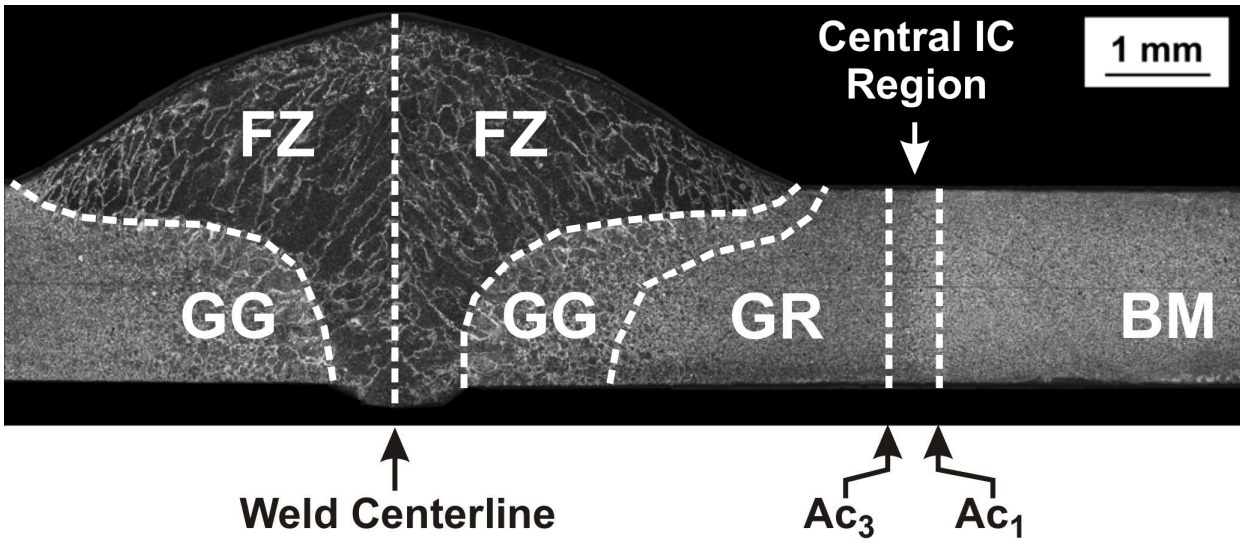

Figure B.1: A typical welded HSLA '17s' sheet steel cross-section showing the weld HAZ. The HAZ is labelled according to microstructural phase boundaries that were observed.

The HAZ half-width measurements were made to this macroscopic transition line and were described as an approximate distance from the weld centerline to the Ac_3 line. There was no visible evidence of microstructural change at the location of the subcritical (SC) region so it was excluded from the study and is not marked on the image of the cross-section.

Typical images of the microstructures that were observed at different locations throughout the HAZ of a GMAW-P bead-on-plate welded HSLA '17s' sheet steel is shown in Figure B.2. The image in Figure B.2a shows the microstructure of the base-metal (BM). The microstructure in this region was observed to be a fine grained structure that consisted solely of ferrite. This region was immediately adjacent to the Ac_1 line and, therefore, there were no visible microstructural changes within the subcritical (SC) region. The image in Figure B.2b shows the transition from the BM into the IC region. The location of the Ac_1 line was marked where there was evidence in the microstructure that refined grains had formed, which are labelled 'A'. These newly refined grains were much smaller than the fine grained BM. These refined grains had formed due to the peak temperature during welding rising above the Ac_1 temperature and into the IC region. At this temperature, austenite grains would have nucleated at different initiation sites such as grain boundaries and micro-carbides. The austenite grains reformed as

ferrite during cooling. Further into the IC region, the temperature was higher and a greater number of austenite grains had formed, which caused an increase in the amount of newly refined grains [15]. The upper boundary of the IC region was identified by the diminishing presence of the larger fine grains that had existed in the BM, which are labelled 'B' on the image.

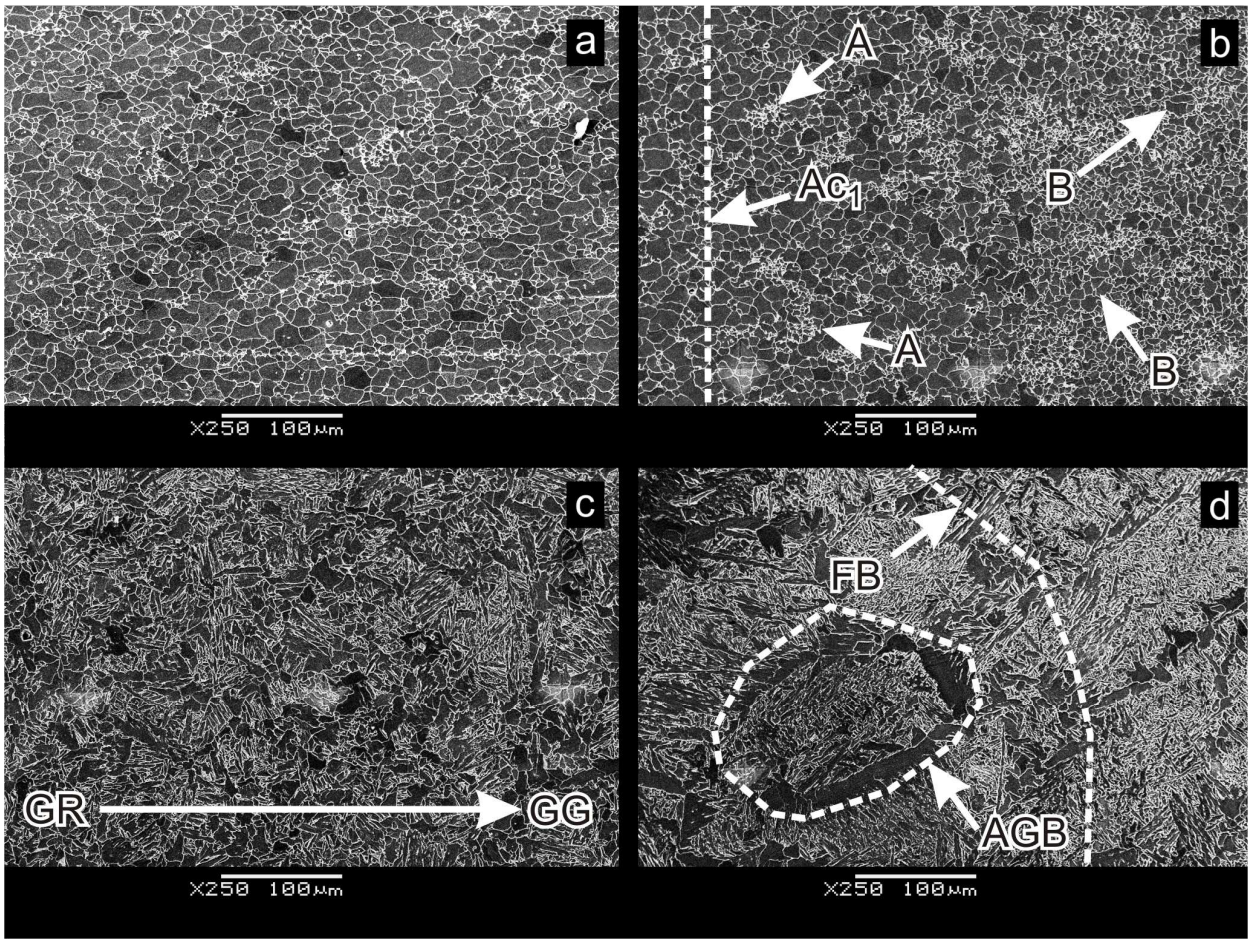

Figure B.2: The typical microstructure throughout the HAZ of a HSLA '17s' welded sheet steel: a) the base-metal (BM), b) shows the intercritical (IC) region, c) the transition from the grain refined (GR) to the grain growth (GG) region, and d) the weld fusion boundary (FB).

This microstructure made it difficult to accurately identify the IC boundaries and therefore the Ac_1 line and Ac_3 line locations are only approximate. This meant that the accuracy of the HAZ half-width measurements was diminished; however, the comparison between different HSLA '17s' welds was good if made to the approximate location of the Ac_3 line. The presence of larger BM ferrite grains near the Ac_3

line was easier to identify than the first signs of newly refined grains that were near the Ac_1 line. This was why the HAZ half-width measurement was taken from the weld centerline to the approximate location of the Ac_3 line.

The image in Figure B.2c shows the microstructure that was observed in the transition between the GR region and the GG region. This area had completely formed into austenite during welding. The austenite at lower peak temperature had reformed into refined grains, which were similar to the refined grains within the IC region. As the peak temperature increased throughout these regions, the austenite grains grew larger. This is indicated on the image with an arrow that points from the smaller grains in the GR region to the larger grains in the GG region. Upon cooling, the grains transformed into different forms of ferrite (polygonal and Widmanstätten), with minimal evidence of pearlite, bainite, or martensite.

The image in Figure B.2d shows the transition from the GG region into the FZ. The fusion boundary is labelled 'FB'. Large columnar grains were observed that had formed at the FB and extended into the FZ to the right. These were directed towards the centerline of the weld FZ. Large prior austenite grain boundaries are labelled 'AGB' on the image. These were located within the GG region of the HAZ microstructure. These large grains had reformed during cooling with a layer of pro-eutectoid ferrite at the boundary. Within the large grain, there were traces of different forms of refined ferrite, Widmanstätten ferrite, and potentially some upper and lower bainite [73].

HAZ Half-width Measurements

The selected welds from the Phase 2 welding trials on the HSLA '17s' sheet steel were cross-sectioned and the Ac_3 HAZ half-width was measured. The results are shown in Table B.1. In the table, the welds are in order from lowest relative heat input to highest relative heat input. The smallest HAZ half-widths were measured on the lowest heat input welds, and it was observed that increasing the relative heat input provided higher HAZ half-width measurements. This trend was expected and was similar to

the trend observed from the DP600 ‘16s’ HAZ half-width measurements. These welds were all relatively close to full penetration.

Table B.1: Welded HSLA ‘17s’ sheet steel HAZ half-width measurements.

Weld Code	Weld Parameters [Trim, TS, WFS, CTWD]	H_{rel} [J/mm]	Root Penetration [%]	Average Ac_3 HAZ Half-Width [mm]
TB72	[1.00, 19.4 mm/s, 169 mm/s, 14.3 mm]	197	96.1%	3.35
TB86	[1.00, 20.3 mm/s, 212 mm/s, 14.3 mm]	213	90.7%	3.37
TB84	[1.00, 23.3 mm/s, 254 mm/s, 14.3 mm]	226	82.2%	3.68
TB83	[1.15, 22.4 mm/s, 212 mm/s, 14.3 mm]	271	81.8%	4.36
TB96	[1.15, 19.1 mm/s, 169 mm/s, 14.3 mm]	293	108.1.2%	4.54
TB97	[1.15, 21.2 mm/s, 212 mm/s, 14.3 mm]	304	95.5%	4.77
TB79	[1.25, 19.1 mm/s, 212 mm/s, 14.3 mm]	342	102.8%	5.29

The Ac_3 HAZ half-width measurements are plotted against their respective relative heat inputs in Figure B.3. The HAZ half-width measurements formed a linear trend. A similar linear trend for the DP600 ‘16s’ Ac_3 HAZ half-width measurements is included on the chart. There was a difference between the HSLA ‘17s’ and the DP600 ‘16s’ Ac3 HAZ half-width measurements of approximately 2 mm. This difference was attributed to the difference in sheet thickness and slight differences in the steel phase diagram. The HSLA ‘17s’ sheet steel had a thickness of approximately 1.80 mm, which was approximately 0.15 mm thicker than the DP600 ‘16s’ sheet steel. This meant that for the same welding heat input, the HSLA ‘17s’ sheet steel would have acted as a more effective path for heat transfer than the DP600 ‘16s’ sheet steel and therefore was not affected as far into the BM.

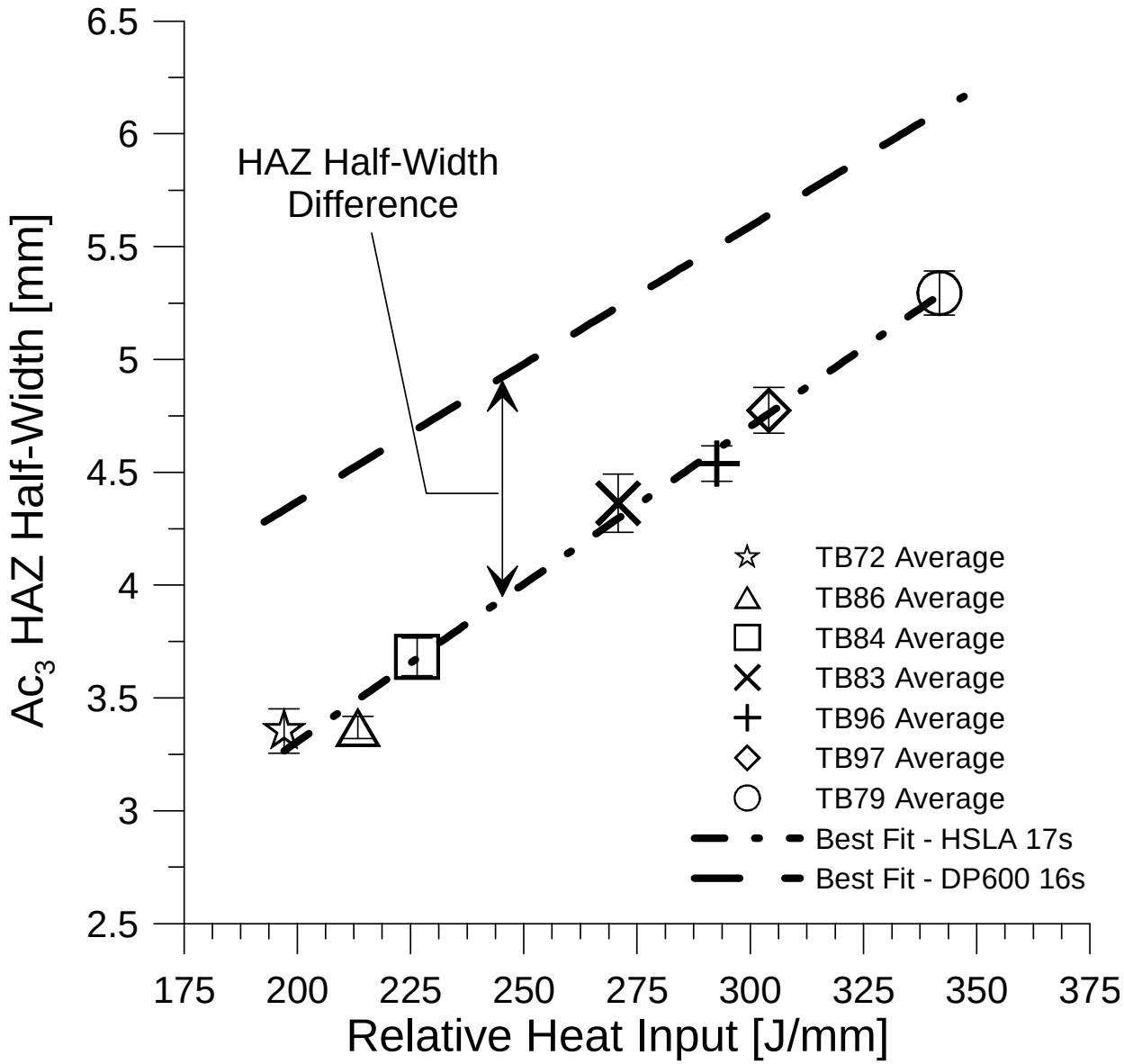

Figure B.3: The Ac_3 half-width measurements verses relative heat input for the HSLA '17s' sheet steel welds.

Two example images of HSLA ‘17s’ welded cross-sections that were used to measure the HAZ half-widths are shown in Figure B.4. The weld centerline, the Ac_3 line, and the Ac_1 line are marked on the images.

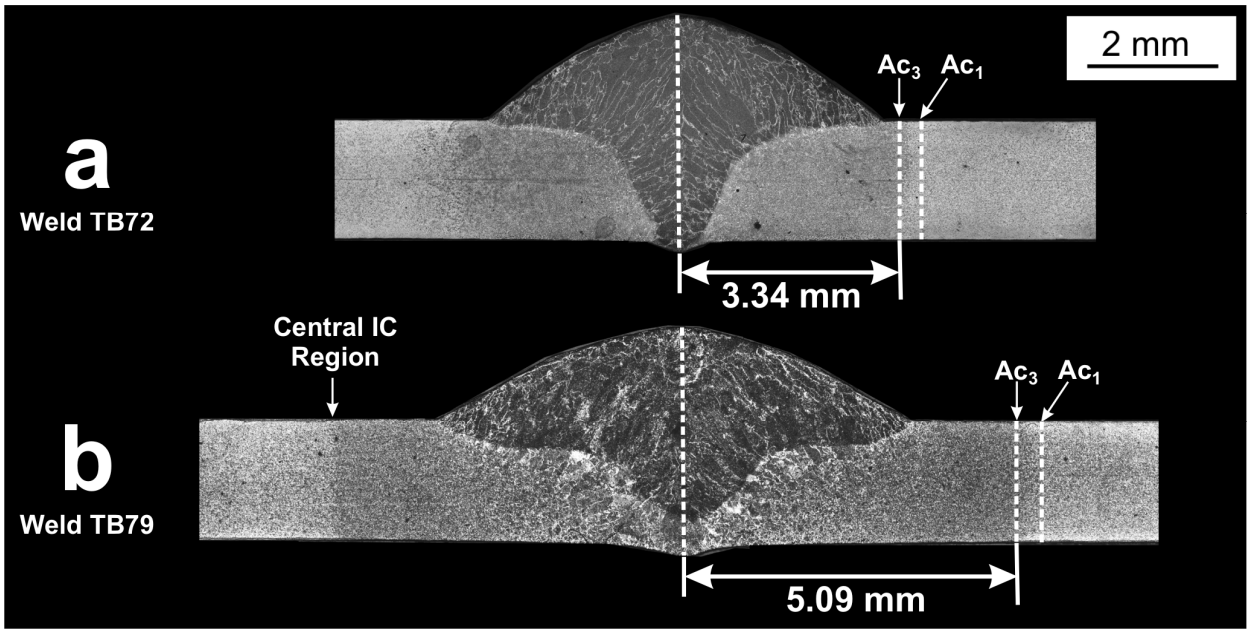

Figure B.4: Example images that were used for the HSLA ‘17s’ sheet steel HAZ measurements of the half-width distances from the weld centerline to the Ac_3 line. Shown is a) the lowest heat input weld, TB72, and b) the highest heat input weld, TB79.

The image in Figure B.4a shows a cross-section from the lowest heat input weld (TB72). A sample measurement of the Ac_3 HAZ half-width for this cross-section is shown, which was measured and found to be 3.34 mm. The average Ac_3 HAZ half-width for the TB72 weld was 3.35 ± 0.10 mm. The image in Figure B.4b shows a cross-section taken from the highest heat input weld (TB79). The average Ac_3 HAZ half-width for the TB79 weld was 5.29 ± 0.10 mm. The transition line within the IC region that was visible on these macroscopic images is labelled ‘central IC region’. This line was easily identified on the majority of HSLA ‘17s’ weld cross-sections. Based on the analysis of the HSLA ‘17s’ microstructure, this distinct macroscopic line was approximately centered between the Ac_1 line and Ac_3 line; however, while measuring Ac_3 HAZ half-width, this line was used to approximate the location of the Ac_3 line.

Microhardness Profile Results

The selected welds were taken to ArcelorMittal Dofasco, Inc. [48] and were tested with a Vicker`s microhardness profile. An example of a typical HSLA '17s' welded sheet steel microhardness profile is shown in Figure B.5. The hardness was relatively constant at locations within the BM region. The BM hardness that is indicated on the profile was an average value that was calculated with the indentations that were at least 1 mm outside of the central IC regions on either side of the weld HAZ. Using these indentations, the BM hardness was found to be 141 ± 6.1 VHN. The hardness increased above the BM hardness at locations within the IC, GR, and GG regions of the HAZ. This increase was gradual and reached a peak at the FZ. These HAZ regions had most likely increased in hardness due to the significant grain refinement that was observed and due to the potential emergence of some bainite. The FZ appeared to match the GG region hardness and was significantly higher than the BM hardness.

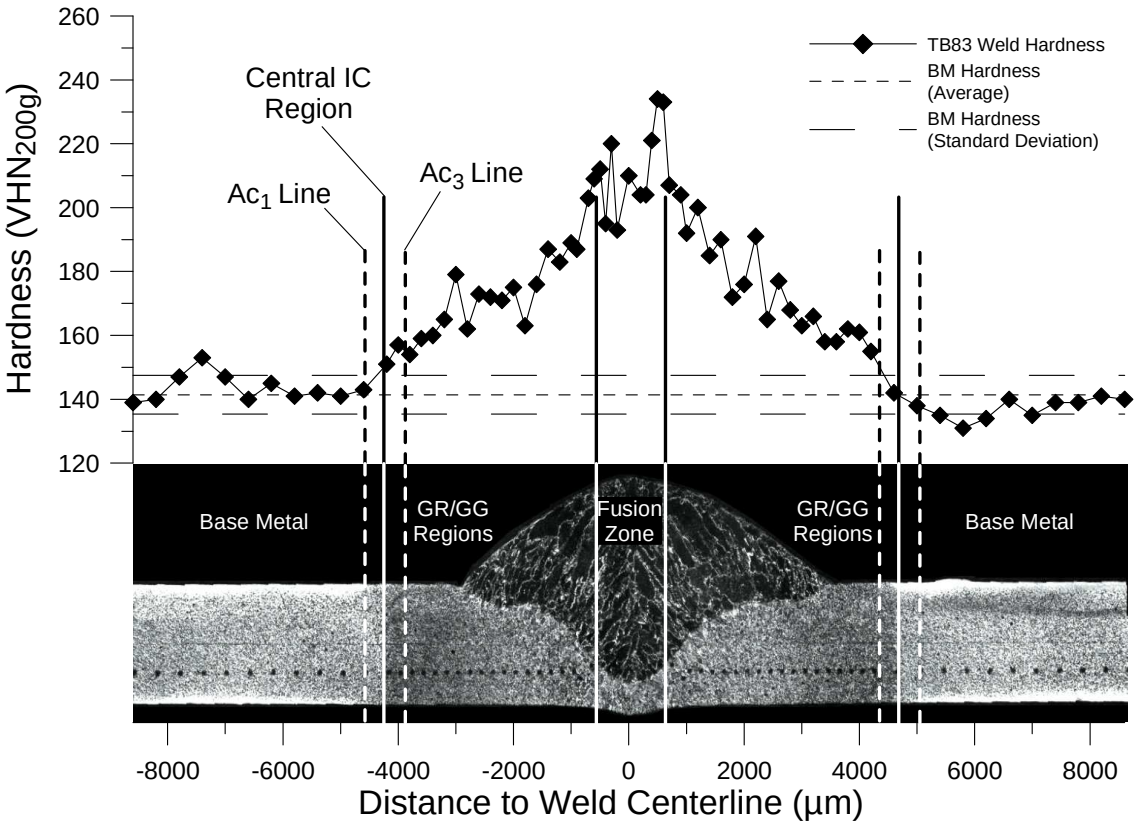

Figure B.5: A typical microhardness profile of an HSLA '17s' welded specimen.

Transverse weld tensile Tests

The 7 selected welds from the Phase 2 welding trials were used to make bead-on-plate welds onto 254 mm × 203 mm HSLA '17s' sheet steel coupons. These welded coupons were used to machine uniaxial transverse weld tensile specimens. The tensile specimens were used for uniaxial tensile testing to complete fracture.

The results from the uniaxial tensile tests showed that for all of the seven selected weld parameter sets from Phase 2 welding trials, 100% of the uniaxial tensile tests failed in the BM. An example of this failure type is shown in Figure B.6. The specimen shown in the figure was from the welded coupon that had used the highest heat input weld parameters (TB79). The BM failure location typically had fracture planes that were perpendicular to the loading direction or to a maximum angle of approximately 22° offset from the specimen cross-sectional plane.

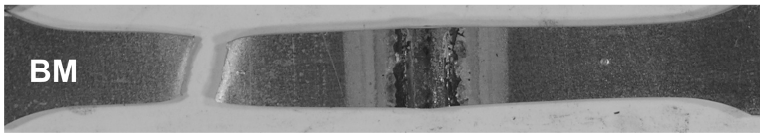

Figure B.6: All of the HSLA '17s' welded tensile specimens failed within the base-metal during uniaxial tensile testing. The image shows the highest heat input weld (TB79) to illustrate this type of weld failure.

These uniaxial tensile testing results suggested that 100% joint efficiency had been achieved. There were no observations from the tests that were used to classify the HSLA '17s' welds that required further study. The HSLA '17s' sheet steel welding trials had not provided a transition of failure location in welded uniaxial tensile specimens and therefore were not studied further.

Appendix C

Summary of Results

From this study, the following observations were made:

- ☑ The DP steel sheet did not have a uniform homogeneous microstructure, but exhibited bands of varying composition and hardness parallel to the rolling direction, especially down the center of the sheet, which was primarily due to macro-segregation in the original rolling ingot. This was especially true in the 1.65 mm DP600 sheet steel, where appreciable amounts of bainite/carbide had formed in the BM microstructure. This made it difficult to obtain consistent microhardness profiles in the horizontal direction through the BM, HAZ, and weld metal. Microhardness mapping and the use of ATTH helped to alleviate the problems associated with variability in the microhardness profiles due to variability in the parent steel microstructure.
- ☑ The 1.65 mm thick and the 1.80 mm thick DP600 '16s' sheet steel could be welded with a full penetration bead-on-plate weld from a GMAW-P welding process and achieve 100% BM failure during uniaxial transverse weld tensile testing and retain the DP600 design UTS.
- ☑ Welded DP600 tensile specimens that fractured in the BM failure location during uniaxial transverse weld tensile testing were consistently observed to have a softened region of microstructure located in the GMAW-P weld HAZ. The softened region for BM failure mode welds was always located immediately adjacent to the Ac_1 line (location where the microstructure had been elevated to a temperature where austenitization initiated) in the subcritical (SC) microstructural region (occurred at temperature just below the Ac_1 temperature). This was an unexpected finding of the study because softening had been cited in the literature as the cause of HAZ fracture.
- ☑ Welded DP600 tensile specimens that fractured in the HAZ failure location during uniaxial transverse weld tensile testing were consistently observed to have a softened region of microstructure located in the GMAW-P weld HAZ. Necking during uniaxial tensile testing

was observed to localize in this softened region. This was an expected finding of the study because HAZ softening was known from the literature to weaken the joint at this location.

- ☑ When the DP600 sheet thickness was increased from 1.68 mm to 1.75 mm in thickness, there was a shift from HAZ failure to BM failure during uniaxial transverse weld tensile testing for similar relative heat input welds. This suggested that a small increase in sheet thickness (~4%) could be welded with much higher heat input (~46%) and would retain high joint efficiency.
- ☑ Uniaxial transverse weld tensile specimens from GMAW-P welded 1.20 mm, 1.65 mm, and 1.80 mm thick DP600 sheet steels that fractured in the BM failure location and/or the HAZ failure location were observed to have a minimal change of UTS when compared to the unwelded BM UTS. Welds of similar geometry, HAZ width, and relative heat input were observed to have more displacement after localized necking had occurred when failure occurred in the BM when compared to the displacement to failure that occurred when the specimens failed in the HAZ.
- ☑ The GMAW-P welded uniaxial transverse weld tensile specimens that were machined from the 1.20 mm thick DP780 sheet steel were observed to fracture in the HAZ failure location in 100% of the uniaxial tensile tests and had minimal change in UTS when compared to the unwelded BM UTS.
- ☑ The GMAW-P welded uniaxial transverse weld tensile specimens that were machined from the 1.20 mm DP980 ‘23s’ sheet steel were observed to fracture in the HAZ failure location through 100% of uniaxial tensile testing and had a significant decrease (~28%) in UTS when compared to the unwelded BM UTS.
- ☑ The GMAW-P welded HAZ that was observed in the 1.65 mm thick DP600 sheet steel consistently had an increase in hardness in the IC, GR, GG, and FZ microstructural regions. The increase in hardness in the IC microstructural region was consistently associated with an increase in percent area of martensite in this region that was caused by

the formation of renucleated martensite. The renucleated martensite had formed when that region of microstructure had been elevated to temperatures above the Ac_1 line and below the Ac_3 line.

- ☑ The HAZ of the GMAW-P welded 1.65 mm thick DP600 sheet steel always had a softened region of microstructure in the subcritical zone immediately adjacent to the Ac_1 line. Tempered martensite was identified in this region of the weld HAZ microstructure. The size of the softened region for a weld that consistently fractured in the BM, when compared to the softened zone width from a weld that consistently fractured in the HAZ, was relatively small (~10%) for the large difference in weld heat input (~45%).
- ☑ The GMAW-P welded HAZ for the 1.80 mm thick DP600, 1.20 mm thick DP600, and 1.20 mm thick DP780 sheet steels were observed to have increased hardness in the IC region due to a visual increase in the percent area of martensite compared to the BM. These steels were also observed to have a softened region in the SC microstructural region immediately adjacent to the Ac_1 line.
- ☑ The GMAW-P welded Cr-Mo DP sheet steels that were analysed using an ATTH profile were observed to have a hardened subcritical (H-SC) region. The H-SC was located between the softened subcritical (S-SC) region and the BM region of the weld HAZ. The H-SC was observed to be wider and have higher peak hardness for welds that were made at a higher relative heat input.
- ☑ The GMAW-P welded HAZ of the 1.20 mm thick DP980 sheet steel was the only non-Cr-Mo DP sheet steel in the study. It exhibited a softened region that was located across the IC and SC microstructural regions. The size of this softened region was significantly larger than all Cr-Mo DP sheet steel welds that were analysed. The HAZ for this welded sheet steel was not observed to have a H-SC region and softening extended to the BM region.

- ☑ The fracture surface of the 1.65 mm thick DP600 sheet steel that had fractured in the HAZ failure location during uniaxial transverse weld tensile testing was observed to have greater reduction of cross-sectional area than a weld that had fractured in the BM failure location. This was caused by increased material flow in the softened region of microstructure, which led to the development of more significant tri-axial strain prior to fracture.
- ☑ Both BM and HAZ failure modes were observed to have a dimpled fracture surface and the largest voids were associated with nucleation around second-phase incoherent particles such as aluminum oxide particles introduced from the steel killing step during making of the steel. Nucleation at the ferrite-martensite interfaces was observed immediately adjacent to the facture surface (observation of cross-sectioned samples) and was more significant in welds that had fractured in the HAZ during uniaxial transverse weld tensile testing.
- ☑ The welded and unwelded BM fracture surfaces were visually interchangeable. The HAZ fracture surface was observed to have a greater reduction of cross-sectional area and had more numerous small shear tearing ledges.
- ☑ The SC region of welded DP steel, immediately adjacent to the Ac_1 line, was consistently observed to have lower percent area of martensite when compared to the BM. There was visual evidence that this region contained tempered martensite.
- ☑ HAZ half-width increased as welding heat input was increased. Intercritical (IC) region width increased as welding heat input increased, but also decreased as sheet thickness increased; the width of the IC region appeared to be a good indication of the relative width of the S-SC.
- ☑ The GMAW-P bead-on-plate weld HAZ of Cr-Mo DP sheet steels exhibited four distinct regions of hardness when analysed with an ATTH profile. The four regions of hardness were the BM, H-SC, S-SC, and IC.

- ☑ There were no HSLA weld fractures associated with the HAZ or FZ through all of testing. The HSLA design total elongation was slightly diminished due to a hardened HAZ. Hardness had increased above the BM properties in the microstructural regions that had been elevated to temperatures that were above the Ac_1 line during welding. These were the weld intercritical (IC), grain-refined (GR), grain growth (GG), and fusion zone (FZ) microstructural regions.